DEEP EUTECTIC SOLVENTS/COMPLEX SALTS-BASED ELECTROLYTE FOR NEXT GENERATION RECHARGEABLE BATTERIES

EDITED BY: Du Yuan, Gen Chen, Chuankun Jia and Haitao Zhang
PUBLISHED IN: Frontiers in Chemistry

frontiers Research Topics

Frontiers eBook Copyright Statement

The copyright in the text of individual articles in this eBook is the property of their respective authors or their respective institutions or funders. The copyright in graphics and images within each article may be subject to copyright of other parties. In both cases this is subject to a license granted to Frontiers.

The compilation of articles constituting this eBook is the property of Frontiers.

Each article within this eBook, and the eBook itself, are published under the most recent version of the Creative Commons CC-BY licence. The version current at the date of publication of this eBook is CC-BY 4.0. If the CC-BY licence is updated, the licence granted by Frontiers is automatically updated to the new version.

When exercising any right under the CC-BY licence, Frontiers must be attributed as the original publisher of the article or eBook, as applicable.

Authors have the responsibility of ensuring that any graphics or other materials which are the property of others may be included in the CC-BY licence, but this should be checked before relying on the CC-BY licence to reproduce those materials. Any copyright notices relating to those materials must be complied with.

Copyright and source acknowledgement notices may not be removed and must be displayed in any copy, derivative work or partial copy which includes the elements in question.

All copyright, and all rights therein, are protected by national and international copyright laws. The above represents a summary only. For further information please read Frontiers' Conditions for Website Use and Copyright Statement, and the applicable CC-BY licence.

ISSN 1664-8714
ISBN 978-2-88966-376-7
DOI 10.3389/978-2-88966-376-7

About Frontiers

Frontiers is more than just an open-access publisher of scholarly articles: it is a pioneering approach to the world of academia, radically improving the way scholarly research is managed. The grand vision of Frontiers is a world where all people have an equal opportunity to seek, share and generate knowledge. Frontiers provides immediate and permanent online open access to all its publications, but this alone is not enough to realize our grand goals.

Frontiers Journal Series

The Frontiers Journal Series is a multi-tier and interdisciplinary set of open-access, online journals, promising a paradigm shift from the current review, selection and dissemination processes in academic publishing. All Frontiers journals are driven by researchers for researchers; therefore, they constitute a service to the scholarly community. At the same time, the Frontiers Journal Series operates on a revolutionary invention, the tiered publishing system, initially addressing specific communities of scholars, and gradually climbing up to broader public understanding, thus serving the interests of the lay society, too.

Dedication to Quality

Each Frontiers article is a landmark of the highest quality, thanks to genuinely collaborative interactions between authors and review editors, who include some of the world's best academicians. Research must be certified by peers before entering a stream of knowledge that may eventually reach the public - and shape society; therefore, Frontiers only applies the most rigorous and unbiased reviews.
Frontiers revolutionizes research publishing by freely delivering the most outstanding research, evaluated with no bias from both the academic and social point of view. By applying the most advanced information technologies, Frontiers is catapulting scholarly publishing into a new generation.

What are Frontiers Research Topics?

Frontiers Research Topics are very popular trademarks of the Frontiers Journals Series: they are collections of at least ten articles, all centered on a particular subject. With their unique mix of varied contributions from Original Research to Review Articles, Frontiers Research Topics unify the most influential researchers, the latest key findings and historical advances in a hot research area! Find out more on how to host your own Frontiers Research Topic or contribute to one as an author by contacting the Frontiers Editorial Office: researchtopics@frontiersin.org

DEEP EUTECTIC SOLVENTS/COMPLEX SALTS-BASED ELECTROLYTE FOR NEXT GENERATION RECHARGEABLE BATTERIES

Topic Editors:
Du Yuan, Nanyang Technological University, Singapore
Gen Chen, Central South University, China
Chuankun Jia, Changsha University of Science and Technology, China
Haitao Zhang, Chinese Academy of Sciences, China

Citation: Yuan, D., Chen, G., Jia, C., Zhang, H., eds. (2021). Deep Eutectic Solvents/Complex Salts-Based Electrolyte for Next Generation Rechargeable Batteries. Lausanne: Frontiers Media SA. doi: 10.3389/978-2-88966-376-7

Table of Contents

frontiers in Chemistry

EDITORIAL
published: 26 November 2020
doi: 10.3389/fchem.2020.613353

Editorial: Deep Eutectic Solvents/Complex Salts-Based Electrolyte for Next Generation Rechargeable Batteries

Du Yuan[1]*, Gen Chen[2], Chuankun Jia[3] and Haitao Zhang[4]

[1] School of Materials Science and Engineering, Nanyang Technological University, Singapore, Singapore, [2] School of Materials Science and Engineering, Central South University, Changsha, China, [3] School of Materials Science and Engineering, Changsha University of Science and Technology, Changsha, China, [4] Key Laboratory of Green Process and Engineering, Institute of Process Engineering, Chinese Academy of Sciences, Beijing, China

Keywords: SEI, redox, electrochemisitry, rechargeable batteries, electrolyte

Editorial on the Research Topic

Deep Eutectic Solvents/Complex Salts-Based Electrolyte for Next Generation Rechargeable Batteries

OPEN ACCESS

Edited by:
Nosang Vincent Myung,
University of Notre Dame,
United States

Reviewed by:
Abhishek Lahiri,
Brunel University London,
United Kingdom

***Correspondence:**
Du Yuan
aduyuandu@gmail.com

Specialty section:
This article was submitted to
Electrochemistry,
a section of the journal
Frontiers in Chemistry

Received: 02 October 2020
Accepted: 22 October 2020
Published: 26 November 2020

Citation:
Yuan D, Chen G, Jia C and Zhang H
(2020) Editorial: Deep Eutectic
Solvents/Complex Salts-Based
Electrolyte for Next Generation
Rechargeable Batteries.
Front. Chem. 8:613353.
doi: 10.3389/fchem.2020.613353

Recent years have seen an expansion of renewable energy technologies driven by global demands for energy alongside social and environmental concerns. One of the most significant solutions, rechargeable batteries have promising features which include high capacity, energy density, rate capability, long lifetime, and cost-effectiveness. As the key component in energy storage devices, the electrolyte has had a major impact on the chemistry/electrochemistry of rechargeable batteries/cells for a number of reasons. These include its potential window, which limits the redox potential of an electrochemical reaction. Its electrochemical activity and conductivity also influence the electrochemical reaction and consequently the battery performance. The composition, as well as the stability, of rechargeable batteries, shapes the electrolyte-electrode interface. Furthermore, its corrosivity cannot be neglected. For these reasons, researchers are highly motivated toward breakthroughs in battery performance, exploring the fundamental properties of electrolytes based on novel formulation/synthesis. Hence, this special issue of *Deep Eutectic Solvents/Complex Salts-Based Electrolyte for Next Generation Rechargeable Batteries* focuses on the effects of electrolytes on the electrochemistry/chemistry of rechargeable batteries and cells.

In this Research Topic, representative types of electrolytes are discussed in relation to next-generation rechargeable batteries, including ionic liquid, solid state electrolyte (polymeric and inorganic), multivalent electrolyte (aqueous and non-aqueous) for multivalent ion batteries, aqueous, and a novel organic electroactive molecule-based electrolyte for flow batteries. Recent developments build upon the correlation between design and synthesis of the electrolyte, its properties, and the related electrochemical properties and performance of batteries and cells. From the perspective of electrolyte design, contributions include exploration of formulating ionic liquid toward designed ion separation for tuning the performance of supercapacitors (Pan et al.). Other submissions discuss the compositing strategy for a polyethylene oxide-based solid state electrolyte for flexible device and lithium metal batteries (Zhao et al.). Another study considers the emerging ionic conductor for an Mg ion solid state electrolyte (Zhan et al.), where another describes how electrolyte modification can be used to depress zinc dendrite in zinc-based flow batteries (Guo et al.). The electrolyte concentration, as well as cation/proton types of diffusion kinetics in a vanadium flow battery (Gui et al.) are also interest. Another contribution examines the molecular design of organic electroactive molecules via functional group modification for redox flow batteries

(Zhong et al.). Furthermore, the electrolyte-electrode interface is also emphasized in this topic, where its material characteristics and stability strongly influence the kinetics and cycling stability of batteries/cells for example in an *in situ* Scanning Electrochemical Microscopy study, which revealed that the SEI formation on carbon depends on voltage range (Liu et al.), or, as described elsewhere, regulating the nature of ionic liquid and the interface compatibility (Pan et al.). Another study designed a novel 3D $MoSe_2$ template for constructing stable SEI for reversible stripping/plating of metallic Mg (Shen et al.), where others discuss regulating the interface between electrolyte and Zn for preventing zinc dendrites (Guo et al.), or investigating the interfacial charge transfer in aqueous zinc electrolytes for zinc ion batteries (Guo et al.).

We would like to thank all the authors for their valuable contributions and the reviewers for their thoughtful insights and suggestions. It is essential to further examine and share the fundamentals of the chemistry and electrochemistry of electrolytes, which serves as the basis for the successful creation of next-generation rechargeable energy storage devices.

Although the papers included here provide significant insights, there are still important developments and points for the future development of this area of research. Safety is a long-term pursuit in rechargeable batteries, and further insights into safe electrolyte design with promising electrochemical properties are essential. The pursuit of high performance and long lifetime in rechargeable batteries will also need to go further than constructing a database of electrolytes, and future explorations on the relation between electrolytes and battery chemistry are essential. It would also be promising to uncover the correlation between electrolyte and charge storage mechanism for any novel electrodes designs, which will synergistically guide the development of new generation battery systems. Moreover, the complexity of the electrolyte-electrode interface creates room for exploring battery chemistry, which will drive cutting-edge characterization and analysis tools and in parallel, boost the development of new battery systems, especially those for utilizing metal anode based or multivalent ion batteries.

We hope that this special issue will inspire future research in the development of novel electrolytes and drive the development of new generation rechargeable energy storage devices. These endeavors will pave the way for realizing a green and sustainable society.

AUTHOR CONTRIBUTIONS

DY, GC, CJ, and HZ co-edited this special issue. All authors contributed to the article and approved the final manuscript.

Conflict of Interest: The authors declare that the research was conducted in the absence of any commercial or financial relationships that could be construed as a potential conflict of interest.

frontiers in Chemistry

MINI REVIEW
published: 25 February 2020
doi: 10.3389/fchem.2020.00125

Recent Development of Mg Ion Solid Electrolyte

Yi Zhan*, Wei Zhang, Bing Lei, Hongwei Liu and Weihua Li

School of Chemical Engineering and Technology, Sun Yat-sen University, Zhuhai, China

Although the successful deployment of lithium-ion batteries (LIBs) in various fields such as consumer electronics, electric vehicles and electric grid, the efforts are still ongoing to pursue the next-generation battery systems with higher energy densities. Interest has been increasing in the batteries relying on the multivalent-ions such as Mg^{2+}, Zn^{2+}, and Al^{3+}, because of the higher volumetric energy densities than those of monovalent-ion batteries including LIBs and Na-ion batteries. Among them, magnesium batteries have attracted much attention due to the promising characteristics of Mg anode: a low redox potential (−2.356 V vs. SHE), a high volumetric energy density (3,833 mAh cm^{-3}), atmospheric stability and the earth-abundance. However, the development of Mg batteries has progressed little since the first Mg-ion rechargeable battery was reported in 2000. A severe technological bottleneck concerns the organic electrolytes, which have limited compatibility with Mg anode and form an Mg-ion insulating passivation layer on the anode surface. Consequently, beneficial to the good chemical and mechanical stability, Mg-ion solid electrolyte should be a promising alternative to the liquid electrolyte. Herein, a mini review is presented to focus on the recent development of Mg-ion solid conductor. The performances and the limitations were also discussed in the review. We hope that the mini review could provide a quick grasp of the challenges in the area and inspire researchers to develop applicable solid electrolyte candidates for Mg batteries.

Keywords: Mg batteries, solid electrolyte, phosphate, borohydride, chalcogenides, metal-organic frame (MOFs)

Edited by:
Du Yuan,
Nanyang Technological University, Singapore

Reviewed by:
Jin Zhao,
Nanjing University of Posts and Telecommunications, China
Tao Dong,
Institute of Process Engineering (CAS), China

***Correspondence:**
Yi Zhan
zhany9@mail.sysu.edu.cn

Specialty section:
This article was submitted to Electrochemistry, a section of the journal Frontiers in Chemistry

Received: *06 January 2020*
Accepted: *11 February 2020*
Published: *25 February 2020*

Citation:
Zhan Y, Zhang W, Lei B, Liu H and Li W (2020) Recent Development of Mg Ion Solid Electrolyte. Front. Chem. 8:125. doi: 10.3389/fchem.2020.00125

INTRODUCTION

Since the commercialization proposed by Sony in 1990, Li-ion batteries (LIBs) have dominated in various fields, such as electronics, electric vehicles, and smart-grids, as the energy storage system (Goodenough and Kim, 2010; Etacheri et al., 2011; Devi et al., 2020). As the most successful battery technology nowadays, LIBs possess several advantages including high energy density, good capacity retention, no memory effect and low self-discharge, surpassing last generation of batteries i.e., lead-acid batteries, nickel metal hydride batteries (Li et al., 2020; Zeng et al., 2020). However, the growing demand for battery with even higher energy density is difficult to be satisfied by LIBs because their energy storage relies on the intercalation mechanism (Cabana et al., 2010; Choi and Aurbach, 2016; Hong et al., 2020). To further increase the energy density, great interest has been again aroused to develop lithium batteries directly using Li metal as the anode, which has remained quiescence from 1980s. The technical challenge of Li anode comes from the lithium dendrite formed on surface during cycling, which could penetrate the separator and result in the short-circuit of the battery and thus fire-catching or even explosion (Janek and Zeier, 2016; Chen et al., 2020). Despite the endeavors to suppress the dendrite formation, the progress is limited and none of the solutions meets the commercial standards (Cengiz et al., 2019; Michel et al., 2019).

Therefore, next generation advanced rechargeable batteries, such as multivalent metal (Mg, Ca, Al etc.) batteries, have aroused much interest due to high energy density in theory (Aurbach et al., 2000, 2007; Yoo et al., 2013; Wang et al., 2019). Among them, rechargeable Mg batteries are considered as the most promising battery technology because of the highest theoretical volumetric energy density of Mg anode (3,866 mAh cm^{-3}), surpassing that of Li anode (2,066 mAh cm^{-3}) (Aurbach et al., 2000; Bucur et al., 2015). While Li metal reacts violently with water, the reaction between Mg and water is much more stable because of the passive Mg hydroxide/oxide film formed on the surface. In addition, there is no dendrite formed for Mg anode during the reversible plating/stripping process. These advantages endow Mg anode high safety compared to Li anode (Aurbach et al., 2001). In addition, Mg is more abundant relative to Li in earth crust.

Several key challenges, however, should be overcome before the Mg battery technology comes true (Yoo et al., 2013; Saha et al., 2014; Bucur et al., 2015; Wang et al., 2020). For instance, due to the electrochemical reduction, a passivation layer is formed on Mg anode surface once Mg is on contact with conventional carbonate-based electrolyte solvents used in LIBs (Muldoon et al., 2012). While conducting for Li ion in LIBs, solid electrolyte interface (SEI) is insulating for Mg ion and thus prevents the conventional electrolyte solvents to be used in Mg batteries (Pan et al., 2020). Novel electrolytes are therefore developed for Mg batteries and most of them are based on Grignard reagents dissolved in ethereal solvents or glymes such as tetrahydrofuran (THF) (Deivanayagam et al., 2019). Nevertheless, concerns on safety and stability still remain for the high vapor pressure and the high flammability of ether-based organic solvents. Furthermore, the presence of Cl^- anions in Grignard reagents results in the high corrosion and the electrolytes also have narrow electrochemical operation window (<2 V vs. Mg/Mg^{2+}), indicating limited practical application (Tutusaus et al., 2015). Therefore, solid-state electrolyte employed by all-solid-state Mg batteries is a safe alternative in terms of heat and mechanical shock resistance (Ikeda et al., 1987; Imanaka et al., 1999; Janek and Zeier, 2016; Famprikis et al., 2019). Nevertheless, the development of solid-state Mg ion conductor with sufficient conductivity is a key challenge at ambient temperature because of the sluggish mobility resulted by the high charge density of Mg ion (Janek and Zeier, 2016; Famprikis et al., 2019). Many efforts are thus devoted to improve the mobility of Mg ion within the solid conductor and the target is 10^{-3}-10^{-4} S cm^{-1} at ambient temperature, which is comparable with those of solid electrolytes used in lithium or sodium batteries (Janek and Zeier, 2016).

In this mini review, we will present a comprehensive development of solid Mg ion conductors, including phosphates, borohydrides, metal-organic frameworks (MOFs) and chalcogenides. It highlights the performance and the limitation of each material and also discusses the conduction mechanism on the basis of the crystal structure and the strategy to improve the ionic conductivity.

PHOSPHATES-BASED Mg ION SOLID CONDUCTORS

The study on solid-state ionic conductors have aroused much interest due to the merits of high stability and good safety. It is well-accepted that the migration of ion species is quite difficult in a solid, highly affected by the valence states of the ion species. Therefore, while there are many kinds of monovalent ionic conductors with high conductivity, few choices are available for multivalent ions such as Mg^{2+} (Janek and Zeier, 2016; Famprikis et al., 2019). Na^+ superionic conductor (NASICON) is well-known for permitting the smooth migration of Na ion species due to the well-ordered three-dimensional network structure, and therefore it is highly interested to develop NASICON-type $MZr_4(PO_4)_6$ ($M = Ca^{2+}, Sr^{2+}, Mg^{2+}, Ba^{2+}$) solids as multivalent ionic conductors (Lee et al., 2019; Shao et al., 2019).

The earliest report on NASICON-type Mg^{2+} conductor came from Ikeda in 1987, who studied the system of Mg-Zr-PO_4 in various molar ratios as Mg ion conductor using mechanochemical synthesis (Ikeda et al., 1987). Among them, $MgZr_4(PO_4)_6$ (MZP) showed the highest conductivity of 2.9×10^{-5} and 6.1×10^{-3} S cm^{-1} at 400 and 800°C, respectively. The Tubandt's method and the electron probe microanalysis were used to confirm the charge carrier to be Mg ions. According to X-ray diffraction (XRD) measurements, the author simply claimed that the crystal structure of MZP similar to $NaZr_2(PO_4)_3$, resulted in the best conductivity relative to analogs with other ratios, while no further evidence was provided in the report.

Imanaka and Adachi continued the exploration on NASICON-type Mg^{2+} conductor. In 1999, they intentionally varied the starting materials of MZP to be non-stoichiometric ratios so as to produce the secondary phase of $Zr_2O(PO_4)_2$ (Imanaka et al., 1999, 2000a). With the increase of the $Zr_2O(PO_4)_2$ content in the composite, the Mg ion conductivity increased to a maximum value of 6.92×10^{-3} S cm^{-1} at 800°C for $Mg_{1+x}Zr_4P_6O_{24+x}$+$xZr_2O(PO_4)_2$ with $x = 0.4$. Too high content of $Zr_2O(PO_4)_2$ however deteriorated the conductivity of the composite because of the insulating property of $Zr_2O(PO_4)_2$. The presence of secondary phase was believed to enhance the relative density and thus the ionic conductivity by microscopically dispersing the $Zr_2O(PO_4)_2$ secondary phase in the composite.

In 2001, Imanaka used the substitution strategy to improve the ionic conductivity of MZP by partially replacing Zr^{4+} with Nb^{5+} (Imanaka et al., 2000b). The substitution was used to statistically distribute mobile Mg ions to make a smooth Mg ion diffusion but it also reduced the number of migrating Mg^{2+} ion species in the solid solution electrolyte. Thus, the optimum conductivity was observed at $x = 0.15$ in $Mg_{1-2x}(Zr_{1-x}Nb_x)_4P_6O_{24}$ with 7.7×10^{-4} S cm^{-1} at 600°C and 3.7×10^{-3} S cm^{-1} at 750°C, demonstrating little enhancement compared to pristine MZP.

Later in 2016, Imanaka and Tamura claimed that most of the attempts to obtain the NASICON-type structure of Mg ion conductor were unsuccessful, because of the small ionic radius of Mg^{2+} resulting in the formation of β-$Fe_2(SO_4)_3$-type structure at high temperature (Tamura et al., 2016). They selected $HfNb(PO_4)_3$ as the mother solid and partially substituted Hf^{4+} with Mg^{2+} to realize Mg^{2+} conduction. Although the ion conductivity of $(Mg_{0.1}Hf_{0.9})_{4/3.8}Nb(PO_4)_3$ at high temperature was lower than that of $Mg_{0.7}(Zr_{0.85}Nb_{0.15})_4(PO_4)_6$, the Mg^{2+} ion conductivity of the former at a moderate temperature of 300°C (2.1×10^{-6} S cm^{-1}) was 20 times higher than that of latter (1.1×10^{-7} S cm^{-1}). The authors proposed that the good ionic conductivity was resulted from the three-dimensionally well-ordered NASICON structure and also the presence of cations with a higher valence than that of the conducting cation Mg^{2+}, enabling the smooth ion migration of the latter.

Adamu and Kale proposed a sol-gel method to synthesize MZP (Adamu and Kale, 2016). The MZP synthesized in this work showed an ionic conductivity of 7.23×10^{-3} S cm^{-1} at 725°C. They attributed improvement in the conductivity to the sol-gel preparation route, which ensured synthesis at the molecular level and avoid the impurity produced by the solid-state route due to the inhomogeneous mixing.

Liang and Laine used spray pyrolysis method to synthesize $Mg_{0.5}Ce_{0.2}Zr_{1.8}(PO_4)_3$ nanopowders, where Ce^{4+} partially substituted Zr^{4+} in $Mg_{0.5}Zr_2(PO_4)_3$ (Liang et al., 2018). $Mg_{0.5}Ce_{0.2}Zr_{1.8}(PO_4)_3$ offered highest conductivity up to 3×10^{-6} S cm^{-1} at 280°C, which was comparable with the previous report by Imanaka.

Inspired by the fabrication of amorphous solid conductor for LIBs, such as Li_3PO_4, Su and Tsuruoka proposed a plasma-assisted atomic layer deposition method to fabricate amorphous oxygen-deficient $Mg_{2.4}P_2O_{5.4}$ thin film in 2019 (Cengiz et al., 2019; Su et al., 2019). It exhibited an ionic conductivity of 1.6 $\times 10^{-7}$ S cm^{-1} at 500°C. The hopping conduction of Mg ions in the disordered amorphous phosphate matrix was believed to result in the conductivity.

Despite the effort devoted to the development of phosphate-based Mg ion conductors, the progress is very limited and the ionic conductivity of Mg solid electrolyte based on MZP is never above 10^{-6} S cm^{-1} at moderate temperature of 300°C. The aim to function well at room temperature is still far for phosphate-based ionic conductors. It seems that phosphate-based materials are not ideal candidates of solid Mg ion conductors and it is necessary to turn to novel Mg ion conductors.

BOROHYDRIDE Mg ION SOLID CONDUCTORS

Since Mohtadi demonstrated the first fully inorganic and halide-free Mg electrolytes, enabling reversible Mg plating and stripping, in 2012, liquid electrolytes based on magnesium borohydride, $Mg(BH_4)_2$, have received significant attention (Mohtadi et al., 2012). Because of the reductive stability of the BH_4^- anion, $Mg(BH_4)_2$ also arouses the interest to develop as solid Mg ion conductor. However, the conductivity of $Mg(BH_4)_2$ is very low at room temperature (10^{-12} S cm^{-1} at 30°C), resulted by the firm tetrahedral sites of BH_4^- hindering the smooth migration of Mg ions. Proper modification of $Mg(BH_4)_2$ are thus necessary to improve the conductivity.

In 2014, Higashi first reported $Mg(BH_4)(NH_2)$ as a new class of solid-state Mg ion conductor (Higashi et al., 2014). The diffusion of Mg ions in $Mg(BH_4)(NH_2)$ was attributed to the Mg zigzag chain and tunneling structures in the *a* and *b* planes. It showed the ionic conductivity of 10^{-6} S cm^{-1} at 150°C and the electrochemical window of ∼3 V in estimation.

Le Ruyet and Janot followed the work on $Mg(BH_4)(NH_2)$ in 2019, and studied the influences of the synthesis parameters on the ionic conductivity (Le Ruyet et al., 2019). They carefully investigated the synthesis parameters and the ionic conductivity could reach as high as 3×10^{-6} S cm^{-1} at 100°C, which was three orders of magnitude higher than that reported by Higashi. The improvement in conductivity was attributed to the creation of a glass-ceramic-like composite due to the presence of an amorphous additional phase.

Roedern and Remhof synthesized a $Mg(BH_4)_2$ derivative by coordinating Mg^{2+} with a neutral bidentate ethylenediamine ligand to replace two BH_4 ligand (Roedern et al., 2017). It showed a high ionic conductivity of 5×10^{-8} S cm^{-1} at 30°C and 6×10^{-5} S cm^{-1} at 70°C. The good conductivity was attributed to the partially chelated, mixed coordination of Mg^{2+} leading to its high mobility. However, the electrochemical stability of this new phase is limited to 1.2 V vs. Mg/Mg^{2+}, due to the stability limitation by the ethylenediamine ligand.

Compared with phosphate-based Mg ion conductors, $Mg(BH_4)_2$ and its derives show a promising future as Mg ion conductors with high ionic conductivity at low temperature. Proper modification of $Mg(BH_4)_2$ are still necessary to improve the conductivity, stability and operating potential window.

CHALCOGENIDE Mg ION SOLID CONDUCTORS

Chalcogenide-based materials have been developed as solid conductors for Li ion and Na ion and have shown high ionic conductivity (Ramos et al., 2018; Xuan et al., 2018; Jia et al., 2019; Wang Y. et al., 2019). It is therefore highly interesting to develop chalcogenide-based ionic conductors for Mg ion.

In 2014, Yamanaka and Tatsumisago prepared the MgS–P_2S_5-MgI_2 glasses and glass-ceramics by a mechanochemical method (Yamanaka et al., 2014). The addition of MgI_2 content in $60MgS{\cdot}40P_2S_5$ helped the formation of glass-ceramic and the conductivity monotonically increased with the increase of MgI_2 content, showing the highest ionic conductivity to be 2.1×10^{-7} S cm^{-1} at 200°C. The authors proposed that the $Mg_2P_2S_6$ crystal phase contributed to the increased conductivities. But no solid evidence was presented to support the claim in the study.

In 2017, Canepa, Bo and Ceder demonstrated the discovery of spinel chalcogenides MgX_2Z_4 [X = (In, Y, Sc) and Z = (S, Se)] as a class of fast Mg ion solid conductors with the combination of theoretical and experimental studies (Canepa et al., 2017). The ambient-temperature ionic conductivity could reach as high as $\sim 10^{-4}$ S cm^{-1} for

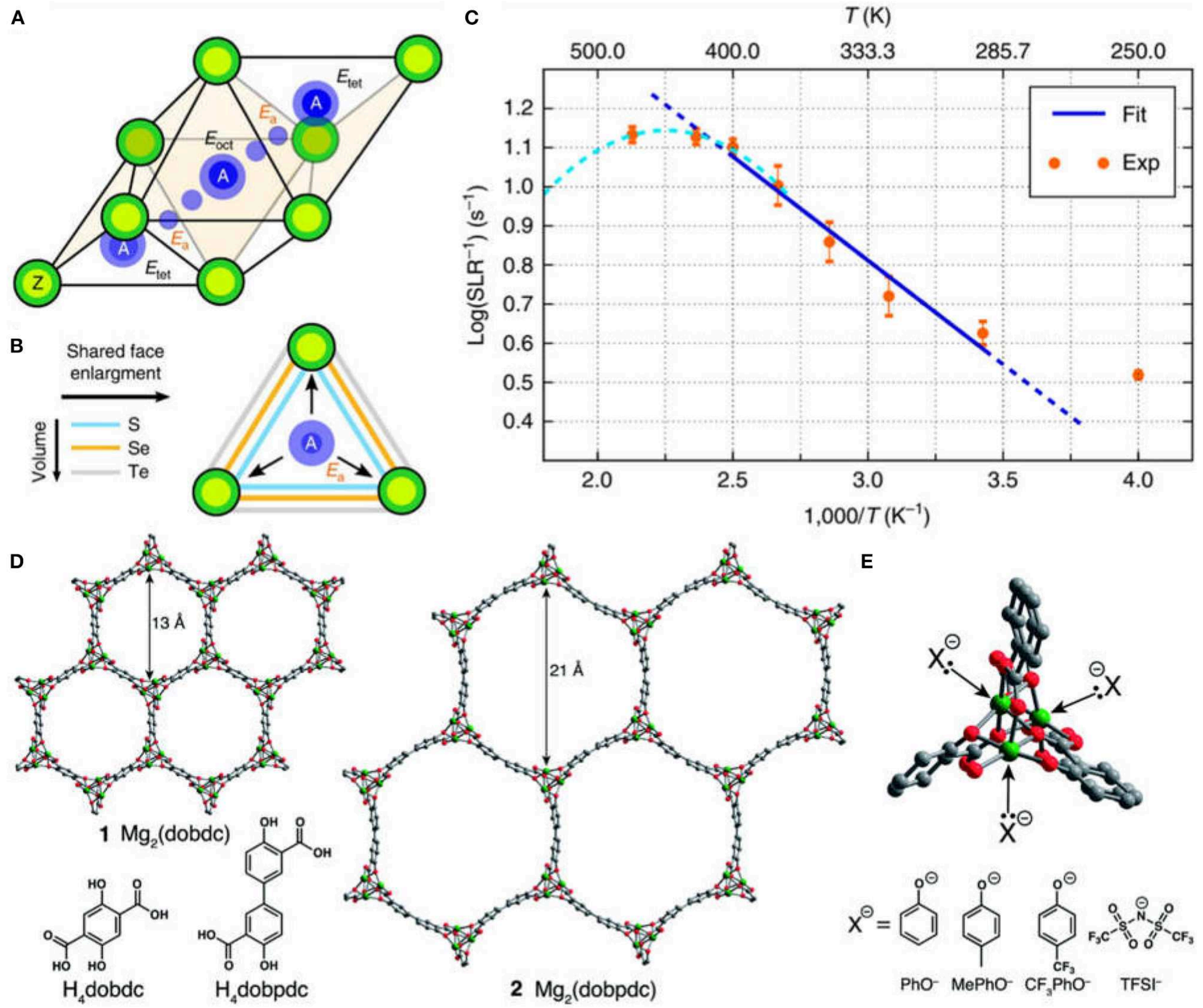

FIGURE 1 | *Tet-oct-tet* migration path in the AX_2Z_4 framework, with energy of the *tet*, *oct*, and transition sites indicated by E_{tet}, E_{oct}, E_a, respectively (Ea corresponds to the migration energy) **(A)**; effect of the anion size on the shared (triangular) face between *tet* and *oct* sites **(B)** and ^{25}Mg static variable temperature spin lattice relaxation data collected at 7.02 T as function of temperature and Arrhenius fit **(C)**. Reproduced from Canepa et al. (2017), licensed under CC BY 4.0. structures of the metal–organic frameworks Mg_2(dobdc) (**1**) and Mg_2(dobpdc) (**2**), as viewed along the *c*-axis **(D)**; a close-up of the open coordination sites at the vertices of the pore that interact with nucleophilic guest species: PhO^- = phenolate, $MePhO^-$ = 4-methylphenolate, CF_3PhO^- = 4-trifluoromethylphenolate, and $TFSI^-$ = bis(trifluoromethanesulfonyl)imide **(E)**. Reproduced with permission from Aubrey et al. (2014), Copyright 2014, Royal Society of Chemistry.

$MgSc_2Se_4$ at 25°C. The fast diffusion of Mg ions was achieved by the occupation of stable Mg^{2+} site in its unfavorable tetrahedral coordination environment within spinel structure (**Figures 1A,B**). The measured Mg migration barrier was consistent with the computed data (**Figure 1C**). Such rationale could be used as a general design rule for multivalent-ion solid conductors. However, the electronic conductivity of $MgSc_2Se_4$ is ∼0.04% of the ionic conductivity, which is substantially larger than other state-of-the-art alkali solid-state electrolytes ($\sigma_e/\sigma_i \sim 10^{-4}$-$10^{-6}$%) and hinders $MgSc_2Se_4$ as an applicable solid-state conductor.

In order to make $MgSc_2Se_4$ as an applicable solid-state conductor, Wang and Fichtner tried two strategies to reduce the electronic conductivity of $MgSc_2Se_4$, including synthesizing Se-rich phase and doping with Ce^{4+} or ti^{4+} to partially substitute Sc^{3+} (Wang et al., 2019). However, neither methods could successfully reduce the electronic conductivity. The authors suggested to employ $MgSc_2Se_4$ as a surface coating to protect Mg anode or cathode materials.

A significant improvement in ionic conductivity is achieved by chalcogenide-based material, which is 10^{-4} S cm^{-1} for $MgSc_2Se_4$ at ambient temperature. Despite the promising conductivity, its high electronic conductivity hinders its application as a suitable solid conductor. Further modifications are necessary to decrease the electronic conductivity and increase the ionic conductivity at the same time.

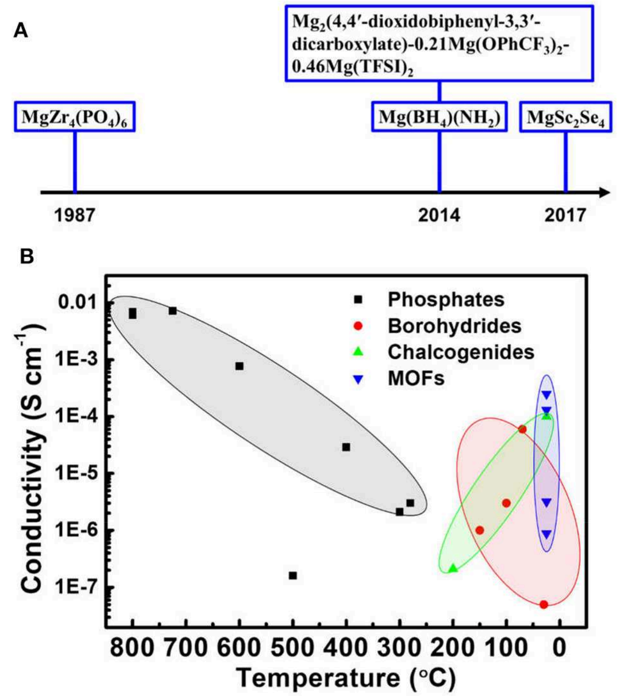

FIGURE 2 | A timeline of key development of Mg ion solid conductors **(A)** and a summary of the ionic conductivities of various solid conductors as a function of temperature in the report **(B)**.

METAL–ORGANIC FRAMEWORKS (MOFs) Mg ION SOLID CONDUCTORS

Metal–organic frameworks (MOFs) are crystalline solids composed of metal ions coordinated by multifunctional organic molecules with a three-dimensional porous structure. The composition and structure of MOFs could be easily adjusted via the rational selection of the metal ion and organic molecule (Rouhani et al., 2019). Furthermore, they feature poor electrical conductivity and well-defined porous structure, allowing for fast ion diffusion (Zhu et al., 2019). Therefore, MOFs could be promising candidates as ideal ionic conductors for selective transport. Many MOFs have been reported as solid Li^+ conductors, with the conductivities as high as 3 × 10^{-4} S cm^{-1} at room temperature. In contrast, the work on solid Mg conductors is still few in the field.

In 2014, Aubrey and Long first presented porous MOFs of Mg_2(dobdc) (dobdc^{4-} = 2,5-dioxidobenzene-1,4-dicarboxylate) and its analog Mg_2(dobpdc) (dobpdc^{4-} =4,4′-dioxidobiphenyl-3,3′-dicarboxylate) as solid Mg^{2+} conductors (Aubrey et al., 2014). These MOFs exhibited ionic conductivities of up to 2.5 × 10^{-4} S cm^{-1} at room temperature after soaked in solution containing Mg salt, comparable with polymer gels. As can be seen in **Figure 1D**, Mg_2(dobdc) shows the pore size of 13 Å and Mg_2(dobpdc) has the pore size up to 21 Å, suggesting their good ability to accommodate the ion species like Mg^{2+} in high charge density. With the insertion of Mg salts, a high density of open metal sites in MOFs could capture nucleophilic anions and thus allow for the favorably free mobility of Mg ions within pores (**Figure 1E**). Therefore, high ionic conductivity was achieved for Mg_2(dobpdc) impregnated with magnesium phenolates.

In 2017, Park and Dinca proposed a Cu(II)–azolate MOF (MIT-20) as a tunable solid electrolyte for Li^+, Na^+ and Mg^{2+} after soaking in the corresponding halide or pseudohalide salts (Park et al., 2017). Its Mg^{2+}-substituted analog, MIT-20-$MgBr_2$, exhibited the Mg ionic conductivity of 8.8 × 10^{-7} S cm^{-1} at the room temperature. MIT-20 was attractive for its feature of immobilizing anions by the Cu(II) metal center, allowing the favorably free migration of cations within the one-dimensional pores. Later in 2019, Miner from Dinca's group continued their work on the tunable solid electrolyte of MOF (Miner et al., 2019). The MOF was $Cu_4(ttpm)_2{\cdot}0.6CuCl_2$, possessing high surface area with plenty of Cu(II) cations to bound halide anions. Its analog, $Cu_4(ttpm)_2{\cdot}0.6CuCl_2$-$MgBr_2$, exhibited an ionic conductivity of 1.3 × 10^{-4} S cm^{-1} for Mg ions, demonstrating the promising future of MOF-based solid electrolyte to optimize the ionic conductivity via the control of identity, geometry and distribution of the cation hopping sites.

Instead of pressed pellets, Luo, Tsung and Wang synthesized a Mg-MOF-74 thin film as the Mg ion conductor to eliminate interparticle gaps that were inevitable for pressed pellets and enabled studies on the inherent ionic conductivity of MOFs (Luo et al., 2019). It showed the ionic conductivity of 3.17 × 10^{-6} S cm^{-1} at the room temperature, which was in consistent with the previous report by Aubrey.

Despite the promising properties, additional salt contents in excess are required for MOFs solid conductors based on the number of available anion binding sites. Furthermore, activation energies are sometimes higher that what are expected, due to the strong pairing between cations and anions of the salts. Electrochemical stability upon cycling is another challenge for some reported MOFs-based conductors.

CONCLUSIONS AND OUTLOOK

Mg battery is considered as a promising next-generation advanced battery technology possessing high theoretical volumetric energy density, good safety and high abundance. Nevertheless, before the battery technology becomes viable, several critical technological challenges should be conquered, including the development of proper electrolyte and cathodes. The SEI formed on the Mg surface is ionic-blocking for Mg ion when Mg batteries employs the conventional carbonate-based solvent commonly used in LIBs. The electrolyte development for Mg batteries therefore cannot simply mimic LIB electrolytes but requires novel design strategies. The proposal of ether-based solvent demonstrated the ability to avoid the formation of insulating passivation layer, but the practical application is still highly limited by the corrosive issues from Grignard salts and the safety concern, as well as the small electrochemical potential window. Featuring high stability and safety, ionic solid conductor could be an ideal solution to the above problems. But Mg ions have sluggish mobility within solid conductor due to the high charge density. Several types of solid conductors, including phosphates, borohydrides, chalcogenides and MOFs, have been developed to improve the performance of Mg ionic solid conductor over the recent years (**Figure 2A**).

As summarized in **Figure 2B**, the impressive progress has been achieved with the conductivity of initially 10^{-3} S cm^{-1} at 800°C improved to be 10^{-4} S cm^{-1} at ambient temperature. Despite the efforts, phosphates are still far from to meet the requirement of high ionic conductivity at low temperature and show poor progress over decades, demonstrating little promise as Mg solid conductors. In contrast, significant improvements in conductivity have been shown by the recent development of borohydrides, chalcogenides and MOFs. These novel solid conductors should be the development emphasis in next stage.

However, more work should be done before the ionic conductors are sufficiently conductive for practical consideration in Mg batteries. The electrochemical potential window should be increased to a sufficiently high level. The feasibility of the solid conductor requires the practical evaluation in combination with Mg anode and cathodes as an all-solid-state Mg battery. Furthermore, theoretical calculation could be a powerful tool to improve the performance of solid conductor.

AUTHOR CONTRIBUTIONS

YZ was in charge of organization and writing of the manuscript. WZ contributed the Phosphate section. BL contributed the Borohydride section. HL contributed the Chalcogenide section. WL contributed the MOFs section.

FUNDING

This work was conducted by Hundred Talents Project that was supported by Sun Yat-Sen University, China.

REFERENCES

Adamu, M., and Kale, G. M. (2016). Novel sol-gel synthesis of MgZr4P6O24 composite solid electrolyte and newer insight into the Mg2+-ion conducting properties using impedance spectroscopy. *J. Phys. Chem. C* 120, 17909–17915. doi: 10.1021/acs.jpcc.6b05036

Aubrey, M. L., Ameloot, R., Wiers, B. M., and Long, J. R. (2014). Metal-organic frameworks as solid magnesium electrolytes. *Energy Environ. Sci.* 7, 667–671. doi: 10.1039/c3ee43143f

Aurbach, D., Gofer, Y., Lu, Z., Schechter, A., Chusid, O., Gizbar, H., et al. (2001). A short review on the comparison between Li battery systems and rechargeable magnesium battery technology. *J. Power Sources* 97–8, 28–32. doi: 10.1016/S0378-7753(01)00585-7

Aurbach, D., Lu, Z., Schechter, A., Gofer, Y., Gizbar, H., Turgeman, R., et al. (2000). Prototype systems for rechargeable magnesium batteries. *Nature* 407, 724–727. doi: 10.1038/35037553

Aurbach, D., Suresh, G. S., Levi, E., Mitelman, A., Mizrahi, O., Chusid, O., et al. (2007). Progress in rechargeable magnesium battery technology. *Adv. Mater.* 19, 4260–4267. doi: 10.1002/adma.200701495

Bucur, C. B., Gregory, T., Oliver, A. G., and Muldoon, J. (2015). Confession of a Magnesium Battery. *J. Phys. Chem. Lett.* 6, 3578–3591. doi: 10.1021/acs.jpclett.5b01219

Cabana, J., Monconduit, L., Larcher, D., and Rosa Palacin, M. (2010). Beyond intercalation-based Li-ion batteries: the state of the Art and challenges of electrode materials reacting through conversion reactions. *Adv. Mater.* 22, E170–E192. doi: 10.1002/adma.201000717

Canepa, P., S.-,Bo, H., Gautam, G. S., Key, B., Richards, W. D., Shi, T., et al. (2017). High magnesium mobility in ternary spinel chalcogenides. *Nat. Commun.* 8:1759. doi: 10.1038/s41467-017-01772-1

Cengiz, M., Oh, H., and Lee, S. H. (2019). Lithium dendrite growth suppression and ionic conductivity of Li2S-P2S5-P2O5 glass solid electrolytes prepared by mechanical milling. *J. Electrochem. Soc.* 166, A3997–A4004. doi: 10.1149/2.0311916jes

Chen, L., Huang, Z., Pang, W., Jin, Z., Li, Y., and Wang, C.-A. (2020) Dual interface layers for solid-state Li metal battery with low interfacial resistance and small polarization based on garnet electrolyte. *Electrochim. Acta* 330:135352. doi: 10.1016/j.electacta.2019.135352

Choi, J. W., and Aurbach, D. (2016). Promise and reality of post-lithium-ion batteries with high energy densities. *Nat. Rev. Mater.* 1:16013. doi: 10.1038/natrevmats.2016.13

Deivanayagam, R., Ingram, B. J., and Shahbazian-Yassar, R. (2019). Progress in development of electrolytes for magnesium batteries. *Energy Storage Mater.* 21, 136–153. doi: 10.1016/j.ensm.2019.05.028

Devi, M. M., Ankush, Guchhait, S. K., Sunaina, Suresh Babu, G. N, Sreekanth, M., et al. (2020) Energy efficient electrodes for lithium-ion batteries: recovered and processed from spent primary batteries. *J. Hazard. Mater.* 384:121112. doi: 10.1016/j.jhazmat.2019.121112

Etacheri, V., Marom, R., Elazari, R., Salitra, G., and Aurbach, D. (2011). Challenges in the development of advanced Li-ion batteries: a review. *Energy Environ. Sci.* 4, 3243–3262. doi: 10.1039/c1ee01598b

Famprikis, T., Canepa, P., Dawson, J. A., Islam, M. S., and Masquelier, C. (2019). Fundamentals of inorganic solid-state electrolytes for batteries. *Nat. Mater.* 18, 1278–1291. doi: 10.1038/s41563-019-0431-3

Goodenough, J. B., and Kim, Y. (2010). Challenges for rechargeable Li batteries. *Chem. Mater.* 22, 587–603. doi: 10.1021/cm901452z

Higashi, S., Miwa, K., Aoki, M., and Takechi, K. (2014). A novel inorganic solid state ion conductor for rechargeable Mg batteries. *Chem. Commun.* 50, 1320–1322. doi: 10.1039/c3cc47097k

Hong, X., Wang, R., Liu, Y., Fu, J., Liang, J., and Dou, S. (2020) Recent advances in chemical adsorption and catalytic conversion materials for Li-S batteries. *J. Energy Chem.* 42, 144–168. doi: 10.1016/j.jechem.2019.07.001

Ikeda, S., Takahashi, M., Ishikawa, J., and Ito, K. (1987). Solid electrolytes with multivalent cation conduction. I. Conducting species in Mg-Zr-PO4 system. *Solid State Ion* 23, 125–129. doi: 10.1016/0167-2738(87)90091-9

Imanaka, N., Okazaki, Y., and Adachi, G. (2000a). Divalent magnesium ion conducting characteristics in phosphate based solid electrolyte composites. *J. Mater. Chem.* 10, 1431–1435. doi: 10.1039/a909599c

Imanaka, N., Okazaki, Y., and Adachi, G. (2000b). Divalent magnesium ionic conduction in Mg1-2x(Zr1-xNbx)(4)P6O24 (x=0-0.4) solid solutions. *Electrochem. Solid State Lett.* 3, 327–329. doi: 10.1149/1.1391138

Imanaka, N., Okazaki, Y., and Adachi, G. Y. (1999). Bivalent magnesium ionic conduction in the magnesium phosphate based composites. *Chem. Lett.* 28, 939–940. doi: 10.1246/cl.1999.939

Janek, J., and Zeier, W. G. (2016). A solid future for battery development. *Nat. Energy* 1:16141. doi: 10.1038/nenergy.2016.141

Jia, H., Sun, Y., Zhang, Z., Peng, L., An, T., and Xie, J. (2019). Group 14 element based sodium chalcogenide Na4Sn0.67Si0.33S4 as structure template for exploring sodium superionic conductors. *Energy Stor. Mater.* 23, 508–513. doi: 10.1016/j.ensm.2019.04.011

Le Ruyet, R., Berthelot, R., Salager, E., Florian, P., Fleutot, B., and Janot, R. (2019). Investigation of Mg(BH4)(NH2)-based composite materials with enhanced Mg2+ ionic conductivity. *J. Phys. Chem. C* 123, 10756–10763. doi: 10.1021/acs.jpcc.9b00616

Lee, W., Tamura, S., and Imanaka, N. (2019). Synthesis and characterization of divalent ion conductors with NASICON-type structures. *J. Asian Ceramic Soc.* 7, 221–227. doi: 10.1080/21870764.2019.1606141

Li, Q., Chen, D., Tan, H., Zhang, X., Rui, X., and Yu, Y. (2020) 3D porous V2O5 architectures for high-rate lithium storage. *J. Energy Chem.* 40, 15–21. doi: 10.1016/j.jechem.2019.02.010

Liang, B., Keshishian, V., Liu, S., Yi, E., Jia, D., Zhou, Y., et al. (2018). Processing liquid-feed flame spray pyrolysis synthesized Mg0.5Ce0.2Zr1.8(PO4)(3) nanopowders to free standing thin films and pellets as potential electrolytes in all-solid-state Mg batteries. *Electrochimica Acta* 272, 144–153. doi: 10.1016/j.electacta.2018.04.015

Luo, J. R., Li, Y., Zhang, H. C., Wang, A. L., Lo, W. S., Dong, Q., et al. (2019). A metal-organic framework thin film for selective Mg2+ transport. *Angew. Chem. Int. Ed.* 58, 15313–15317. doi: 10.1002/anie.201908706

Michel, F., Becker, M., Janek, J., and Polity, A. (2019). Investigations of the solid electrolyte interphase using X-ray photoelectron spectroscopy *in situ* experiment on the lithium-based solid electrolyte LiPSON. *Phys. Status Solidi B-Basic Solid State Phys*. doi: 10.1002/pssb.201900336. [Epub ahead of print].

Miner, E. M., Park, S. S., and Dinca, M. (2019). High Li+ and Mg2+ conductivity in a Cu-azolate metal-organic framework. *J. Am. Chem. Soc.* 141, 4422–4427. doi: 10.1021/jacs.8b13418

Mohtadi, R., Matsui, M., Arthur, T. S., and, Hwang, S.-J. (2012). Magnesium borohydride: from hydrogen storage to magnesium battery. *Angew. Chem. Int. Ed.* 51, 9780–9783. doi: 10.1002/anie.201204913

Muldoon, J., Bucur, C. B., Oliver, A. G., Sugimoto, T., Matsui, M., Kim, H. S., et al. (2012). Electrolyte roadblocks to a magnesium rechargeable battery. *Energy Environ. Sci.* 5, 5941–5950. doi: 10.1039/c2ee03029b

Pan, W., Guan, W., and Jiang, Y. (2020). Research advances in polyanion-type cathodes for sodium-ion batteries. *Acta Phys. Chim. Sin*. 36:1600275. doi: 10.1002/advs.201600275

Park, S. S., Tulchinsky, Y., and Dinca, M. (2017). Single-Ion Li+, Na+, and Mg2+ solid electrolytes supported by a mesoporous anionic cu-azolate metal-organic framework. *J. Am. Chem. Soc.* 139, 13260–13263. doi: 10.1021/jacs.7b06197

Ramos, E. P., Zhang, Z., Assoud, A., Kaup, K., Lalere, F., and Nazar, L. F. (2018). Correlating ion mobility and single crystal structure in sodium-ion chalcogenide-based solid state fast ion conductors: Na(11)Sn(2)PnS(12) (Pn = Sb, P). *Chem. Mater.* 30, 7413–7417. doi: 10.1021/acs.chemmater.8b02077

Roedern, E., R.-,Kuehnel, S., Remhof, A., and Battaglia, C. (2017). Magnesium ethylenediamine borohydride as solid-state electrolyte for magnesium batteries. *Sci. Rep*. 7:46189. doi: 10.1038/srep46189

Rouhani, F., Rafizadeh-Masuleh, F., and Morsali, A. (2019). Highly electroconductive metal-organic framework: tunable by metal ion sorption quantity. *J. Am. Chem. Soc.* 141, 11173–11182. doi: 10.1021/jacs.9b04173

Saha, P., Datta, M. K., Velikokhatnyi, O. I., Manivannan, A., Alman, D., and Kumta, P. N. (2014). Rechargeable magnesium battery: current status and key challenges for the future. *Prog. Mater. Sci.* 66, 1–86. doi: 10.1016/j.pmatsci.2014.04.001

Shao, Y. J., Zhong, G. M., Lu, Y. X., Liu, L. L., Zhao, C. L., Zhang, Q. Q., et al. (2019). A novel NASICON-based glass-ceramic composite electrolyte with enhanced Na-ion conductivity. *Energy Stor. Mater.* 23, 514–521. doi: 10.1016/j.ensm.2019.04.009

Su, J., Tsuruoka, T., Tsujita, T., Nishitani, Y., Nakura, K., and Terabe, K. (2019). Atomic layer deposition of a magnesium phosphate solid electrolyte. *Chem. Mater*. 31, 5566–5575. doi: 10.1021/acs.chemmater.9b01299

Tamura, S., Yamane, M., Hoshino, Y., and Imanaka, N. (2016). Highly conducting divalent Mg2+ cation solid electrolytes with well-ordered three-dimensional network structure. *J. Solid State Chem.* 235, 7–11. doi: 10.1016/j.jssc.2015.12.008

Tutusaus, O., Mohtadi, R., Arthur, T. S., Mizuno, F., Nelson, E. G., and Sevryugina, Y. V. (2015). An efficient halogen-free electrolyte for use in rechargeable magnesium batteries. *Angew. Chem. Int. Ed.* 54, 7900–7904. doi: 10.1002/anie.201412202

Wang, C., Zeng, Y., Xiao, X., Wu, S., Zhong, G., Xu, K., et al. (2020) gamma-MnO2 nanorods/graphene composite as efficient cathode for advanced rechargeable aqueous zinc-ion battery. *J. Energy Chem*. 43, 182–187. doi: 10.1016/j.jechem.2019.08.011

Wang, L.-P., Zhao-Karger, Z., Klein, F., Chable, J., Braun, T., Schuer, A. R., et al. (2019). MgSc(2)Se(4)A magnesium solid ionic conductor for all-solid-state Mg batteries? *ChemSusChem* 12, 2286–2293. doi: 10.1002/cssc.201900225

Wang, Y., Lu, X., Zheng, C., Liu, X., Chen, Z., Yang, W., et al. (2019). Chemistry design towards a stable sulfide-based superionic conductor Li4Cu8Ge3S12. *Angew. Chem. Int. Ed.* 58, 7673–7677. doi: 10.1002/anie.201901739

Xuan, M., Xiao, W., Xu, H., Shen, Y., Li, Z., Zhang, S., et al. (2018). Ultrafast solid-state lithium ion conductor through alloying induced lattice softening of Li6PS5Cl. *Journal of Materials Chemistry A* 6, 19231–19240. doi: 10.1039/C8TA07240J

Yamanaka, T., Hayashi, A., Yamauchi, A., and Tatsuinisago, M. (2014). Preparation of magnesium ion conducting MgS-P2S5-MgI2 glasses by a mechanochemical technique. *Solid State Ionics* 262, 601–603. doi: 10.1016/j.ssi.2013.10.037

Yoo, H. D., Shterenberg, I., Gofer, Y., Gershinsky, G., Pour, N., and Aurbach, D. (2013). Mg rechargeable batteries: an on-going challenge. *Energy Environ. Sci.* 6, 2265–2279. doi: 10.1039/c3ee40871j

Zeng, J., Peng, C., Wang, R., Cao, C., Wang, X., and Liu, J. (2020) Micro-sized FeS2@FeSO4 core-shell composite for advanced lithium storage. *J. Alloys Compounds* 814:151922. doi: 10.1016/j.jallcom.2019.151922

Zhu, F., Bao, H., Wu, X., Tao, Y., Qin, C., Su, Z., et al. (2019). High-performance metal-organic framework-based single ion conducting solid-state electrolytes for low-temperature lithium metal batteries. *Acs Appl. Mater. Interfaces* 11, 43206–43213. doi: 10.1021/acsami.9b15374

Conflict of Interest: The authors declare that the research was conducted in the absence of any commercial or financial relationships that could be construed as a potential conflict of interest.

frontiers in Chemistry

ORIGINAL RESEARCH
published: 25 February 2020
doi: 10.3389/fchem.2020.00114

Understanding the Conductive Carbon Additive on Electrode/Electrolyte Interface Formation in Lithium-Ion Batteries via *in situ* Scanning Electrochemical Microscopy

Shuai Liu [1,2†], ***Xiaojie Zeng*** [1,2†], ***Dongqing Liu*** [1*], ***Shuwei Wang*** [1,2], ***Lihan Zhang*** [1,2], ***Rui Zhao*** [1,2], ***Feiyu Kang*** [1,2] **and *Baohua Li*** [1*]

[1] Shenzhen Key Laboratory on Power Battery Safety Research and Shenzhen Geim Graphene Center, Tsinghua Shenzhen International Graduate School, Shenzhen, China, [2] Laboratory of Advanced Materials, School of Materials Science and Engineering, Tsinghua University, Beijing, China

Edited by:
Du Yuan,
Nanyang Technological University, Singapore

Reviewed by:
Hao Ren,
Nanyang Technological University, Singapore
Xingke Cai,
Shenzhen University, China

****Correspondence:***
Dongqing Liu
liu.dongqing@sz.tsinghua.edu.cn
Baohua Li
libh@mail.sz.tsinghua.edu.cn

† These authors have contributed equally to this work

Specialty section:
This article was submitted to Electrochemistry, a section of the journal Frontiers in Chemistry

Received: *02 January 2020*
Accepted: *07 February 2020*
Published: *25 February 2020*

Citation:
Liu S, Zeng X, Liu D, Wang S, Zhang L, Zhao R, Kang F and Li B (2020) Understanding the Conductive Carbon Additive on Electrode/Electrolyte Interface Formation in Lithium-Ion Batteries via in situ Scanning Electrochemical Microscopy. Front. Chem. 8:114. doi: 10.3389/fchem.2020.00114

The role of conductive carbon additive on the electrode/electrolyte interface formation mechanism was examined in the low-potential (3.0–0 V) and high-potential (3.0–4.7 V) regions. Here the most commonly used conductive carbon Super P was used to prepared electrode with polyvinylidene fluoride binder without any active material. The dynamic process of interface formation was observed with *in situ* Scanning Electrochemical Microscopy. The electronically insulating electrode/electrolyte passivation layer with areal heterogeneity was formed after cycles in both potential regions. The low-potential interface layer is mainly composed of inorganic compounds covering the conductive carbon surface; While the electrode after high-potential sweep tends to lose its original carbon structure and has more organic species formed on its surface.

Keywords: conductive carbon additive, electrode/electrolyte interface, lithium-ion batteries, scanning electrochemical microscopy, solid electrolyte interface (SEI)

INTRODUCTION

Lithium-ion batteries (LIBs) are one of the most commonly used energy storage devices and have been used in portable electronics devices and electric vehicles. During the (dis)charge reactions, interfacial reactions take place between the electrode and electrolyte to form the electrode/electrolyte interface (EEI), which is crucial for cell performance (Gauthier et al., 2015; Tripathi et al., 2018). In the composite electrode, the conductive carbon additive is added to improve the electrical conductivity of active materials and was once considered as an "inactive" component. Recently, the high surface reactivity of conductive carbon on EEI formation has been revealed gradually (Hou et al., 2017; Li and Manthiram, 2019).

In the composite electrode, even though the weight percent of conductive additive is low, it has high surface area and atomic percentage to cover most of the electrode surface (Younesi et al., 2015). In addition, the carbonaceous materials have various chemical functional groups on its surface, including hydroxyl-, carboxyl-, carbonyl-, and aromatic groups. The large surface area and various functional groups of conductive carbon react with electrolyte to form the EEI both spontaneously and during electrochemical cycling. During the spontaneous reaction, the carbon additive interacts with electrolyte through corrosion-like reactions. The spontaneous polymerization of solvent molecules form the EEI with similar composition as the EEI after electrochemical cycling (Membreño et al., 2015). This may partially explain the detection of similar degradation products on the negative and positive electrodes even though different reactions (reduction and oxidation) are involved (Gauthier et al., 2015). When cycling in the low-potential region, the conductive carbon has lithium storage property but shows large irreversible capacity through the formation of the solid electrolyte interface (SEI) (Fransson et al., 2001; Gnanamuthu and Lee, 2011; Anothumakkool et al., 2018). In the high-potential region, the spontaneously formed EEI will be partially decomposed via oxidization or desorption when charged to 4.3–4.5V (Younesi et al., 2015). The passivation role of carbon black for the Ni-rich electrodes has been considered between 3.0V and 4.5V, suggesting that the organic complexes generated on carbon migrate across the active material's surface to suppress the unwanted interfacial reactions to certain extent (Li et al., 2017a). In addition, the dynamic evolution of interface by the mass transfer between carbon black and active material was observed (Li and Manthiram, 2019); However, the passivation effect of conductive carbon lose stability at extreme potentials (>4.5 V), which is mainly due to (de)intercalation of anions, irreversible electrolyte oxidation and degradation of conductive carbon (Zheng et al., 2013; Li et al., 2014; Qi et al., 2014; Kajiyama et al., 2015; Metzger et al., 2015; Younesi et al., 2015; He et al., 2016; Scipioni et al., 2016).

In the composite electrode, the contribution of conductive carbon to interfacial composition is equivalent or larger than the contribution of the active material. Therefore, the reactivity of conductive carbon, and its influence on the EEI formation once considered "inactive" toward electrolytes, should be reconsidered. However, most of the EEI studies were derived from composite electrodes that contain active material, carbon additive and binder, which leads to an ambiguous interpretation of the individual components for the EEI formation. This calls for the investigation of individual cell component and its effect on the interfacial changes (Li et al., 2017b). In addition, the application of *in situ/operando* technique is necessary to capture the dynamic formation of EEI (Gauthier et al., 2015; Wang et al., 2018; Liu et al., 2019a).

In the present study, the reactivity of conductive carbon additives on the EEI was investigated individually to give a better understanding of its contribution on interface dynamics. The interface formation process was examined in the low-potential and high-potential regions, with the EEI termed as solid electrolyte interface (SEI) and cathode electrolyte interface (CEI), respectively. The electrode was prepared with the commonly used conductive carbon additive Super P and binder polyvinylidene fluoride (PVDF) without any active material (Zheng et al., 2013; Li et al., 2014; Qi et al., 2014; Kajiyama et al., 2015; Metzger et al., 2015; Younesi et al., 2015). The dynamic evolution of the interfaces was observed with *in situ* Scanning Electrochemical Microscopy (SECM). SECM is a four-electrode electroanalytical scanning probe technique and has been applied for the interface study of Li-ion batteries in recent years (Polcari et al., 2016; Liu et al., 2019a). The feedback mode of SECM is commonly used for interface study (Zampardi et al., 2013; Heinz et al., 2014; Liu et al., 2019b). During the measurement, the scanning probe detected the electrochemical reactivity of electrode substrate through the regeneration rate of redox mediator from the substrate. It is understood that the conductivity of the electrode will decrease with the SEI/CEI passivation layer formed on the surface. By using the feedback curve and feedback image of SECM, the reactivity of the electrode substrate and interfacial dynamic change with cycles could be revealed.

EXPERIMENTAL SECTION

The electrode was prepared by mixing equal amounts of conductive carbon Super P (TIMCAL) and binder PVDF (Arkema) (1:1 by wt.%) dissolved in N-methyl pyrrolidone (NMP) to obtain a uniform slurry. Then the slurry was deposited on to the SECM substrate with glass carbon as current collector and dried at 80°C overnight. The electrolyte used was 1 M $LiPF_6$ in EC:DMC:DEC (1:1:1 vol %) (CAPCHEM) containing 10 mM ferrocene (Macklin, 99%) as redox mediator. All the electrochemical cyclic voltammetry (CV) tests and SECM measurement were performed using Bio-Logic M470 in the Ar-filled glovebox (MIKROUNA). The experiment setup consists of a four-electrode open cell as shown in detail in our previous publication (Liu et al., 2019c). One working electrode is the electrode pasted substrate, the other working electrode is the 15 μm Pt microprobe sealed in glass (RG = 10), the counter electrode and reference electrode were all made of Li foils. The substrate electrode was cycled at a scan rate of 5 mV/s in the potential windows of 3.0–0.0 V and 3.0–4.7 V, referred to as the low-potential region and high-potential region, respectively. Prior to SECM measurement, the substrate was tilt corrected with a gradienter, and then the microprobe was loaded at the vicinity of the electrode. The approach curve was recorded with step size of 2 μm and 0.5 μm when the feedback change was larger than 115% or smaller than 75%. The area scan was recorded with the tip near the substrate surface, at a step size of 8 μm for the 120 μm × 120 μm area. A Scanning Electron Microscope (SEM, HITACHI, SU8010) was used to characterize the morphology information. X-ray Photoelectron Spectroscopy (XPS, PHI5000VersaProbeII) using monochromatic Al Kα radiation (1486.6 eV) with depth profiling was used to analyze the chemical composition of electrode surface. The microscopic structure of the electrode surface was further analyzed by transmission electron microscopy (TEM, FEI Tecnai G2 F30). Prior to the material characterizations, the cycled electrodes were all rinsed with dimethyl carbonate (DMC) in the glovebox.

RESULTS AND DISCUSSION

The Feedback Mode of SECM

The feedback mode of SECM is frequently used for the interface evolution study in LIBs (Liu et al., 2019a). In this

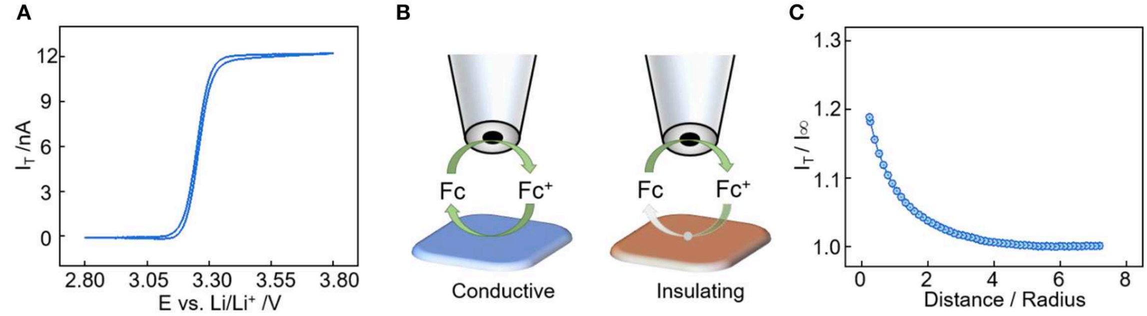

FIGURE 1 | (A) Cyclic voltammetry of the SECM probe in 1 M $LiPF_6$ in EC:DMC:DEC (1:1:1 by vol.%) electrolyte with 10 mM ferrocene at scan rate of 10 mV/s. **(B)** SECM feedback mode over an conductive substrate (positive feedback) and insulating substrate (negative feedback). **(C)** SECM approach curve toward the Super P electrode at step size of 2 μm.

mode, the microprobe monitors the regeneration rate of the redox mediator from the substrate to determine its electronic character. Ferrocene was chosen as the free-diffusion redox mediator and the corresponding cyclic voltammetry between 2.8 and 3.8 V is shown in **Figure 1A**. The redox potential of the ferrocene/ferrocenium (Fc/Fc^+) combination is 3.26 V vs. Li^+/Li, which is suitable for solid electrolyte interface characterization in LIBs (Zampardi et al., 2013; Ventosa et al., 2017). During the feedback measurement (**Figure 1B**), the microprobe has an applied potential of 3.6 V vs. Li^+/Li as it moves toward the substrate, and the current at the microprobe increases when the substrate is conductive due to the increase of Fc regeneration rate (positive feedback). The microprobe current decreases when the substrate is passivated because the regeneration and diffusion of Fc are all hindered by the insulating substrate (negative feedback). In **Figure 1C**, a positive feedback is observed when approaching the pristine electrode surface, indicating the conductive nature of the carbon additive electrode. SEM pictures of Super P powder and electrode are shown in **Figure S1**, the Super P powder has sub-hundred nanometer spherical shaped particles, and the morphology doesn't change much after being made into an electrode. In addition, the Super P has high surface area of 63.41 m^2 g^{-1} from the BET measurement result.

EEI Formation via *in situ* SECM in the Low-Potential Region

To investigate the effect of conductive carbon on the EEI formation, the approach curve and area scan of SECM were employed to examine the change of substrate conductivity. **Figure 2A** shows the first five cycles of Super P electrode ranged between 3.0 and 0.0 V vs. Li^+/Li. Two characteristic reversible capacity regions were observed, one in 1.4–0.6V and the other below 0.6V. This is ascribed to the specific lithium storage mechanism of Super P, i.e., in the vicinity of turbostratic graphene edges (Anothumakkool et al., 2018). In addition, the irreversible capacity is high especially for the first few cycles, which is caused by the electrolyte reduction and SEI formation (Fransson et al., 2001; Gnanamuthu and Lee, 2011). In **Figure 2B**, the approach curves were recorded over the electrodes at a pristine state and after cycles. The approach curves change from positive feedback to negative feedback, and the normalized current densities decrease with cycles, indicating the kinetics for the Fc^+ reduction get slower on the electrode with SEI formation. **Figure 2C** shows the corresponding area scan of an identical 120 × 120 μm region with cycles. For a better comparison, the different sets of area scan were all plotted with the normalized current densities varying <0.03. At pristine state, the normalized current densities are larger than 1.02, indicating the good conductivity of the electrode substrate. In addition, it's commonly assumed that the pristine electrode is uniformly distributed and the variation in the feedback current density is solely caused by topographical difference (Heinz et al., 2014; Liu et al., 2019b,c,d). Thus, the area scan of the pristine electrode in **Figure 2C** was converted to topographical information via calculation with the approach curve (**Figure S2**). In **Figure 2D**, the scanned area has a topographical variation of ∼8.5 μm, corresponding to the increase of feedback current with substrate height (**Figure 2C**).

With the cycling process, SEI evolves and thus the feedback images are not only reflecting the topography but also the lateral heterogeneity of SEI (Heinz et al., 2014). Since the thickness of SEI are in the range of 20∼50 nm, the thickness can't induce feedback current change larger than 1 pA, which is negligible compared to the ∼nA scale feedback image. So the feedback image in **Figure 2C** (6 and 10th cycles) are a result of the pristine topographical difference and the heterogeneous passivating properties of SEI for the scanned area. With the pristine topography (**Figure 2D**), the evolution of passivating SEI can be determined via calculation in combination with their corresponding approach curves (detailed calculation in **Supplementary Materials**). In **Figure 2E**, the heterogenous passivating SEI can be seen more clearly with the pristine topography subtracted. For the 6th cycle in **Figure 2E**, the feedback currents change from 70 to −120 pA as the image changes from red to purple, indicating the decrease of the mediator regeneration rate with SEI passivation. In accordance with the topography (**Figure 2D**), the passivation layer tends to form in the $y < 70$ μm region. But the SEI passivation sites do not necessarily correlate with the substrate height. This can be seen clearly from the identical height region (**Figure 2D**: 20 μm $< y <$ 110 μm), which has the mixture of positive

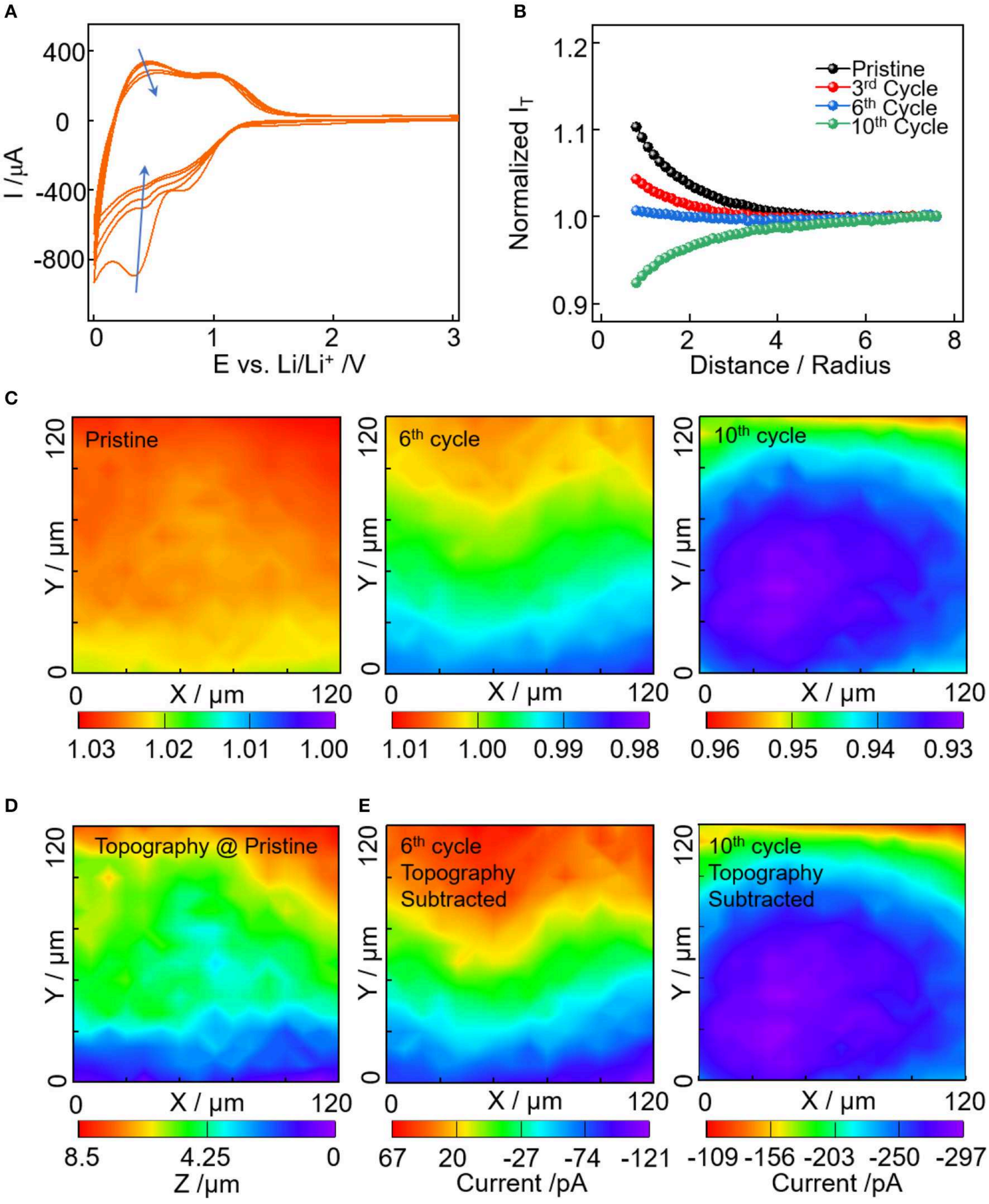

FIGURE 2 | (A) Cyclic voltammetry of Super P electrode from 3.0 to 0 V vs. Li^+/Li in electrolyte of 1M $LiPF_6$ in EC:DMC:DEC at a scan rate of 5 mV/s. **(B)** Normalized approach curves toward electrode at pristine, after 3rd, 6th, and 10th cycles. **(C)** SECM area scan with normalized current density of the electrode at pristine, after 6 and 10th cycles. **(D)** SECM feedback current converted topography of the scanned area. **(E)** SECM area scan with the topography induced feedback current subtracted for the 6 and 10th cycle.

and negative feedbacks (**Figure 2E**). Upon the 10th cycle, the feedback current drops to the range of $-100 \sim -300$ pA, indicating a much slower mediator regeneration rate and more severe SEI passivation effect. Compared with the 6th cycle, the passivation region expands to a larger area with an elliptical shape covering the majority of the scanned area. It demonstrate that the passivating SEI grows with cycles and the growth has lateral heterogeneous properties.

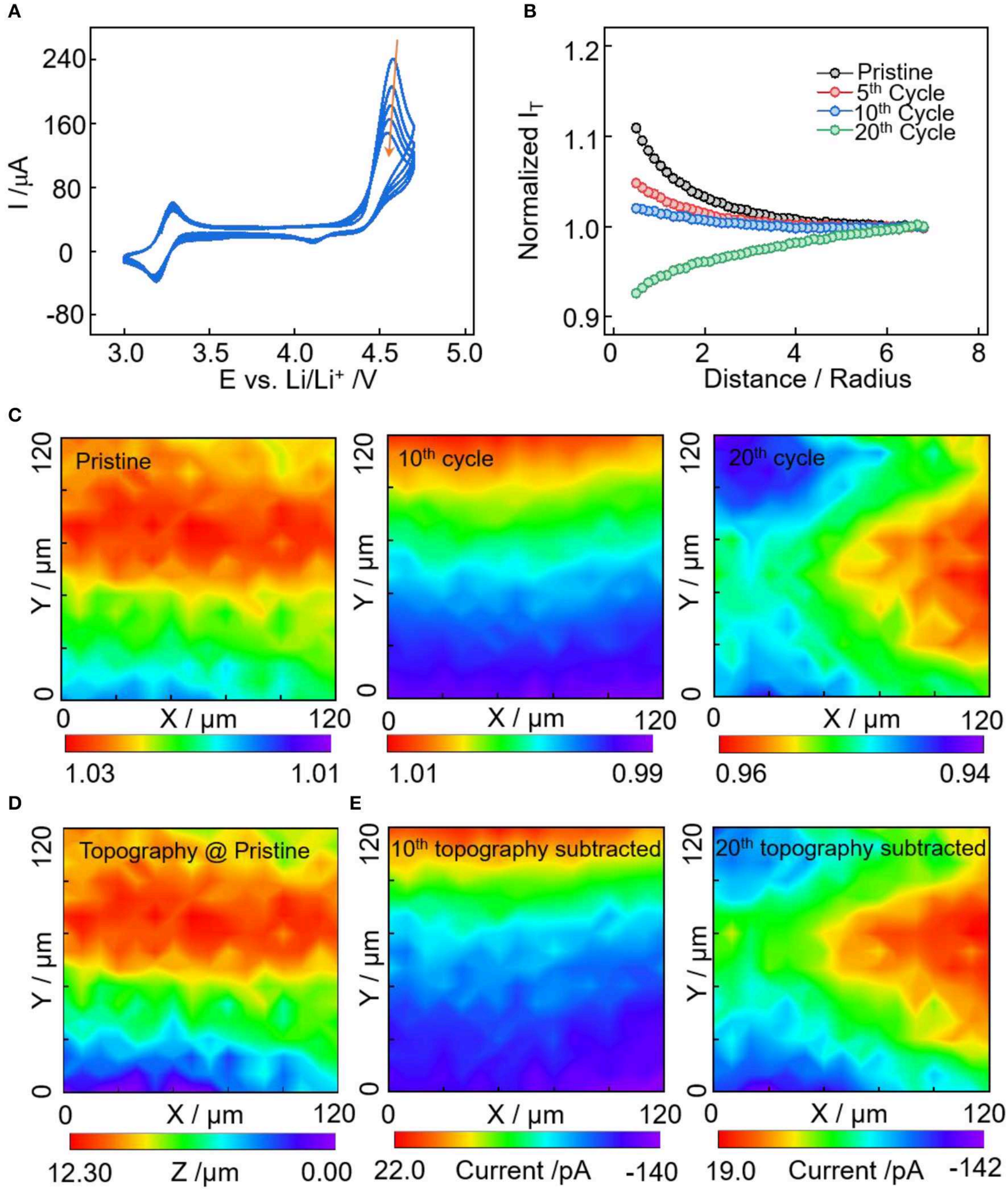

FIGURE 3 | (A) Cyclic voltammetry of Super P electrode from 3.0 to 4.7 V vs. Li^+/Li in electrolyte of 1 M $LiPF_6$ in EC:DMC:DEC at a scan rate of 5 mV/s. **(B)** Normalized approach curves toward electrodes at pristine, after 5, 10, and 20th cycles. **(C)** SECM area scan with normalized current density of electrodes at pristine, and after 10 and 20th cycles. **(D)** SECM feedback current converted topography of the scanned area. **(E)** SECM area scan with the topography feedback current subtracted for the 10 and 20th cycle.

EEI Formation via *in situ* SECM in the High-Potential Region

The conductive carbon electrode is cycled between 3.0 and 4.7 V vs. Li^+/Li to examine the interface evolution in the high-potential region. In **Figure 3A** of the cyclic voltammetry curves, a pair of reversible redox peaks were observed at 3.28/3.18 V, corresponding to the oxidation and reduction reactions of ferrocene. In addition, the redox peaks at 4.56/4.10 V have obvious larger anodic peak than the cathodic peak, demonstrating the existence of an irreversible oxidation process.

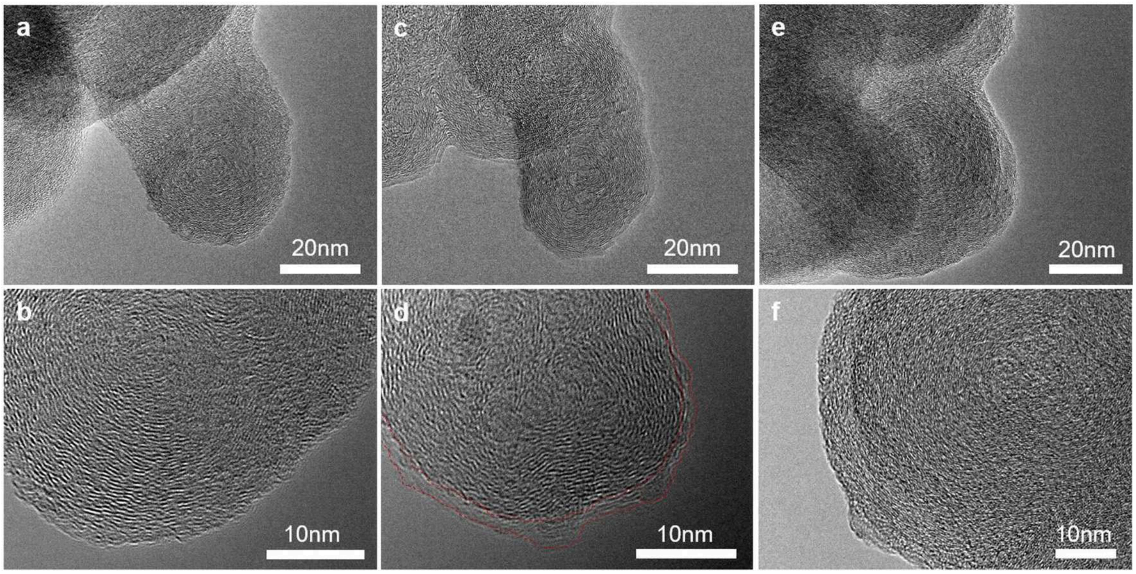

FIGURE 4 | Transmission electron microscopy images of carbon black electrode **(a,b)** at pristine state, **(c,d)** after cycles in the low-potential and **(e,f)** high-potential regions.

The anodic peak can be induced by anion intercalation, oxidative decomposition of electrolyte and conductive carbon oxidation (itself or its functional groups) (Qi et al., 2014, 2015; Soon et al., 2018). With these three contributions, the reversible part could be the (de)intercalation of PF_6^- anions to/from the electrodes (Qi et al., 2014). The oxidation of electrolyte on conductive carbon at potential larger than 4.6 V is irreversible once the cathode electrolyte interface has formed (La Mantia et al., 2013; Li et al., 2013, 2014). The interface layer prefers to form on the carbon additive of the electrodes (Nordh et al., 2015). In addition, carbon black degrades with cycling via agglomeration and loss of crystallinity to amorphous structure. This leads to the decrease of the electrical conductivity, increase in the heterogeneity of the conductive carbon network, and reduction in the electron percolation of the composite electrode (Ngo et al., 2016; Scipioni et al., 2016).

The change of electronic character of the electrode substrate with cycles was examined by the approach curve and area scan of SECM (**Figures 3B,C**). In accordance with the result of low-potential sweep (**Figure 2B**), the approach curves change from positive feedback to negative feedback with cycles, indicating the decrease of electrode substrate conductivity induced by electrolyte decomposition and conductive carbon degradation. At the same sweep rate of CV, the passivation rate of the interface layer in the high-potential region (3.0–4.7V) is slower than that in the low-potential region (3.0–0.0V), which is caused by the different interface components. SECM area scan was applied to visualize the areal heterogeneity of interface evolution (**Figure 3C**), here we also converted the pristine feedback image to topographical information (**Figure 3D**), and the area scan after cycles having the topography feedback subtracted, i.e., passivation property feedback (**Figure 3E**). In **Figure 3D**, the scanned area has a topographical variation of ~12 μm with higher upper region ($60 < y < 100$). After the 10th cycle, the passivation layer covers the majority of the electrode surface with negative feedback current densities, which is induced by electrolyte decomposition and conductive carbon degradation. Upon the 20th cycle, the magnitude of areal feedback current is not decreased, while the areal heterogeneity of the passivation layer is becoming more obvious. The nearly unchanged areal feedback current magnitude from the 10 to 20th cycles is unexpected. This could because the surface of conductive carbon has been covered by the electrolyte degradation products in the first ten cycles; for the second ten cycles, when a large amount of the surface area and active functional groups of conductive carbon has been covered, the oxidative decomposition of electrolytes is less severe. While the structural degradation, aggregation, and agglomeration of conductive carbon last throughout the whole cycling process, which may leads to the evolution of passivation layer and increase of areal heterogeneity.

TABLE 1 | Element concentration on the surface of electrodes after cycling in the low-potential and high-potential regions.

Electrodes	C1s	O1s	F1s	Li1s
0–3 V	9.35	7.36	38.45	44.85
3–4.7V	30.02	6.33	31.54	31.76

Morphology, Chemical and Structure Information of EEI

TEM was applied to investigate the morphology and microstructure of the pristine and cycled conductive carbon electrodes at nanoscale. At pristine state in **Figures 4a,b**, the Super P particles have spherical shape with diameter of 30–50 nm. The particles have quasi-crystal structure and the graphitic structures are oriented concentrically tangent

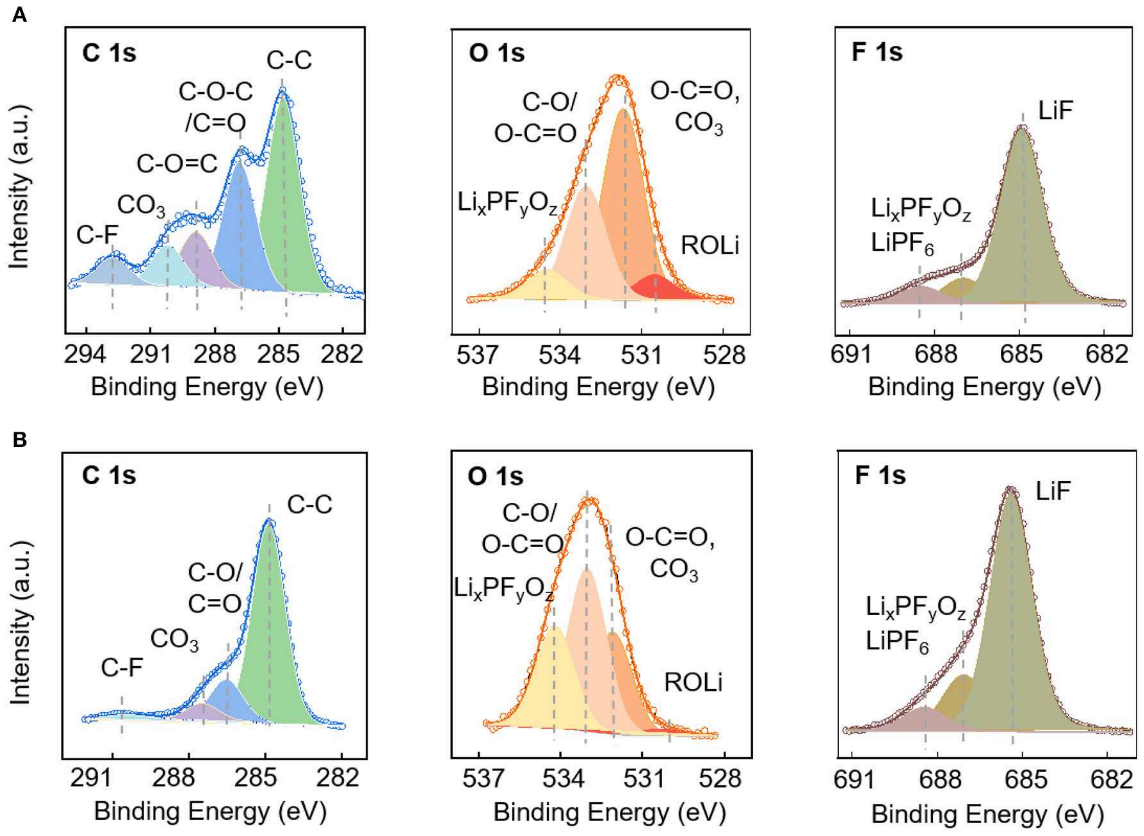

FIGURE 5 | XPS characterization of electrodes: C1s, O1s, and F1s spectra of the electrodes cycled in the potential window of 0–3 V **(A)** and 3.0–4.7 V **(B)**.

toward the surface of the primary particles (Gnanamuthu and Lee, 2011). After lithiation, the internal structure of the Super P particles were preserved while ∼5 nm thick SEI layer is formed on the particle surface (**Figures 4c,d**) (Anothumakkool et al., 2018). In **Figures 4e,f**, the particles of the charged sample swelled and lost crystallinity. The structural degradation can be partially explained by the anion intercalation and co-intercalation of solvent molecules to expand the interlayer and electrolyte decomposition inside the carbon (Qi et al., 2014).

The electrodes after cycles in the low-potential and high-potential regions were analyzed by XPS to provide information about the chemical composition on the surface. The elemental concentration of major components are listed in **Table 1** with the corresponding C1s, O1s, and F1s spectra shown in **Figure 5**. The chemical composition of the solid electrolyte interfaces cycled in the low-potential and high-potential windows are similar except for the difference in the composition amount. This might start from the spontaneous reaction between the carbonate electrode and electrolyte after immersion in the electrolyte. Membreño et al. revealed the spontaneous decomposition of electrolyte on the carbon additive in a corrosion-like reaction with spontaneous polymerization reactions on the carbon surface (Membreño et al., 2015). The functional groups include alkanes (C-C), alkoxides and ethers (RCO), lithium carboxylate and esters (ROCO), carbonates (RCO_3), fluoroalkanes (RCF_n), lithium fluoride (LiF) and degraded lithium salt products (Li_xPF_y and $Li_xPO_yF_z$) (Qi et al., 2015; Younesi et al., 2015). The spontaneously formed SEI evolves during the electrochemical cycling in the low and high potential regions. After cycles in the 0–3 V vs. Li^+/Li, the electrode is covered by a large fraction of inorganic compounds, LiF (mostly), Li_2CO_3, and $Li_xPF_yO_z$, and fewer organic species (RCO, ROCO, $ROCO_2$, and RCO_3) formed via the degradation of salt and solvents. In comparison, the electrode cycled in the high-potential region has fewer inorganic species, which can be told from the lower amount of Li1s, F1s, and much higher C1s element concentration (**Table 1**). In addition, the much higher ratio between C-C bonds and carbon oxygen bonds demonstrates that the electrode surface has less oxygen-containing species and less electrolyte decomposition (Soon et al., 2018; Tatara et al., 2019).

CONCLUSION

The influence of conductive carbon Super P on the electrode/electrolyte interface formation mechanism has been investigated by *in situ* SECM in combination with *ex situ* SEM, TEM, and XPS. After cycles in the low-potential region (3.0–0 V), the interface is covered by a passivation layer composed of salt and solvent degradation components. The interface layer grows with cycles and has lateral heterogenous properties. In the high-potential region (3.0–4.7 V), a similar passivation layer is formed while the passivation effect is relatively weaker with more organic species formed on the surface. In addition to the oxidative decomposition of electrolyte, the conductive carbon oxidation and anion intercalation lead to the degradation of conductive carbon itself. The EEI study with conductive carbon electrode helps to give a better understanding of its contribution to the interface dynamics in the composite electrode.

DATA AVAILABILITY STATEMENT

All datasets generated for this study are included in the article/**Supplementary Material**.

AUTHOR CONTRIBUTIONS

SL and XZ designed and finished the SECM experiment. DL organized the data and finalized the paper. SW, LZ, and RZ helped for the material characterization. FK and BL provided the experiment platform and funding support.

SUPPLEMENTARY MATERIAL

The Supplementary Material for this article can be found online at: https://www.frontiersin.org/articles/10.3389/fchem.2020.00114/full#supplementary-material

REFERENCES

Anothumakkool, B., Dupré, N., Moreau, P., Guyomard, D., Brousse, T., and Gaubicher, J. (2018). Peculiar Li-storage mechanism at graphene edges in turbostratic carbon black and their application in high energy Li-ion capacitor. *J. Power Sources* 378, 628–635. doi: 10.1016/j.jpowsour.2018.01.010

Fransson, L., Eriksson, T., Edström, K., Gustafsson, T., and Thomas, J. O. (2001). Influence of carbon black and binder on Li-ion batteries. *J. Power Sources* 101, 1–9. doi: 10.1016/S0378-7753(01)00481-5

Gauthier, M., Carney, T. J., Grimaud, A., Giordano, L., Pour, N., Chang, H.-H., et al. (2015). Electrode–electrolyte interface in Li-ion batteries: current understanding and new insights. *J. Phys. Chem. Lett.* 6, 4653–4672. doi: 10.1021/acs.jpclett.5b01727

Gnanamuthu, R. M., and Lee, C. W. (2011). Electrochemical properties of super P carbon black as an anode active material for lithium-ion batteries. *Mater. Chem. Phys.* 130, 831–834. doi: 10.1016/j.matchemphys.2011.08.060

He, M., Boulet-Roblin, L., Borel, P., Tessier, C., Novák, P., Villevieille, C., et al. (2016). Effects of solvent, lithium salt, and temperature on stability of carbonate-based electrolytes for 5.0 V $LiNi_{0.5}Mn_{1.5}O_4$ electrodes. *J. Electrochem. Soc.* 163, A83–A89. doi: 10.1149/2.0201602jes

Heinz, B., Fabian, P., Julian, S., and Gunther, W. (2014). Spatiotemporal changes of the solid electrolyte interphase in Lithium-ion batteries detected by scanning electrochemical microscopy. *Angew. Chem. Int. Ed. Engl.* 53, 10531–10535. doi: 10.1002/anie.201403935

Hou, P., Yin, J., Ding, M., Huang, J., and Xu, X. (2017). Surface/interfacial structure and chemistry of high-energy nickel-rich layered oxide cathodes: advances and perspectives. *Small* 13:1701802. doi: 10.1002/smll.201701802

Kajiyama, A., Masaki, R., Wakiyama, T., Matsumoto, K., Yoda, A., Inada, T., et al. (2015). Principal factors of carbon conductive agents that contribute to the gas formation in high-voltage cathode systems. *J. Electrochem. Soc.* 162, A1516–A1522. doi: 10.1149/2.0571508jes

La Mantia, F., Huggins, R. A., and Cui, Y. (2013). Oxidation processes on conducting carbon additives for lithium-ion batteries. *J. Appl. Electrochem.* 43, 1–7. doi: 10.1007/s10800-012-0499-9

Li, J., and Manthiram, A. (2019). A Comprehensive analysis of the interphasial and structural evolution over long-term cycling of ultrahigh-nickel cathodes in Lithium-ion batteries. *Adv. Energy Mater.* 6:1902731. doi: 10.1002/aenm.201902731

Li, S. R., Sinha, N. N., Chen, C. H., Xu, K., and Dahn, J. R. (2013). A consideration of electrolyte additives for $LiNi_{0.5}Mn_{1.5}O_4/Li_4Ti_5O_{12}$ Li-Ion Cells. *J. Electrochem. Soc.* 160, A2014–A2020. doi: 10.1149/2.048311jes

Li, W., Dolocan, A., Oh, P., Celio, H., Park, S., Cho, J., et al. (2017a). Dynamic behaviour of interphases and its implication on high-energy-density cathode materials in lithium-ion batteries. *Nat. Commun.* 8:14589. doi: 10.1038/ncomms14589

Li, W., Song, B., and Manthiram, A. (2017b). High-voltage positive electrode materials for lithium-ion batteries. *Chem. Soc. Rev.* 46, 3006–3059. doi: 10.1039/C6CS00875E

Li, X., Chen, Y., Nguyen, C. C., Nie, M., and Lucht, B. L. (2014). Stability of inactive components of cathode laminates for Lithium ion batteries at high potential. *J. Electrochem. Soc.* 161, A576–A582. doi: 10.1149/2.060404jes

Liu, D., Shadike, Z., Lin, R., Qian, K., Li, H., Li, K., et al. (2019a). Review of recent development of *in situ*/operando characterization techniques for lithium battery research. *Adv. Mater.* 31:1806620. doi: 10.1002/adma.201806620

Liu, D., Yu, Q., Liu, S., Qian, K., Wang, S., Sun, W., et al. (2019b). Evolution of solid electrolyte interface on TiO_2 electrodes in an aqueous Li-ion battery studied using scanning electrochemical microscopy. *J. Phys. Chem. C* 123, 12797–12806. doi: 10.1021/acs.jpcc.9b01412

Liu, D., Zeng, X., Liu, S., Wang, S., Kang, F., and Li, B. (2019c). Application of alternating current scanning electrochemical microscopy in Lithium-ion batteries: local visualization of the electrode surface. *ChemElectroChem.* 6, 4854–4858. doi: 10.1002/celc.201901431

Liu, S., Liu, D., Wang, S., Cai, X., Qian, K., Kang, F., et al. (2019d). Understanding the cathode electrolyte interface formation in aqueous electrolyte by scanning electrochemical microscopy. *J. Mater. Chem. A* 7, 12993–12996. doi: 10.1039/C9TA03199E

Membreño, N., Park, K., Goodenough, J. B., and Stevenson, K. J. (2015). Electrode/electrolyte interface of composite α-$Li_3V_2(PO_4)_3$ Cathodes In A Nonaqueous Electrolyte for Lithium ion batteries and the role of the carbon additive. *Chem. Mater.* 27, 3332–3340. doi: 10.1021/acs.chemmater.5b00447

Metzger, M., Marino, C., Sicklinger, J., Haering, D., and Gasteiger, H. A. (2015). Anodic oxidation of conductive carbon and ethylene carbonate in high-voltage Li-ion batteries quantified by on-line electrochemical mass spectrometry. *J. Electrochem. Soc.* 162, A1123–A1134. doi: 10.1149/2.0951506jes

Ngo, D.-T., Scipioni, R., Simonsen, S. B., Jørgensen, P. S., and Jensen, S. H. (2016). A TEM study of morphological and structural degradation phenomena in $LiFePO_4$-CB cathodes. *Inte. J. Energy Res.* 40, 2022–2032. doi: 10.1002/er.3575

Nordh, T., Younesi, R., Brandell, D., and Edström, K. (2015). Depth profiling the solid electrolyte interphase on lithium titanate ($Li_4Ti_5O_{12}$) using synchrotron-based photoelectron spectroscopy. *J. Power Sources* 294, 173–179. doi: 10.1016/j.jpowsour.2015.06.038

Polcari, D., Dauphin-Ducharme, P., and Mauzeroll, J. (2016). Scanning Electrochemical microscopy: a comprehensive review of experimental parameters from 1989 to 2015. *Chem. Rev.* 116, 13234–13278. doi: 10.1021/acs.chemrev.6b00067

Qi, X., Blizanac, B., Dupasquier, A., Lal, A., Niehoff, P., Placke, T., et al. (2015). Influence of thermal treated carbon black conductive additive on the performance of high voltage spinel Cr-doped $LiNi_{0.5}Mn_{1.5}O_4$ composite cathode electrode. *J. Electrochem. Soc.* 162, A339–A343. doi: 10.1149/2.0401503jes

Qi, X., Blizanac, B., Dupasquier, A., Meister, P., Placke, T., Oljaca, M., et al. (2014). Investigation of PF_6^- and $TFSI^-$ anion intercalation into graphitized carbon blacks and its influence on high voltage lithium ion batteries. *Phys. Chem. Chem. Phys.* 16, 25306–25313. doi: 10.1039/C4CP04113E

Scipioni, R., Jørgensen, P. S., Ngo, D.-T., Simonsen, S. B., Liu, Z., Yakal-Kremski, K. J., et al. (2016). Electron microscopy investigations of changes in morphology and conductivity of $LiFePO_4$/C electrodes. *J. Power Sources* 307, 259–269. doi: 10.1016/j.jpowsour.2015.12.119

Soon, J., Chae, S., Lee, T. J., Jung, J., Ryu, J. H., and Oh, S. M. (2018). Grafting nitrophenyl groups on carbon surfaces by diazonium chemistry to suppress irreversible reactions in high-voltage $LiNi_{0.5}Mn_{1.5}O_4$ positive electrodes. *J. Electrochem. Soc.* 165, A1372–A1376. doi: 10.1149/2.0691807jes

Tatara, R., Karayaylali, P., Yu, Y., Zhang, Y., Giordano, L., Maglia, F., et al. (2019). The effect of electrode-electrolyte interface on the electrochemical impedance spectra for positive electrode in Li-ion battery. *J. Electrochem. Soc.* 166, A5090–A5098. doi: 10.1149/2.0121903jes

Tripathi, A. M., Su, W.-N., and Hwang, B. J. (2018). *In situ* analytical techniques for battery interface analysis. *Chem. Soc. Rev.* 47, 736–851. doi: 10.1039/C7CS00180K

Ventosa, E., Madej, E., Zampardi, G., Mei, B., Weide, P., Antoni, H., et al. (2017). Solid electrolyte interphase (SEI) at TiO_2 electrodes in Li-ion batteries: defining apparent and effective SEI based on evidence from X-ray Photoemission spectroscopy and scanning electrochemical microscopy. *ACS Appl. Mater. Inter.* 9, 3123–3130. doi: 10.1021/acsami.6b13306

Wang, S., Liu, Q., Zhao, C., Lv, F., Qin, X., Du, H., et al. (2018). Advances in understanding materials for rechargeable Lithium batteries by atomic force microscopy. *Energy Environ. Mater.* 1, 28–40. doi: 10.1002/eem2.12002

Younesi, R., Christiansen, A. S., Scipioni, R., Ngo, D.-T., Simonsen, S. B., Edström, K., et al. (2015). Analysis of the interphase on carbon black formed in high voltage batteries. *J. Electrochem. Soc.* 162, A1289–A1296. doi: 10.1149/2.0761507jes

Zampardi, G., Ventosa, E., La Mantia, F., and Schuhmann, W. (2013). In situ visualization of Li-ion intercalation and formation of the solid electrolyte interphase on TiO_2 based paste electrodes using scanning electrochemical microscopy. *Chem. Commun.* 49, 9347–9349. doi: 10.1039/c3cc44576c

Zheng, J., Xiao, J., Xu, W., Chen, X., Gu, M., Li, X., et al. (2013). Surface and structural stabilities of carbon additives in high voltage lithium ion batteries. *J. Power Sources* 227, 211–217. doi: 10.1016/j.jpowsour.2012.11.038

Conflict of Interest: The authors declare that the research was conducted in the absence of any commercial or financial relationships that could be construed as a potential conflict of interest.

frontiers in Chemistry

REVIEW
published: 05 May 2020
doi: 10.3389/fchem.2020.00261

Recognition of Ionic Liquids as High-Voltage Electrolytes for Supercapacitors

Shanshan Pan [1,2], **Meng Yao** [1,2], **Jiahe Zhang** [1], **Bosen Li** [1,2], **Chunxian Xing** [1], **Xianli Song** [1,2], **Peipei Su** [1,2] and **Haitao Zhang** [1,2,3]*

[1] Beijing Key Laboratory of Ionic Liquids Clean Process, CAS Key Laboratory of Green Process and Engineering, Institute of Process Engineering, Chinese Academy of Sciences, Beijing, China, [2] School of Chemical Engineering, University of Chinese Academy of Science, Beijing, China, [3] Hebei Institute of Process Innovation Co. Ltd, Langfang, China

The electrochemical stability of electrolytes is essential to the working potential of supercapacitors. Ionic liquids (ILs) are being considered as safe alternatives to current organic electrolytes and attracting extensive interests owing to their inflammability, widened potential windows, and superior ionic conductivity. Novel supercapacitors with IL electrolytes exhibit attractive energy density and can be utilized in various energy storage systems. Most previous studies focused on electrochemical performances, while rare attentions were devoted to energy storage process details or mechanisms. This review comprehensively summarizes the latest progress on formulated IL electrolytes for different types of supercapacitors, with an emphasis on the intrinsic understanding of the related energy storage mechanisms. Subsequently, comparisons of various IL-based liquid-state electrolytes as well as the state-of-the-art advancements in optimizing ILs electrolytes are introduced. The authors attempt to reveal the inherent correlation between the usage of IL electrolytes and the properties of supercapacitors via referenced works. Some emerging applications of ionogel electrolytes based on conventional polymers and poly(IL)s for flexible supercapacitors are also presented, including the existing problems. In addition, challenges and future perspectives of research in this field are highlighted.

Keywords: ionic liquids, high-voltage electrolytes, liquid electrolytes, ionogel electrolytes, supercapacitors, mechanisms

Edited by:
Syed Mubeen Jawahar Hussaini,
The University of Iowa, United States

Reviewed by:
Abhishek Lahiri,
Brunel University London,
United Kingdom
Steven G. Greenbaum,
Hunter College (CUNY), United States

***Correspondence:**
Haitao Zhang
htzhang@ipe.ac.cn

Specialty section:
This article was submitted to
Electrochemistry,
a section of the journal
Frontiers in Chemistry

Received: *18 January 2020*
Accepted: *18 March 2020*
Published: *05 May 2020*

Citation:
Pan S, Yao M, Zhang J, Li B, Xing C, Song X, Su P and Zhang H (2020) Recognition of Ionic Liquids as High-Voltage Electrolytes for Supercapacitors. Front. Chem. 8:261. doi: 10.3389/fchem.2020.00261

INTRODUCTION

Electrochemical energy storage systems have attracted extensive interests in recent years due to their widespread applications in smart electronics, electric vehicles, as well as hybrid load-leveling systems for intermittent green sources. Among various energy storage devices, lithium-ion batteries (LIBs) and supercapacitors (SCs) are the two most extensively used energy storage systems (Ding et al., 2018; Li M. et al., 2018). Nowadays, commercial LIBs with low power density and potential safety issues cannot meet the growing energy needs. Fortunately, SCs with rapid power output and long cycle life can be used independently or supplement batteries in many fields such as electric buses, light rail, wearable electronics, and energy storage systems for intermittent renewable energy sources, triggering growing tremendous interests (Conway and Pell, 2003; Simon and Gogotsi, 2008; Shao et al., 2018). Thus, it is highly desirable to understand the mechanisms of supercapacitors and develop advanced supercapacitors.

SCs can store and release charges rapidly since the charging and discharging processes are limited by surface processes rather than ion diffusion. Generally, SCs can be classified into three categories: electric double-layer capacitors (EDLCs), pseudocapacitors, and hybrid supercapacitors. Energy density, as one of the main parameters, could evaluate the properties of supercapacitors. However, low energy density hampered the widespread commercialization of supercapacitors. The energy density (E) of supercapacitors is determined by voltage window (V) and capacitance (C) of the device according to Equation 1 (Simon and Gogotsi, 2008):

$$E = \frac{1}{2}CV^2 \tag{1}$$

On the one hand, the energy density of supercapacitors can be elevated by developing electrode materials with high specific capacity; on the other hand, a significant increase in energy density can be achieved by widening the potential window of the device as the energy density is proportional to V^2. The potential window of the device is mainly limited by the electrochemical stability of the used electrolytes. One means of raising the voltage is to employ organic electrolytes with higher decomposition voltage instead of aqueous electrolytes. Unfortunately, organic electrolytes suffered from inflammability and toxicity, resulting in serious safety issues. Therefore, developing safe and high-voltage electrolytes can promote the performances of SCs.

Compared to aqueous and organic electrolytes, ionic liquids (ILs) composed of a discrete anion and cation have many merits, including widened electrochemical stability window (~4.5 V), superior ionic conductivity, negligible volatility, and low flammability (Armand et al., 2009; Van Aken et al., 2015; Watanabe et al., 2017). Therefore, ILs are promising alternatives to traditional electrolytes of supercapacitors and thus have attracted widespread attentions. Till now, various IL-based electrolytes including pure ILs, eutectic ILs, and ILs/organic solvent mixtures have been extensively investigated in supercapacitors. Most of IL electrolytes previously studied were non-amphiphilic ILs. In the published literatures so far, non-amphiphilic ILs based on imidazolium and pyrrolidinium were extensively researched due to the relatively lower viscosity and reasonable ionic conductivity (Balducci et al., 2004; Galinski et al., 2006). In general, imidazolium salts possess high ionic conductivity, while pyrrolidinium salts exhibit wide electrochemical stability windows. More recently, Mao et al. discovered surface-active IL electrolytes for EDLCs, exhibiting unusual interfacial ion distributions owing to significant van der Waals interactions, which enhanced the performance of EDLCs (Mao et al., 2019). Furthermore, IL electrolytes allow safe operation at higher temperatures due to their outstanding thermostability, and one of the first demonstrations of this was that of Mastragostino's group (Largeot et al., 2011). Although tremendous efforts have been devoted to IL electrolytes for supercapacitors and much progress has been made, IL electrolytes still have some drawbacks such as high viscosity and limited ionic conductivity at low temperatures and poor contact with electrodes, which greatly limited their applications in supercapacitors (Balducci et al., 2005). Forming eutectic IL mixtures is considered as an effective route to improve the low temperature performance of supercapacitors, which violates the traditional concept that IL electrolytes can only be used above room temperature. The extended temperature range of −50 to 100 °C for a supercapacitor was achieved by employing an eutectic IL mixture (1:1 $\text{Pip}_{13}\text{FSI}$:$\text{Pyr}_{14}\text{FSI}$) (Lin et al., 2011). In addition, with the increased consumption of flexible electronic devices, IL-based solid or gel electrolytes are the most promising electrolyte candidates for solid supercapacitors (Lu et al., 2014). Compared to typical solid electrolytes, gel electrolytes exhibit better flexibility, higher ionic conductivity, as well as acceptable compatibility with electrode, being suitable as electrolytes for flexible supercapacitors. More importantly, ILs are not only widely employed in energy storage devices but also as model materials/electrolytes to solve fundamental problems caused by increased capacitance and ion transfer in carbon nanopores. Besides these actual applications, IL media are direct systems for basic research to understand the properties of the electrodes/electrolytes interface in supercapacitors because there is no solvent. Unfortunately, the cost issue is still a problem in considering commercial applications, which is due to the purification cost, not synthesis.

Although ILs have price and purity issues, their significant advantages as electrolytes are undeniable. Exploiting advanced IL electrolytes matching with nanostructured carbon is certainly a promising direction for constructing the next generation of high-energy density supercapacitors with broad temperature range. In addition, the design of novel electrolytes based on ILs is of vital importance to the standardization of electrochemical tests and methods, which can evaluate the stabilities of electrolytes employed in supercapacitors. So far, electrolytes based on ILs for supercapacitors have been widely investigated with the purpose of widening the potential window of devices, and some related reviews have been made (Yin et al., 2019). However, there are limited reviews concerning the intrinsic mechanisms of IL-based supercapacitors. The latest research progress also needs to be concluded, which will provide the guidance for future studies of supercapacitors with IL electrolytes. In this review, storage mechanisms of different kinds of supercapacitors will be explained in order to understand the behaviors of IL electrolytes in different types of supercapacitors. We emphatically present the recent advances in liquid-state IL electrolytes and IL-based solid electrolytes for supercapacitors (**Figure 1**). We also focus on the common improvement strategies of IL electrolytes and the latest developments. In addition, some remaining challenges for future supercapacitors are enumerated.

ENERGY STORAGE MECHANISMS

ILs play a crucial role in the field of energy storage devices such as lithium ion batteries, supercapacitors, and fuel cells, usually as their electrolytes. Different energy storage devices have diverse basic principles and different requirements for IL electrolytes. ILs are generally divided into three categories: aprotic, protic, and zwitterionic, as shown in **Figure 2**. Among them, aprotic type

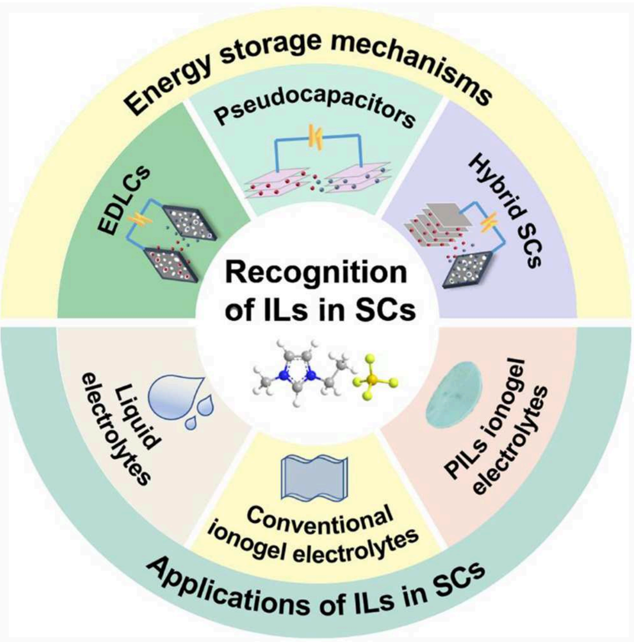

FIGURE 1 | Energy storage mechanisms and applications of ionic liquids (ILs) in supercapacitors (SCs).

ILs are suitable as high-voltage electrolytes for supercapacitors and lithium ion batteries, while protic ILs can be applied to fuel cells (Armand et al., 2009). Understanding the mechanisms of ILs in various supercapacitors including electric double-layer capacitors, pseudocapacitors, and hybrid supercapacitors is important for guiding the selection and engineering optimization of IL electrolytes.

Electric Double-Layer Capacitors With ILs

EDLCs are the simplest supercapacitors based on charge separation process, which stores energy by the charge arrangement in the Helmholtz bilayer. **Figure 3A** shows the typical double-layer charge storage mechanism. The cyclic voltammogram curve of ideal EDLCs should maintain a rectangular shape when the solution resistance is ignored, which shows a typical capacitive behavior, as illustrated in **Figure 3B**. The charge storage process in EDLCs only involves physical absorption and desorption on the surface of electrodes, without the occurrence of Faradaic reaction (Conway, 1991; Stoller and Ruoff, 2010), thus providing high power density. The stored energy of EDLCs is restricted by the specific surface areas of the electrode materials, and carbon-based materials with high specific surface areas are usually selected as the electrodes of EDLCs (Liu et al., 2010; Simon and Gogotsi, 2013). Capacitance is the physical characteristic of the electrodes/electrolytes coupling performance for EDLCs, which can be described as Equation 2 (Zhang and Zhao, 2009):

$$C_{dl} = \frac{Q}{V} = \frac{\varepsilon_r \varepsilon_0}{d} A \tag{2}$$

where C_{dl} is the capacitance of one electrode of EDLCs, Q is the charge transferred at a applied voltage V, ε_{r} is the dielectric constant of the electrolyte, ε_{o} is the dielectric constant of vacuum, d is Debye length, which represents the effective charge separation distance, and A is the surface area of electrodes. When C_{dl} is constant for EDLCs, the following Equation 3 describing the response current I can be derived from the above Equation 2:

$$I = \frac{dQ}{dt} = C_{dl} \frac{dV}{dt} \tag{3}$$

In Equation 3, t is the charge time. If the potential V changes linearly with time t, $\frac{dV}{dt}$ can be considered as a constant and denoted as γ. As a result, Equation 3 can be simplified to Equation 4:

$$I = C_{dl} \gamma \tag{4}$$

Up to now, tetraethylammonium tetrafluoroborate (Et_4NBF_4) in organic carbonates is the most widely used electrolytes (Pandolfo and Hollenkamp, 2006). However, the electrochemical stability window of organic carbonates is lower than IL system, limiting the energy density of EDLCs. The energy density of EDLCs can be elevated to that of Ni/MH batteries (>100 W h/kg) by employing IL electrolytes with widened voltage window (Liu et al., 2010; Tamailarasan and Ramaprabhu, 2012), which is much higher than that of supercapacitors with organic electrolytes. However, the structure of electric double layer in IL media with no solvent is different from that in traditional electrolytes since the solvent molecules will distribute charged ions. Kornyshev proposed the classical model, Gouy–Chapman–Stern (GCS), was inaccurate for many of the basic assumptions are inadequate (Kornyshev, 2007). Especially, GCS model not only ignores the correlation between ions but also treats all ions as a point charge. It was okay for organic or aqueous system, but in ILs, the relationship between anions and cations was the center of physical properties of ILs. Thus, he put forward a new theory called mean-field theory accounting for the finite size of ions and the mutual interactions between ions (Bazant et al., 2012), which showed that different differential capacitance curves would appear in different electrolytes. Pean proposed a simulation methodology using a hybrid supercapacitor simulation cell to compute a single-electrode capacitance in pure IL electrolytes at 100°C (Pean et al., 2015). For the IL system, the strong correlation between ions of ILs is the main obstruction in standalone electrolytes consisting of ILs. Some groups diluted the IL electrolytes to maintain ions of ILs separated in order to address the above issue. Recently, the first insight of IL interface using various experimental techniques was reported. By atomic force microscopy (AFM), a strong delamination effect was observed at the interface of electrodes/electrolytes (Atkin and Warr, 2007; Hayes et al., 2010; Atkin et al., 2011). Later, this was confirmed by surface force apparatus (SFA) (Smith et al., 2013) or by high-energy X-ray reflectivity (Mezger et al., 2008, 2015).

However, the above studies focused on the interfacial properties between ILs and planar electrodes. Compared to planar electrodes, porous carbons are the most widely used due to their high accessible surface area. Burt et al. used a

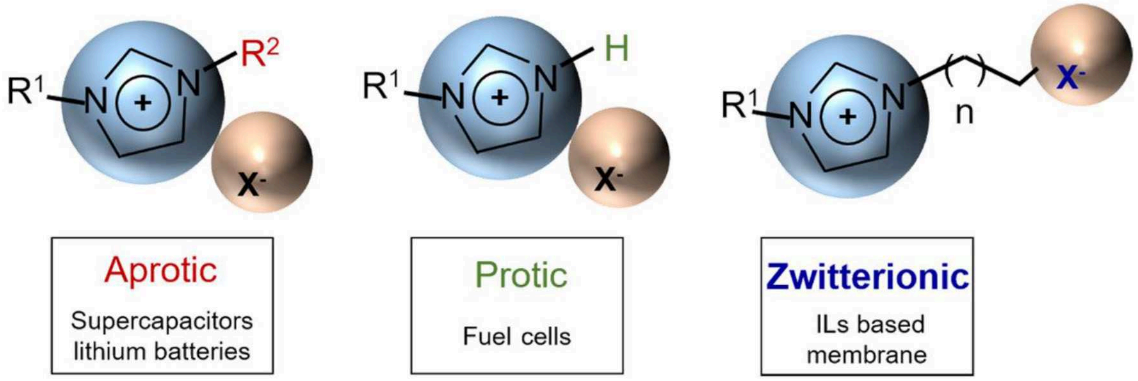

FIGURE 2 | Three categories of ionic liquids (ILs) (aprotic, protic, and zwitterionic) and their corresponding applications. Adapted from Armand et al. (2009), Nature Publishing Group.

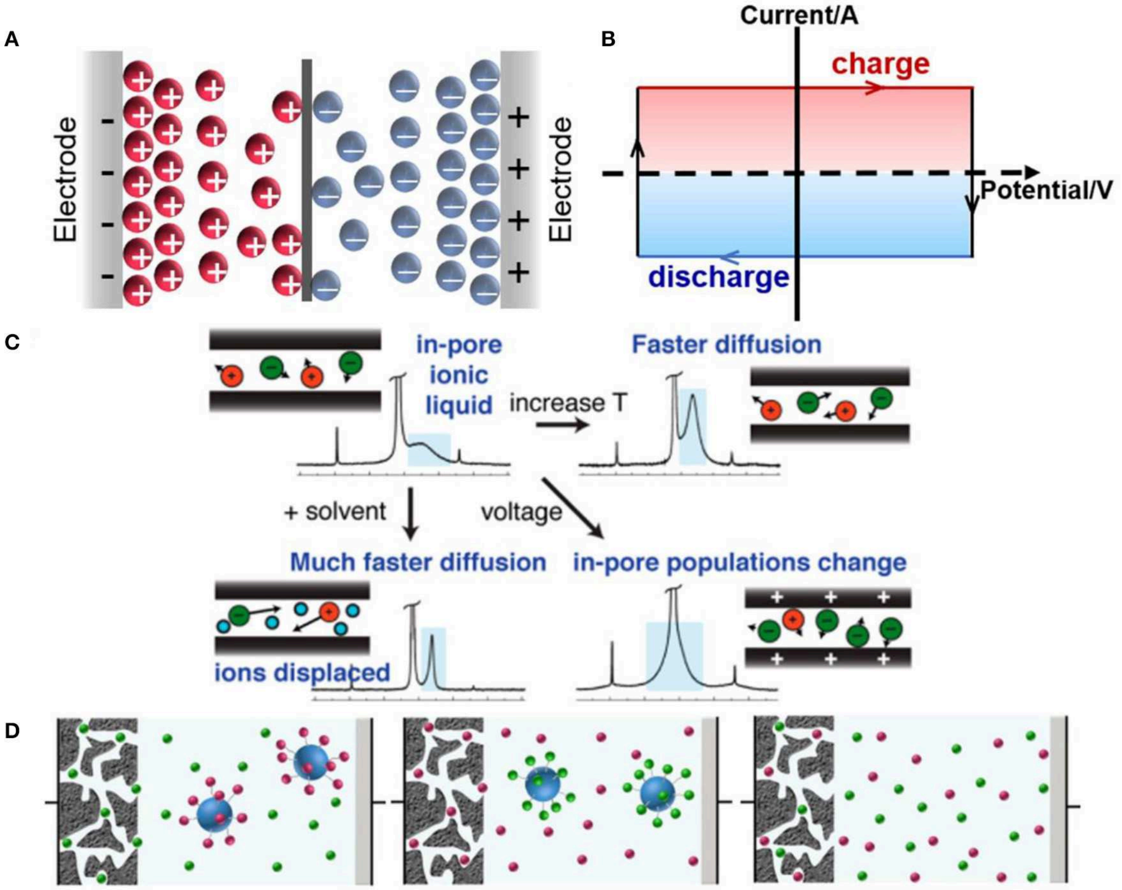

FIGURE 3 | Schematics of **(A)** charge-storage mechanisms and **(B)** cyclic voltammogram curve of ideal EDLCs; **(C)** charging mechanism of in-pore ionic liquids (ILs) and the effects of temperature, solvent, and voltage on ions dynamic. Reproduced from: **(C)** Forse et al. (2015), American Chemical Society, and **(D)** Dou et al. (2017), Nature Publishing Group.

combined electrochemical/simulation method to elucidate the behaviors and mechanisms of pure ILs and its mixture with acetonitrile (ACN) in nanoporous carbons (Burt et al., 2016). The results indicated that higher concentrated ions of pure ILs did not result in significant increase in capacitance of nanoporous carbon-based EDLCs, which was attributed to the increased difficulty in separating ions of opposite charges of pure ILs. The mechanism of EDLCs changes from counterion adsorption in diluted ACN to ion exchange in pure ILs. In addition, the interface structure is affected by the structure of the electrode surface and IL electrolytes. Planar electrodes show a layered structure with ordered or disordered layers of ions, while electrodes with defects may break the layered structure. EDLCs with nanoporous carbons exhibit the best performance (Salanne, 2017). Remarkably, the introduction of IL electrolytes may not lead to the obvious increase in capacitance, but the structures of electrodes affect the capacitance. Till now, great efforts have been devoted to improving the energy density of EDLCs in consideration of the matching of pore size and IL size (Chmiola et al., 2006). From Jose's research, he showed that the size of bulk ILs mostly depends on the length of the alkyl chain of the ions (Lopes and Padua, 2006). Furthermore, Liu demonstrated that the influence of the alkyl chains of ILs on the electrochemical properties of graphene nanosheets was studied by electrochemical experiments (Liu et al., 2011). More recently, the performance of ILs in electrode models of different structures was investigated using molecular dynamics simulations by Pereira et al. (2019). For a planar electrode, ILs formed a layered structure that changed with the polarity of the electrode due to the asymmetry of ions. For nanoporous electrodes, a monolayer of ions inside smaller pores was observed, while a multilayered structure was observed in wider pores. They also proposed that higher energy density was achieved by employing electrodes with narrower pores at lower voltages. However, at high potentials, supercapacitors employing electrodes with wider pores exhibited higher energy density.

The obvious advantages of ILs are widened voltage window and high thermostability, ensuring high energy density and wide operating temperature range of EDLCs. A wide electrochemical window (up to 3.6 V) and good high-temperature durability of the 1-ethyl-3-methylimidazolium and *N*, *N*-dimethyl pyrrolidinium cation-based electrolytes were demonstrated by Zhu et al., exhibiting a good application prospect in supercapacitors (Zhu et al., 2007). Besides, some new ILs have been employed, such as azepanium used for supercapacitors (Pohlmann et al., 2015). However, compared to organic electrolytes, conventional ILs exhibit no significant increase in capacitance. In addition, the power performance of ILs cannot compete with organic electrolytes. Therefore, Forse et al. used nuclear magnetic resonance (NMR) spectroscopy to study ion dynamics and charge storage of ILs in porous carbons, thus explaining the power properties of ILs in EDLCs. They found that the mechanism of IL-based EDLCs involved both counterion adsorption and coion desorption. In addition, the effects of temperatures, voltages, and addition of organic solvent on the rate of ionic diffusion were investigated (**Figure 3C**). Elevated temperatures and the addition of solvent enhanced ionic mobility, and higher applied voltages changed the in-pore populations of ions. Faster diffusion meant more rapid power output (Forse et al., 2015). Thus, the power density could be improved by developing ILs with faster ionic diffusion. Recently, this group observed ion dynamics in supercapacitors during charging via *in situ* NMR measurements, indicating that in-pore ion populations, ion–ion interaction, and carbon porous structure would affect ion dynamics (Forse et al., 2017). These works may be favorable for the adjustment of the energy and power density of IL-based supercapacitors. In addition, Dou et al. monitored cations and anions independently using silica nanoparticle-grafted ILs, as shown in **Figure 3D**; silica nanoparticle-grafted ions cannot enter the pores of activated carbon, whereas free counterions can enter upon charging (Dou et al., 2017).

Pseudocapacitors With ILs

The mechanism of pseudocapacitors is based on fast Faradaic redox reactions that occur at the surface or near-surface region of the electrode materials with electron transfer but without any bulk phase transformation during charging/discharging (Conway, 1995). The key difference between EDLCs and pseudocapacitors is that the former store energy by charge separation precisely like traditional physical capacitors, while the energy storage mechanism of the latter is exactly similar to that of battery systems. No chemical transformation occurred during charging and discharging process of pseudocapacitors, but due to the Faraday reaction, a reversible functionalized molecular layer was formed on the surface of the active materials. It is worth noting that the features of pseudocapacitors are completely different from the redox reactions involved in battery systems where bulk phase transformation occurs. The term pseudocapacitance is used to describe the capacitance, which comes from capacitive electrode materials undergoing fast electron-transfer Faradaic reactions. Thus, pseudocapacitance is not the real capacitance arising from double-layer charging but the pseudocapacitance generated by redox reactions without phase transformation.

Pseudocapacitance was divided into three categories: (1) underpotential deposition, (2) surface redox system, and (3) intercalation system, as illustrated in **Figure 4A** (Conway, 1991; Conway and Pell, 2003; Augustyn et al., 2014). From the cyclic voltammetry (CV) curves of reversible pseudocapacitors in **Figure 4B** (Conway, 1991), the presence of critical sweep rate (ν_0) is one typical feature of pseudocapacitors because the presence of effective equivalent series resistance causes polarization effect. In addition, the charge transfer resistance limits the kinetic of pseudocapacitors, and the behavior of pseudocapacitors will deviated from ideal capacitive behavior. The kinetic reaction of pseudocapacitors would change from reversible to irreversible with the increase in sweep rate.

As we all know, ions (e.g., H^+ or Pd^{2+}) in solution can be adsorbed on the surface of the noble metal (e.g., Pt or Au) to form a monolayer under their equilibrium potentials for cation reduction, and the process was called underpotential deposition, which can be described by Equation 5 (Sudha and Sangaranarayanan, 2002):

$$M + xC^{z+} + xz^{+} \leftrightarrow C.M \tag{5}$$

where M is the noble metal, C^{z+} is the deposited ions, x is the number of deposited ions, and z is the charges of the deposited ions. The capacitance produced by this process is usually limited

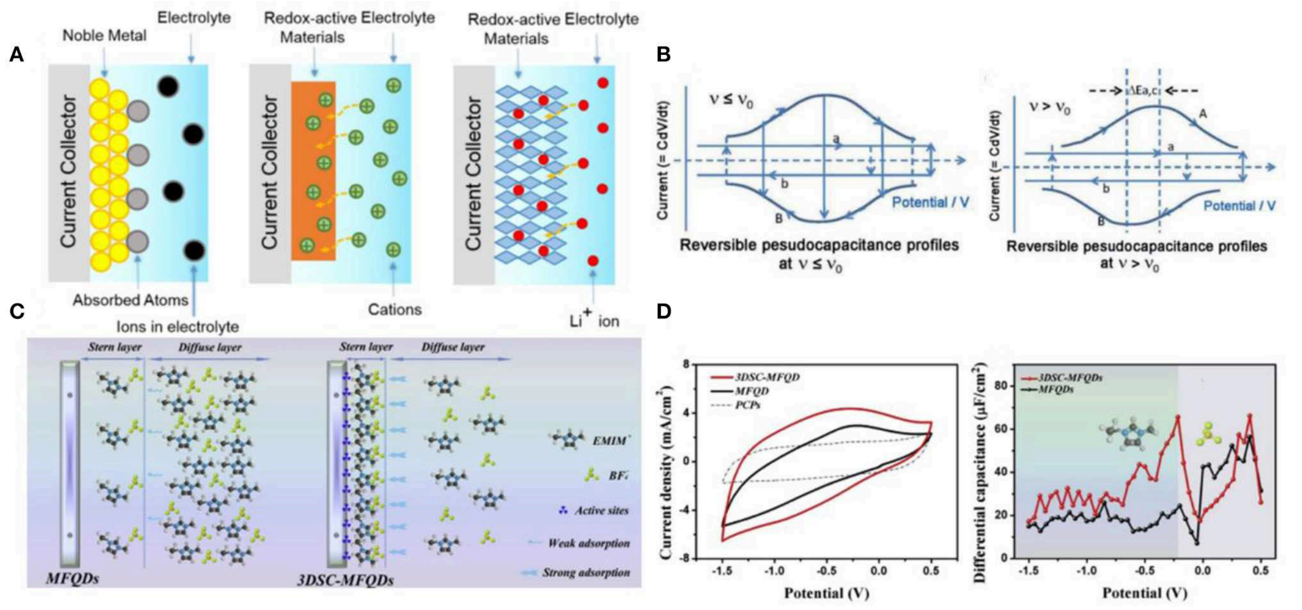

FIGURE 4 | (A) Schematic diagrams of three different energy storage mechanisms of pseudocapacitors; **(B)** cyclic voltammetry (CV) profiles of reversible pseudocapacitors at different sweep rate *v*, where *v*$_0$ is the critical sweep rate; **(C)** schematic diagrams of Stern/diffusion layer and **(D)** Cd–E curves of MFQDs and 3DSC-MFQDs. Reproduced from: **(A)** Augustyn et al. (2014), Royal Society of Chemistry; **(B)** Conway (1991), Electrochemical Society; and **(C,D)** Yang et al. (2020), Elsevier.

due to the narrow potential ranges (0.3–0.6 V), which results in low energy density.

The surface redox system undergoes a Faraday reaction with electron transfer, such as transition metal oxides (e.g., RuO_2, MnO_2, conductive polymers) (Subramanian et al., 2004; Jiang et al., 2012a,b; Xia et al., 2012). The first pseudocapacitive material was RuO_2, delivering a specific capacitance of over 800 F g^{-1}. However, RuO_2 suffers from the disadvantage of high cost, which still cannot be settled (Mayrand-Provencher et al., 2010). MnO_2 is the promising low-cost electroactive material to replace RuO_2 due to its versatility in the electrochemical behaviors. Meanwhile, ILs exhibited well performance in pseudocapacitors based on MnO_2. Unfortunately, the specific capacitance is noticeably low (∼100 F g^{-1}) (Li and Wei, 2012; Li et al., 2012). Some groups used X-ray photoelectron spectroscopy, X-ray absorption spectroscopy, and electrochemical quartz crystal microbalance to reveal that large cations of IL electrolytes only adsorb on surface without permeation into the lattice structure of MnO_2 (Benedetti et al., 2008; Chang et al., 2009; Lee et al., 2010). Compared with conventional electrolytes, ILs cannot widely dispersed within the pores of solid materials. In addition, the electronic conductivity of these metal oxides is rather low, and the wettability of electrode materials in ILs determines the charge transfer resistance. In addition, some groups found that many pseudocapacitors with IL electrolytes suffered from a huge iR drop (Brandt and Balducci, 2014; Rai et al., 2014; Navathe et al., 2015). One effective strategy is to use gold-modified electrodes, which can markedly promote the pseudocapacitive behaviors of active materials in ILs. Another way is to design the nanostructured active materials geometrically in order to match the interacting ions of electrolytes, which can achieve an energy density of 163 W h kg^{-1} of MnO_2-based pseudocapacitors (Maiti et al., 2015). More recently, Yang et al. developed a 3D space-confined $MnFe_2O_4$ exhibiting superior interfacial properties and pseudocapacitive storage (Yang et al., 2020). They studied the mechanism of the Stern/diffusion layer of IL ions near electrode surface and concluded that the characteristic adsorption between this electrode and $EMIM^+$ led to huge amounts of $EMIM^+$ absorbed densely in the Stern layer, which enhanced capacitance, as shown in **Figures 4C,D**.

Intercalation pseudocapacitance is another Faraday process that occurs without crystalline phase transition and when the intercalation of quasi-two-dimensional electroactive substances occur, as illustrated in Equation 6:

$$BA_y + xLi^+ + xe^- \leftrightarrow Li_xBA_y \tag{6}$$

where BA_y is the intercalation electrode material (e.g., Nb_2O_5), and x is the transferred electrons number. The difference between this intercalation process for pseudocapacitors and batteries is whether the electrode materials undergo a crystal phase transition during electrons transfer. An embedded system in a tantalum capacitor includes inserting Li^+ into the bulk of materials such as MoS_2 (Yang et al., 2015; Yoo et al., 2016).

These three mechanisms of pseudocapacitors are based on different Faraday processes and appear in diverse materials; however, they provide similar thermodynamic characteristics such as the logarithmic relationship shown in Equation 7.

$$E = E^0 + \frac{RT}{nF}\ \ln\frac{X}{(1-X)} \tag{7}$$

where E is the electrode potential (V), R is the ideal gas constant (8.314 J mol^{-1} K^{-1}), T is the temperature (K), n is the number of electrons, F is Faraday's constant (96,485 C mol^{-1}), and X is the occupancy fraction of the surface or lattice layer.

Although the electrochemical responses of pseudocapacitive and double layer charging are similar, their mechanisms are totally different. Shen proposed a possible energy storage mechanism of γ-FeOOH electrode in IL electrolytes (EMIM-NTF$_2$) (Shen et al., 2016). If the cations of ILs intercalate into the lattice, the size and the geometry of the organic cations should match the pores and channels of the lattice. Compared with the simple inorganic cations, the organic cations of ILs are larger, while IL cations have an asymmetrical charge distribution.

Hybrid Supercapacitors With ILs

Hybrid supercapacitors can maximize the operating voltage window of supercapacitors via employing one battery-type anode and one capacitive-type cathode and thus have attracted extensive efforts (Li B. et al., 2018). Until now, lithium and sodium ion capacitors are the mostly investigated hybrid supercapacitors. Furthermore, using IL electrolytes can also widen the potential window of hybrid supercapacitors (dos Santos et al., 2019). Unlike IL electrolytes in EDLCs or pseudocapacitors, lithium or sodium salt is usually added to IL electrolytes in hybrid supercapacitors.

Lithium Ion Capacitors

Lithium ion capacitors (LICs), as a typical representative of hybrid supercapacitors, employ capacitive-type positives with large surface area and battery-type negatives with high capacity and thereby include both the intercalation/deintercalation and rapid adsorption/desorption charge–discharge mechanisms. During the charge and discharge process, ions were adsorbed/desorbed on the surface of the capacitive-type electrodes, while Li$^+$ were intercalated/deintercalated in the bulk of battery-type electrodes. Electrolytes are of importance to the inherent storage mechanism and overall performance of LICs. IL electrolytes with high ionic conductivity and non-volatility in a wide temperature range as well as widened electrochemical windows can promote the performance of LICs. Therefore, tremendous studies were focused on ILs, which can be employed as the electrolytes of LICs.

Most of published works focused on electrode materials of LICs systems but rarely on electrolytes especially IL electrolytes and their transport mechanisms. The ions of ILs distinctly differ from solvated anions of conventional electrolytes, which would affect both the structure of double layer and the nature of ILs. The schematic of IL-based LICs configuration and the development history are illustrated in **Figures 5A,C**. Unfortunately, high viscosity of IL electrolytes may lead to poor rate capability compared to that of common organic electrolytes. Norihisa Handa et al. reported an IL electrolyte of 1-ethyl-3-methyl imidazolium bis(fluorosulfonyl)imide (EMIMFSI) for EDLCs, exhibiting superior rate capability regardless of whether the electrode materials contained a binder or not. In addition, employing EMIMFSI as electrolyte can inhibit self-discharge behavior. In contrast, the charge/discharge process of LICs includes Li$^+$ intercalation/deintercalation mechanism, which is different from typical EDLCs. Therefore, additional lithium salts are needed to provide Li$^+$. Previous work reported an LiFSI/EMIMFSI electrolyte for LIBs, showing well cycle durability and rapid charge–discharge performance.

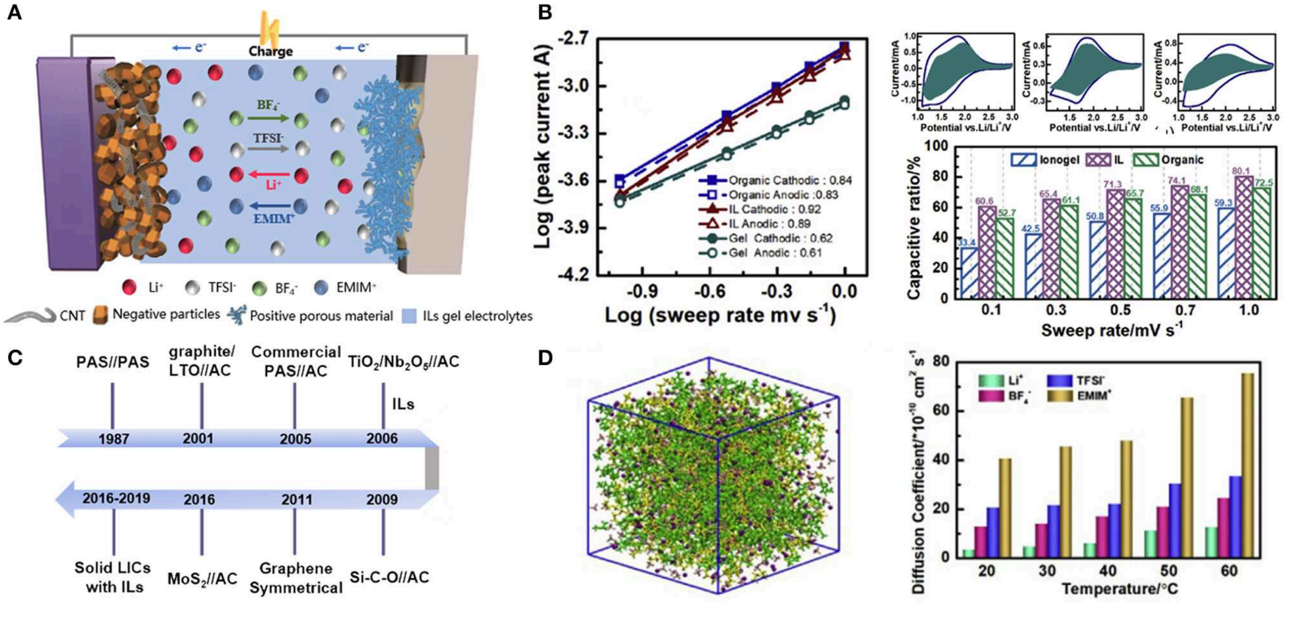

FIGURE 5 | (A) Schematic illustration of ionic liquid (IL)-based lithium ion capacitors (LICs) structure; **(B)** specific current peaks of the three electrolytes (organic, IL, and IL gel) and their corresponding capacitive contribution with different sweep rates; **(C)** the evolution history of LICs; **(D)** simulated microstructures and dependence of the diffusion coefficients of different ions on temperature in the formulated IL electrolyte. Reproduced from: **(B,D)** Zhang J. H. et al. (2019), Elsevier.

These results may be favorable for the design of IL-based electrolytes for LICs. More recently, an IL electrolyte system of LiFSI/EMIMFSI for LICs was proposed by Hirota et al. (2018). The LiFSI/EMIMFSI electrolyte is more stable than $LiPF_6$-based solvent electrolyte at both high and low temperatures.

To comprehensively understand the effect of electrolytes on energy storage mechanism, the respective contributions of the capacitive- and Faradaic-type elements in three different electrolytes (organic, the formulated IL, and IL gel) were quantitatively calculated by Zhang J. H. et al. (2019), as shown in **Figure 5B**. The group found that the formulated IL ($EMIMBF_4$) system gave the highest b value, indicating that the capacitive contribution was the most significant in the IL system. Furthermore, a simulation of the molecular dynamics was conducted to explain why the formulated IL enhanced capacitive contributions. **Figure 5D** illustrated that the diffusion coefficient of Li^+ was the lowest among all ions in the IL electrolyte, which was due to the form of Li^+ clusters. In contrast, $EMIM^+$ possessed a relatively high diffusion coefficient and thus enhancing capacitive contributions. Through this work, we can get a good understanding of the internal storage mechanism of LICs with IL electrolytes.

Sodium Ion Capacitors

In consideration of the limited resources of lithium, sodium ion batteries (SIBs) are considered one of the most promising alternative energy storage systems due to the adequate resources and low cost of sodium (Shen et al., 2018). Inspired by the research progress of SIBs and LICs, immense research interests have been focused on sodium ion capacitors (SICs). SICs feature the similar mechanism and kinetics to LICs, except that the transport ions (Na^+ or Li^+) and anions in the electrolytes are different. The ionic radius of Na^+ is larger than Li^+, which may result in sluggish ion diffusion dynamics and large volume expansion of electrode materials. Electrode modification including structural optimization and carbon modification have been proposed to address the above disadvantages. Stettner et al. investigated the possibility of using IL-based electrolytes for SICs (Stettner et al., 2018). Mixtures of 1-butyl-1-methylpyrrolidinium bis(trifluoromethanesulfonyl)imide ($Pyr_{14}TFSI$), 1-butylpyrrolidinium bis(trifluoromethanesulfonyl)imide ($PyrH_4TFSI$), and bis(2-methoxyethyl)ether diglyme solvent were fabricated and applied to sodium-based devices, showing attractive prospects for future sodium-based systems. In addition, NaTFSI has been used as conducting salt to ensure that the electrolyte is suitable for sodium-based systems. Presser's group conducted proof-of-concept study of hybrid supercapacitors lithium titanate (LTO)/AC with ILs/LiTFSI or NaTFSI electrolytes (Fleischmann et al., 2019).

IL-BASED LIQUID ELECTROLYTES IN SUPERCAPACITORS

The properties of electrolytes play a vital role in determining the overall performance of supercapacitors. Room-temperature ILs (RTILs), as liquid electrolytes for energy storage devices, have attracted tremendous efforts due to their advantageous ionic conductivity, electrochemical stability, and non-flammability. ILs based on imidazolium, pyrrolidinium, as well as aliphatic quaternary ammonium salts were the extensively used in supercapacitors, which will be discussed in detail below. Recently, eutectic IL mixtures are considered as the most promising electrolytes for supercapacitors at extreme temperatures compared to imidazolium, pyrrolidinium, and quaternary ammonium-based ILs (Lin et al., 2011). The molecular structure of common IL electrolytes are shown in **Figure 6**. The following section will focus on these four kinds of ILs and their applications in supercapacitors, as well as some effective strategies of improving the performance of IL electrolytes.

Categorization and Comparison of Various Liquid IL Electrolytes

Imidazolium-Based Electrolytes

Immense research efforts have been aimed at imidazolium-based ILs owing to their low viscosity, high conductivity, and other special physicochemical properties, showing potential applications in supercapacitors. Most of the imidazolium-based ILs investigated previously are non-amphiphilic, while recently surface-active IL electrolytes have been applied to supercapacitors, which exhibits broad implications for supercapacitors.

Non-amphiphilic IL Electrolytes

Among various imidazolium-based RTILs, 1-ethyl-3-methylimidazolium ($EMIM^+$)- and 1-butyl-3-methylimidazolium ($BMIM^+$)-based electrolytes have been

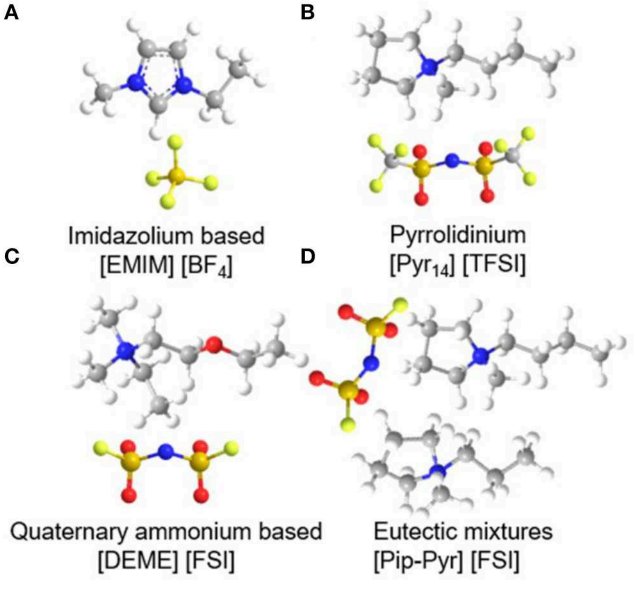

FIGURE 6 | The molecular structure of four kinds of common ionic liquids (ILs): **(A)** imidazolium-, **(B)** pyrrolidinium-, **(C)** quaternary ammonium-based, and **(D)** eutectic mixtures IL electrolytes.

extensively investigated. Lei et al. used KOH, $LiPF_6$, and 1-butyl-3-butyl imidazole tetrafluoroborat ($BMIMBF_4$) as electrolytes for the reduced graphene oxide and CMK-5 composites electrode (RGO-CMK-5) based supercapacitors (Lei et al., 2013). Based on CV tests (**Figure 7A**), $EMIMBF_4$ featured the widest electrochemical window, followed by $LiPF_6$, and KOH electrolytes possessed the narrowest. As a consequence, the supercapacitor with $EMIMBF_4$ electrolytes exhibited higher specific energy density than the supercapacitors using $LiPF_6$ and KOH electrolytes (**Figure 7B**). However, the high viscosity of ILs especially at low temperatures is one of the key obstacles that hamper their industrial applications. 1-Ethyl-3-methylimidazole fluoride (EMIF·2.3HF) electrolyte with relatively low viscosity and superior low-temperature properties for supercapacitors was reported by Ue et al. (2003) In this work, the double-layer capacitor employing EMIF·2.3HF manifested higher capacitance than $EMIMBF_4$ and the others even at low temperatures but showed lower energy density due to its lower decomposition voltage (**Figure 7C**). At 70 °C, the cycle performance and thermal stability performance of EMIF·2.3HF electrolytes were not ideal (**Figure 7D**), coupled with HF toxicity. In order to further improve the electrical conductivity of imidazolium-based IL electrolytes and reduce their viscosity, while maintaining a wide electrochemical window, some convenient strategies including mixing imidazolium-based ILs with hydrophobic proton organic solvents have been proposed. Dagousset et al. fabricated three binary mixtures of ILs (EMIMTFSI, $Pyr_{13}FSI$, and $Pyr_{14}TFSI$) and organic solvents γ-butyrolactone (GBL) and investigated their electrochemical characteristics in supercapacitors within a wide temperature range (-50 °C; $+100$ °C) (Dagousset et al., 2017). EMIMTFSI/GBL electrolytes presented the most excellent cycling performance (only 6.6 % loss of capacitance after 500 h) at -50 °C, which may be attributed to the remarkably low temperature stability of these mixtures. On the contrary, different results were obtained at high temperature of 100 °C. $Pyr_{14}TFSI$ electrolytes showed better stability at higher temperature. Although the mixtures of ILs/organic solvents could reduce the viscosity and enhance durability in severe environments, this is not a universal strategy, and the wide electrochemical windows of ILs would be sacrificed. More recently, Zhang et al. developed the porous carbons with high specific surface area and suitable micropore diameter to match IL ions (Zhang L. et al., 2019). They emphasized the importance of ion matching porous carbons in providing an ion highway for rapid ion transport to form more effective electric double layers, which resulted in superior performance (**Figures 7E–G**).

Surface-Active IL Electrolytes

Surface-active ILs (SAILs) are an emerging IL class with surface active cations or anions, which can form self-assembled nanostructures at ILs/electrodes interfaces. More recently, Mao et al. first investigated the electrocapacitive characteristics and novel EDL structures of SAIL electrolytes (Mao et al., 2019). This work revealed that the self-assembly of SAILs could facilitate the energy storage of supercapacitors. The comparison of electrochemical properties and interfacial nanostructures between non-amphiphilic ILs (NAILs) ($C_4C_1IMBF_4$) and SAILs (C_4C_1IMAOT) was performed by simulations and experiments (**Figure 8**). C_4C_1IMAOT exhibited larger capacitance than $C_4C_1IMBF_4$ at higher temperatures, which may be due to their

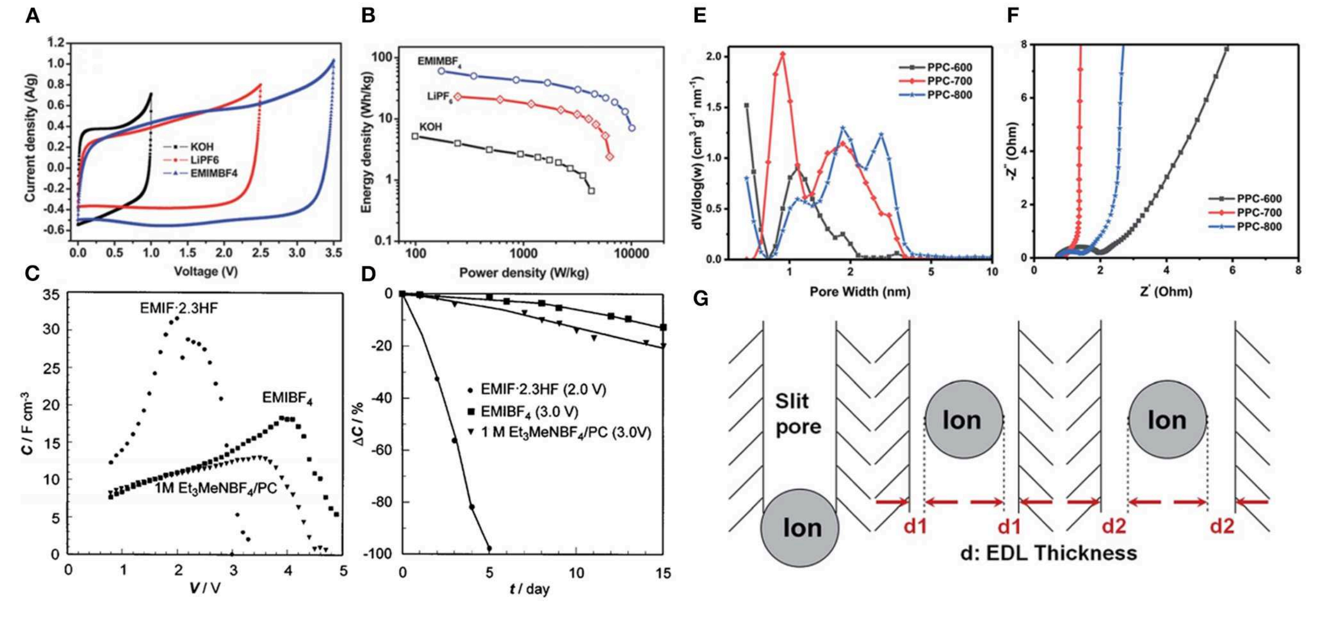

FIGURE 7 | (A) Cyclic voltammetry (CV) profiles and **(B)** Ragone plots of the prepared electrode in different electrolytes; **(C)** voltage dependence of capacitances and **(D)** cycle test of electric double-layer capacitors (EDLCs) with various electrolytes at 70 °C; **(E)** pore size distribution and **(F)** Nyquist plots of carbon samples carbonized at different temperatures; **(G)** schematic diagrams of ion matching pores with different diameters. Reproduced from: **(A,B)** Lei et al. (2013), Royal Society of Chemistry; **(C,D)** Ue et al. (2003), Electrochemical Society; **(E–G)** Zhang L. et al. (2019), Royal Society of Cemistry.

different EDL structures. NAILs at interface showed a typical layered structure of alternating charges, while SAILs exhibited an unusual structure with charged polar domains and non-polar domains of bilayer ions due to the self-assembly of the non-polar groups. For C_4C_1IMAOT, the polar head of $[AOT]^-$ was attracted to the interface and the non-polar tails outwards, close to non-polar of the next $[AOT]^-$ layer, preventing overscreening effects. Therefore, the presence of an $[AOT]^-$ bilayer squeezed excess cations into the first ion layer near the interface to generate abundant free counterions concentration and form thinner EDLs and thus enhancing the capacitive performance. Furthermore, the group also investigated other SAILs with $[DDS]^-$ and $[TC]^-$, exhibiting similar EDL structures to that of C_4C_1IMAOT and thereby indicated that these phenomena are universal features of SAILs. Notably, SAILs showed larger capacitance under higher temperatures and wider voltage windows.

Pyrrolidinum-Based Electrolytes

In addition to imidazolium-based RTILs, pyrrolidinum-based RTILs belonging to cyclic quaternary ammonium salts were also widely applied to the electrolytes of supercapacitors. The asymmetry of substituting pyrrolidine cation resulted in low melting point and high conductivity. *N*-Butyl-*N*-methylpyrrolidine (trifluoromethyl sulfonyl) imide salt (Pyr_{14}TFSI) has attracted a lot of attention for its excellent electrochemical and thermal stability at high temperature. An AC/Pyr_{14}TFSI/pMeT hybrid supercapacitor with long cycle life and high voltage was constructed by A. Balducci et al. (2006). This supercapacitor delivered energy density of 24 W h kg^{-1} and power density of 14 kW kg^{-1} as maximum values at 10 mA cm^{-2} and 60 °C. M. Lazzari et al. studied the interfacial behaviors of Pyr_{14} TFSI and EMIMTFSI electrolytes on the surface of AC electrode, indicating that the capacitance of AC electrode was largely determined by the polarization of the cations of ILs when cathode was charged (Lazzari et al., 2007). The porosity and chemical properties of carbon materials play crucial roles in influencing the conductivity and polarization of ILs. Recently, Xu et al. synthesized novel anionic surfactant ILs Pyr_{14}AOT, which was mixed with Pyr_{13}TFSI to form electrolytes for supercapacitors (Xu et al., 2019). The highest specific capacitance was achieved for 10 wt% Pyr_{14}AOT in Pyr_{13}TFSI at 150 °C, which was attributed to the improved wettability by surfactant ILs. However, the larger non-polar of surfactant ILs resulted in reduced conductivity and poor performance at low temperatures.

Quaternary Ammonium-Based Electrolytes

In comparison with imidazolium-based ILs, the primary competitive advantage of quaternary ammonium-based ILs with short chain is their outstanding stability to large specific surface area of AC electrode. The electrochemical and physicochemical properties of *N*, *N*-diethyl-*N*-methyl-*N*-(2-methoxyethyl) ammonium tetrafluoroborate (DEME-BF_4) electrolytes for EDLCs were investigated by T. Sato et al. (2004). DEME-BF_4 electrolytes could facilitate the performance of electrochemical capacitors owing to their extremely widened potential window (6.0 V) and high ionic conductivity (4.8 mS cm^{-1} at 25 °C) in practice compared to EMIMBF_4 electrolytes.

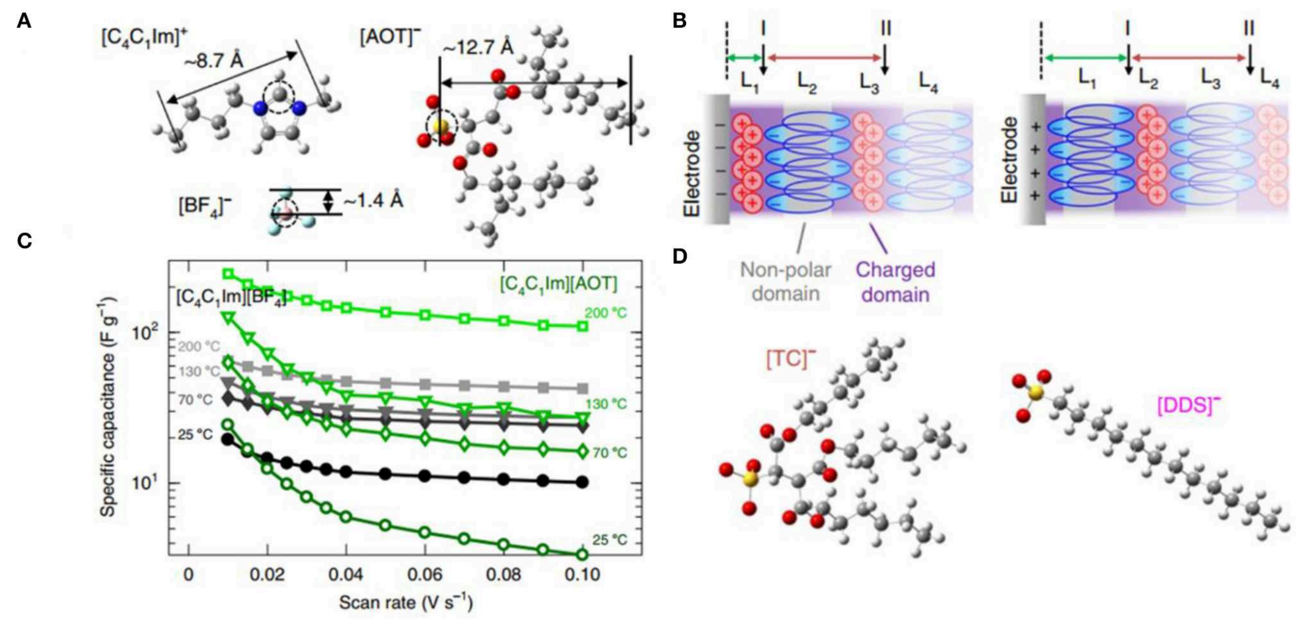

FIGURE 8 | (A) Molecular structures of $[C_4C_1Im]^+$, $[BF_4]^-$, and $[AOT]^-$; **(B)** the specific capacitance vs. the scan rate for $[C_4C1Im][BF_4]$ and $[C_4C_1Im][AOT]$ at 25, 70, 130, and 200 °C; **(C)** schematics of hypothesized electric double-layer (EDL) structures of $[C_4C_1Im][AOT]$ at negatively and positively charged interfaces with $U = \pm 2$ V; **(D)** molecular structures of $[DDS]^-$ and $[TC]^-$. Reproduced from: **(A–D)** Mao et al. (2019), Nature Publishing Group.

Eutectic IL Mixtures Electrolytes

Eutectic IL mixtures are also promising candidate electrolytes for supercapacitors due to their lower viscosity and good stability. More importantly, eutectic ILs can broaden the range of temperatures for supercapacitors (**Figure 9A**). Recently, a novel eutectic IL mixture of EMIMTFSI and 1-propyl-3-methylpyrrolidinium bis(trifluoromethylsulfonyl)imide was fabricated by Rodrigo Newell et al. (2018). From **Figure 9B**, the conducted electrochemical measurements revealed that the eutectic IL mixtures electrolytes were suitable for supercapacitors with a cell voltage of 3.5 V at a wide temperature range from −70 to 80 °C. The Ni-foam supercapacitor assembled with such electrolytes exhibited superior cycling stability at a current density of 0.6 mA cm^{-2} and room temperature, as shown in **Figure 9C**. Mahanta et al. studied the eutectic electrolytes of 1-butyl-3-methyl imidazolium methanesulfonate ([BMIM][$MeSO_3$])/N-methylacetamide (NMAc) (Mahanta et al., 2020). The results indicated that [BMIM][$MeSO_3$]/NMAc showed higher thermal stability and lower viscosity compared to pure ILs but higher internal resistance.

Improvements of IL Electrolytes

Although ILs have many advantages compared with conventional liquid electrolytes, their low degree of dissociation, high viscosity, as well as poor power performance need to be improved. Various ways such as adding organic solvents or carbon materials and introducing redox-active species to ILs have been proposed to optimize IL electrolytes. Wong et al. studied IL electrolytes with different amounts of acetonitrile (AN) in order to obtain optimum electrolytes (Wong et al., 2020). They concluded that 4 M $EMIMBF_4$/AN achieved the highest capacitance, and pure ILs achieved the highest energy density. Nagao et al. proposed $BaTiO_3$ additive, which could boost the capacitance of electrodes and enhanced the rate capability of EDLCs with $EMIMBF_4$ electrolytes (Nagao et al., 2007). Compared with EDLCs without $BaTiO_3$, EDLCs employing $BaTiO_3$ powder/activated carbon composite as electrodes and the $EMIMBF_4$ as electrolytes delivered larger capacitance and better rate performance. The positive effect of $BaTiO_3$ was attributed to the fact that it could increase the dissociation degree of $EMIMBF_4$. Then, the carrier concentration to form electric double layer would be increased, and the performance of EDLCs would be enhanced.

IL-BASED SOLID ELECTROLYTES IN SUPERCAPACITORS

Solid supercapacitors show broad applications prospect in many fields such as safe energy storage devices and flexible electronics (Deng et al., 2019) because there are no issues of leakages and explosions. Obviously, the demand of non-liquid electrolytes for solid supercapacitors is growing. Gel electrolytes, consisting of a polymer skeleton as a host, an organic/aqueous solvent as a plasticizer, and a supporting electrolyte salt (Sekhon, 2003), are most widely used as non-liquid electrolytes that function both as separators and ion carriers in supercapacitors. Since Fuller et al. began to explore gel electrolytes based on ILs, much efforts have been devoted to the applications of IL gel electrolytes for various electrochemical systems, especially for quasi-solid lithium ion batteries and supercapacitors (Fuller et al., 1997). In the past years, polymer matrix doping ILs have been demonstrated to improve the thermal stability of gel electrolytes and expand the electrochemical window of the devices to 3.5–4.0 V (Fuller et al., 1998; Lyu et al., 2016).

Ionogel electrolytes are fabricated by trapping ILs into the polymer matrix. Supercapacitors utilizing ionogel electrolytes are regarded as quasi-solid supercapacitors due to the presence of ILs with some degree of fluidity into the polymer matrix. Generally, conventional neutral polymers and poly(IL)s (PILs) are widely used as the solid polymer matrix. Various methods including solution casting, electrostatic spinning, and *in situ* polymerization of various monomer in ILs medium have been used to obtain ionogel electrolytes.

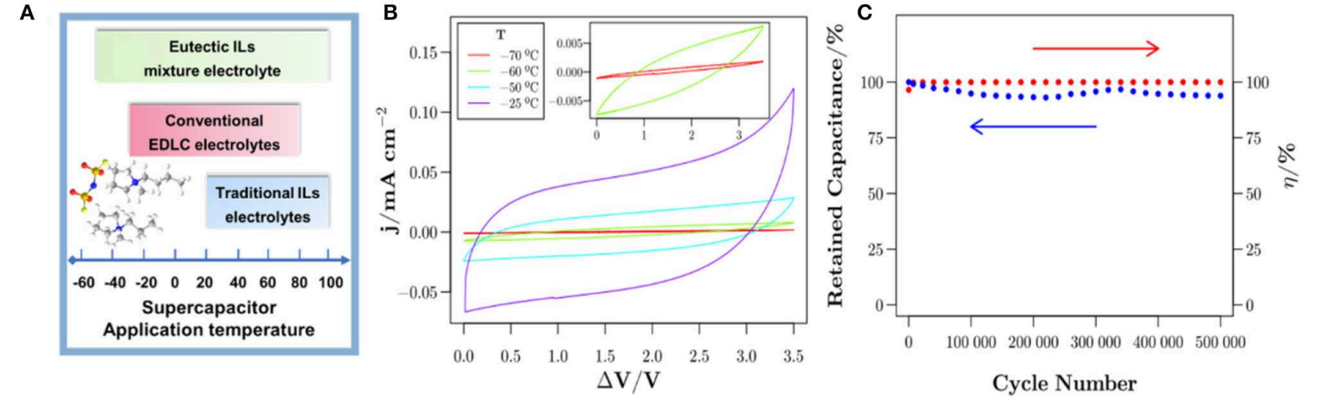

FIGURE 9 | (A) Operating temperature of supercapacitors with different electrolytes system. **(B)** Cyclic voltammetry (CV) curves at low temperatures at a scan rate of 1 V s^{-1} and **(C)** cycling stability at a current density of 0.6 mA cm^{-2} of Ni-foam supercapacitor at room temperature. Reproduced from: **(A)** Lin et al. (2011), American Chemical Society; **(B,C)** Newell et al. (2018), Elsevier.

Conventional Polymer-Based Ionogel Electrolytes

The properties of ILs and polymer matrixes and the interaction between them play an important role in determining the ionic conductivity and electrochemical stable windows of ionogel electrolytes. Till now, various conventional polymers including poly(ethyl oxide) (PEO), poly(vinylidene fluoride) (PVDF), and poly(vinylidene fluoride-co-hexafluoropropylene) [P(VDF-HFP)] have been extensively investigated as polymeric host materials of ionogel electrolytes for energy storage devices. Most of the efforts were devoted to the ionogel electrolyte-based EDLCs and pseudocapacitors. There was also more and more attention paid to the investigation of emerging LICs employing ionogel electrolytes. Furthermore, based on ionogel electrolytes, flexible supercapacitors were developed.

Among various polymers that can be used as the skeleton of ionogel electrolytes for supercapacitors, P(VDF-HFP) is the most popular polymer due to its low glass conversion temperature and strong mechanical strength (Ramesh and Ling, 2010). The chemical structures of P(VDF-HFP) and ionogel electrolytes based on P(VDF-HFP) are illustrated in **Figure 10A**. [EMIM][FAP]/P(VDF-HFP) ionogel electrolytes containing $LiPF_6$ were reported by Pandey and Hashmi (2013). They found that the specific capacitance of EDLCs with carbon nanotube (CNT) electrodes could be enhanced evidently by adding Li-salt into ionogel electrolytes. Using P(VDF-HFP) as a polymer skeleton, Shen et al. prepared [EMIM][NTF_2]/P(VDF-HFP)/SiO_2 ionogel electrolytes with high ion conductivity (Shen et al., 2015). The assembled [EMIM][NTF_2]/P(VDF-HFP)/SiO_2-based asymmetric microsupercapacitors with graphene quantum dots and MnO_2 electrodes exhibited superior rate capability at 2,000 V s^{-1} and ultrafast frequency response ($\tau_0 = 206.9$ μs) owing to the enhanced ion conductivity of the fabricated ionogel electrolytes and fast ion diffusion. Moreover, some other polymers were also studied. For example, Kadokowa et al. synthesized a gel complexed with an IL (1-allyl-3-methyl-3-methylimidazole amide) and chitin/cellulose (Takegawa et al., 2010). Recently, an ionogel electrolyte based on graft copolymer (PEGBEM-g-PAEMA) was reported by Kang et al. Up to 200% [EMIM][BF_4] content could be achieved in the fabricated electrolyte, and the assembled flexible supercapacitors showed better performance than other polymer/[EMIM][BF_4]-based capacitors (Kang et al., 2020).

In addition, P(VDF-HFP)-based ionogel electrolytes also show a wide range of applications in quasi-solid LICs. Jiao et al. fabricated P(VDF-HFP) (Kang et al., 2020)/LiTFSI/$EMIMBF_4$ ionogel electrolytes with a thickness of ~50 µm via a solution-casting method, which could widen the working potential of the assembled T-Nb_2O_5/rGO//AC LICs to 4 V, and thus, the energy density of 70 W h kg^{-1} at 1 kW kg^{-1} could be achieved at 60 °C (Jiao et al., 2018). The similar ionogel electrolytes but with different amounts of Li-salt and ILs were reported by Zhang J. H. et al. (2019). A quasi-solid LIC was obtained using P(VDF-HFP)/LiTFSI/$EMIMBF_4$ as electrolytes and (Nb_2O_5@C)/rGO and AC as electrodes, showing a specific capacitance of 46.8 F g^{-1} at 1 A g^{-1} and a maximum energy

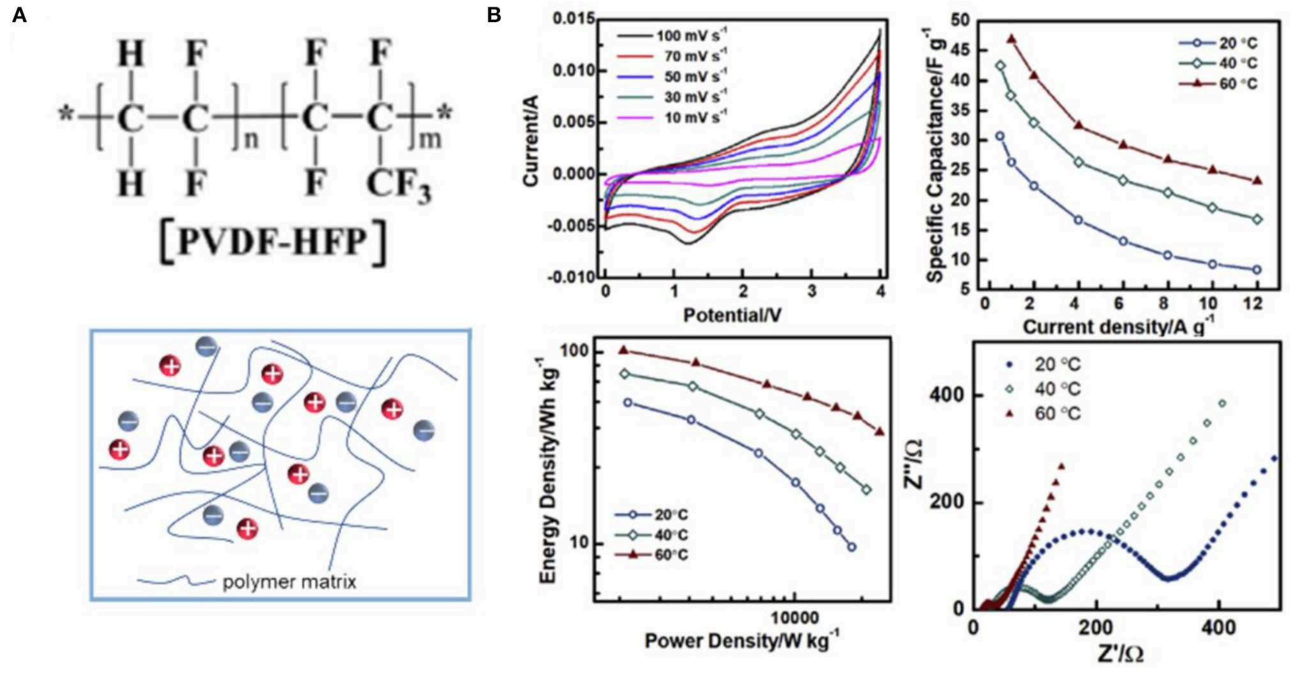

FIGURE 10 | (A) Structural representation of poly(vinylidene fluoride-co-hexafluoropropylene) [P(VDF-HFP)] and P(VDF-HFP)-based ionogel electrolytes; **(B)** electrochemical performance of solid lithium ion capacitors (LICs) with P(VDF-HFP)–$EMIMBF_4$-LiTFSI ionogel electrolytes. Reproduced from Zhang J. H. et al. (2019), Elsevier.

density of 101 W h kg^{-1} at 60 °C (**Figure 10B**). From the shape of CV curves, a combination mechanism of fast adsorption on cathode and the sluggish Faradaic reaction in anode could be concluded. In addition, the effect of temperature on the charge transfer resistance (R_{ct}) of the obtained device was also investigated, which showed a significant decrease in R_{ct} as the temperature rose.

Ionogel electrolytes could be used as flexible electrolytes and they determined the performance of quasi-solid flexible supercapacitors such as operating voltage window, stability, and rate capability. Sanjeev Kumar et al. designed flexible EDLCs with graphene electrodes using P(VDF-HFP)/EMIMBF$_4$ ionogel electrolytes, delivering high capacitance of 242 F g^{-1} at 5 mV s^{-1} and long cycle life (Ujjain et al., 2015). In addition, a flexible sandwich EDLCs based on PS–PEO–PS/[EMIM][NTf$_2$]/PTFE ionogel electrolytes and carbon nanotube electrodes was constructed by Kang et al. (2016). Such ionogel electrolytes with PS–PEO–PS host could self-assemble to form a nanostructure due to the hydrophobicity of PS segments and hydrophily of PEO segments, which would enhance the ionic conductivity. More recently, Pan et al. represented a fiber supercapacitor utilizing P(VDF-HFP)/EMIMTFSI ionogel electrolytes (Pan et al., 2019). The as-assembled solid fiber supercapacitor could be operated at 3.5 V, and thus, an ultrahigh energy density of 61.2 mW h cm^{-3} could be achieved.

Although the safety issues are suppressed using gel electrolytes instead of liquid electrolytes, the thermodynamic properties and mechanical stability are far from ideal. One promising approach is to construct hybrid IL gel electrolytes with inorganic substances. Moreover, the performance of hybrid IL gel electrolytes can still be further enhanced by selecting modified ceramics and oxide-based materials as a support. For instance, hybrid IL gel electrolytes composed of cage-structured polyhedral oligomeric silsesquioxanes (POSS), amine-terminated polypropylene glycol, ILs, and LiTFSI were reported, indicating that POSS could enhance the mechanical stability while the polyetheramine offers epoxy network structures linked through Li$^+$ dissociative polyether linkages (Na et al., 2017).

Poly(Ionic Liquid)-Based Ionogel Electrolytes

The history of PILs can be traced back to 1970s when the corresponding ionic organic salts undergone free radical polymerization. PILs are composed of a polymer backbone and anionic and cationic groups in monomer repeating units, which combine the properties of polymers and ILs, as shown in **Figure 11A**. In common synthesis processes, PILs are embodied in backbone PILs or pendant PILs depending on where the ionic species bind to the polymer chain, as illustrated in the following **Figure 11A** (Kuray et al., 2019). No matter what type of PILs, the transport of ions is achieved by the migration of the ionic species that can move freely. PILs can be utilized as the polymer hosts of ionogel electrolytes for supercapacitors. Compared to conventional polymers, PIL-based ionogel electrolytes can be regarded as superior solid electrolytes for solid supercapacitors,

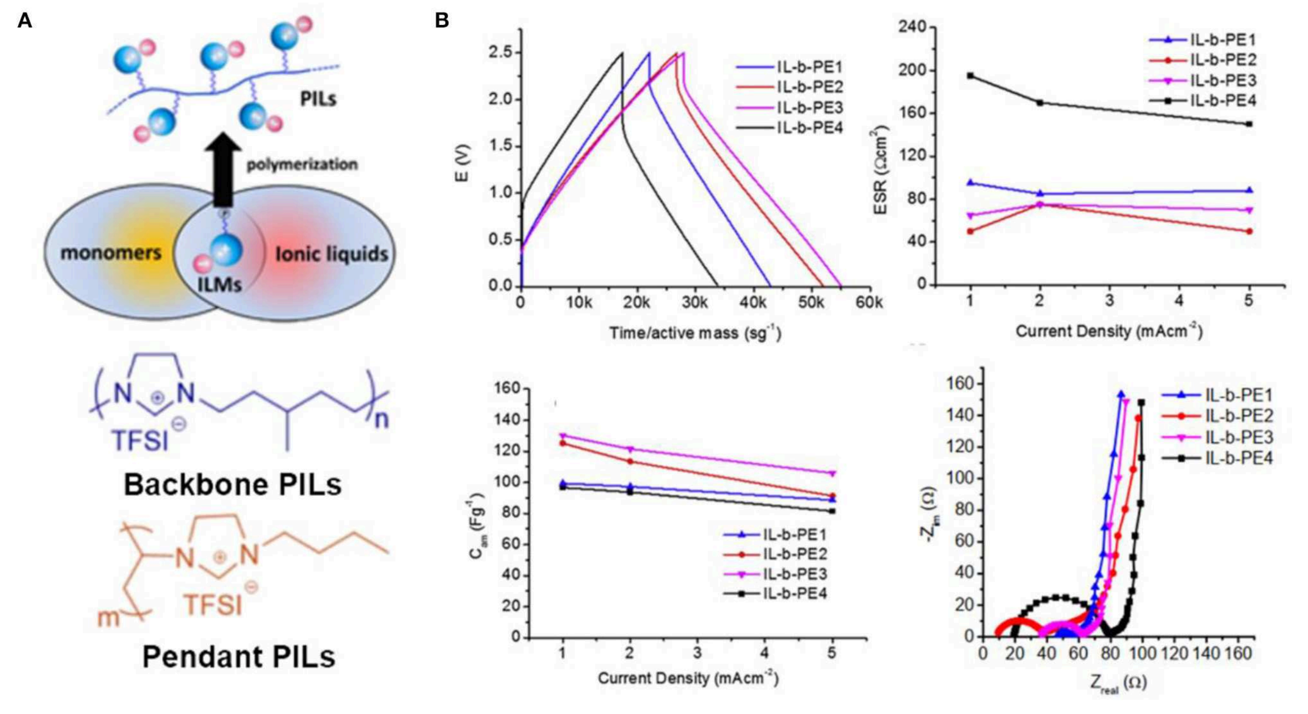

FIGURE 11 | (A) Illustration of the structure of poly(ionic liquid)s (PILs) and molecular structures of backbone PIL and pendant PIL. **(B)** The electrochemical performance of solid-state supercapacitors assembled with the four electrolytes containing poly(diallyldimethylammonium) bis(trifluoromethanesulfonyl)imide (PILTFSI) and different ILs (Pyr$_{14}$TFSI, Pyr$_{14}$FSI, Pyr$_{14}$DCA, and HEMimTFSI). Reproduced from Tiruye et al. (2016), Elsevier.

which possess advantages of high miscibility between PILs and ILs and high interactions of ions and PILs.

In the past years, the reviews on PILs in terms of their synthesis, chemical structure, physical properties, and applications were available (Lu et al., 2009; Mecerreyes, 2011; Yuan et al., 2013). Nevertheless, there are only limited reports related on PIL/IL electrolytes for supercapacitors. For instance, PIL/IL ionogel electrolytes containing poly(diallyldimethylammonium) bis(trifluoromethanesulfonyl)imide (pDADMATFSI) and their corresponding ILs were synthesized and applied to solid-state supercapacitors (Tiruye et al., 2015). The experimental results indicated that the voltage potential could achieve 3.5 V due to the high electrochemical stability of this PIL electrolyte. Further work fabricated four IL-based polymer electrolytes blending a PIL, poly(diallyldimethylammonium) bis(trifluoromethanesulfonyl)imide (PILTFSI), with four different ILs (Tiruye et al., 2016). The results of this work revealed that ionic conductivity was significantly aggrandized when the ILs contain small size anions (FSI^- and DCA^-) than bigger anions ($TFSI^-$), as shown in **Figure 11B**. In this way, the specific capacitance of assembled supercapacitors could be improved by increasing the ionic conductivity. In addition, recent works about [PIL-M-(Br)] and [PIL-M-(TFSI)] solid electrolytes composed of PIL and ILs were reported by Wang et al. (2018). Two solid electrolytes exhibited maximum energy density of 107 and 59.9 W h kg^{-1} when they were used for symmetric supercapacitors, respectively.

Previous studies have shown that the addition of ILs during the preparation of PIL electrolytes could increase the ionic conductivity of electrolytes. However, Yanga et al. prepared an anion-conducting poly(VAC-co-EVImBr) thin-film electrolyte without additional ILs, and a 4.2 V flexible all-solid-state C/C supercapacitor was assembled (Yang et al., 2017). The aim of this work was to demonstrate the feasibility of using inorganic anion-dominated conducting polymers as solid polymer electrolytes. More importantly, by comparing two types of solid polymer electrolytes, the cationic and non-ionic copolymer poly(VAC-co-EVImBr) is more rational than the cationic polymer PEVImBr. Furthermore, ILs cannot only be used as electrolytes directly but also can modify electrode materials. Ponkratov et al. proposed two families of PILs via different methods: one synthesized by free radical copolymerization was applied as electrolyte due to its high ionic conductivity; the other obtained by polymer modification and ion exchange was used as the components of the thin electrode films owing to their good ability to form coatings (Ponkratov et al., 2018). Based on this, all-polymer solid-state flexible supercapacitors with thickness of 480–500 μm were assembled using PILs as electrolytes. Although the performances of the assembled flexible supercapacitors were unsatisfactory, the proof-of-concept demonstration of novel flexible configuration was confirmed by this work for the first time.

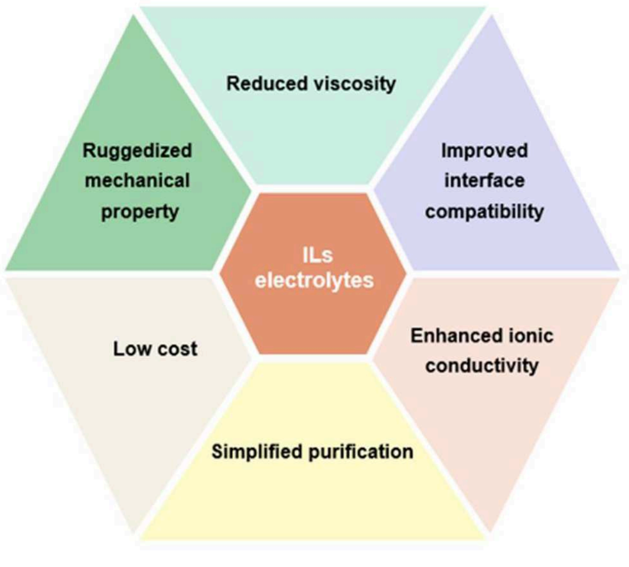

FIGURE 12 | Challenges and future perspectives of ionic liquids (ILs) electrolytes for advanced supercapacitors.

CONCLUSION AND FUTURE PERSPECTIVE

Seeking for or formulating electrolytes with widened electrochemical window is a vital research orientation for constructing high-performance supercapacitors. According to the published research reports, IL electrolytes show enormous potentials in this field. Pure ILs system is significantly different from traditional aqueous and organic electrolytes. The energy storage mechanisms of supercapacitors with ILs need to be reconsidered. Conventional IL electrolytes enable the widened voltage windows of supercapacitors but may not lead to enhanced capacitance due to the difficulty in separating ions. Selecting and manipulating IL electrolytes reasonably according to diverse operating conditions and requirements are necessary on account of different characteristics of various IL electrolytes. Furthermore, the electrode structures affect the arrangement of ILs at the interface. A layered structure is formed at the planar electrodes, while a monolayer structure is formed on porous electrodes with proper pore size and a multilayer structure is formed on porous electrodes with wider pores. Nanoporous electrodes matching well with ion dimension of ILs exhibit the best performance under certain conditions. More recently, the properties and special interfacial nanostructures of self-assembly SAILs were demonstrated, which would be favorable for EDL structures and charge storage of EDLCs. High temperatures and wide voltage windows are advantageous for the application of supercapacitors with SAILs. Unlike conventional ILs, the unusual interfacial structure of SAILs results in enhanced capacitance. Mixing ILs with organic electrolytes can improve conductivity and durability in extreme environments. Obviously, this approach sacrifices the voltage window of IL electrolytes, and thus, the energy density of supercapacitors will be limited. Eutectic IL mixtures electrolytes may be favorable for advanced supercapacitors over a wider temperature range. Although great progress has been made in

ILs/organic solvents and eutectic IL mixtures electrolytes, pure IL electrolytes sometimes exhibit better performance. Therefore, it is highly desirable to exploit universal strategies to tune the properties of the existing IL systems without the sacrifice of the voltage window and explore novel versatility of IL electrolytes for supercapacitors.

Besides liquid-state electrolytes, ionogel electrolytes may be a dominating tendency for future research due to the requirements of safe and high-voltage electrolytes for prosperous solid and flexible supercapacitors. Ionogel electrolytes based on conventional polymers and PILs have been extensively explored. Various strategies including the preparation of PILs/ILs and anion-dominated conducting polymers have been proven to construct advanced solid supercapacitors. More efforts need to be devoted to regulating the nature of IL electrolytes and the interface compatibility between electrolytes and electrodes. Ionogel electrolytes offer better interface compatibility and higher ionic conductivity but poor mechanical stability in comparison with solid polymer electrolytes. Inorganic substances may improve their mechanical stability.

Although previous research has proposed various strategies to settle these shortcomings of IL electrolytes, there still remains some problems needed to be further addressed such as high cost and high viscosity, as shown in **Figure 12**. Additionally, ILs exhibit poorer power performance than that of organic electrolytes. It is controversial whether ILs can replace traditional organic electrolyte of commercial supercapacitors. Despite these disadvantages, ILs as high-voltage electrolytes for supercapacitors promote research surge in constructing high-energy-density supercapacitors. The fundamental investigations of IL electrolytes is still essential to comprehend the basic characteristics of ILs, which is favorable for the development of safe and high-voltage electrolytes, thereby enhancing the performance of supercapacitors. Therefore, devoting more efforts to IL electrolytes is still needed to achieve advanced supercapacitors for energy storage.

AUTHOR CONTRIBUTIONS

All authors drafted the manuscript and approved it for application.

FUNDING

This study was funded by The National Key Research and Development Program of China (No. 2016YFB0100303), the Major Program of National Natural Science Foundation of China (No. 21890762), Beijing–Tianjin–Hebei Cooperative Innovation Community Construction Project (18244409D), and K.C. Wong Education Foundation.

REFERENCES

Armand, M., Endres, F., MacFarlane, D. R., Ohno, H., and Scrosati, B. (2009). Ionic-liquid materialsfor the electrochemical challenges of the future. *Nat. Mater.* 8, 621–629. doi: 10.1038/nmat2448

Atkin, R., Borisenko, N., Druschler, M., El Abedin, S. Z., Endres, F., Hayes, R., et al. (2011). An *in situ* STM/AFM and impedance spectroscopy study of the extremely pure 1-butyl-1-methylpyrrolidinium tris(pentafluoroethyl) trifluorophosphate/Au(111) interface: potential dependent solvation layers and the herringbone reconstruction. *Phys. Chem. Chem. Phys.* 13, 6849–6857. doi: 10.1039/c0cp02846k

Atkin, R., and Warr, G. G. (2007). Structure in confined room-temperature ionic liquids. *J. Phys. Chem. C* 111, 5162–5168. doi: 10.1021/jp067420g

Augustyn, V., Simon, P., and Dunn, B. (2014). Pseudocapacitive oxide materials for high-rate electrochemical energy storage. *Energy Environ. Sci.* 7, 1597–1614. doi: 10.1039/c3ee44164d

Balducci, A., Bardi, U., Caporali, S., Mastragostino, M., and Soavi, F. (2004). Ionic liquids for hybrid supercapacitors. *Electrochem. Commun.* 6, 566–570. doi: 10.1016/j.elecom.2004.04.005

Balducci, A., Henderson, W. A., Mastragostino, M., Passerini, S., Simon, P., and Soavi, F. (2005). Cycling stability of a hybrid activated carbon//poly(3-methylthiophene) supercapacitor with N-butyl-N-methylpyrrolidinium bis(trifluoromethanesulfonyl)imide ionic liquid as electrolyte. *Electrochim. Acta* 50, 2233–2237. doi: 10.1016/j.electacta.2004.10.006

Balducci, A., Soavi, F., and Mastragostino, M. (2006). The use of ionic liquids as solvent-free green electrolytes for hybrid supercapacitors. *Appl. Phys. A* 82, 627–632. doi: 10.1007/s00339-005-3402-2

Bazant, M. Z., Storey, B. D., and Kornyshev, A. A. (2012). Double layer in ionic liquids: overscreening versus crowding. *Phys. Rev. Lett.* 109:2. doi: 10.1103/PhysRevLett.109.149903

Benedetti, T. M., Bazito, F. F. C., Ponzio, E. A., and Torresi, R. M. (2008). Electrostatic layer-by-layer deposition and electrochemical characterization of thin films composed of MnO_2 nanoparticles in a room-temperature ionic liquid. *Langmuir* 24, 3602–3610. doi: 10.1021/la702347x

Brandt, A., and Balducci, A. (2014). Theoretical and practical energy limitations of organic and ionic liquid-based electrolytes for high voltage electrochemical double layer capacitors. *J. Power Sources* 250, 343–351. doi: 10.1016/j.jpowsour.2013.10.147

Burt, R., Birkett, G., Salanne, M., and Zhao, X. S. (2016). Molecular dynamics simulations of the influence of drop size and surface potential on the contact angle of ionic-liquid droplets. *J. Phys. Chem. C* 120, 15244–15250. doi: 10.1021/acs.jpcc.6b04696

Chang, J. K., Lee, M. T., Tsai, W. T., Deng, M. J., and Sun, I. W. (2009). X-ray photoelectron spectroscopy and in situ x-ray absorption spectroscopy studies on reversible insertion/desertion of dicyanamide anions into/from manganese oxide in ionic liquid. *Chem. Mater.* 21, 2688–2695. doi: 10.1021/cm9000569

Chmiola, J., Yushin, G., Gogotsi, Y., Portet, C., Simon, P., and Taberna, P. L. (2006). Anomalous increase in carbon capacitance at pore sizes less than 1 nanometer. *Science* 313, 1760–1763. doi: 10.1126/science.1132195

Conway, B. E. (1991). Transition from supercapacitor to battery behavior in electrochemical energy-storage. *J. Electrochem. Soc.* 138, 1539–1548. doi: 10.1149/1.2085829

Conway, B. E. (1995). Electrochemical oxide film formation at noble-metals as a surface-chemical process. *Prog. Surf. Sci.* 49, 331–452. doi: 10.1016/0079-6816(95)00040-6

Conway, B. E., and Pell, W. G. (2003). Double-layer and pseudocapacitance types of electrochemical capacitors and their applications to the development of hybrid devices. *J. Solid State Electrochem.* 7, 637–644. doi: 10.1007/s10008-003-0395-7

Dagousset, L., Pognon, G., Nguyen, G. T. M., Vidal, F., Jus, S., and Aubert, P. H. (2017). Electrochemical characterisations and ageing of ionic liquid/gamma-butyrolactone mixtures as electrolytes for supercapacitor applications over a wide temperature range. *J. Power Sources* 359, 242–249. doi: 10.1016/j.jpowsour.2017.05.068

Deng, X. L., Jiang, Y. Q., Wei, Z. X., Mao, M. L., Pothu, R., Wang, H. X., et al. (2019). Flexible quasi-solid-state dual-ion asymmetric supercapacitor based on

$Ni(OH)_2$ and Nb_2O_5 nanosheet arrays. *Green Energy Environ.* 4, 382–390. doi: 10.1016/j.gee.2019.02.001

Ding, J., Hu, W. B., Paek, E., and Mitlin, D. (2018). Review of hybrid ion capacitors: from aqueous to lithium to sodium. *Chem. Rev.* 118, 6457–6498. doi: 10.1021/acs.chemrev.8b00116

dos Santos, G. A., Fortunato, V. D. S., Silva, G. G., Ortega, P. F. R., and Lavall, R. L. (2019). High-performance Li-Ion hybrid supercapacitor based on $LiMn_2O_4$ in ionic liquid electrolyte. *Electrochim. Acta* 325:9. doi: 10.1016/j.electacta.2019.134900

Dou, Q., Liu, L., Yang, B., Lang, J., and Yan, X. (2017). Silica-grafted ionic liquids for revealing the respective charging behaviors of cations and anions in supercapacitors. *Nat. Commun.*8:2188. doi: 10.1038/s41467-017-02152-5

Fleischmann, S., Widmaier, M., Schreiber, A., Shim, H., Stiemke, F. M., Schubert, T. J. S., et al. (2019). High voltage asymmetric hybrid supercapacitors using lithium-and sodium-containing ionic liquids. *Energy Stor. Mater.* 16, 391–399. doi: 10.1016/j.ensm.2018.06.011

Forse, A. C., Griffin, J. M., Merlet, C., Bayley, P. M., Wang, H., Simon, P., et al. (2015). NMR study of ion dynamics and charge storage in ionic liquid supercapacitors. *J. Am. Chem. Soc.* 137, 7231–7242. doi: 10.1021/jacs.5b03958

Forse, A. C., Griffin, J. M., Merlet, C., Carretero-Gonzalez, J., Raji, A. R. O., Trease, N. M., et al. (2017). Direct observation of ion dynamics in supercapacitor electrodes using *in situ* diffusion NMR spectroscopy. *Nat. Energy* 2:16216. doi: 10.1038/nenergy.2016.216

Fuller, J., Breda, A. C., and Carlin, R. T. (1997). Ionic liquid-polymer gel electrolytes. *J. Electrochem. Soc.* 144, L67–L70. doi: 10.1149/1.1837555

Fuller, J., Breda, A. C., and Carlin, R. T. (1998). Ionic liquid-polymer gel electrolytes from hydrophilic and hydrophobic ionic liquids. *J. Electroanal. Chem.* 459, 29–34. doi: 10.1016/S0022-0728(98)00285-X

Galinski, M., Lewandowski, A., and Stepniak, I. (2006). Ionic liquids as electrolytes. *Electrochim. Acta* 51, 5567–5580. doi: 10.1016/j.electacta.2006.03.016

Hayes, R., Warr, G. G., and Atkin, R. (2010). At the interface: solvation and designing ionic liquids. *Phys. Chem. Chem. Phys.* 12, 1709–1723. doi: 10.1039/b920393a

Hirota, N., Okuno, K., Majima, M., Hosoe, A., Uchida, S., and Ishikawa, M. (2018). High-performance lithiumion capacitor composed of electrodes with porous three-dimensional current collector and bis(fluorosulfonyl) imide-based ionic liquid electrolyte. *Electrochim. Acta* 276, 125–133. doi: 10.1016/j.electacta.2018.04.148

Jiang, H., Li, C. Z., Sun, T., and Ma, J. (2012a). A green and high energy density asymmetric supercapacitor based on ultrathin MnO_2 nanostructures and functional mesoporous carbon nanotube electrodes. *Nanoscale* 4, 807–812. doi: 10.1039/C1NR11542A

Jiang, H., Sun, T., Li, C. Z., and Ma, J. (2012b). Hierarchical porous nanostructures assembled from ultrathin MnO_2 nanoflakes with enhanced supercapacitive performances. *J. Mater. Chem.* 22, 2751–2756. doi: 10.1039/C1JM14732C

Jiao, Y. Z., Zhang, H. T., Zhang, H. L., Liu, A., Liu, Y. X., and Zhang, S. J. (2018). Highly bonded T-Nb_2O_5/rGO nanohybrids for 4 V quasi-solid state asymmetric supercapacitors with improved electrochemical performance. *Nano Res.* 11, 4673–4685. doi: 10.1007/s12274-018-2049-1

Kang, D. A., Kim, K., Karade, S. S., Kim, H., and Kim, J. H. (2020). High-performance solid-state bendable supercapacitors based on PEGBEM-g-PAEMA graft copolymer *electrolyte*. *Chem. Eng. J.* 384:123308. doi: 10.1016/j.cej.2019.123308

Kang, Y. J., Yoo, Y., and Kim, W. (2016). 3-V Solid-State flexible supercapacitors with ionic-liquid-based polymer gel electrolyte for AC line filtering. *Acs Appl. Mater. Interfaces* 8, 13909–13917. doi: 10.1021/acsami.6b02690

Kornyshev, A. A. (2007). Double-layer in ionic liquids: Paradigm change? *J. Phys. Chem. B* 111, 5545–5557. doi: 10.1021/jp067857o

Kuray, P., Noda, T., Matsumoto, A., Iacob, C., Inoue, T., Hickner, M. A., et al. (2019). Ion transport in pendant and backbone polymerized ionic liquids. *Macromolecules* 52, 6438–6448. doi: 10.1021/acs.macromol.8b02682

Largeot, C., Taberna, P. L., Gogotsi, Y., and Simon, P. (2011). Microporous carbon-based electrical double layer capacitor operating at high temperature in ionic liquid electrolyte. *Electrochem. Solid State Lett.* 14, A174–A176. doi: 10.1149/2.013112esl

Lazzari, M., Mastragostino, M., and Soavi, F. (2007). Capacitance response of carbons in solvent-free ionic liquid electrolytes. *Electrochem. Commun.* 9, 1567–1572. doi: 10.1016/j.elecom.2007.02.021

Lee, M. T., Tsai, W. T., Deng, M. J., Cheng, H. F., Sun, I. W., and Chang, J. K. (2010). Pseudocapacitance of MnO_2 originates from reversible insertion/desertion of thiocyanate anions studied using *in situ* X-ray absorption spectroscopy in ionic liquid electrolyte. *J. Power Sources* 195, 919–922. doi: 10.1016/j.jpowsour.2009.08.047

Lei, Z. B., Liu, Z. H., Wang, H. J., Sun, X. X., Lu, L., and Zhao, X. S. (2013). A high-energy-density supercapacitor with graphene-CMK-5 as the electrode and ionic liquid as the electrolyte. *J. Mater. Chem. A* 1, 2313–2321. doi: 10.1039/c2ta01040b

Li, B., Zheng, J. S., Zhang, H. Y., Jin, L. M., Yang, D. J., Lv, H., et al. (2018). Electrode materials, electrolytes, and challenges in nonaqueous lithium-ion capacitors. *Adv. Mater.* 30:1705670. doi: 10.1002/adma.201705670

Li, M., Lu, J., Chen, Z., and Amine, K. (2018). 30 Years of lithium-ion batteries. *Adv. Mater*. 30:e1800561. doi: 10.1002/adma.201800561

Li, X., and Wei, B. Q. (2012). Facile synthesis and super capacitive behavior of SWNT/MnO_2 hybrid films. *Nano Energy* 1, 479–487. doi: 10.1016/j.nanoen.2012.02.011

Li, Y. S., Sun, I. W., Chang, J. K., Su, C. J., and Lee, M. T. (2012). Doped butylmethylpyrrolidinium-dicyanamide ionic liquid as an electrolyte for MnO_2 supercapacitors. *J. Mater. Chem.* 22, 6274–6279. doi: 10.1039/c2jm16391h

Lin, R. Y., Taberna, P. L., Fantini, S., Presser, V., Perez, C. R., Malbosc, F., et al. (2011). Capacitive energy storage from−50 to 100 degrees C using an ionic liquid electrolyte. *J. Phys. Chem. Lett.* 2, 2396–2401. doi: 10.1021/jz201065t

Liu, C. G., Yu, Z. N., Neff, D., Zhamu, A., and Jang, B. Z. (2010). Graphene-based supercapacitor with an ultrahigh energy density. *Nano Lett.* 10, 4863–4868. doi: 10.1021/nl102661q

Liu, W. W., Yan, X. B., Lang, J. W., and Xue, Q. J. (2011). Electrochemical behavior of graphene nanosheets in alkylimidazolium tetrafluoroborate ionic liquid electrolytes: influences of organic solvents and the alkyl chains. *J. Mater. Chem.* 21, 13205–13212. doi: 10.1039/c1jm11930c

Lopes, J., and Padua, A. A. H. (2006). Using spectroscopic data on imidazolium cation conformations to test a molecular force field for ionic liquids. *J. Phys. Chem. B* 110, 7485–7489. doi: 10.1021/jp057533k

Lu, J. M., Yan, F., and Texter, J. (2009). Advanced applications of ionic liquids in polymer science. *Prog. Polymer Sci.* 34, 431–448. doi: 10.1016/j.progpolymsci.2008.12.001

Lu, X. H., Yu, M. H., Wang, G. M., Tong, Y. X., and Li, Y. (2014). Flexible solid-state supercapacitors: design, fabrication and applications. *Energy Environ. Sci.* 7, 2160–2181. doi: 10.1039/c4ee00960f

Lyu, X. M., Su, F. H., and Miao, M. H. (2016). Two-ply yarn supercapacitor based on carbon nanotube/stainless steel core-sheath yarn electrodes and ionic liquid electrolyte. *J. Power Sources* 307, 489–495. doi: 10.1016/j.jpowsour.2015.12.114

Mahanta, U., Choudhury, S., Venkatesh, R. P., SarojiniAmma, S., Ilangovan, S. A., and Banerjee, T. (2020). Ionic-liquid-based deep eutectic solvents as novel electrolytes for supercapacitors: COSMO-SAC predictions, synthesis, and characterization. *ACS Sustain. Chem. Eng.* 8, 372–381. doi: 10.1021/acssuschemeng.9b05596

Maiti, S., Pramanik, A., and Mahanty, S. (2015). Influence of imidazolium-based ionic liquid electrolytes on the performance of nano-structured MnO_2 hollow spheres as electrochemical supercapacitor. *Rsc Advances* 5, 41617–41626. doi: 10.1039/C5RA05514H

Mao, X. W., Brown, P., Cervinka, C., Hazell, G., Li, H., Ren, Y. Y., et al. (2019). Self-assembled nanostructures in ionic liquids facilitate charge storage at electrified interfaces. *Nat. Mater.* 18, 1350–1357. doi: 10.1038/s41563-019-0449-6

Mayrand-Provencher, L., Lin, S. X., Lazzerini, D., and Rochefort, D. (2010). Pyridinium-based protic ionic liquids as electrolytes for RuO2 electrochemical capacitors. *J. Power Sources* 195, 5114–5121. doi: 10.1016/j.jpowsour.2010.02.073

Mecerreyes, D. (2011). Polymeric ionic liquids: broadening the properties and applications of polyelectrolytes. *Prog. Polymer Sci.* 36, 1629–1648. doi: 10.1016/j.progpolymsci.2011.05.007

Mezger, M., Roth, R., Schroder, H., Reichert, P., Pontoni, D., and Reichert, H. (2015). Solid-liquid interfaces of ionic liquid solutions-interfacial layering and bulk correlations. *J. Chem. Phys.* 142:164707. doi: 10.1063/1.4918742

Mezger, M., Schroder, H., Reichert, H., Schramm, S., Okasinski, J. S., Schoder, S., et al. (2008). Molecular layering of fluorinated ionic liquids at a charged sapphire (0001) surface. *Science* 322, 424–428. doi: 10.1126/science.1164502

Na, W. J., Lee, A. S., Lee, J. H., Hong, S. M., Kim, E., and Koo, C. M. (2017). Hybrid ionogel electrolytes with POSS epoxy networks for high temperature lithium ion capacitors. *Solid State Ionics* 309, 27–32. doi: 10.1016/j.ssi.2017.06.017

Nagao, Y., Nakayama, Y., Oda, H., and Ishikawa, M. (2007). Activation of an ionic liquid electrolyte for electric double layer capacitors by addition of $BaTiO_3$ to carbon electrodes. *J. Power Sources* 166, 595–598. doi: 10.1016/j.jpowsour.2007.01.068

Navathe, G. J., Patil, D. S., Jadhav, P. R., Awale, D. V., Teli, A. M., Bhise, S. C., et al. (2015). Rapid synthesis of nanostructured copper oxide for electrochemical supercapacitor based on novel HPMIM Cl ionic liquid. *J. Electroanal. Chem.* 738, 170–175. doi: 10.1016/j.jelechem.2014.11.036

Newell, R., Faure-Vincent, J., Iliev, B., Schubert, T., and Aradilla, D. (2018). A new high performance ionic liquid mixture electrolyte for large temperature range supercapacitor applications (-70 degrees C to 80 degrees C) operating at 3.5V cell voltage. *Electrochim. Acta* 267, 15–19. doi: 10.1016/j.electacta.2018.02.067

Pan, Z. H., Yang, J., Zhang, Q. C., Liu, M. N., Hu, Y. T., Kou, Z. K., et al. (2019). All-Solid-state fiber supercapacitors with ultrahigh volumetric energy density and outstanding flexibility. *Adv. Energy Mater.* 9:1802753. doi: 10.1002/aenm.201802753

Pandey, G. P., and Hashmi, S. A. (2013). Solid-state supercapacitors with ionic liquid based gel polymer electrolyte: effect of lithium salt addition. *J. Power Sources* 243, 211–218. doi: 10.1016/j.jpowsour.2013.05.183

Pandolfo, A. G., and Hollenkamp, A. F. (2006). Carbon properties and their role in supercapacitors. *J. Power Sources* 157, 11–27. doi: 10.1016/j.jpowsour.2006.02.065

Pean, C., Daffos, B., Merlet, C., Rotenberg, B., Taberna, P. L., Simon, P., et al. (2015). Single electrode capacitances of porous carbons in neat ionic liquid electrolyte at 100 degrees C: a combined experimental and modeling approach. *J. Electrochem. Soc.* 162, A5091–A5095. doi: 10.1149/2.0151505jes

Pereira, G. F. L., Pereira, R. G., Salanne, M., and Amaral Siqueira, L. J. (2019). Molecular dynamics simulations of ether-modified phosphonium ionic liquid confined in between planar and porous graphene electrode models. *J. Phys. Chem. C* 123, 10816–10825. doi: 10.1021/acs.jpcc.9b01821

Pohlmann, S., Olyschlager, T., Goodrich, P., Vicente, J. A., Jacquemin, J., and Balducci, A. (2015). Mixtures of azepanium based ionic liquids and propylene carbonate as high voltage electrolytes for supercapacitors. *Electrochim. Acta* 153, 426–432. doi: 10.1016/j.electacta.2014.11.189

Ponkratov, D. O., Lozinskaya, E. I., Vlasov, P. S., Aubert, P. H., Plesse, C., Vidal, F., et al. (2018). Synthesis of novel families of conductive cationic poly(ionic liquid)s and their application in all-polymer flexible pseudo-supercapacitors. *Electrochim. Acta* 281, 777–788. doi: 10.1016/j.electacta.2018.05.191

Rai, A. K., Kim, S., Gim, J., Alfaruqi, M. H., Mathew, V., and Kim, J. (2014). Electrochemical lithium storage of a $ZnFe_2O_4$/graphene nanocomposite as an anode material for rechargeable lithium ion batteries. *Rsc Adv.* 4, 47087–47095. doi: 10.1039/C4RA08414D

Ramesh, S., and Ling, O. P. (2010). Effect of ethylene carbonate on the ionic conduction in poly(vinylidenefluoride-hexafluoropropylene) based solid polymer electrolytes. *Polymer Chem.* 1, 702–707. doi: 10.1039/b9py00244h

Salanne, M. (2017). Ionic liquids for supercapacitor applications. *Top. Curr. Chem.* 375:63. doi: 10.1007/s41061-017-0150-7

Sato, T., Masuda, G., and Takagi, K. (2004). Electrochemical properties of novel ionic liquids for electric double layer capacitor applications. *Electrochim. Acta* 49, 3603–3611. doi: 10.1016/j.electacta.2004.03.030

Sekhon, S. S. (2003). Conductivity behaviour of polymer gel electrolytes: role of polymer. *Bull. Mater. Sci.* 26, 321–328. doi: 10.1007/BF02707454

Shao, Y. L., El-Kady, M. F., Sun, J. Y., Li, Y. G., Zhang, Q. H., Zhu, M. F., et al. (2018). Design and mechanisms of asymmetric supercapacitors. *Chem. Rev.* 118, 9233–9280. doi: 10.1021/acs.chemrev.8b00252

Shen, B. S., Guo, R. S., Lang, J. W., Liu, L., Liu, L. Y., and Yan, X. B. (2016). A high-temperature flexible supercapacitor based on pseudocapacitive behavior of FeOOH in an ionic liquid electrolyte. *J. Mater. Chem. A* 4, 8316–8327. doi: 10.1039/C6TA01734G

Shen, B. S., Lang, J. W., Guo, R. S., Zhang, X., and Yan, X. B. (2015). Engineering the electrochemical capacitive properties of microsupercapacitors based on graphene quantum Dots/MnO_2 using ionic liquid gel electrolytes. *Acs Appl. Mater. Interf.* 7, 25378–25389. doi: 10.1021/acsami.5b07909

Shen, L. F., Wang, Y., Lv, H. F., Chen, S. Q., van Aken, P. A., Wu, X. J., et al. (2018). Ultrathin Ti2Nb2O9 nanosheets with pseudocapacitive properties as superior anode for sodium-ion batteries. *Adv. Mater.* 30, 1804378. doi: 10.1002/adma.201804378

Simon, P., and Gogotsi, Y. (2008). Materials for electrochemical capacitors. *Nat. Mater.* 7, 845–854. doi: 10.1038/nmat2297

Simon, P., and Gogotsi, Y. (2013). Capacitive energy storage in nanostructured carbon-electrolyte systems. *Acc. Chem. Res.* 46, 1094–1103. doi: 10.1021/ar200306b

Smith, A. M., Lovelock, K. R. J., Gosvami, N. N., Licence, P., Dolan, A., Welton, T., et al. (2013). Monolayer to bilayer structural transition in confined pyrrolidinium-based ionic liquids. *J. Phys. Chem. Lett.* 4, 378–382. doi: 10.1021/jz301965d

Stettner, T., Huang, P., Goktas, M., Adelhelm, P., and Balducci, A. (2018). Mixtures of glyme and aprotic-protic ionic liquids as electrolytes for energy storage devices. *J. Chem. Phys.* 148:193825. doi: 10.1063/1.5013117

Stoller, M. D., and Ruoff, R. S. (2010). Best practice methods for determining an electrode material's performance for ultracapacitors. *Energy Environ. Sci.* 3, 1294–1301. doi: 10.1039/c0ee00074d

Subramanian, V., Hall, S. C., Smith, P. H., and Rambabu, B. (2004). Mesoporous anhydrous RuO_2 as a supercapacitor electrode material. *Solid State Ionics* 175, 511–515. doi: 10.1016/j.ssi.2004.01.070

Sudha, V., and Sangaranarayanan, M. V. (2002). Underpotential deposition of metals: structural and thermodynamic considerations. *J. Phys. Chem. B* 106, 2699–2707. doi: 10.1021/jp013544b

Takegawa, A., Murakami, M., Kaneko, Y., and Kadokawa, J. (2010). Preparation of chitin/cellulose composite gels and films with ionic liquids. *Carbohydr. Polym.* 79, 85–90. doi: 10.1016/j.carbpol.2009.07.030

Tamailarasan, P., and Ramaprabhu, S. (2012). Carbon nanotubes-graphene-solidlike ionic liquid layer-based hybrid electrode material for high performance supercapacitor. *J. Phys. Chem. C* 116, 14179–14187. doi: 10.1021/jp302785j

Tiruye, G. A., Munoz-Torrero, D., Palma, J., Anderson, M., and Marcilla, R. (2015). All-solid state supercapacitors operating at 3.5 V by using ionic liquid based polymer electrolytes. *J. Power Sources* 279, 472–480. doi: 10.1016/j.jpowsour.2015.01.039

Tiruye, G. A., Munoz-Torrero, D., Palma, J., Anderson, M., and Marcilla, R. (2016). Performance of solid state supercapacitors based on polymer electrolytes containing different ionic liquids. *J. Power Sources* 326, 560–568. doi: 10.1016/j.jpowsour.2016.03.044

Ue, M., Takeda, M., Toriumi, A., Kominato, A., Hagiwara, R., and Ito, Y. (2003). Application of low-viscosity ionic liquid to the electrolyte of double-layer capacitors. *J. Electrochem. Soc.* 150, A499–A502. doi: 10.1149/1.1559069

Ujjain, S. K., Sahu, V., Sharma, R. K., and Singh, G. (2015). High performance, all solid state, flexible supercapacitor based on ionic liquid functionalized graphene. *Electrochim. Acta* 157, 245–251. doi: 10.1016/j.electacta.2015.01.061

Van Aken, K. L., Beidaghi, M., and Gogotsi, Y. (2015). Formulation of ionic-liquid electrolyte to expand the voltage window of supercapacitors. *Angew. Chem Int. Ed.* 54, 4806–4809. doi: 10.1002/anie.201412257

Wang, P. H., Wang, T. L., Lin, W. C., Lin, H. Y., Lee, M. H., and Yang, C. H. (2018). Crosslinked polymer ionic liquid/ionic liquid blends prepared by photopolymerization as solid-state electrolytes in supercapacitors. *Nanomaterials* 8:225. doi: 10.3390/nano8040225

Watanabe, M., Thomas, M. L., Zhang, S. G., Ueno, K., Yasuda, T., and Dokko, K. (2017). Application of ionic liquids to energy storage and conversion materials and devices. *Chem. Rev.* 117, 7190–7239. doi: 10.1021/acs.chemrev.6b00504

Wong, S. I., Lin, H., Sunarso, J., Wong, B. T., and Jia, B. J. A. M.T. (2020). Optimization of ionic-liquid based electrolyte concentration for high-energy density graphene *supercapacitors*. *Appl. Mater. Today* 18:100522. doi: 10.1016/j.apmt.2019.100522

Xia, H., Meng, Y. S., Yuan, G. L., Cui, C., and Luc, L. (2012). A symmetric RuO_2/RuO_2 supercapacitor operating at 1.6 V by using a neutral aqueous electrolyte. *Electrochem. Solid State Lett.* 15, A60–A63. doi: 10.1149/2.023204esl

Xu, N., Klein, J. M., Huang, P., Alwusaydi, H. A., Mann, E. K., and Gurkan, B. E. (2019). Improved accessibility of porous carbon electrodes with surfactant ionic liquids for supercapacitors. *J. Appl. Electrochem.* 49, 151–162. doi: 10.1007/s10800-018-1266-3

Yang, C., Shi, M., Nuli, Y., Song, X., Zhao, L., Liu, J., et al. (2020). Interfacial electrochemical investigation of 3D space-confined $MnFe_2O_4$ for high-performance ionic liquid-based supercapacitors. *Electrochim. Acta* 331:135386. doi: 10.1016/j.electacta.2019.135386

Yang, M., Jeong, J. M., Huh, Y. S., and Choi, B. G. (2015). High-performance supercapacitor based on three-dimensional MoS_2/graphene aerogel composites. *Compos. Sci. Technol.* 121, 123–128. doi: 10.1016/j.compscitech.2015.11.004

Yang, Y. H., Cao, B. M., Li, H., and Liu, H. T. (2017). A flexible polycation-type anion-dominated conducting polymer as potential all-solid-state supercapacitor film electrolyte. *Chem. Eng. J.* 330, 753–756. doi: 10.1016/j.cej.2017.08.012

Yin, L., Li, S., Liu, X. H., and Yan, T. Y. (2019). Ionic liquid electrolytes in electric double layer capacitors. *Sci. China Mater.* 62, 1537–1555. doi: 10.1007/s40843-019-9458-3

Yoo, H. D., Li, Y. F., Liang, Y. L., Lan, Y. C., Wang, F., and Yao, Y. (2016). Intercalation pseudocapacitance of exfoliated molybdenum disulfide for ultrafast energy storage. *Chemnanomat* 2, 688–691. doi: 10.1002/cnma.201600117

Yuan, J. Y., Mecerreyes, D., and Antonietti, M. (2013). Poly(ionic liquid)s: an update. *Prog. Polym. Sci.* 38, 1009–1036. doi: 10.1016/j.progpolymsci.2013.04.002

Zhang, J. H., Zhang, H. T., Zhang, Y. Q., Zhang, J. W., He, H. Y., Zhang, X. X., et al. (2019). Unveiling of the energy storage mechanisms of multi -modified (Nb_2O_5@C)/rGO nanoarrays as anode for high voltage supercapacitors with formulated ionic liquid electrolytes. *Electrochim. Acta* 313, 532–543. doi: 10.1016/j.electacta.2019.04.160

Zhang, L., Guo, Y., Shen, K., Huo, J., Liu, Y., and Guo, S. (2019). Ion-matching porous carbons with ultra-high surface area and superior energy storage performance for supercapacitors. *J. Mater. Chem. A* 7, 9163–9172. doi: 10.1039/C9TA00781D

Zhang, L. L., and Zhao, X. S. (2009). Carbon-based materials as supercapacitor electrodes. *Chem. Soc. Rev.* 38, 2520–2531. doi: 10.1039/b813846j

Zhu, Q., Song, Y., Zhu, X. F., and Wang, X. L. (2007). Ionic liquid-based electrolytes for capacitor applications. *J. Electroanal. Chem.* 601, 229–236. doi: 10.1016/j.jelechem.2006.11.016

Conflict of Interest: HZ was employed by company *Hebei Institute of Process Innovation Co. Ltd.*

The remaining authors declare that the research was conducted in the absence of any commercial or financial relationships that could be construed as a potential conflict of interest.

ORIGINAL RESEARCH
published: 18 June 2020
doi: 10.3389/fchem.2020.00459

Magnesiophilic Interface of 3D $MoSe_2$ for Reduced Mg Anode Overpotential

Tong Shen[1], *Chengzhao Luo*[1], *Yu Hao*[1] *and Yu Chen*[1,2]*

[1] School of Optoelectronic Science and Engineering & Collaborative Innovation Center of Suzhou Nano Science and Technology, Soochow University, Suzhou, China, [2] National University of Singapore Suzhou Research Institute, Dushu Lake Science and Education Innovation District, Suzhou, China

A large overpotential is often reported for rechargeable magnesium batteries during the deposition/stripping of magnesium, which can be detrimental to the cell performance. In this work, a three-dimensional electrode that mainly composed magnesiophilic $MoSe_2$ (MMSE) has been fabricated and proposed as the substrate for the electrochemical deposition/stripping of magnesium metal. The magnesiophilic interface of $MoSe_2$ has been proven by electrochemical tests of magnesium deposition test. In addition, the electrochemical property of 3D MMSE has been examined by a large-capacity (10 mAh/cm^2) magnesium deposition/stripping test. The stable magnesiophilic interface of MMSE has been further confirmed by SEM characterization. Finally, the crucial effect of the magnesiophilic interface of MMSE on the overpotentials have been demonstrated by Mg deposition/stripping test under various current densities.

Keywords: magnesiophilic interface, Magnesium battery anode, $MoSe_2$, low voltage hysteresis, porous structure

Edited by:
Chuankun Jia,
Changsha University of Science and Technology, China

Reviewed by:
Shufeng Song,
Chongqing University, China
Hui Xia,
Nanjing University of Science and Technology, China

****Correspondence:***
Yu Chen
chenyu_ny@suda.edu.cn

Specialty section:
This article was submitted to Electrochemistry, a section of the journal Frontiers in Chemistry

Received: *27 March 2020*
Accepted: *04 May 2020*
Published: *18 June 2020*

Citation:
Shen T, Luo C, Hao Y and Chen Y (2020) Magnesiophilic Interface of 3D $MoSe_2$ for Reduced Mg Anode Overpotential. Front. Chem. 8:459. doi: 10.3389/fchem.2020.00459

INTRODUCTION

Strong interest in alternative energy storage systems has been caused due to the cost constraints and operational safety issues of lithium-ion batteries. Rechargeable magnesium battery is considered to be one of the most promising alternatives due to the low electrode potential (−2.36 V vs. NHE) and high-volume specific capacity (3,833 mA h cm^{-3}) of Mg metal (Yoo et al., 2013; Mohtadi and Mizuno, 2014; Muldoon et al., 2014). The most fascinating feature of Mg metal anode is that there is no dendrite generation during the magnesium charge and discharge process, which eliminates the potential safety hazard of the battery short circuit caused by dendrite puncturing of the separator. However, the development of magnesium rechargeable battery is still limited by multiple obstacles, including the slow diffusion of highly polar divalent magnesium ions in the cathode material, the narrow voltage window of the electrolyte limiting the requirements of high energy density, the compatibility of the electrolyte with the magnesium metal anode, and the huge overpotential of both cathode and anode (Cheng et al., 2016; Canepa et al., 2017). Extensive effort has been devoted in the performance enhancement of rechargeable magnesium batteries. However, there are few studies focusing on the reduction of Mg anode overpotential (Li et al., 2018; Tang et al., 2019).

Electrode polarization can be categorized into electrochemical polarization, concentration polarization, and ohmic polarization. In magnesium battery, due to the bivalency of magnesium, the transmission and diffusion of magnesium ion is more difficult than those of lithium ion, making electrochemical polarization and concentration polarization of magnesium particularly important (Yang et al., 2015; Chi et al., 2017; Li Q. et al., 2017; Xia et al., 2018). As a result, the overpotential of Mg anode is usually prominent. Extensive efforts have been made to the reduction of overpotential of lithium and sodium metal electrodes, and multiple methods have been proposed, including three-dimensional stable ion-conducting solid-matrix lithium metal anodes (Lin et al., 2017), composite lithium metal anode consisting of a 3D conductive scaffold with a sulfur-repellent coating (Liang et al., 2016), nitrogen, and oxygen co-doped graphitized carbon fibers with rich sodiophilic sites for sodium metal anodes (Zheng et al., 2018). Therefore, constructing a lithiopholic/sodiophilic substrate for the deposition of lithium/sodium metal have been proven to be an effective method for the overpotential reduction, which can be used as a reference for reducing the overpotential of magnesium metal batteries (Su et al., 2015; Zhang et al., 2016).

Herein, $MoSe_2$ clusters consisting of two-dimensional nanosheets have been synthesized by hydrothermal method and utilized as substrate for the magnesium deposition. The as-obtained $MoSe_2$ possesses a robust layered structure and is able to store magnesium within these layers (Fan et al., 2018; Lin et al., 2019). More importantly, $MoSe_2$ has a magnesiopholic surface, thus facilitating the deposition of metallic magnesium on its surface. Owing to the three-dimensional porous structure and high specific surface area, the magnesiophilic $MoSe_2$ electrode (MMSE) possessed large number of interfacial deposition sites of magnesium, which is beneficial to the reduction of the electrode overpotential during its operation.

MATERIALS AND METHODS

Synthesis of $MoSe_2$

First, 2 mmol of selenium powder was slowly added to 10 ml of hydrazine hydrate (85%). The mixture was continuously stirred for 1 h until it became dark red. One millimoles of $Na_2MoO_4 \cdot 2H_2O$ was then dissolved in a mixed solution of 45 ml of water and 5 ml of ethylenediamine. Next, the solution ($Se\text{-}N_2H_4 \cdot 2H_2O$) was added dropwise to the $Na_2MoO_4 \cdot 2H_2O$-ethylenediamine solution and stirred for 30 min. Finally, the above mixed solution was transferred to an autoclave lined with a 100 ml polytetrafluoroethylene liner and hydrothermally treated at 200°C for 10 h. The precipitate was washed several times with deionized water and ethanol and then freeze-dried for 24 h. The samples were heat treated at 600°C for 1 h and 800°C for 1 h in an argon atmosphere to the final $MoSe_2$ material.

MMSE Preparation

$MoSe_2$ (70 wt%), acetylene black (20 wt%), PVDF (10 wt%), and N-methyl-2-pyrrolidone were mixed to form a slurry and coated on Mo foil, followed by vacuum dry at 60°C for 12 h. MMSE was assembled with metal magnesium and firstly discharged at a current density of 50 $\mu A/cm^2$ for 20 h, followed by charge and discharge at a current density of 10 A/cm^2 and a capacity of 1 A h/cm^2 for several hours.

Material Characterization and Testing

The micro-morphology of molybdenum selenide was observed by field emission transmission electron microscope (TEM) (FETEM, FEI Tecnai G220, FEI NanoPorts, Ltd.) and field emission scanning electron microscope (SEM) (SU8010, Hitachi Ltd.). The powder X-ray diffractometer (D8 Advance, Bruker) and X-ray photoelectron spectroscopy (Escalab 250Xi, Thermo Fisher) were used to analyze the crystal structure of $MoSe_2$. CR2025 coin-type battery was chosen for assembly test. The metal magnesium foil was used as the counter electrode, with the glass fiber as separator. The electrolyte was all perphenyl complex (APC) containing 0.2 M aluminum chloride ($AlCl_3$), 0.4 M phenyl magnesium chloride (PhMgCl), and anhydrous tetrahydrofuran (THF) solvent. The constant current charge and discharge test was performed by a LAND battery analyzer.

RESULTS

$MoSe_2$ were synthesized through a hydrothermal method followed by high temperature sintering, with their morphology observed by TEM (Ge et al., 2018). As shown in **Figure 1a**, $MoSe_2$ clearly demonstrates a cluster structure consisting of nanosheets. Ethylenediamine was added as a surfactant to control the obtained morphology so that the $MoSe_2$ nanosheets self-assembled into clusters rather than arbitrarily stacked, thus tremendously increasing its contact area with the electrolyte. Such a feature was crucial for the effective current density reduction and subsequent magnesium deposition. As shown in **Figure S1**, the SEM image of the material also shows that it is the microscopic appearance of the nanosheet, and at the same time shows the overall morphology of the material in the micro-size (Li J. et al., 2017). The corresponding EDX also proves the uniformity of the material through element distribution (Ge et al., 2018). High-resolution transmission electron microscopy (HRTEM) in **Figure 1b** clearly shows the lattice fringes of $MoSe_2$, with a 0.68 nm interplanar spacing corresponding to the $MoSe_2$ (002) plane (Li J. et al., 2017). The X-ray diffraction (XRD) pattern of molybdenum selenide is shown in **Figure 1c**, which confirms the high crystallinity of $MoSe_2$. The well-defined peaks at 13.5°, 31.4°, 37.9°, and 57.0° correspond to (002), (100), (103), and (110) crystal planes of $MoSe_2$ (JCPDS No. 29-0914), respectively (Zheng et al., 2017). At the same time, the XPS test was performed on the material, as shown in **Figure S3**, and peak separation was performed on Mo 3d and Se 3d to prove the existence of Mo^{4+} and Se^{2-} respectively (Tang et al., 2014; Liu et al., 2015; Xie et al., 2016; Ding et al., 2017), proving the existence of $MoSe_2$ by means of element chemical bonds.

In order to confirm the magnesiophilic feature of $MoSe_2$, magnesium nucleation potentials of various materials, including MMSE, $MoSe_2$, acetylene black, and polyvinylidene fluoride (PVDF), and Mg metal, were obtained from the respective discharge curves by depositing magnesium at low currents (Chen et al., 2019). At a current density of 50 $\mu A/cm^2$, Mg plating started when the MMSE was discharged to -0.083 V (**Figure 1d**). The MMSE contained two parts: pure $MoSe_2$, and acetylene black and PVDF. Therefore, electrochemical deposition tests were performed to investigate the magnesium nucleation potential of each part at the same current density.

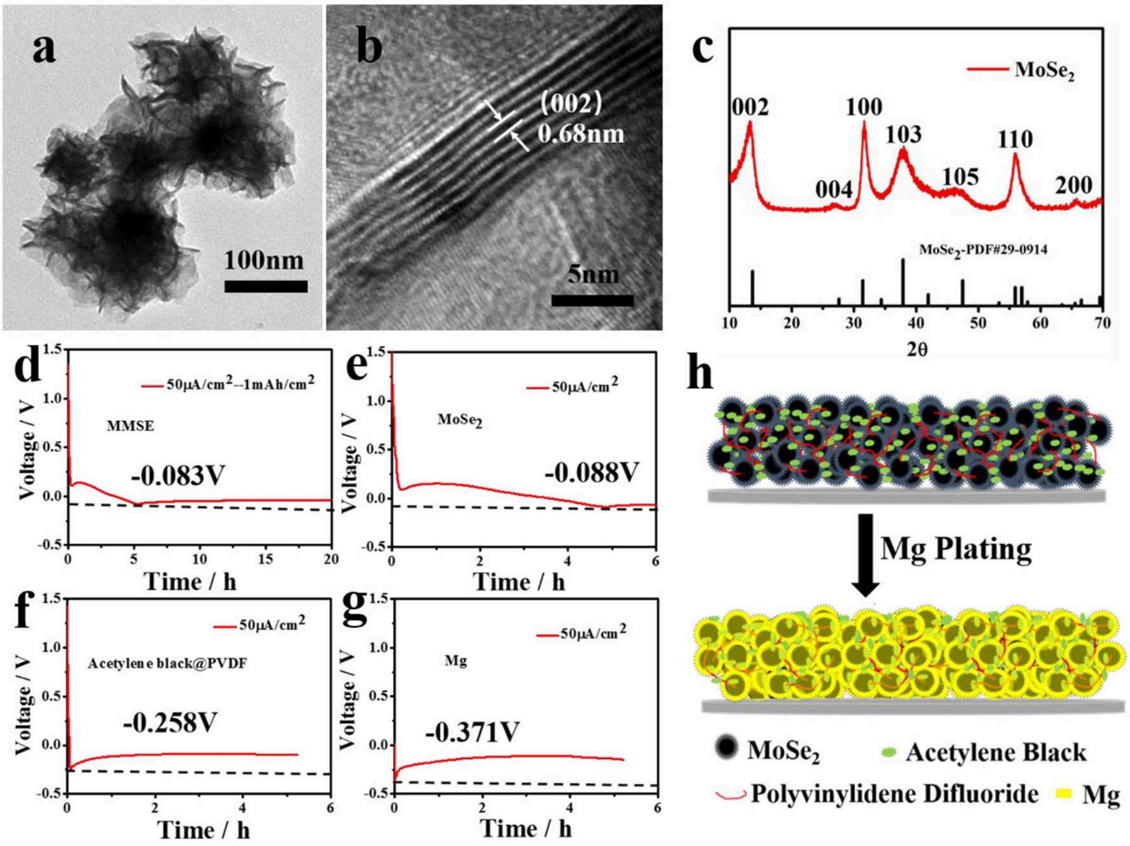

FIGURE 1 | (a) TEM image, **(b)** HRTEM image, and **(c)** XRD spectrum of $MoSe_2$. **(d–g)** Electrochemical curves showing the Mg deposition behavior on **(d)** MMSE, **(e)** $MoSe_2$, **(f)** Acetylene black and PVDF, and **(g)** Mg. The current density was fixed at $50\,\mu$ A/cm^2 for Mg plating processes. **(h)** Schematic showing the Mg deposition behavior on MMSE.

The pure $MoSe_2$ electrode started Mg plating when discharged to −0.088 V (**Figure 1e**), while the acetylene black and PVDF and Mg electrodes started Mg plating when discharged to −0.258 and −0.371 V, respectively (**Figures 1f,g**). Therefore, the nucleation potential of pure $MoSe_2$ electrode is much lower than those of acetylene black and PVDF and Mg electrodes, confirming that $MoSe_2$ has a more magnesiophilic interface. The schematic diagram of magnesium deposition on MMSE is shown in **Figure 1h**. Cluster-like flaky $MoSe_2$ preferentially embeds part of magnesium. It is reported that $MoSe_2$ and carbon composite material has extremely low capacity as an electrode material for magnesium batteries (Fan et al., 2018; Lin et al., 2020). Herein, choosing this special shape of $MoSe_2$ as the electrode material to assemble the magnesium battery for test, referring to **Figure S2**, the data displays that the amount of magnesium embedded in $MoSe_2$ is low, which means the volume expansion is small, so its limited capacity determines that the amount of magnesium embedded has little effect on its microstructure and magnesiophilic surface. Therefore, the magnesiophilic surface and 3D porous strucuture of MMSE promoted the preferential deposition of magnesium and reduced the effective current density, thus being beneficial to the reduction of magnesium deposition potential.

The SEM images in **Figures 2a–d** depict the morphologies of MMSE at different stages of plating and striping process of Mg at a current density of 10 mA/cm^2. The 3D porous feature of MMSE can be confirmed in **Figure 2a** and its inset, which correspond to the pristine MMSE prior to Mg deposition. After the deposition of a large capacity of 10 mA h/cm^2 magnesium on MMSE (**Figure 2b**), owing to its porous nature, no crack was generated in MMSE and the abundant pores within MMSE were filled with Mg metal. **Figure 2c** shows the morphology of MMSE after 10 mA h/cm^2 of magnesium was completely released, with its morphology being very similar to those of pristine electrode shown in **Figure 2a**. The morphology of MMSE after 1,000 cycles under a capacity of 1 mA h/cm^2 is shown in **Figure 2d**. The MMSE after 1,000 cycles shows similar morphology with that of pristine MMSE (Song et al., 2019). The insets at the upper right corner of each SEM image are the cross-sectional view of corresponding electrode, with similar cross-sectional thicknesses, being 18.8, 19.2, 19.0, and 19.3 μm,

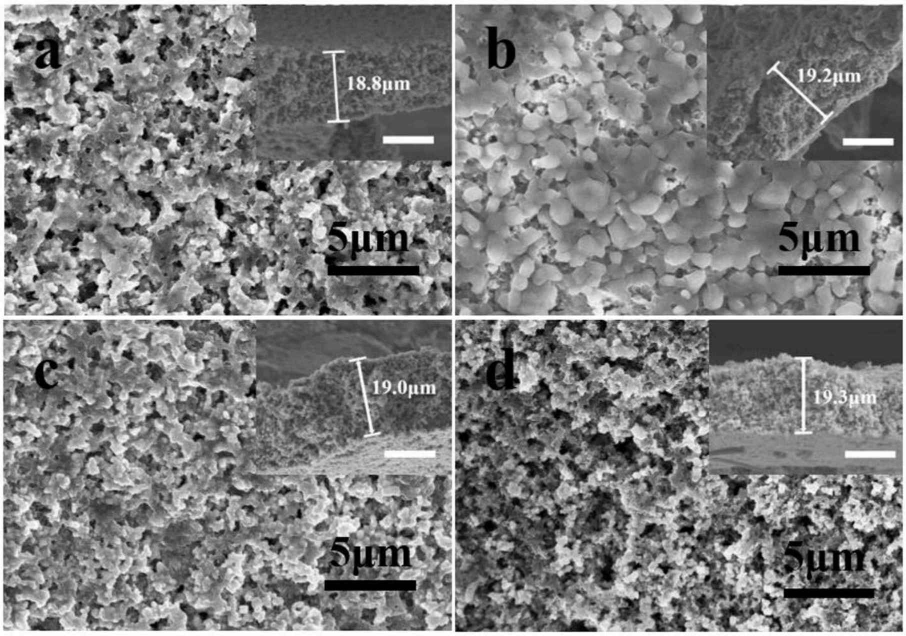

FIGURE 2 | SEM images and corresponding cross-section (inset) of **(a)** pristine MMSE, MMSE after **(b)** plating 10 mA h/cm^2, then **(c)** stripping 10 mA h/cm^2 of Mg, and **(d)** MMSE after 1,000 cycles under a capacity of 1 mA h/cm^2 at a current density of 10 mA/cm^2. The white scale bar in the inset is 10 μm. Electrochemical performance of MMSE symmetric cell.

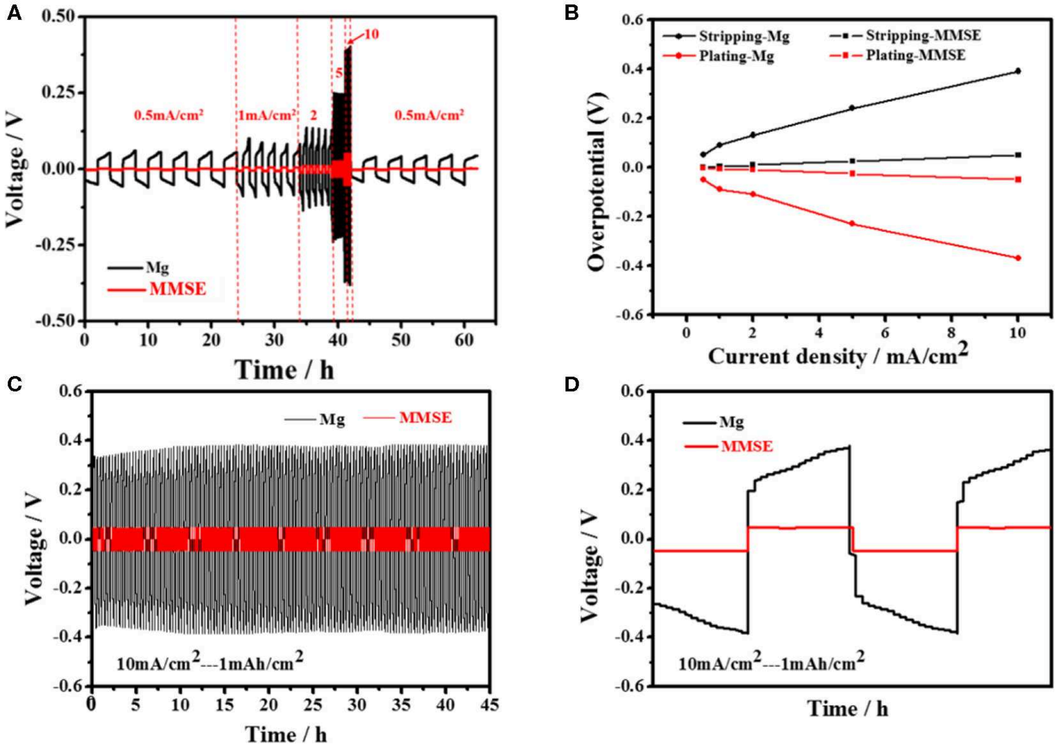

FIGURE 3 | (A) Voltage profile of Mg symmetric cell (black) and that of MMSE symmetric cell (red) at different rate various from 0.5 to 10 mA/cm^2. **(B)** Overpotentials for plating and stripping of Mg electrode and MMSE during cycling. **(C)** The voltage profiles of Mg symmetric cells (black) and MMSE symmetric cells (red) at the current densities of 10 mA/cm^2 and **(D)** magnified Mg plating/stripping profiles.

for pristine MMSE, MMSE after first Mg deposition then first Mg exfoliation, and MMSE after 1,000 cycles, respectively (Chen et al., 2019). The stable electrode structure of MMSE after deposition of large amounts of Mg was benefited by the three-dimensional porous structure and large magnesiophilic interface of MMSE.

To investigate its constant current electrochemical performance, symmetrical cells of MMSE were assembled to evaluate the voltage change during Mg plating/stripping. Comparing the deposition/stripping curves between MMSE and Mg electrodes at different current densities shown in **Figure 3A**, it can be clearly observed that the deposition/stripping potentials of MMSE are much smaller than those of Mg electrode. The deposition/stripping potentials of the MMSE and Mg electrodes in **Figure 3A** were extracted and plotted against various current densities in **Figure 3B**. Specifically, at the current density of 0.5, 1, 2, 5, 10 mA/cm^2, the magnesium deposition potential of MMSE and Mg are −0.003, −0.005, −0.011, −0.026, −0.051 V, and −0.05, −0.09, −0.11, −0.23, −0.37 V, respectively, confirming the much smaller hysteresis voltages of MMSE than those of metallic magnesium. In addition, for more detailed data comparison with other methods in reducing the overpotential of magnesium metal anode, Li et al. added a small amount of iodine to the (TFSI) $_2$-DME electrolyte as an additive (Li et al., 2018). Voltage hysteresis is defined as the voltage difference between magnesium plating and stripping, which depends on multiple factors, including current density, charge transfer resistance, and interface characteristics. MMSE, with a large magnesiophilic interface, can effectively reduce both equivalent current density and Mg nucleation potential, thus delivering low overpotentials at various current densities. In the long cycling process under a current density of 10 mA/cm^2 (**Figure 3C**), both the MMSE and Mg electrode show stable cycles. But the voltage lag of the MMSE is much smaller than that of the Mg electrode. The much larger overpotential of Mg electrode can be clearly observed in the locally enlarged cycling curve in **Figure 3D**. Besides, owing to the concentration polarization of magnesium ions by the solvation effect, it can be observed that the deposition/stripping potential of Mg gradually increased in each cycle (Canepa et al., 2015). Referring to **Figure S4** for comparison of other current densities, under a current density of 1 and 5 mA/cm^2, the same as 10 mA/cm^2, MMSE does have better performance in reducing overpotential than magnesium metal electrode. In contrast, the potential of the MMSE remained stable during the plating/striping process.

DISCUSSION

In summary, MMSE has been successfully fabricated by utilizing magnesiophilic flaky $MoSe_2$ nanoclusters synthesized by hydrothermal method and heat treatment. The magnesiophilic interface of MMSE has been confirmed by magnesium deposition electrochemical tests. Benefiting from its 3D porous structure, MMSE shows excellent structural stability after deposition and stripping of large-capacity of magnesium. By assembling in a symmetric battery, MMSE shows much smaller overpotential of that of metal magnesium under different current densities, which shows the excellent ability of MMSE in reducing the hysteresis voltage of magnesium anode. This work shows a method to reduce the Mg overpotential by adopting a three-dimensional $MoSe_2$-based electrode with magnesium-affinitive interface, which provides an alternative route for the development of Mg metal anode.

DATA AVAILABILITY STATEMENT

The raw data supporting the conclusions of this article will be made available by the authors, without undue reservation.

AUTHOR CONTRIBUTIONS

All authors listed have made a substantial, direct and intellectual contribution to the work, and approved it for publication.

FUNDING

This work was supported by the National Natural Science Foundation of China (Grant No. 51502183), the Natural Science Foundation of Jiangsu Province of China (Grant Nos. BK20190098, BK20150325), the Natural Science Foundation of the Jiangsu Higher Education Institutions of China (19KJA550001), Key Lab of Modern Optical Technologies of Education Ministry of China, Key Lab of Advanced Optical Manufacturing Technologies of Jiangsu Province, Priority Academic Program Development (PAPD) of Jiangsu Higher Education Institutions, and Jiangsu Shuangchuang Plan.

SUPPLEMENTARY MATERIAL

The Supplementary Material for this article can be found online at: https://www.frontiersin.org/articles/10.3389/fchem.2020.00459/full#supplementary-material

REFERENCES

Canepa, P., Gautam, G. S., Malik, R., Jayaraman, S., Rong, Z., Zavadil, K. R., et al. (2015). Understanding the initial stages of reversible Mg deposition and stripping in inorganic nonaqueous electrolytes. *Chem. Mater.* 27, 3317–3325. doi: 10.1021/acs.chemmater.5b00389

Canepa, P., Sai Gautam, G., Hannah, D. C., Malik, R., Liu, M., Gallagher, K. G., et al. (2017). Odyssey of multivalent cathode materials: open questions and future challenges. *Chem. Rev.* 117, 4287–4341. doi: 10.1021/acs.chemrev.6b00614

Chen, L., Fan, X., Ji, X., Chen, J., Hou, S., and Wang, C. (2019). High-energy Li metal battery with lithiated host. *Joule* 3, 732–744. doi: 10.1016/j.joule.2018.11.025

Cheng, Y., Choi, D., Han, K. S., Mueller, K. T., Zhang, J. G., Sprenkle, V. L., et al. (2016). Toward the design of high voltage magnesium-lithium hybrid batteries using dual-salt electrolytes. *Chem. Commun.* 52, 5379–5382. doi: 10.1039/C6CC00986G

Chi, S. S., Liu, Y., Song, W. L., Fan, L. Z., and Zhang, Q. (2017). Prestoring lithium into stable 3D nickel foam host as dendrite-free lithium metal anode. *Adv. Funct. Mater*. 27:1700348. doi: 10.1002/adfm.201700348

Ding, J., Zhou, H., Zhang, H., Stephenson, T., Li, Z., Karpuzov, D., et al. (2017). Exceptional energy and new insight with a sodium–selenium battery based on a carbon nanosheet cathode and a pseudographite anode. *Energy Environ. Sci*. 10, 153–165. doi: 10.1039/C6EE02274J

Fan, J. J., Shen, S. Y., Chen, Y., Wu, L. N., Peng, J., Peng, X. X., et al. (2018). A rechargeable Mg^{2+}/Li^{+} hybrid battery based on sheet-like $MoSe_2/C$ nanocomposites cathode. *Electrochem. Commun*. 90, 16–20. doi: 10.1016/j.elecom.2018.03.004

Ge, J., Fan, L., Wang, J., Zhang, Q., Liu, Z., Zhang, E., et al. (2018). $MoSe_2$/N-doped carbon as anodes for potassium-Ion batteries. *Adv. Energy Mater*. 8:1801477. doi: 10.1002/aenm.201801477

Li, J., Hu, H., Qin, F., Zhang, P., Zou, L., Wang, H., et al. (2017). Flower-like $MoSe_2/C$ composite with expanded (0 0 2) planes of few-layer $MoSe_2$ as the anode for high-performance sodium-ion batteries. *Chem. A Eur. J*. 23, 14004–14010. doi: 10.1002/chem.201702791

Li, Q., Zhu, S., and Lu, Y. (2017). 3D porous Cu current collector/Li-metal composite anode for stable lithium-metal batteries. *Adv. Funct. Mater*. 27:1606422. doi: 10.1002/adfm.201606422

Li, X., Gao, T., Han, F., Ma, Z., Fan, X., Hou, S., et al. (2018). Reducing Mg anode overpotential via ion conductive surface layer formation by iodine additive. *Adv. Energy Mater*. 8:1701728. doi: 10.1002/aenm.201701728

Liang, Z., Lin, D., Zhao, J., Lu, Z., Liu, Y., Liu, C., et al. (2016). Composite lithium metal anode by melt infusion of lithium into a 3D conducting scaffold with lithiophilic coating. *Proc. Natl. Acad. Sci. U.S.A*. 113, 2862–2867. doi: 10.1073/pnas.1518188113

Lin, B., Zhu, X., Fang, L., Liu, X., Li, S., Zhai, T., et al. (2019). Birnessite nanosheet arrays with high K content as a high-capacity and ultrastable cathode for K-Ion batteries. *Adv. Mater*. 31:1900060. doi: 10.1002/adma.201900060

Lin, D., Zhao, J., Sun, J., Yao, H., Liu, Y., Yan, K., et al. (2017). Three-dimensional stable lithium metal anode with nanoscale lithium islands embedded in ionically conductive solid matrix. *Proc. Natl. Acad. Sci. U.S.A*. 114, 4613–4618. doi: 10.1073/pnas.1619489114

Lin, L., Ning, H., Song, S., Xu, C., and Hu, N. (2020). Flexible electrochemical energy storage: the role of composite materials. *Compos. Sci. Technol*. 192:108102. doi: 10.1016/j.compscitech.2020.108102

Liu, Y., Zhu, M., and Chen, D. (2015). Sheet-like $MoSe_2/C$ composites with enhanced Li-ion storage properties. *J. Mater. Chem. A* 3, 11857–11862. doi: 10.1039/C5TA02100F

Mohtadi, R., and Mizuno, F. (2014). Magnesium batteries: current state of the art, issues and future perspectives. *Beilstein J. Nanotechnol*. 5, 1291–1311. doi: 10.3762/bjnano.5.143

Muldoon, J., Bucur, C. B., and Gregory, T. (2014). Quest for nonaqueous multivalent secondary batteries: magnesium and beyond. *Chem. Rev*. 114, 11683–11720. doi: 10.1021/cr500049y

Song, S., Wu, Y., Tang, W., Deng, F., Yao, J., Liu, Z., et al. (2019). Composite solid polymer electrolyte with garnet nanosheets in poly (ethylene oxide). *ACS Sust. Chem. Eng*. 7, 7163–7170. doi: 10.1021/acssuschemeng.9b00143

Su, S., Huang, Z., NuLi, Y., Tuerxun, F., Yang, J., and Wang, J. (2015). A novel rechargeable battery with a magnesium anode, a titanium dioxide cathode, and a magnesium borohydride/tetraglyme electrolyte. *Chem. Commun*. 51, 2641–2644. doi: 10.1039/C4CC08774G

Tang, H., Dou, K., Kaun, C. C., Kuang, Q., and Yang, S. (2014). $MoSe_2$ nanosheets and their graphene hybrids: synthesis, characterization and hydrogen evolution reaction studies. *J. Mater. Chem. A* 2, 360–364. doi: 10.1039/C3TA13584E

Tang, K., Du, A., Dong, S., Cui, Z., Liu, X., Lu, C., et al. (2019). A stable solid electrolyte interphase for magnesium metal anode evolved from a bulky anion lithium salt. *Adv. Mater*. 32:1904987. doi: 10.1002/adma.201904987

Xia, H., Zhu, X., Liu, J., Liu, Q., Lan, S., Zhang, Q., et al. (2018). A monoclinic polymorph of sodium birnessite for ultrafast and ultrastable sodium ion storage. *Nat. Commun*. 9, 1–10. doi: 10.1038/s41467-018-07595-y

Xie, D., Tang, W., Wang, Y., Xia, X., Zhong, Y., Zhou, D., et al. (2016). Facile fabrication of integrated three-dimensional C-$MoSe_2$/reduced graphene oxide composite with enhanced performance for sodium storage. *Nano Res*. 9, 1618–1629. doi: 10.1007/s12274-016-1056-

Yang, C. P., Yin, Y. X., Zhang, S. F., Li, N. W., and Guo, Y. G. (2015). Accommodating lithium into 3D current collectors with a submicron skeleton towards long-life lithium metal anodes. *Nat. Commun*. 6, 1–9. doi: 10.1038/ncomms9058

Yoo, H. D., Shterenberg, I., Gofer, Y., Gershinsky, G., Pour, N., and Aurbach, D. (2013). Mg rechargeable batteries: an on-going challenge. *Energy Environ. Sci*. 6, 2265–2279. doi: 10.1039/c3ee40871j

Zhang, Z., Xu, H., Cui, Z., Hu, P., Chai, J., Du, H., et al. (2016). High energy density hybrid Mg^{2+}/Li^{+} battery with superior ultra-low temperature performance. *J. Mater. Chem. A* 4, 2277–2285. doi: 10.1039/C5TA09591C

Zheng, C., Chen, C., Chen, L., and Wei, M. (2017). A CMK-5-encapsulated $MoSe_2$ composite for rechargeable lithium-ion batteries with improved electrochemical performance. *J. Mater. Chem. A* 5, 19632–19638. doi: 10.1039/C7TA06286A

Zheng, Z., Zeng, X., Ye, H., Cao, F., and Wang, Z. (2018). Nitrogen and oxygen Co-doped graphitized carbon fibers with sodiophilic-rich sites guide uniform sodium nucleation for ultrahigh-capacity sodium-metal anodes. *ACS Appl. Mater. Interfaces* 10, 30417–30425. doi: 10.1021/acsami.8b10292

Conflict of Interest: The authors declare that the research was conducted in the absence of any commercial or financial relationships that could be construed as a potential conflict of interest.

frontiers in Chemistry

REVIEW
published: 19 June 2020
doi: 10.3389/fchem.2020.00451

Organic Electroactive Molecule-Based Electrolytes for Redox Flow Batteries: Status and Challenges of Molecular Design

Fangfang Zhong[1], *Minghui Yang*[1], *Mei Ding*[1,2]* *and Chuankun Jia*[1,2,3]

[1] College of Materials Science and Engineering, Changsha University of Science & Technology, Changsha, China, [2] National Engineering Laboratory of Highway Maintenance Technology, School of Traffic & Transportation Engineering, Changsha University of Science & Technology, Changsha, China, [3] Key Laboratory of Advanced Energy Materials Chemistry (Ministry of Education), Nankai University, Tianjin, China

This is a critical review of the advances in the molecular design of organic electroactive molecules, which are the key components for redox flow batteries (RFBs). As a large-scale energy storage system with great potential, the redox flow battery has been attracting increasing attention in the last few decades. The redox molecules, which bridge the interconversion between chemical energy and electric energy for RFBs, have generated wide interest in many fields such as energy storage, functional materials, and synthetic chemistry. The most widely used electroactive molecules are inorganic metal ions, most of which are scarce and expensive, hindering the broad deployment of RFBs. Thus, there is an urgent motivation to exploit novel cost-effective electroactive molecules for the commercialization of RFBs. RFBs based on organic electroactive molecules such as quinones and nitroxide radical derivatives have been studied and have been a hot topic of research due to their inherent merits in the last decade. However, few comprehensive summaries regarding the molecular design of organic electroactive molecules have been published. Herein, the latest progress and challenges of organic electroactive molecules in both non-aqueous and aqueous RFBs are reviewed, and future perspectives are put forward for further developments of RFBs as well as other electrochemical energy storage systems.

Keywords: organic electrolyte, molecular design, redox flow battery, energy storage, electrochemistry

Edited by:
Yuxin Tang,
University of Macau, China

Reviewed by:
Qian Xu,
Jiangsu University, China
Yi-Chun Lu,
The Chinese University of Hong Kong, China

***Correspondence:**
Mei Ding
dingmei@csust.edu.cn

Specialty section:
This article was submitted to Electrochemistry, a section of the journal Frontiers in Chemistry

Received: *03 March 2020*
Accepted: *30 April 2020*
Published: *19 June 2020*

Citation:
Zhong F, Yang M, Ding M and Jia C (2020) Organic Electroactive Molecule-Based Electrolytes for Redox Flow Batteries: Status and Challenges of Molecular Design. Front. Chem. 8:451. doi: 10.3389/fchem.2020.00451

INTRODUCTION

Energy Storage Systems

To decrease the use of fossil fuels and the emission of CO_2, which causes global warming, the development of renewable and clean energy has become an urgent issue in many research fields, particularly in energy source (Turner, 1999; Dunn et al., 2011; Soloveichik, 2015) and eco-environmental (Yang et al., 2011) studies. Solar and wind energy are environmentally friendly and are regarded as promising alternative energy resources for the future. However, inherent intermittency and instability limit the market penetration of these renewable resources (Holdren, 2007; Dunn et al., 2011; Yang et al., 2011). Energy storage technology, which is an effective solution for the intermittency, is crucial for the expansion of renewable energy (Armand and Tarascon, 2008; Dunn et al., 2011; Yang et al., 2011; Leadbetter and Swan, 2012; Ding et al., 2013; Zhang et al., 2019). So far, the most common approach for grid-scale energy storage is a pumped hydro-electric system, which exhibits noticeable geographic constraints. Consequently, exploiting new energy storage technology with high performance and flexible design has been one of the top topics of research in the past few decades. Electrochemical energy storage systems, also known as rechargeable batteries (secondary battery), which use redox-active molecules to fulfill the energy conversion, are well-developed (Ding et al., 2018; Luo et al., 2019) and offer highly efficient energy conversion and smart design feasibility. Examples are lead-acid batteries, lithium-ion batteries, supercapacitors, and redox flow batteries (RFBs) (Schon et al., 2016; Ding et al., 2018).

Due to its low capital cost and mature technological support, the lead-acid battery was employed for massive energy storage and dominated the electrochemical energy storage market in the twentieth century (Yang et al., 2011). However, the limited cycling lifetime, the high maintenance cost, and the severe contamination caused by lead contributed to it being replaced by other electrochemical approaches (Ma et al., 2015; Liu et al., 2018; Yang et al., 2018a). Nowadays, the most dominant electrochemical energy storage pathway is the lithium-ion battery in which lithium (Li^+) ions shuttle between the positive and negative electrodes (Xu et al., 2015; Chen et al., 2017). During the cycling process, Li^+ ions repeatedly take part in intercalation/de-intercalation at the two electrodes in a round-trip fashion. During the charging process, Li^+ ions de-intercalate from the positive electrode, migrate across the separator, and then intercalate into the negative electrode, accompanied by oxidation and reduction reactions at the positive and negative electrode, respectively. During discharging, the reverse processes occur (Wei et al., 2018). To tackle the challenges that the lithium-ion battery faces, researchers have done extensive, in-depth investigations into improvements in the electrodes, electrolytes, and separator materials. Prior work has pointed out the electrolyte can work in liquid, gel, and solid states (Li et al., 2015b, 2016b). Liquid electrolytes, which incorporate organic alkyl carbonate solvents, for instance, ethylene, dimethyl, diethyl, and ethyl methyl carbonate, with dissolved lithium salts like $LiBF_4$, $LiClO_4$, $LiPF_6$, $LiBC_4O_8$, and $Li[PF_3(C_2F_5)_3]$, are most widely used due to their good fluidity and ionic conductivity (Chen et al., 2013; Li et al., 2015c). Due to the advances such as high energy density and long cycling lifetime that have been achieved, lithium-ion batteries have exerted enormous, and dramatic effects on society (Li et al., 2015a,d; Chen et al., 2019; Yang et al., 2019). However, there are some tough issues, such as low abundance of materials, short discharge time, and the flammability of the solvents used in the battery, to be dealt with for industrial and residential implementation of lithium-ion batteries for large-scale energy storage (Yang et al., 2011; Li et al., 2016a). Inspired by the fact that the inherent electrochemical properties of sodium are close to those of lithium and its abundant distribution on the earth, sodium-ion batteries, as well as potassium-ion batteries, are attracting increasing amounts of interest in the last few decades, though these are still in their infancy in terms of application in large-scale energy storage (Chen et al., 2018; Rajagopalan et al., 2020a,b).

Supercapacitors, which have fast charge/discharge response, high power density, and excellent cycling performance, are also regarded as a promising energy storage avenue (Qin et al., 2019; Wu et al., 2019a). Based on energy storage mechanism, supercapacitors are grouped into electrical double-layer capacitors (EDLCs) and pseudocapacitors (faradaic capacitors). EDLCs, comprised of high specific surface area materials like activated carbon, carbon nanotubes, and graphene derivatives, adsorb ions at the electrode/electrolyte interface to achieve the energy storage. Pseudocapacitors, meanwhile, adopt transition metal oxides (such as RuO_2, MnO_2, NiO, and Co_3O_4) with high theoretical specific capacity and excellent redox reversibility as electrodes to realize energy storage via redox reactions at the electrodes (Wu et al., 2018b; Zeng et al., 2019). Low energy density, poor cyclability, and high cost due to the use of precious metals limit the application of supercapacitors for storing massive amounts of energy (Wu et al., 2018a, 2019b).

Given the deficiencies of the above-mentioned technologies, to broaden the market penetration of renewable resources for electricity generation, any novel electrochemical energy storage system that operates at grid-scale needs to address both technical and economic concerns. The RFB, invented in 1974 and exhibiting merits like design flexibility, safety, and scalability, is considered a very promising pathway toward practical large-scale energy storage (Leung et al., 2017). The most striking advantage of RFBs is the independent engineering of energy (number of moles of redox materials and cell voltage) and power (electrode area) owing to the unique cell configuration (Kamat et al., 2017; Park et al., 2017). It is noted that the chemical stability, electrochemical reversibility, and reduction potentials of redox materials contribute to the cell performance of RFBs, and the cost of redox materials is associated with the system capital cost. Undoubtedly, redox materials ranging from inorganic metal ions, halogens, and polysulfides to organic electroactive molecules play a crucial role in the improvement of RFBs. In this review, the research status and advances of organic electroactive molecules in both non-aqueous and aqueous RFBs are presented, as are the challenges and future perspectives in this promising field.

Redox Flow Batteries

The main components of RFBs include two electrolyte tanks (anodic and cathodic reservoirs), anodic-active and cathodic-active materials (anolyte and catholyte), an ion-exchange membrane, and the battery framework (**Figure 1**). Energy interconversion between chemical energy and electric energy is accomplished via the redox reaction of electroactive materials dissolved in supporting electrolyte, which circulates between the tanks and corresponding compartments of the electrochemical cell, driven by external pumps at the electrodes. Selective ions migrate across the ion-exchange membrane to complete the current circulation. According to the dissolving condition of electrolytes, RFBs can be divided into aqueous RFBs and non-aqueous (organic) RFBs.

The state-of-the-art RFB systems employ all-vanadium ions as electroactive materials, and the largest (200 MW/800 MWh)

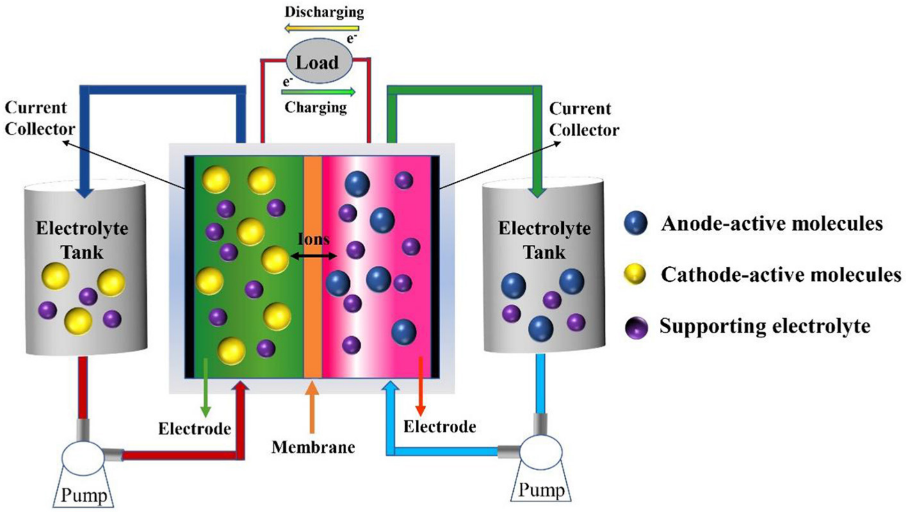

FIGURE 1 | Schematic illustration of a typical redox flow battery.

is under construction by Rongke Co. Ltd. Low energy density, the need for strong sulfuric acid as the supporting electrolyte, a spatially inhomogeneous distribution, and the volatile price of vanadium constrain the widespread deployment of all-vanadium RFBs. As alternative approaches, RFBs with electroactive materials based on other inorganic redox ions, such as $Fe^{0/2+/3+}$, $Cr^{2+/3+}$, $Zn^{0/2+}$, Br_2/Br^-, I_2/I_3^-, and S_x^{2-} (Park et al., 2017; Ding et al., 2018; Luo et al., 2019) have been proposed and investigated. Along with advances in electrodes and the ion-exchange membrane, improvements in RFB cell performance have also been achieved to some extent (Ye et al., 2018, 2019a,b, 2020; Chang et al., 2019; Lou et al., 2019; Xia et al., 2019). However, these systems are still facing technological challenges, such as the high viscosity of a strong sulfuric acid supporting electrolyte, dendritic deposition of zinc, the strong corrosivity of halogen, high cost, and so on, hindering practical application. Organic redox molecules, which have been known of for a long time, have attracted increasing interest in the field of synthetic chemistry, catalysts, functional materials, and industrial applications. Given their inherent redox nature, the low cost of raw starting materials, and the flexibility of their chemical and physical properties (solubility, stability, redox potential, et al.) when tailored by substituents, organic redox molecules, such as anthraquinone derivatives, nitroxide radicals, and polymers, have been adopted for energy storage materials to construct high cell performance and cost-effective RFB systems in the past decade. Depending on the supporting electrolytes, RFBs with organic electroactive materials can be simply classified as aqueous and non-aqueous systems, respectively.

Design Principles of Organic Electroactive Molecules

Physicochemical and Electrochemical Properties

It is worth noting that the energy density of RFBs is dependent on the number of electrons involved in the electrode reaction, the concentration of electroactive molecules in the electrolytes, and the potential difference between the cathodic and anodic active molecules.

The solubility limit, corresponding to the highest concentration of organic electroactive molecules possible, which varies with solvent, needs to be as high as possible. As pointed out in prior work, the physical properties of the solvent, such as the pH value, viscosity, polarity, and dielectric constant, have huge impacts on the solubility limit (Ding et al., 2018; Luo et al., 2019). Moreover, the supporting electrolyte in the same solvent changes the solubility of the redox molecule as well as the internal resistance of a cell. The organic electroactive molecule, solvent, and supporting electrolyte should be taken into account together to develop an RFB with high energy efficiency and coulombic efficiency. Given a large variety of solvents consisting of aqueous and non-aqueous solvents, a higher solubility limit for organic electroactive molecules can be achieved than for inorganic redox materials. In other words, under the same solvent and supporting electrolyte conditions, taking advantage of flexible modification by substituents of organic molecules, the concentration can be increased as envisioned. Based on the rule that likes dissolve each other, molecules with higher relative permittivity in solvents can increase the solubility as well as the stability. Thus, in aqueous RFBs, water-soluble ionic or polar substituents such as the quaternary ammonium, sulfonic, carboxyl, and hydroxy groups can be employed to increase the concentration of organic electroactive molecules. As for the organic electroactive molecules in non-aqueous RFBs, fat-soluble substituents such as alkyl, carbonyl, and ester groups can be helpful to increase the solubility limitation. The desirable values of solubility of redox species in aqueous solvents are around 1–2 M, while in non-aqueous electrolytes 4–5 M is required to satisfy the demand for cost-effective energy storage (Darling et al., 2014).

The formal cell voltage of an RFB is obtained by the difference in reduction potential between the cathodic and anodic active molecules. As reported in previous work, the reduction potential of organic electroactive molecules can be shifted more to the positive or negative side by the electrostatic properties and positions of functional groups on the backbone (Burgess et al., 2018). The cell voltage of aqueous RFBs is constrained by the electrolysis of water, with a potential window limit of 1.24 V. Freedom from problems caused by water electrolysis enables non-aqueous RFBs to reach high cell voltages, which compensates for the higher concentration requirement in view of economic viability. Commonly, within the potential window of the solvent, a higher cell voltage can be designed and obtained with a non-aqueous organic RFB than with an aqueous organic RFB. Moreover, the lifetime duration is another important indicator parameter for the performance of an RFB. The chemical and electrochemical stability of organic redox species both play a crucial role in the cycling lifetime. The proposed decomposition mechanisms of organic electroactive materials used in RFBs have been summarized in the latest review (Kwabi et al., 2020), namely nucleophilic addition and hydrolysis, disproportionation, dimerization, and tautomerization. Hence, according to the inherent nature of organic molecules, by rational substituent design to prevent the redox core from degradation, more stable electroactive materials and longer cycling time can be realized.

Chemical Cost

One prerequisite for the commercialization of RFBs is low cost. Note that the grid-scale application of the well-known all-vanadium RFB is hindered by the low earth-abundance and volatile price of vanadium. Because they utilize organic molecules consisting of high earth-abundance elements such as carbon, hydrogen, oxygen, nitrogen, the capital cost of most RFBs with organic electroactive materials can drastically drop to the expected value for practical applications. Despite this, some special organic electroactive materials such as radicals still cost much more than common inorganic electroactive species. By screening the reported RFBs with organic redox couples, it has been found that synthesis of organic materials must be performed under an inert atmosphere or even in an argon or nitrogen-purged glovebox to avoid side reactions with oxygen from the ambient atmosphere. The use of such harsh synthesis conditions, along with the requirement of catalysts comprised of noble metals, is not a cost-effective strategy. According to the target of $ 150/kWh for industrial application of RFB systems by the year of 2023 set up by the Department of Energy of the United States, cost estimates for electroactive materials of under a standard of \$5/kg are desired (Darling et al., 2014). The development of robust organic electroactive molecules that can be derived from cheap, commercially available raw materials with easy-to-handle synthetic steps must be targeted to enable low-cost RFB systems.

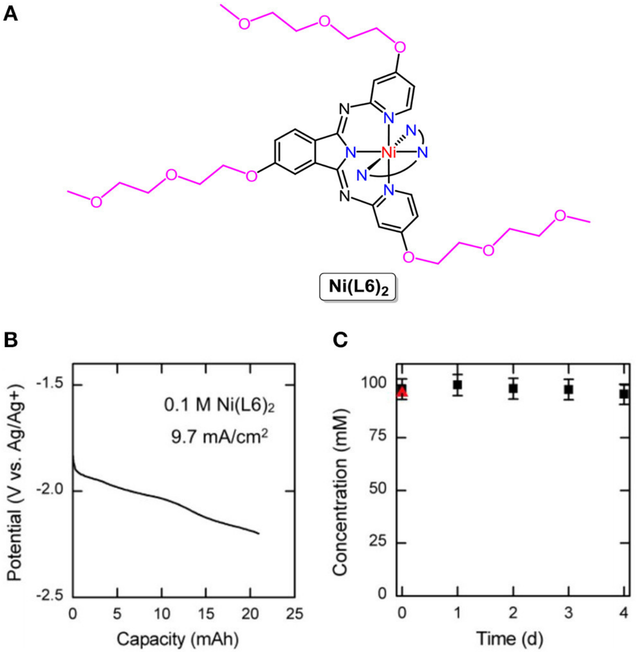

FIGURE 2 | (A) Molecular structure of **Ni(L6)$_2$**. **(B)** Charging potential curve for a 2e reduction of a 100 mM solution of **Ni(L6)$_2$**. **(C)** Concentration of the charged **Ni(L6)$_2$** as a function of time. The red triangle represents the concentration of the neutral solution before cycling. Reproduced with permission from Sevov et al. (2016). Copyright 2016, American Chemical Society.

Non-Aqueous Organic RFBs

Non-aqueous organic RFBs employ organic electroactive molecules and supporting electrolytes in organic solvents, such as butyrolactone, acetonitrile (ACN), dimethylacetamide (DMA), and propylene carbonate (PC). The first non-aqueous organic RFB was reported by Matsuda and co-workers in 1988, in which a ruthenium complex $[Ru(bpy)_3](BF_4)_2$ (bpy = 2,2′-bipyridine) served as the energy storage material in acetonitrile solution with an open-circuit voltage of 2.60 V (Matsuda et al., 1988). Since conventional aqueous RFBs have a limit of the cell voltage window of 1.24 V, more and more research interest is shining a light on non-aqueous systems to pursue higher voltage output from RFBs. Moreover, non-aqueous organic RFBs exhibit other advantages, such as higher energy density, wider operating temperature range, faster reaction kinetics, and more combinations of organic redox couples. Organic electroactive molecules employed in non-aqueous organic RFBs can be classified into four groups, namely: coordination compounds and organometallic complexes, quinones, radicals, and polymers (Ding et al., 2018; Luo et al., 2019).

Coordination Compounds and Organometallic Complexes

Coordination complexes, consisting of metal ions ligated with ligands, are the earliest-studied organic electroactive molecules in non-aqueous RFBs. $[Ru(bpy)_3](BF_4)_2$, $Ru(acac)_3$ (acac = acetylacetonate) (Chakrabarti et al., 2007), $Cr(acac)_3$ (Liu et al., 2010), $[Ni(bpy)_3]^{0/2+}$, $[Fe(bpy)_3]^{2+/3+}$ (Kim et al., 2011), $Mn(acac)_3$ (Sleightholme et al., 2011), $VO(acac)_2$ (Herr et al., 2013), $[V(mnt)_3]^{2-}$ (mnt = $(NC)_2C_2S_2^{2-}$) (Cappillino et al., 2014), $[Fe(phen)_3]^{2+/3+}$, $[Co(phen)_3]^{2+/3+}$ (phen = phenanthroline) (Xing et al., 2015), and $V(acac)_3$ (Bamgbopa and Almheiri, 2017) were successively utilized to store energy in non-aqueous RFBs. Although the resulting RFBs exhibit high open-circuit voltages (1.2–3.4 V), the energy density is severely limited by the solubility of coordination complexes in organic solvents, which are mostly <1 M. By rational substituent design, the Sanford group designed and synthesized a series of coordination complexes combining earth-abundant metals with tridentate bipyridyliminoisoindoline (BPI) ligands, revealing improved physicochemical properties and cell performance. The solubility of the nickel complex abbreviated as **$Ni(L6)_2$** (molecular structure is shown in **Figure 2A**) was more than 0.7 M in acetonitrile (ACN), higher than that of other nickel complexes under the same conditions. Furthermore, the charged **$Ni(L6)_2$** remained stable and soluble in ACN with 0.5 M $TBABF_4$ as the supporting electrolyte for days at a high concentration (0.1 M, **Figure 2C**). The nickel-BPI complexes could undergo over 200 charge-discharge cycles with a 5% capacity fade. It is worth noting that more than one electron was involved in the redox reactions of **$Ni(L6)_2$** at low redox potentials (**Figure 2B**), suggesting an effective way to lower the molecular weight per mole of electrons transferred and higher energy density (Sevov et al., 2016).

Ferrocene, recognized as the progenitor of organometallic chemistry, has given rise to an enormous number of ferrocene-containing ligands, molecules, and materials since its discovery in 1951 (Kealy and Pauson, 1951; Butler and Thomas, 2007; Štěpnička, 2008; Dai and Hou, 2010; Phillips, 2011; Ding et al., 2019). Synthetic flexibility, well-defined redox properties, and fast reaction kinetics make them very promising for RFBs. However, the solubility of pristine ferrocene in propylene carbonate (PC, a commonly used solvent in non-aqueous RFBs) is only 0.2 M. To address this issue, Wang and co-workers attached the Cp ring (the cyclopentene moiety of ferrocene) to different ionic charged tetraalkylammonium groups to yield a series of ferrocene derivatives. By screening the solubilities of the resulting derivatives, it was concluded that tetraalkylammonium groups could improve the solubility compared to ferrocene without any substituent. However, to some extent, the stability of ferrocene derivatives was sacrificed. For example, when PF_6^- and BF_4^- anions serve as counterions, the corresponding derivatives with enhanced solubility show poor chemical stability, which hinders further application in RFB systems (Cosimbescu et al., 2015; Wei et al., 2015). Other effective strategies like using electron withdrawing groups such as an acetyl substituent to improve the solubility of ferrocene by breaking the symmetrical electron cloud distribution of ferrocene (Kim et al., 2016) may simultaneously maintain good stability.

Although advances have been made, non-aqueous RFBs with coordination compounds and organometallic complexes still face technical and economic challenges before practical application. Concern about the utilization of precious metal catalysts in the materials synthesis process, increasing the chemical costs of RFBs, motivates efforts on investigating RFBs with metal-free organic electroactive materials.

Quinones

Quinones are aromatic molecules with fully conjugated cyclic diketone structures and are considered the most promising electroactive molecules of the natural organic materials (Scott et al., 1998; Park et al., 2015; Jing et al., 2017). The electronegative oxygen atom draws electron density away from the carbon atom through the double bond in the carbonyl group, increasing the polarity and reactivity of the carbonyl compound. The carbonyl functional group, which acts as a redox center, and the aromatic structure, which affects the reduction potential position and stability, in combination with fast reaction kinetics, an easily modified backbone, and cost-effective synthesis processes (Häupler et al., 2015) make quinones promising candidates for RFBs (Quan et al., 2007; Huskinson et al., 2014; Er et al., 2015; Lin et al., 2015).

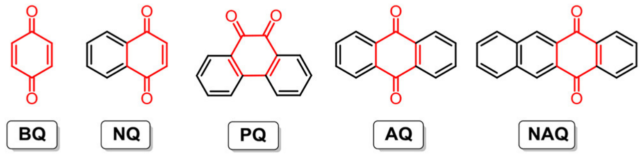

FIGURE 3 | Molecular structures of quinone derivatives in non-aqueous RFBs.

It is thought that the physicochemical and electrochemical properties of quinones and the cell performance of RFBs are strongly dependent on the molecular aromaticity and electronic structures. To reveal the structure-performance correlation, the Yu group studied five quinones with regular structural variations, namely 1,4-benzoquinone (**BQ**), 1,4-naphthoquinone (**NQ**), 9,10-phenanthrenequinone (**PQ**), anthraquinone (**AQ**), and 5,12-naphthacenequinone (**NAQ**) (molecular structures are shown in **Figure 3**). Their experimental and computational results indicated that with the increase in aromaticity (densities of arenes) from **BQ** to **NAQ**, both the solubility and redox potential of the quinone derivatives decreased. Cell performance tests of non-aqueous RFBs with the above-mentioned quinone and derivatives show that the **NQ**-based battery reached a relatively high energy density of 60 Wh L^{-1}, with nearly 100% capacity retention after 100 cycles, which can be further improved by enhancing carbonyl utilization with structural modification (Ding et al., 2016).

Radicals

Radicals containing one or more unpaired or open-shell electrons show redox activity, enabling energy storage and conversion. However, poor stability ascribed to the formation of dimers and polymers and reactions with other molecules (Nishide et al., 2004) have become a barrier to the use of radicals in RFBs. By employing steric hindrance, resonance effects, and a stabilizer, the stability of radicals is enhanced, and the application territory is broadened. At present, radicals used for RFBs can be grouped into the following three types according to molecular construction: nitroxide radicals, alkoxybenzene-based radicals, and heterocyclic-based radicals. Among them, nitroxide radicals, as exemplified by 2,2,6,6-tetramethyl-1-piperidinyloxy (**TEMPO**; the structure is shown in **Figure 4**), have been widely investigated. TEMPO is a commercially available organic radical that is stabilized by the steric hindrance of four methyl groups, as well as the resonance effect between the unpaired electron and the N–O bond (hyperconjugation). With good redox reversibility and outstanding solubility in organic solvent (5.2 M in EC/PC/EMC mixture solvents), TEMPO and its derivatives have attracted increasing attention for application in RFBs (Li et al., 2011; Wei et al., 2014; Milshtein et al., 2016).

In 2011, Li et al. reported a novel all-organic redox flow battery with **TEMPO** as the positive electroactive material and 1.00 M $NaClO_4$/acetonitrile as the supporting electrolyte. Stable charge-discharge curves and high coulombic efficiency (90%) were achieved in the **TEMPO**-based non-aqueous RFB (Li et al., 2011). In 2014, the Wang group prepared a high concentration solution of **TEMPO** in mixed organic solvents by the addition of excess $LiPF_6$ as the supporting charge carriers. The redox potential of this **TEMPO**-based electrolyte reached 3.5 V vs. Li/Li^+, and an RFB constructed by pairing up the **TEMPO** redox couple with the lithium redox pair output an energy density of 126 Wh L^{-1}, which is approximately five times that of the all-vanadium RFBs and much higher than the majority of non-aqueous RFBs (Wei et al., 2014). It is well known that the electrochemical properties of organic molecules can be easily modified by substituents. Milshtein et al. synthesized and studied 4-acetamido-2,2,6,6-tetramethylpiperidine-1-oxyl (**AcNH-TEMPO**; the chemical structure is shown in **Figure 4**) to reveal the effects of an electron withdrawing functional group on the radical. The results show that **AcNH-TEMPO** exhibits a more positive reversible one-electron redox reaction at 3.63 V vs. Li/Li^+. However, the low solubility (0.5 M in 1 M $LiBF_4$/PC) of **AcNH-TEMPO** constrains the cell performance of RFBs (Milshtein et al., 2016). Inspired by this challenge, Takechi et al. employed "supercooled liquid" to improve the solubility of TEMPO derivatives, as exemplified by 4-methoxy-2,2,6,6-tetramethylpiperidine-1-oxyl (**MeO-TEMPO**; the chemical structure is shown in **Figure 4**). **MeO-TEMPO** was mixed with LiTFSI (lithium bis-trifluoromethanesulfonimide) at a molar ratio of 1:1, leading to the formation of a new ionic couple and "supercooled liquid." It is worth noting that by replacing the acetamido group with a methoxy group, the resulting **TEMPO** derivative shows a comparable redox potential (3.6 V vs. Li/Li^+) with **AcNH-TEMPO**, whereas the solubility could reach a much higher value of 2.5 M in LiTFSI/ACN solution (Takechi et al., 2015). Another limit of RFBs with radical redox materials is their high capacity loss rate, which can be conquered due to the merits of the smart design nature of organic molecules. However, the high price of TEMPO and derivatives is an obstacle to the wide deployment of **TEMPO**-based RFBs.

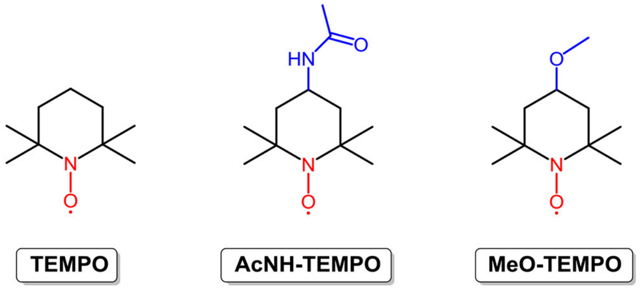

FIGURE 4 | Molecular structures of **TEMPO** derivatives.

Polymers

One common critical issue in improving the cell performance of RFBs with electrochemical small molecules is the permeability of redox species across the ion-exchange membrane, known as crossover contamination, which leads to Coulombic efficiency fade (Lai et al., 2020). It was believed that larger-sized macromolecules would have difficulty migrating through the membrane, and so electroactive polymers were employed as redox centers in RFBs (Nagarjuna et al., 2014; Burgess et al., 2016, 2018; Iyer et al., 2017). The Rodríguez-Lopez group conducted a study on size-based selective transport across commercial off-the-shelf separators for non-aqueous RFBs by preparing a series of viologen-based redox-active polymers (**RAPs 1-5**; the chemical structures are shown in **Figure 5A**) with different molecular weights. The severe crossover behavior of a monomer with a small molecular size through the separator could be largely suppressed by the formation of polymers (**Figure 5B**). It is also noted that polymer **RAPs 1-5** exhibit similar permeabilities as well as solubility, viscosity, and electrochemical properties, with negligible influence from molecular weight. For **RAPs 1-5**, good solubility (above 2.0 M in ACN and PC), electrochemical and chemical reversibility, and limited crossover contamination across porous separators make them promising energy storage materials for non-aqueous RFBs (Nagarjuna et al., 2014).

To evaluate the cell performance, the Rodríguez-Lopez group assembled RFBs employing viologen monomer or polymer and ferrocene as redox couples with inexpensive nano-porous separators and 0.1 M $LiBF_4$ supporting electrolyte in acetonitrile. The results show that an RFB with polymer-based electroactive materials could achieve a high coulombic efficiency of 98% and a capacity efficiency of 80% (50 cycles). The high viscosity of polymer-containing solution slows down the mass transport of redox species and decreases the ionic conductivity of electrolyte, hindering further advances in the cell performance of RFBs. Seeking more redox polymers with improved physicochemical and electrochemical properties as well as high-performance for RFBs is an urgent tack in view of molecule design (Burgess et al., 2016; Montoto et al., 2017, 2018).

Even though much research work has been put forward, few non-aqueous RFBs have been commercialized due to their higher chemical cost, poorer cycle stability in high concentrations, and smaller ionic conductivity compared with aqueous RFBs. For non-aqueous RFBs, the ionic conductivity can be efficiently improved by increasing the concentration of organic electrolytes, which endows the non-aqueous RFBs with a higher energy density comparable to that of aqueous RFBs. However, the high concentration leads to complex side reactions in the redox cell, which lead to capacity decay after several to dozens of cycles. Bipolar molecules, which are realized by adding specific functional groups according to the environment of the redox cell and that have high solubility and enhanced chemical stability, can be employed to solve this problem. Despite their shortcomings in

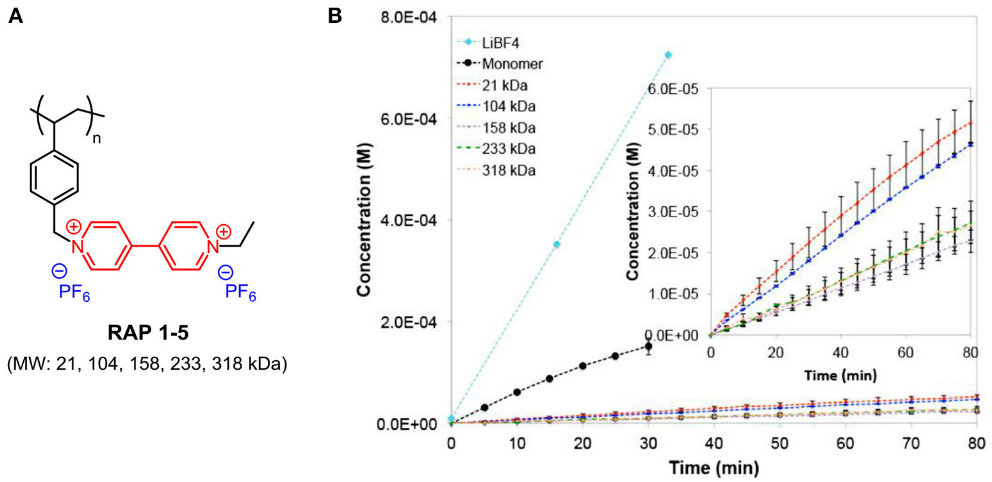

FIGURE 5 | (A) Molecular structure of **RAPs 1-5**. **(B)** Time-dependent transport of $LiBF_4$, monomer and **RAPs 1–5** across Celgard 2325 at 0.01 M. Inset shows the **RAPs 1–5** region of the plot. Reproduced with permission from Nagarjuna et al. (2014). Copyright 2014, American Chemical Society.

terms of processing, the significantly wider potential windows, extensive options for both anode and cathode-active molecules, abundance of organic solvents, high operating temperature, and faster reaction kinetics all indicate the great potential of non-aqueous RFBs for electrochemical storage in the future.

AQUEOUS RFBs

Organic solvents used in non-aqueous systems are known to have disadvantages such as volatility, toxicity, corrosiveness, and flammability. When targeting residential and industrial implementation, environmentally benign aqueous RFBs are more promising. Aqueous RFBs, featuring redox species dissolved in water with supporting electrolyte, exhibit many advantages, such as high ionic conductivity, safety, cost-effectiveness, and well-developed technology to compensate for the narrow voltage window, which is limited by the electrolysis of water. Aqueous RFBs have been a hotspot in research on electrochemical energy storage in past decades. According to the pH value of electrolytes, aqueous RFBs can be grouped into three classes, namely acidic, alkaline, and neutral aqueous RFBs.

Organic Electroactive Molecules for Acidic Aqueous RFBs

The proton, which has the smallest size (1.6×10^{-15} m) among cations, shows an amazingly high limiting molar conductivity of $349.8 \times 10^4\ \Omega^{-1}\ m^2\ mol^{-1}$ at 298 K and promises acidic aqueous RFBs with rapid charge/discharge rates and high energy efficiencies and power densities. Since the first acidic RFBs with organic electroactive molecules were reported by Huskinson et al. (2014), this approach has been attracting increasing attention (Xu et al., 2010; Lin et al., 2015; Carney et al., 2017; Li et al., 2017; Goulet and Aziz, 2018; Luo et al., 2019).

Given merits like good redox reversibility, fast electron-transfer kinetics, longtime stability, and cost-effective raw materials, quinones and their derivatives are widely employed in both non-aqueous RFBs, as stated above, and aqueous RFBs. In 2014, the Aziz group constructed a new aqueous RFB with 9,10-anthraquinone-2,7-disulphonic acid (**AQDS**; the chemical structure is shown in **Figure 6**) as the anolyte. Thanks to the hydrophilic effect of sulfonic groups, **AQDS** shows an aqueous solubility of up to 1 M in sulphuric acid, and the resultant RFB exhibits above 99% storage capacity retention per cycle and a high energy density of 50 W h L^{-1} (Huskinson et al., 2014; Lin et al., 2016). However, in this RFB system, both the concentrated sulphuric acid serving as the supporting electrolyte and the Br^-/Br_2 employed as a negative electrolyte are strong corrosives, engendering extra hardware cost and maintenance fees. Besides, the low open-circuit voltage of only 0.7 V of the **AQDS**-based RFB blocks further improvements in cell performance.

Taking advantage of sulfonic groups for enhancement of the solubility of AQDS through hydrophilic effects, more substituents were introduced to study the variations in electrochemical properties. 1,8-dihydroxy-9,10-anthraquinone-2,7-disulphonic acid (**DHAQDS**; the chemical structure is shown in **Figure 6**) was synthesized using hydroxyl substituents. The open-circuit voltage of the **DHAQDS**-based RFB was shifted to a higher value of 1.2 V, attributed to the electron-donating effect of hydroxyl groups. Moreover, a series of anthraquinone derivatives (the chemical structures are shown in **Figure 6**) such as 9,10-anthraquinone-2-sulfonic acid (**AQS**), 1,4-dihydroxy-9,10-anthraquinone-2,3-dimethylsulfonic acid (**DHAQDMS**), and Alizarin Red S (**ARS**) were synthesized and characterized electrochemically to reveal the influences of the amounts and positions of substituents. As mentioned above, smart design and modifications of organic electroactive molecules is an effective approach to obtain high-performance RFBs aimed at large-scale energy storage (Gerhardt et al., 2017).

Organic Electroactive Molecules for Alkaline Aqueous RFBs

To address concerns arising for acidic aqueous RFBs, organic electroactive molecules dissolved in alkaline supporting electrolyte were investigated as a promising alternative for storing massive energy. In 2015, the Aziz group demonstrated highly soluble quinone-based flow batteries in aqueous potassium hydroxide solutions. At the initial stage, commercially available 2,6-dihydroxyanthraquinone (**2,6-DHAQ**; the chemical structure is shown in **Figure 7A**) was used as one of the redox couples in alkaline aqueous RFBs. The open-circuit voltage of the **2,6-DHAQ**-based RFB reached 1.2 V (**Figure 7B**), and the capacity loss decreased to only 0.1% per cycle via the replacement of bromine with non-toxic ferricyanide as positive electrolyte (Lin et al., 2015). However, the energy output of the proposed RFB was limited by the poor solubility of highly stabilized **2,6-DHAQ**. To address this issue, a substituent with highly alkali-soluble carboxylate terminal groups was utilized to increase the solubility in alkaline electrolyte. The resulting compound, 4,4'-((9,10-anthraquinone-2,6-diyl)dioxy)dibutyrate (**2,6-DBEAQ**; the chemical structure is shown in **Figure 7A**), was six times more soluble than **2,6-DHAQ** at pH 12. At a pH value of as low as 12, an RFB assembled with **2,6-DBEAQ** as negative electrolyte exhibited a high open-circuit voltage of 1.05 V and a theoretical volumetric energy density of ca. 17 Wh L^{-1}. Moreover, the symmetric cell with **2,6-DBEAQ** as both negative and positive electrolytes revealed a very low capacity fade rate (<0.01%/day and <0.001%/cycle, **Figure 7C**) (Kwabi et al., 2018).

Given above-stated advantages of anthraquinones, the use of benzoquinone and derivatives as analogs of anthraquinone is anticipated to be more promising in RFBs for large-scale energy storage, as they are inexpensive and a high theoretical energy density of 400 W h L^{-1} can be achieved from a redox reaction involving two electrons. However, it is reported that most benzoquinone-based acidic aqueous RFBs show low open-circuit voltage (<0.4 V) and poor cycling stability (Yang et al., 2014, 2016; Hoober-Burkhardt et al., 2017). To improve cell performance, benzoquinone derivatives were employed in alkaline aqueous RFBs, and advances were obtained. For example, an RFB working with 2,5-dihydroxy-1,4-benzoquinone as negative electrolyte showed an output voltage of 1.21 V, a peak galvanic power density of 300 mW cm^{-2}, and a coulombic efficiency exceeding 99%, indicating that this would be a very promising direction for developing high-performance RFBs for practical applications (Yang et al., 2018b).

Besides the quinones, there are other organic electroactive molecules that have impressive performances in alkaline aqueous RFBs, such as alloxazine (Lin et al., 2016; Orita et al., 2016) and phenazine derivatives (Hollas et al., 2018). In 2016, Roy G. Gordon and co-workers reported a highly alkaline-soluble alloxazine-based organic electrolyte that enabled an aqueous RFB to exhibit an open-circuit voltage approaching 1.2 V with high current efficiency (99.7%) and capacity retention (99.98%) per cycle (Lin et al., 2016). The carboxylic group was introduced into the alloxazine derivative to increase the solubility in alkaline solutions, and the resulting alloxazine 7/8-carboxylic acid exhibited sufficiently high electrochemical and chemical stability, which opens up a new direction for designing organic electrolytes in aqueous RFBs. Later, Ying Shirley Meng and co-workers reported a biomimetic redox flow battery based on isoalloxazine, in which phosphate and hydroxy groups were used to enhance both the stabilization and solubility in alkaline solution. The isoalloxazine-based alkaline aqueous RFBs shows good cycling performance, with over 99% capacity retention over 100 cycles (Orita et al., 2016). With good redox properties and easily derivable structures, phenazine derivatives are promising organic anolytes for alkaline aqueous RFBs. In 2018, Wei Wang and co-workers reported a high-capacity alkaline aqueous RFB with phenazine-based organic electrolyte. Exceptionally high reversible anolyte capacity (67 Ah L^{-1}) and capacity retention (99.98% per cycle over 500 cycles) have been achieved (Hollas et al., 2018). The pristine phenazine can hardly dissolve at all in aqueous solutions, but the solubility was increased to as much as 1.8 M by strategic modification with the hydroxy and sulfonic groups. Thus, tailoring functional groups is an effective strategy to improve both the solubility and stability of organic heterocyclic molecules, which usually show poor solubilities in aqueous solutions.

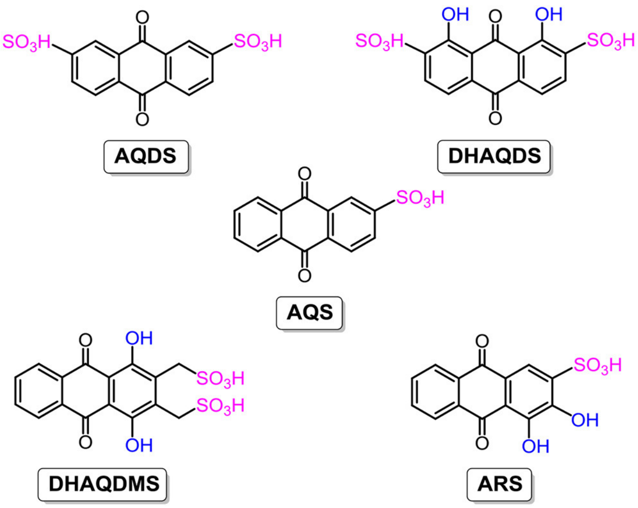

FIGURE 6 | Molecular structures of anthraquinone derivatives for acidic aqueous RFBs.

Organic Electroactive Molecules for Neutral Aqueous RFBs

Improvements in the cell performance of aqueous RFBs haven been achieved through continuous efforts and have paved the way for practical application. However, RFBs systems employing strong acid and base have striking disadvantages, such as corrosivity, high maintenance cost, and environmental pollution hazard. Given the inherent merits such as being non-corrosive, non-flammable, environmentally benign and cheap, neutral aqueous supporting electrolytes (e.g., NaCl solution) in RFBs can effectively eliminate side reactions such as hydrogen evolution

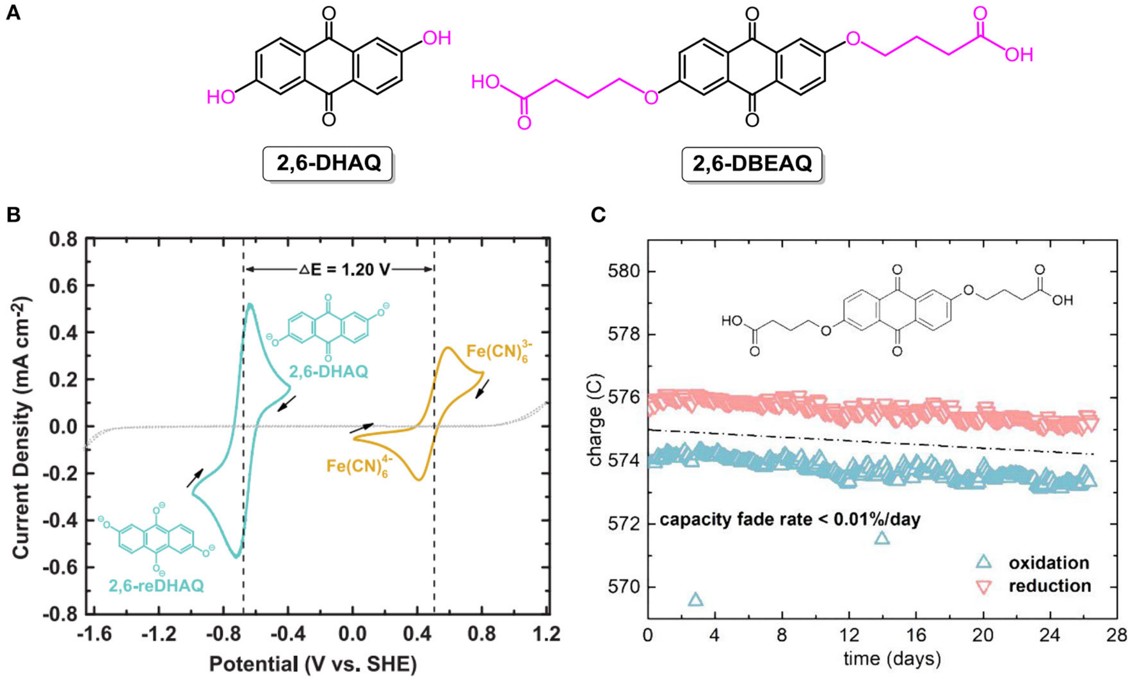

FIGURE 7 | (A) Molecular structures of **2,6-DHAQ** and **2,6-DBEAQ**. **(B)** Cyclic voltammogram of 2 mM **2,6-DHAQ** (dark cyan curve) and ferrocyanide (gold curve) scanned at 100 mV/s on glassy carbon electrode; arrows indicate scan direction. Dotted line represents CV of 1 M KOH background scanned at 100 mV/s on graphite foil electrode. Reproduced with permission from ref. 76. Copyright 2015, American Association for the Advancement of Science. **(C)** Unbalanced compositionally symmetric cell cycling of 2,6-DBEAQ. Reproduced with permission from Kwabi et al. (2018). Copyright 2018, Elsevier.

(common in acids), oxygen evolution (common in alkaline solutions), and other degradation of electroactive molecules catalyzed by acid and base (Beh et al., 2017; DeBruler et al., 2017; Ding and Yu, 2017; Hu et al., 2017).

In 2015, the Schubert group reported an affordable, safe, and scalable neutral pH aqueous battery system with organic polymers as the electroactive materials. The TEMPO radical (**P1**; the chemical structure is shown in **Figure 8A**) and viologen derivative (**P2**; the chemical structure is shown in **Figure 8A**) were used as the cathode-active and anode-active molecules, respectively. Note that ammonium cation pendant groups were introduced to modify the backbones of both **P1** and **P2** to enhance their solubility in aqueous NaCl supporting solution. Compared to non-aqueous supporting electrolytes, the aqueous NaCl solution exhibits higher conductivity, lower cost, and great environmentally friendliness. Given the large molecular sizes of polymers, as stated above, the hydrodynamic radii of **P1** and **P2** are ∼2 nm, larger than the pore sizes of the dialysis membrane (around 1 nm), and the permeability constants of the electroactive materials are remarkedly decreased. The cycling stability of the RFB supports the assumption that hardly any change occurred in the concentration of **P1** in the deficient compartment through migration through the membrane from the enriched side over 10,000 charging/discharging cycles, and this fits well with the undiminished coulombic efficiency (ca. 99%, **Figure 8B**) (Janoschka et al., 2015). Furthermore, the proposed RFB outputs an energy density of 10 W L^{-1} and maintains good performance at a current density reaching more than 100 mA cm^2.

In combination with the flexible design of organic molecules, hydrophilic substituents like hydroxy groups were employed to modify the backbone of **TEMPO.** The resulting solubility of 4-hydroxy-tetramethylpiperidin-1-oxyl in water reaches a value as high as 2.1 M or more. By matching the TEMPO derivative with methyl viologen, a neutral aqueous RFB has been constructed and shows an exceptionally high cell voltage of 1.25 V, a high working current density of 100 mA cm^{-2}, and nearly 100% coulombic efficiency within 100 cycles (Liu et al., 2016).

Note that ferrocene and derivatives have been adopted for energy storage in non-aqueous RFBs due to their poor solubility in water. Inspired by molecular synthesis approaches, the utilization of substituents with hydrophilic groups can effectively address the solubility concern. Liu and co-workers designed and synthesized two ferrocene derivatives (the chemical structures shown are in **Figure 9A**), namely ferrocenylmethyl trimethyl ammonium chloride (**FcNCl**) and N^1-ferrocenylmethyl- N^1, N^1, N^2, N^2, N^2-pentamethylpropane-1,2-diaminium dibromide (**FcN$_2$Br$_2$**). Under the hydrophilic effect of the tetraammonium moiety and halide counter ion, the solubilities of **FcNCl** and **FcN$_2$Br$_2$** were increased to 4.0 and 3.1 M in water, respectively (Hu et al., 2017).

This strategy was also verified by reported work of the Aziz group, in which the solubility limit of bis((3-trimethylammonio)propyl)-ferrocene dichloride was enhanced

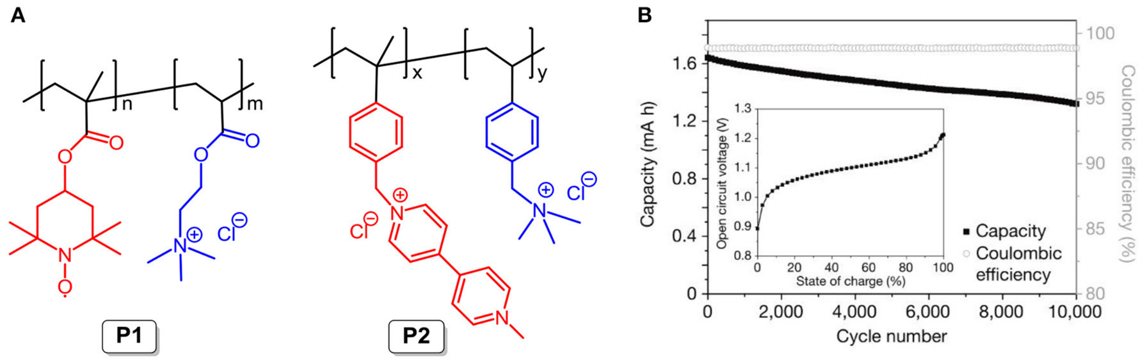

FIGURE 8 | (A) Molecular structures of **P1** and **P2**. **(B)** The long-term stability of the polymer-based electrolytes was studied by repeated charge/discharge cycling over 10,000 cycles at 20 mA cm^{-2} in an unpumped test cell (inset) the open-circuit voltage of a polymer-based RFB as a function of the state of charge. Reproduced with permission from Janoschka et al. (2015). Copyright 2015, Springer Nature.

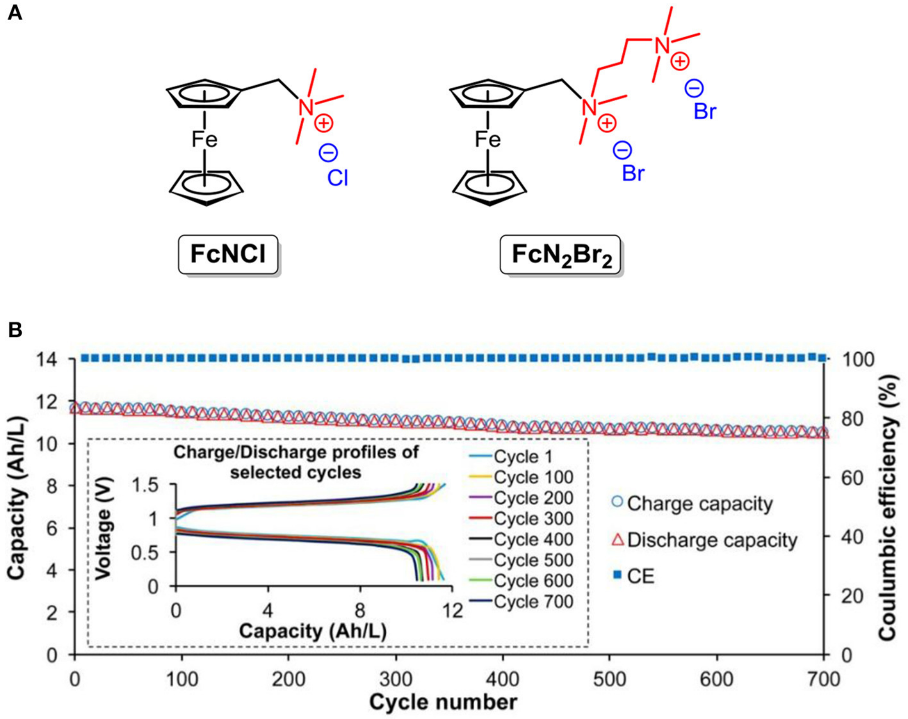

FIGURE 9 | (A) Molecular structures of **FcNCl** and **FcN_2Br_2**. **(B)** Extended 700 cycle testing data of the 0.5 M **FcNCl/MV** aqueous RFB at 60 mA/cm^2: capacity and coulombic efficiency vs. cycling numbers (for clarity, data points with an increment of 10 cycles were used for plotting) (inset) representative charge and discharge profiles of selected cycles. Reproduced with permission from Hu et al. (2017). Copyright 2017, American Chemical Society.

to nearly 2 M (Beh et al., 2017). With high concentration and good redox reversibility, the **FcNCl**-based neutral aqueous RFB exhibits a power density of 125 mW cm^{-2} and 99.99% capacity retention per cycle (the structures are shown in **Figure 9B**) throughout a 700-cycle tests (Hu et al., 2017).

PERSPECTIVES

The RFB has been recognized as the most promising electrochemical technology for large-scale energy storage, as such batteries can have the advantages of low cost, vast molecular diversity, highly tailorable properties, and high safety. However, some technical and economic challenges are still in urgent need of being issued before the widespread deployment of RFB systems at grid scale. Energy conversion between chemical energy and electric energy is achieved by redox reactions of electroactive materials at electrodes. The solubility limitation, electrochemical stability, permeability across a membrane, and cost of electroactive materials are crucial to the cell performance of an RFB and the capital cost. Compared to inorganic redox

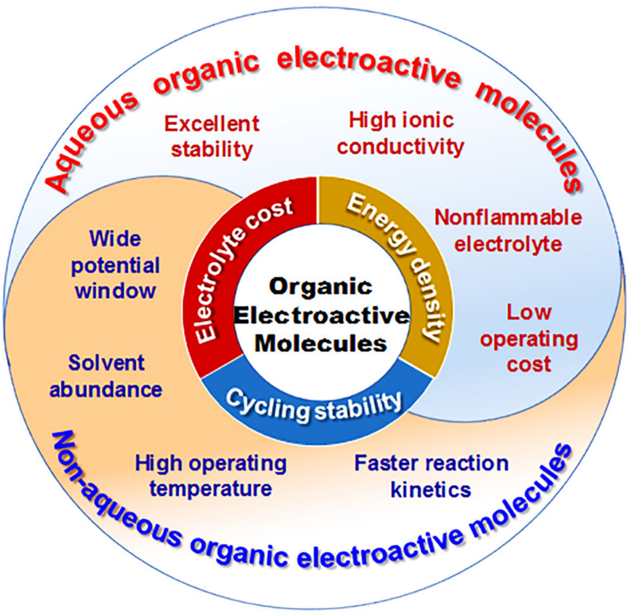

FIGURE 10 | Correlation diagram of features of organic electroactive molecules in aqueous and non-aqueous RFBs, respectively.

species (represented by metal ions), organic redox molecules, which can have inherent features such as flexible design, stable, easily tailored electrochemical properties, and cost-effectiveness, are more promising for RFBs targeted toward residential and industrial applications.

RFBs with organic electroactive materials are categorized as aqueous and non-aqueous systems according to the supporting electrolytes. The features of organic electroactive molecules in aqueous and non-aqueous RFBs are summarized and shown in **Figure 10**. So far, aqueous RFBs are still dominating work targeted at practical applications due to their high ionic conductivity, excellent stability, low operating cost, and high safety as a result of not using hazardous or flammable solvent. However, an intrinsically low operational voltage window and poor energy density have become obstacles for the commercialization of aqueous RFBs. In contrast, non-aqueous RFBs exhibit wider redox potential windows and operating temperature ranges, as well as good flexibility through tuning both the physical and electrochemical properties of organic electroactive molecules. Moreover, the cell performance of non-aqueous RFBs can be dramatically improved with advances in molecule design. It is worth noting that low ionic conductivity, side reactions of organic electrolytes, and poor battery cycling performance have limited the wide-scale development of non-aqueous RFBs up until now.

It is well-known that the physicochemical and electrochemical properties of organic electroactive materials can be easily and effectively modified by functional groups. Herein, a series of prior results on tailoring organic redox molecules are summarized. Through improvements in solubility, stability, and safety, the proposed RFBs with those organic electroactive materials have achieved advances in cell performance. However, this field is still in its initial stage, as no superior RFB has been demonstrated to replace the well-developed all-vanadium RFB. Hopefully, this review will inspire more continuous interest and efforts in this field so as to encourage the development of more advanced RFBs with organic electroactive materials toward practical applications.

AUTHOR CONTRIBUTIONS

FZ wrote the main body of the manuscript. MY was responsible for the drawing of some figures and the formatting of the references. MD was in charge of the whole manuscript. CJ put forward the central idea of the manuscript and gives final modification. All authors contributed to the article and approved the submitted version.

ACKNOWLEDGMENTS

The authors acknowledge support from the 100 Talented Team of Hunan Province (XiangZu [2016] 91), the Huxiang high-level talents program (Nos. 2018RS3077 and 2019RS1046), and the 111 project (B12015) at the Key Laboratory of Advanced Energy Materials Chemistry (Ministry of Education), Nankai University. MD was grateful for the Open Fund of the National Engineering Laboratory of Highway Maintenance Technology (No. kfj170105, Changsha University of Science & Technology).

REFERENCES

Armand, M., and Tarascon, J. M. (2008). Building better batteries. *Nature* 451, 652–657. doi: 10.1038/451652a

Bamgbopa, M. O., and Almheiri, S. (2017). Influence of solvents on species crossover and capacity decay in non-aqueous vanadium redox flow batteries: Characterization of acetonitrile and 1, 3 dioxolane solvent mixture. *J. Power Sources* 342, 371–381. doi: 10.1016/j.jpowsour.2016.12.050

Beh, E. S., De Porcellinis, D., Gracia, R. L., Xia, K. T., Gordon, R. G., and Aziz, M. J. (2017). A Neutral pH aqueous organic–organometallic redox flow battery with extremely high capacity retention. *ACS Energy Lett.* 2, 639–644. doi: 10.1021/acsenergylett.7b00019

Burgess, M., Hernández-Burgos, K., Schuh, J. K., Davila, J., Montoto, E. C., Ewoldt, R. H., et al. (2018). Modulation of the electrochemical reactivity of solubilized redox active polymers via polyelectrolyte dynamics. *J. Am. Chem. Soc.* 140, 2093–2104. doi: 10.1021/jacs.7b08353

Burgess, M., Moore, J. S., and Rodríguez-López, J. (2016). Redox active polymers as soluble nanomaterials for energy storage. *Acc. Chem. Res.* 49, 2649–2657. doi: 10.1021/acs.accounts.6b00341

Butler, I. R., and Thomas, D. (2007). "6.05 - mononuclear iron compounds: ferrocenes," in *Comprehensive Organometallic Chemistry III*, eds Mingos, D. M. P. and Crabtree, R. H. (Oxford: Elsevier), 185–220.

Cappillino, P. J., Pratt Iii, H. D., Hudak, N. S., Tomson, N. C., Anderson, T. M., and Anstey, M. R. (2014). Application of redox non-innocent ligands to non-aqueous flow battery electrolytes. *Adv. Energy Mater.* 4:1300566. doi: 10.1002/aenm.201300566

Carney, T. J., Collins, S. J., Moore, J. S., and Brushett, F. R. (2017). Concentration-dependent dimerization of anthraquinone disulfonic acid and its impact on charge storage. *Chem. Mater.* 29, 4801–4810. doi: 10.1021/acs.chemmater.7b00616

Chakrabarti, M. H., Dryfe, R. A. W., and Roberts, E. P. L. (2007). Evaluation of electrolytes for redox flow battery applications. *Electrochim. Acta* 52, 2189–2195. doi: 10.1016/j.electacta.2006.08.052

Chang, S., Ye, J., Zhou, W., Wu, C., Ding, M., Long, Y., et al. (2019). A low-cost SPEEK-K type membrane for neutral aqueous zinc-iron redox flow battery. *Surf. Coat. Technol.* 358, 190–194. doi: 10.1016/j.surfcoat.2018.11.028

Chen, J., Li, L., Wu, L., Yao, Q., Yang, H., Liu, Z., et al. (2018). Enhanced cycle stability of $Na_{0.9}Ni_{0.45}Mn_{0.55}O_2$ through tailoring O3/P2 hybrid structures for sodium-ion batteries. *J. Power Sources* 406, 110–117. doi: 10.1016/j.jpowsour.2018.10.058

Chen, J., Yang, H., Li, T., Liu, C., Tong, H., Chen, J., et al. (2019). The effects of reversibility of H_2-H_3 phase transition on Ni-rich layered oxide cathode for high-energy lithium-ion batteries. *Front. Chem.* 7:500. doi: 10.3389/fchem.2019.00500

Chen, Z., Xu, M., Zhu, H., Xie, T., Wang, W., and Zhao, Q. (2013). Enhanced electrochemical performance of polyacene coated $LiMn_2O_{3.95}F_{0.05}$ for lithium ion batteries. *Appl. Surf. Sci.* 286, 177–183. doi: 10.1016/j.apsusc.2013.09.044

Chen, Z., Yan, X., Xu, M., Cao, K., Zhu, H., Li, L., et al. (2017). Building honeycomb-like hollow microsphere architecture in a bubble template reaction for high-performance lithium-rich layered oxide cathode materials. *ACS Appl. Mater. Interf.* 9, 30617–30625. doi: 10.1021/acsami.7b07542

Cosimbescu, L., Wei, X., Vijayakumar, M., Xu, W., Helm, M. L., Burton, S. D., et al. (2015). Anion-tunable properties and electrochemical performance of functionalized ferrocene compounds. *Sci. Rep.* 5:14117. doi: 10.1038/srep14117

Dai, L.-X., and Hou, X.-L. (2010). *Chiral Ferrocenes in Asymmetric Catalysis: Synthesis and Applications.* Weinheim: John Wiley and Sons Ltd (2010).

Darling, R. M., Gallagher, K. G., Kowalski, J. A., Ha, S., and Brushett, F. R. (2014). Pathways to low-cost electrochemical energy storage: a comparison of aqueous and nonaqueous flow batteries. *Energy Environ. Sci.* 7, 3459–3477. doi: 10.1039/C4EE02158D

DeBruler, C., Hu, B., Moss, J., Liu, X., Luo, J., Sun, Y., et al. (2017). Designer two-electron storage viologen anolyte materials for neutral aqueous organic redox flow batteries. *Chemistry* 3, 961–978. doi: 10.1016/j.chempr.2017.11.001

Ding, C., Zhang, H., Li, X., Liu, T., and Xing, F. (2013). Vanadium flow battery for energy storage: prospects and challenges. *J. Phys. Chem. Lett.* 4, 1281–1294. doi: 10.1021/jz4001032

Ding, M., Hickey, A. K., Pink, M., Telser, J., Tierney, D. L., Amoza, M., et al. (2019). Magnetization slow dynamics in ferrocenium complexes. *Chem. A Eur. J.* 25, 10625–10632. doi: 10.1002/chem.201900799

Ding, Y., Li, Y., and Yu, G. (2016). Exploring bio-inspired quinone-based organic redox flow batteries: a combined experimental and computational study. *Chemistry* 1, 790–801. doi: 10.1016/j.chempr.2016.09.004

Ding, Y., and Yu, G. (2017). The promise of environmentally benign redox flow batteries by molecular engineering. *Angewan. Chem. Int. Edn*. 56, 8614–8616. doi: 10.1002/anie.201701254

Ding, Y., Zhang, C., Zhang, L., Zhou, Y., and Yu, G. (2018). Molecular engineering of organic electroactive materials for redox flow batteries. *Chem. Soc. Rev.* 47, 69–103. doi: 10.1039/C7CS00569E

Dunn, B., Kamath, H., and Tarascon, J.-M. (2011). Electrical energy storage for the grid: a battery of choices. *Science* 334, 928–935. doi: 10.1126/science.1212741

Er, S., Suh, C., Marshak, M. P., and Aspuru-Guzik, A. (2015). Computational design of molecules for an all-quinone redox flow battery. *Chem. Sci.* 6, 885–893. doi: 10.1039/C4SC03030C

Gerhardt, M. R., Tong, L., Gómez-Bombarelli, R., Chen, Q., Marshak, M. P., Galvin, C. J., et al. (2017). Anthraquinone derivatives in aqueous flow batteries. *Adv. Energy Mater.* 7:1601488. doi: 10.1002/aenm.201601488

Goulet, M.-A., and Aziz, M. J. (2018). Flow battery molecular reactant stability determined by symmetric cell cycling methods. *J. Electrochem. Soc.* 165:A1466–A1477. doi: 10.1149/2.0891807jes

Häupler, B., Wild, A., and Schubert, U. S. (2015). Carbonyls: powerful organic materials for secondary batteries. *Adv. Energy Mater.* 5:1402034. doi: 10.1002/aenm.201402034

Herr, T., Noack, J., Fischer, P., and Tübke, J. (2013). 1,3-Dioxolane, tetrahydrofuran, acetylacetone and dimethyl sulfoxide as solvents for non-aqueous vanadium acetylacetonate redox-flow-batteries. *Electrochim. Acta* 113, 127–133. doi: 10.1016/j.electacta.2013.09.055

Holdren, J. P. (2007). Energy and sustainability. *Science* 315, 737–737. doi: 10.1126/science.1139792

Hollas, A., Wei, X., Murugesan, V., Nie, Z., Li, B., Reed, D., et al. (2018). A biomimetic high-capacity phenazine-based anolyte for aqueous organic redox flow batteries. *Nature Energy* 3, 508–514. doi: 10.1038/s41560-018-0167-3

Hoober-Burkhardt, L., Krishnamoorthy, S., Yang, B., Murali, A., Nirmalchandar, A., Prakash, G. K. S., et al. (2017). A new michael-reaction-resistant benzoquinone for aqueous organic redox flow batteries. *J. Electrochem. Soc*. 164, A600–A607. doi: 10.1149/2.0351704jes

Hu, B., DeBruler, C., Rhodes, Z., and Liu, T. L. (2017). Long-cycling aqueous organic redox flow battery (AORFB) toward sustainable and safe energy storage. *J. Am. Chem. Soc.* 139, 1207–1214. doi: 10.1021/jacs.6b10984

Huskinson, B., Marshak, M. P., Suh, C., Er, S., Gerhardt, M. R., Galvin, C. J., et al. (2014). A metal-free organic–inorganic aqueous flow battery. *Nature* 505, 195–198. doi: 10.1038/nature12909

Iyer, V. A., Schuh, J. K., Montoto, E. C., Pavan Nemani, V., Qian, S., Nagarjuna, G., et al. (2017). Assessing the impact of electrolyte conductivity and viscosity on the reactor cost and pressure drop of redox-active polymer flow batteries. *J. Power Sources* 361, 334–344. doi: 10.1016/j.jpowsour.2017.06.052

Janoschka, T., Martin, N., Martin, U., Friebe, C., Morgenstern, S., Hiller, H., et al. (2015). An aqueous, polymer-based redox-flow battery using non-corrosive, safe, and low-cost materials. *Nature* 527, 78–81. doi: 10.1038/nature15746

Jing, Y., Liang, Y., Gheytani, S., and Yao, Y. (2017). Cross-conjugated oligomeric quinones for high performance organic batteries. *Nano Energy* 37, 46–52. doi: 10.1016/j.nanoen.2017.04.055

Kamat, P. V., Schanze, K. S., and Buriak, J. M. (2017). Redox flow batteries. *ACS Energy Lett.* 2, 1368–1369. doi: 10.1021/acsenergylett.7b00361

Kealy, T. J., and Pauson, P. L. (1951). A new type of organo-iron compound. *Nature* 168, 1039–1040. doi: 10.1038/1681039b0

Kim, H.-s., Yoon, T., Kim, Y., Hwang, S., Ryu, J. H., and Oh, S. M. (2016). Increase of both solubility and working voltage by acetyl substitution on ferrocene for non-aqueous flow battery. *Electrochem. Commun.* 69, 72–75. doi: 10.1016/j.elecom.2016.06.002

Kim, J.-H., Kim, K. J., Park, M.-S., Lee, N. J., Hwang, U., Kim, H., et al. (2011). Development of metal-based electrodes for non-aqueous redox flow batteries. *Electrochem. Commun.* 13, 997–1000. doi: 10.1016/j.elecom.2011.06.022

Kwabi, D. G., Ji, Y., and Aziz, M. J. (2020). Electrolyte lifetime in aqueous organic redox flow batteries: a critical review. *Chem. Rev.* doi: 10.1021/acs.chemrev.9b00599. [Epub ahead of print].

Kwabi, D. G., Lin, K., Ji, Y., Kerr, E. F., Goulet, M.-A., De Porcellinis, D., et al. (2018). Alkaline quinone flow battery with long lifetime at pH 12. *Joule* 2, 1894–1906. doi: 10.1016/j.joule.2018.07.005

Lai, Y. Y., Li, X., and Zhu, Y. (2020). Polymeric active materials for redox flow battery application. *ACS Appl. Polymer Mater*. 2, 113–128. doi: 10.1021/acsapm.9b00864

Leadbetter, J., and Swan, L. G. (2012). Selection of battery technology to support grid-integrated renewable electricity. *J. Power Sources* 216, 376–386. doi: 10.1016/j.jpowsour.2012.05.081

Leung, P., Shah, A. A., Sanz, L., Flox, C., Morante, J. R., Xu, Q., et al. (2017). Recent developments in organic redox flow batteries: a critical review. *J. Power Sources* 360, 243–283. doi: 10.1016/j.jpowsour.2017.05.057

Li, G., Jia, Y., Zhang, S., Li, X., Li, J., and Li, L. (2017). The crossover behavior of bromine species in the metal-free flow battery. *J. Appl. Electrochem.* 47, 261–272. doi: 10.1007/s10800-016-1033-2

Li, L., Chen, Z., Song, L., Xu, M., Zhu, H., Gong, L., et al. (2015a). Characterization and electrochemical performance of lithium-active titanium dioxide inlaid $LiNi_{0.5}Co_{0.2}Mn_{0.3}O_2$ material prepared by lithium residue-assisted method. *J. Alloys Compd.* 638, 77–82. doi: 10.1016/j.jallcom.2015.03.071

Li, L., Chen, Z., Zhang, Q., Xu, M., Zhou, X., Zhu, H., et al. (2015b). A hydrolysis-hydrothermal route for the synthesis of ultrathin $LiAlO_2$-inlaid $LiNi_{0.5}Co_{0.2}Mn_{0.3}O_2$ as a high-performance cathode material for lithium ion batteries. *J. Mater. Chem. A* 3, 894–904. doi: 10.1039/C4TA05902F

Li, L., Xu, M., Chen, Z., Zhou, X., Zhang, Q., Zhu, H., et al. (2015c). High-performance lithium-rich layered oxide materials: Effects of chelating agents on microstructure and electrochemical properties. *Electrochim. Acta* 174, 446–455. doi: 10.1016/j.electacta.2015.05.171

Li, L., Xu, M., Yao, Q., Chen, Z., Song, L., Zhang, Z., et al. (2016a). Alleviating surface degradation of nickel-rich layered oxide cathode material by encapsulating with nanoscale Li-ions/electrons superionic conductors hybrid membrane for advanced Li-ion batteries. *ACS Appl. Mater. Interfaces* 8, 30879–30889. doi: 10.1021/acsami.6b09197

Li, L., Yao, Q., Chen, Z., Song, L., Xie, T., Zhu, H., et al. (2015d). Effects of lithium-active manganese trioxide coating on the structural and electrochemical characteristics of $\mathrm{LiNi_{0.5}Co_{0.2}Mn_{0.3}O_2}$ as cathode materials for lithium ion battery. *J. Alloys Compd.* 650, 684–691. doi: 10.1016/j.jallcom.2015.08.041

Li, L., Yao, Q., Zhu, H., Chen, Z., Song, L., and Duan, J. (2016b). Effect of Al substitution sites on $\mathrm{Li_{1-x}Al_x(Ni_{0.5}Co_{0.2}Mn_{0.3})_{1-y}Al_yO_2}$ cathode materials for lithium ion batteries. *J Alloys Compd.* 686, 30–37. doi: 10.1016/j.jallcom.2016.05.333

Li, Z., Li, S., Liu, S., Huang, K., Fang, D., Wang, F., et al. (2011). Electrochemical properties of an all-organic redox flow battery using 2,2,6,6-tetramethyl-1-piperidinyloxy and N-methylphthalimide. *Electrochem. Solid State Lett.* 14, A171–A173. doi: 10.1149/2.012112esl

Lin, K., Chen, Q., Gerhardt, M. R., Tong, L., Kim, S. B., Eisenach, L., et al. (2015). Alkaline quinone flow battery. *Science* 349, 1529–1532. doi: 10.1126/science.aab3033

Lin, K., Gómez-Bombarelli, R., Beh, E. S., Tong, L., Chen, Q., Valle, A., et al. (2016). A redox-flow battery with an alloxazine-based organic electrolyte. *Nat. Energy* 1, 1–8. doi: 10.1038/nenergy.2016.102

Liu, K., Yang, J., Liang, S., Hou, H., Chen, Y., Wang, J., et al. (2018). An emission-free vacuum chlorinating process for simultaneous sulfur fixation and lead recovery from spent lead-acid batteries. *Environ. Sci. Technol.* 52, 2235–2241. doi: 10.1021/acs.est.7b05283

Liu, Q., Shinkle, A. A., Li, Y., Monroe, C. W., Thompson, L. T., Sleightholme, A. E. S. (2010). Non-aqueous chromium acetylacetonate electrolyte for redox flow batteries. *Electrochem. Commun.* 12, 1634–1637. doi: 10.1016/j.elecom.2010.09.013

Liu, T., Wei, X., Nie, Z., Sprenkle, V., and Wang, W. (2016). A total organic aqueous redox flow battery employing a low cost and sustainable methyl viologen anolyte and 4-HO-TEMPO catholyte. *Adv. Energy Mater*. 6:1501449. doi: 10.1002/aenm.201501449

Lou, X., Ye, J., Xia, L., Chang, S., Zhao, X., Wu, C., et al. (2019). Highly efficient and low cost SPEEK/$\mathrm{TiO_2}$ nanocomposite membrane for vanadium redox flow battery. *J. Nanosci. Nanotechnol.* 19, 2247–2252. doi: 10.1166/jnn.2019.16467

Luo, J., Hu, B., Hu, M., Zhao, Y., and Liu, T. L. (2019). Status and prospects of organic redox flow batteries toward sustainable energy storage. *ACS Energy Lett.* 4, 2220–2240. doi: 10.1021/acsenergylett.9b01332

Ma, C., Shu, Y., and Chen, H. (2015). Recycling lead from spent lead pastes using oxalate and sodium oxalate and preparation of novel lead oxide for lead-acid batteries. *RSC Adv.* 5, 94895–94902. doi: 10.1039/C5RA18627G

Matsuda, Y., Tanaka, K., Okada, M., Takasu, Y., Morita, M., and Matsumura-Inoue, T. (1988). A rechargeable redox battery utilizing ruthenium complexes with non-aqueous organic electrolyte. *J. Appl. Electrochem.* 18, 909–914. doi: 10.1007/BF01016050

Milshtein, J. D., Barton, J. L., Darling, R. M., and Brushett, F. R. (2016). 4-acetamido-2,2,6,6-tetramethylpiperidine-1-oxyl as a model organic redox active compound for nonaqueous flow batteries. *J. Power Sources* 327, 151–159. doi: 10.1016/j.jpowsour.2016.06.125

Montoto, E. C., Cao, Y., Hernández-Burgos, K., Sevov, C. S., Braten, M. N., Helms, B. A., et al. (2018). Effect of the backbone tether on the electrochemical properties of soluble cyclopropenium redox-active polymers. *Macromolecules* 51, 3539–3546. doi: 10.1021/acs.macromol.8b00574

Montoto, E. C., Nagarjuna, G., Moore, J. S., and Rodríguez-López, J. (2017). Redox active polymers for non-aqueous redox flow batteries: validation of the size-exclusion approach. *J. Electrochem. Soc*. 164, A1688–A1694. doi: 10.1149/2.1511707jes

Nagarjuna, G., Hui, J., Cheng, K. J., Lichtenstein, T., Shen, M., Moore, J. S., et al. (2014). Impact of redox-active polymer molecular weight on the electrochemical properties and transport across porous separators in nonaqueous solvents. *J. Am. Chem. Soc*. 136, 16309–16316. doi: 10.1021/ja508482e

Nishide, H., Iwasa, S., Pu, Y.-J., Suga, T., Nakahara, K., and Satoh, M. (2004). Organic radical battery: nitroxide polymers as a cathode-active material. *Electrochim. Acta* 50, 827–831. doi: 10.1016/j.electacta.2004.02.052

Orita, A., Verde, M. G., Sakai, M., and Meng, Y. S. (2016). A biomimetic redox flow battery based on flavin mononucleotide. *Nat. Commun.* 7, 1–8. doi: 10.1038/ncomms13230

Park, M., Ryu, J., Wang, W., and Cho, J. (2017). Material design and engineering of next-generation flow-battery technologies. *Nat. Rev. Mater.* 2:16080. doi: 10.1038/natrevmats.2016.80

Park, M., Shin, D.-S., Ryu, J., Choi, M., Park, N., Hong, S. Y., et al. (2015). Organic-catholyte-containing flexible rechargeable lithium batteries. *Adv. Mater.* 27, 5141–5146. doi: 10.1002/adma.201502329

Phillips, E. S. (2011). *Ferrocenes: Compounds, Properties and Applications*. New York, NY: Nova Science Publishers.

Qin, W., Li, J., Liu, X., Zhou, N., Wu, C., Ding, M., et al. (2019). Formation of needle-like porous CoNi2S4-MnOOH for high performance hybrid supercapacitors with high energy density. *J. Coll. Interface Sci.* 554, 125–132. doi: 10.1016/j.jcis.2019.07.010

Quan, M., Sanchez, D., Wasylkiw, M. F., and Smith, D. K. (2007). Voltammetry of quinones in unbuffered aqueous solution: reassessing the roles of proton transfer and hydrogen bonding in the aqueous electrochemistry of quinones. *J. Am. Chem. Soc.* 129, 12847–12856. doi: 10.1021/ja0743083

Rajagopalan, R., Tang, Y., Ji, X., Jia, C., and Wang, H. (2020a). Advancements and challenges in potassium ion batteries: a comprehensive review. *Adv. Funct. Mater*. 30:1909486. doi: 10.1002/adfm.201909486

Rajagopalan, R., Tang, Y., Jia, C., Ji, X., and Wang, H. (2020b). Understanding the sodium storage mechanisms of organic electrodes in sodium ion batteries: issues and solutions. *Energy Environ. Sci*. doi: 10.1039/C9EE03637G. [Epub ahead of print].

Schon, T. B., McAllister, B. T., Li, P.-F., and Seferos, D. S. (2016). The rise of organic electrode materials for energy storage. *Chem. Soc. Rev*. 45, 6345–6404. doi: 10.1039/C6CS00173D

Scott, D. T., McKnight, D. M., Blunt-Harris, E. L., Kolesar, S. E., and Lovley, D. R. (1998). Quinone moieties act as electron acceptors in the reduction of humic substances by humics-reducing microorganisms. *Environ. Sci. Technol.* 32, 2984–2989. doi: 10.1021/es980272q

Sevov, C. S., Fisher, S. L., Thompson, L. T., and Sanford, M. S. (2016). Mechanism-based development of a low-potential, soluble, and cyclable multielectron anolyte for nonaqueous redox flow batteries. *J. Am. Chem. Soc.* 138, 15378–15384. doi: 10.1021/jacs.6b07638

Sleightholme, A. E. S., Shinkle, A. A., Liu, Q., Li, Y., Monroe, C. W., and Thompson, L. T. (2011). Non-aqueous manganese acetylacetonate electrolyte for redox flow batteries. *J. Power Sources* 196, 5742–5745. doi: 10.1016/j.jpowsour.2011.02.020

Soloveichik, G. L. (2015). Flow batteries: current status and trends. *Chem. Rev.* 115, 11533–11558. doi: 10.1021/cr500720t

Štěpnička, S. (2008). *Ferrocenes: Ligands, Materials and Biomolecules,* Chichester: John Wiley & Sons, Ltd.

Takechi, K., Kato, Y., and Hase, Y. (2015). A highly concentrated catholyte based on a solvate ionic liquid for rechargeable flow batteries. *Adv. Mater*. 27, 2501–2506. doi: 10.1002/adma.201405840

Turner, J. A. (1999). A realizable renewable energy future. *Science* 285, 687–689. doi: 10.1126/science.285.5428.687

Wei, D., Zhong, S., Hang, Z., Zhang, X., Zhu, C., Duan, J., et al. (2018). In situ construction of interconnected $\mathrm{SnO_2}$/nitrogen-doped Carbon@$\mathrm{TiO_2}$ networks for lithium-ion half/full cells. *Electrochim. Acta* 290, 312–321. doi: 10.1016/j.electacta.2018.08.094

Wei, X., Cosimbescu, L., Xu, W., Hu, J. Z., Vijayakumar, M., Feng, J., et al. (2015). Towards high-performance nonaqueous redox flow electrolyte via ionic modification of active species. *Adv. Energy Mater.* 5:1400678. doi: 10.1002/aenm.201400678

Wei, X., Xu, W., Vijayakumar, M., Cosimbescu, L., Liu, T., Sprenkle, V., et al. (2014). TEMPO-based catholyte for high-energy density nonaqueous redox flow batteries. *Adv. Mater*. 26, 7649–7653. doi: 10.1002/adma.201403746

Wu, C., Chen, L., Lou, X., Ding, M., and Jia, C. (2018a). Fabrication of cobalt-nickel-zinc ternary oxide nanosheet and applications for supercapacitor electrode. *Front. Chem.* 6:597. doi: 10.3389/fchem.2018.00597

Wu, C., Lou, X., and Jia, C. (2019a). Porous Ni-Mo-Co hydroxide nanoflakes on carbon cloth for supercapacitor application. *J. Nanosci. Nanotechnol.* 19, 272–276. doi: 10.1166/jnn.2019.16450

Wu, C., Zhu, Y., Ding, M., Jia, C., and Zhang, K. (2018b). Fabrication of plate-like MnO2 with excellent cycle stability for supercapacitor electrodes. *Electrochim. Acta* 291, 249–255. doi: 10.1016/j.electacta.2018.08.126

Wu, C., Zhu, Y., Guan, C., Jia, C., Qin, W., Wang, X., et al. (2019b). Mesoporous aluminium manganese cobalt oxide with pentahedron structures for energy storage devices. *J. Mater. Chem. A* 7, 18417–18427. doi: 10.1039/C9TA06319F

Xia, L., Zhang, Q., Wu, C., Liu, Y., Ding, M., Ye, J., et al. (2019). Graphene coated carbon felt as a high-performance electrode for all vanadium redox flow batteries. *Surf. Coat. Technol.* 358, 153–158. doi: 10.1016/j.surfcoat.2018.11.024

Xing, X., Zhang, D., and Li, Y. (2015). A non-aqueous all-cobalt redox low battery using 1,10-phenanthrolinecobalt(II) hexafluorophosphate as active species. *J. Power Sources* 279, 205–209. doi: 10.1016/j.jpowsour.2015.01.011

Xu, M., Chen, Z., Zhu, H., Yan, X., Li, L., and Zhao, Q. (2015). Mitigating capacity fade by constructing highly ordered mesoporous Al_2O_3/polyacene double-shelled architecture in Li-rich cathode materials. *J. Mater. Chem. A* 3, 13933–13945. doi: 10.1039/C5TA03676C

Xu, Y., Wen, Y.-H., Cheng, J., Cao, G.-P., and Yang, Y.-S. (2010). A study of tiron in aqueous solutions for redox flow battery application. *Electrochim. Acta* 55, 715–720. doi: 10.1016/j.electacta.2009.09.031

Yang, B., Hoober-Burkhardt, L., Krishnamoorthy, S., Murali, A., Prakash, G. K. S., and Narayanan, S. R. (2016). High-performance aqueous organic flow battery with quinone-based redox couples at both electrodes. *J. Electrochem. Soc*. 163, A1442–A1449. doi: 10.1149/2.1371607jes

Yang, B., Hoober-Burkhardt, L., Wang, F., Surya Prakash, G. K., and Narayanan, S. R. (2014). An inexpensive aqueous flow battery for large-scale electrical energy storage based on water-soluble organic redox couples. *J. Electrochem. Soc.* 161, A1371–A1380. doi: 10.1149/2.1001409jes

Yang, H., Wu, H.-H., Ge, M., Li, L., Yuan, Y., Yao, Q., et al. (2019). Simultaneously dual modification of Ni-rich layered oxide cathode for high-energy lithium-ion batteries. *Adv. Funct. Mater.* 29:1808825. doi: 10.1002/adfm.201808825

Yang, S., Li, R., Cai, X., Xue, K., Yang, B., Hu, X., et al. (2018a). Enhanced cycle performance and lifetime estimation of lead-acid batteries. *N. J. Chem.* 42, 8900–8904. doi: 10.1039/C8NJ00542G

Yang, Z., Tong, L., Tabor, D. P., Beh, E. S., Goulet, M.-A., De Porcellinis, D., et al. (2018b). Alkaline benzoquinone aqueous flow battery for large-scale storage of electrical energy. *Adv. Energy Mater*. 8:1702056. doi: 10.1002/aenm.201702056

Yang, Z., Zhang, J., Kintner-Meyer, M. C. W., Lu, X., Choi, D., Lemmon, J. P., et al. (2011). Electrochemical energy storage for green grid. *Chem. Rev.* 111, 3577–3613. doi: 10.1021/cr100290v

Ye, J., Cheng, Y., Sun, L., Ding, M., Wu, C., Yuan, D., et al. (2019a). A green SPEEK/lignin composite membrane with high ion selectivity for vanadium redox flow battery. *J. Membr. Sci.* 572, 110–118. doi: 10.1016/j.memsci.2018.11.009

Ye, J., Lou, X., Wu, C., Wu, S., Ding, M., Sun, L., et al. (2018). Ion selectivity and stability enhancement of SPEEK/lignin membrane for vanadium redox flow battery: the degree of sulfonation effect. *Front. Chem.* 6:549. doi: 10.3389/fchem.2018.00549

Ye, J., Wu, C., Qin, W., Zhong, F., and Ding, M. (2020). Advanced sulfonated poly(ether ether ketone)/graphene-oxide/titanium dioxide nanoparticle composited membrane with superior cyclability for vanadium redox flow battery. *J. Nanosci. Nanotechnol.* 20, 4714–4721. doi: 10.1166/jnn.2020.18503

Ye, J., Xia, L., Wu, C., Ding, M., Jia, C., and Wang, Q. (2019b). Redox targeting-based flow batteries. *J. Phys. D Appl. Phys.* 52:443001. doi: 10.1088/1361-6463/ab3251

Zeng, L., Lou, X., Zhang, J., Wu, C., Liu, J., and Jia, C. (2019). Carbonaceous mudstone and lignin-derived activated carbon and its application for supercapacitor electrode. *Surf. Coat. Technol.* 357, 580–586. doi: 10.1016/j.surfcoat.2018.10.041

Zhang, H., Lu, W., and Li, X. (2019). Progress and perspectives of flow battery technologies. *Electrochem. Energy Rev.* 2, 492–506. doi: 10.1007/s41918-019-00047-1

Conflict of Interest: The authors declare that the research was conducted in the absence of any commercial or financial relationships that could be construed as a potential conflict of interest.

frontiers in Chemistry

ORIGINAL RESEARCH
published: 14 July 2020
doi: 10.3389/fchem.2020.00502

Systematic Investigation of the Physical and Electrochemical Characteristics of the Vanadium (III) Acidic Electrolyte With Different Concentrations and Related Diffusion Kinetics

Minghua Jing [1,3], Chengjie Li [2], Xinyu An [3], Zeyu Xu [1], Jianguo Liu [1], Chuanwei Yan [1], Dawei Fang [3] and Xinzhuang Fan [1,4]*

[1] Liaoning Engineering Research Center for Advanced Battery Materials, Institute of Metal Research, Chinese Academy of Sciences, Shenyang, China, [2] Shandong Engineering Research Center of Green and High-Value Marine Fine Chemical, Weifang University of Science and Technology, Shouguang, China, [3] Institute of Rare and Scattered Elements, College of Chemistry, Liaoning University, Shenyang, China, [4] Building Energy Research Center, Guangzhou HKUST Fok Ying Tung Research Institute, Guangzhou, China

OPEN ACCESS

Edited by:
Du Yuan,
Nanyang Technological University, Singapore

Reviewed by:
Jingyu Xi,
Tsinghua University, China
Yunguang Zhu,
Massachusetts Institute of Technology, United States
Binyu Xiong,
Wuhan University of Technology, China

***Correspondence:**
Xinzhuang Fan
mexzfan@gmail.com

Specialty section:
This article was submitted to Electrochemistry, a section of the journal Frontiers in Chemistry

Received: *15 April 2020*
Accepted: *15 May 2020*
Published: *14 July 2020*

Citation:
Jing M, Li C, An X, Xu Z, Liu J, Yan C, Fang D and Fan X (2020) Systematic Investigation of the Physical and Electrochemical Characteristics of the Vanadium (III) Acidic Electrolyte With Different Concentrations and Related Diffusion Kinetics. Front. Chem. 8:502. doi: 10.3389/fchem.2020.00502

Owing to the lack of systematic kinetic theory about the redox reaction of V(III)/V(II), the poor electrochemical performance of the negative process in vanadium flow batteries limits the overall battery performance to a great extent. As the key factors that influence electrode/electrolyte interfacial reactivity, the physicochemical properties of the V(III) acidic electrolyte play an important role in the redox reaction of V(III)/V(II), hence a systematic investigation of the physical and electrochemical characteristics of V(III) acidic electrolytes with different concentrations and related diffusion kinetics was conducted in this work. It was found that the surface tension and viscosity of the electrolyte increase with increasing V(III) concentration, while the corresponding conductivity shows an opposite trend. Both the surface tension and viscosity change slightly with increasing concentration of H_2SO_4, but the conductivity increases significantly, indicating that a lower V(III) concentration and a higher H_2SO_4 concentration are conducive to the ion transfer process. The electrochemical measurements further show that a higher V(III) concentration will facilitate the redox reaction of V(III)/V(II), while the increase in H_2SO_4 concentration only improves the ion transmission and has little effect on the electron transfer process. Furthermore, the diffusion kinetics of V(III) have been further studied with cyclic voltammetry and chronopotentiometry. The results show that an elevated temperature facilitates the V(III)/V(II) redox reaction and gives rise to an increased electrode reaction rate constant (k_s) and diffusion coefficient [$D_{V(III)}$]. On this basis, the diffusion activation energy (13.7 kJ·mol^{-1}) and the diffusion equation of V(III) are provided to integrate kinetic theory in the redox reaction of V(III)/V(II).

Keywords: temperature, concentration, diffusion equation, trivalent vanadium ion, vanadium flow battery (VFB)

INTRODUCTION

Vanadium flow batteries (VFBs) have been widely developed as a green energy storage technology because of their high energy efficiency, flexible design, long life cycle, high safety, and low cost (Rychcik and Skyllas-Kazacos, 1988; Sun and Skyllas-Kazacos, 1992; Joerissen et al., 2004; Sukkar and Skyllas-Kazacos, 2004; Zhao et al., 2006; Rahman and Skyllas-Kazacos, 2009; Ding et al., 2013; Chakrabarti et al., 2014; Zheng et al., 2016). In general, VFBs are mainly composed of the electrolyte, electrode, ion exchange membrane, and a bipolar plate. They store energy through the chemical changes in electroactive species, which are separated by the ion exchange membrane (Wang et al., 2014; Xia et al., 2019; Ye et al., 2019, 2020a,b; Yu et al., 2019; Lou et al., 2020). The V(V)/V(IV) and V(III)/V(II) redox couples are used as the catholyte and the anolyte, respectively, and the sulfuric acid solution acts as the supporting electrolyte. The concentrations of vanadium and H^+ ions play an important role in the determination of the electrochemical reaction processes and the battery performance.

The most commonly used electrolyte in VFBs is an equivalent volume mixture of V(III) and V(IV) sulfuric acid solution. Previous studies have noted that the concentration of V(IV) and acid as well as the operating temperature have important effects on the physicochemical properties and electrochemical activity of the positive electrode reaction (Sum et al., 1985; Kazacos et al., 1990; Zhong and Skyllas-Kazacos, 1992; Iwasa et al., 2003; Yi et al., 2003; Liu et al., 2011). However, few studies have reported on the negative process. Sun and Skyllas-Kazacos (Sum and Skyllas-Kazacos, 1982) investigated the electrochemical behavior of the V(III)/V(II) redox couple at glassy carbon electrodes using cyclic voltammetry (CV). They found that the oxidation/reduction reaction is electrochemically irreversible and the surface preparation is very critical in determining the electrochemical behavior. Yamamura et al. (2005) determined the standard rate constants of the electrode reactions of vanadium on different carbon electrodes. Most studies (Sum and Skyllas-Kazacos, 1982; Oriji et al., 2005; Lee et al., 2012; Aaron et al., 2013; Sun et al., 2016) found that the electrode reaction rate of V(III)/V(II) is much less than that of V(IV)/V(V); however, systematic investigations into the detailed mechanism remain scarce.

Owing to the sluggish kinetics of V(III)/V(II) and the significant hydrogen evolution reaction, the negative process contributes almost 80% polarization during the discharging process (Sun et al., 2016). Agar et al. (2013) further verified that the negative electrode process was the limiting factor in VFB performance by using an asymmetric cell configuration. As the key factors influencing electrode/electrolyte interfacial reactivity, the concentration and physicochemical properties of the V(III) acidic electrolyte as well as the temperature play an important role in the redox reaction of V(III)/V(II) (Xiao et al., 2016). For instance, the viscosity of the electrolyte affects the mass transfer kinetics and the conductivity directly influences the reversibility of the electrochemical reaction, which both depend on the concentration of vanadium and H_2SO_4 (Zhang, 2014). In short, it is necessary to conduct a systematic investigation into the physical and electrochemical characteristics of V(III) acidic electrolytes using different concentrations and diffusion kinetics.

In our previous work (Wang et al., 2014), the temperature-related reaction kinetics of the V(IV)/V(V) redox couple on a graphite electrode in sulfuric acid solutions was investigated. Herein, we will investigate the physicochemical properties of the electrolytes with different concentrations of V(III) and sulfuric acid and conduct a systematic study of the diffusion kinetics of V(III). Our aim is to clarify the kinetic rules of the diffusion behavior of V(III) and further establish a diffusion equation, providing a better understanding of the V(III)/V(II) redox reaction in the negative half-cell of VFBs.

EXPERIMENTAL

Preparations of the Electrode and Electrolyte

A spectroscopically pure graphite rod (SPGR) (Sinosteel Shanghai Advanced Graphite Material Co. Ltd, China) was used as the working electrode. The working area of the SPGR was $\sim$0.28 cm^2. This was ground with silicon carbide papers (down to 2,000 grit in grain size) and thoroughly rinsed with deionized water and alcohol before use.

All chemicals used in this work were analytically pure agents and all solutions were prepared with deionized water. V(III) acidic solutions were initially prepared by the electrochemical reduction of $VOSO_4$ with an electrolytic cell and then diluted to produce solutions with the required H^+ and V(III) concentrations. In addition, the concentration of the electrolytes was measured with a ultraviolet spectrometer (TU-1900; Persee General Instrument Co. Ltd, Beijing, China).

Physical Characterization of the Electrolyte

The viscosity was measured by means of an Ubbelohde viscometer. The electrical conductivity was determined using a conductivity meter (Mettler Toledo) at 293 K. The surface tensions of the solutions were measured by the bubble-pressure method.

Electrochemical Measurements

The electrochemical measurements were performed using a Reference 600 electrochemical workstation (Gamry Instruments, USA) with a conventional three-electrode cell with an SPGR as the working electrode, a platinum plate as the counter electrode, and a saturated calomel electrode as the reference electrode. A salt bridge was used to eliminate the liquid junction potential between the Luggin capillary and the working electrode. The electrolyte was purged with nitrogen for 10 min before the electrochemical test to reduce the influence of oxygen on the electrochemical oxidation of V(II). Temperature was controlled by a water bath.

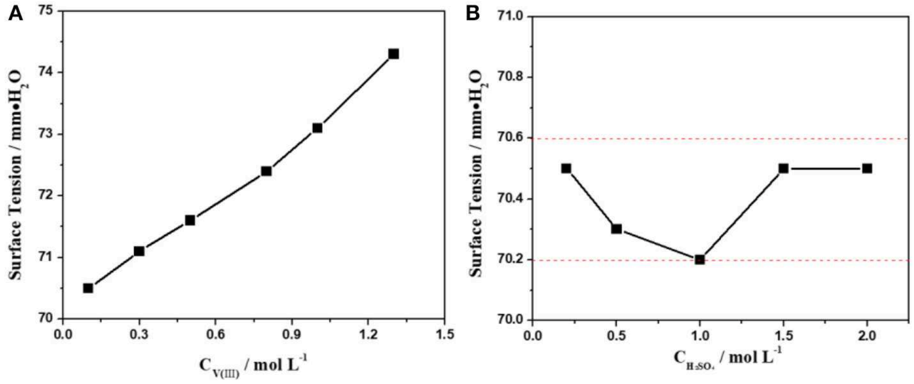

FIGURE 1 | Changes in the surface tension with different concentrations of V(III) **(A)** and H_2SO_4 **(B)**.

RESULTS AND DISCUSSION

Physical Characteristics of the V(III) Acidic Electrolyte at Different Concentrations

The physical parameters of the electrolyte, such as the surface tension, viscosity, and conductivity, significantly affect the ion transmission process and the electrochemical properties of the electrode/electrolyte interface (Jing et al., 2016). In general, higher surface tension will hinder the contact between the electrolyte and the electrode, leading to a decrease in the effective reaction area, while higher conductivity often means faster transmission of ions and higher viscosity usually leads to a lower diffusion rate. However, the three physical parameters are not all proportional to the concentration of the electrolyte, so it is not reasonable to simply increase or decrease the electrolyte concentration in engineering applications. In particular, vanadium ions often exist in a very complex form in the electrolyte, which may result in a significant difference in the physicochemical properties of the electrolyte at different concentrations (Sepehr and Paddison, 2016). Hence, it is necessary to investigate the influence of the electrolyte concentration on its physicochemical properties.

The influence of the concentration of V(III) and H_2SO_4 on the surface tension of the electrolyte was investigated first. **Figure 1A** shows the surface tension of 2.0 mol·L^{-1} H_2SO_4 solutions with different concentrations of V(III) (from 0.1 to 1.3 mol·L^{-1}). Obviously, the surface tension of the electrolytes gradually increases with an increasing concentration of V(III). Actually, the higher the concentration of vanadium, the higher the surface tension and the greater the effect on the contact between the electrolyte and the electrode. However, in practice, we want to increase the concentration of vanadium to achieve high volumetric capacities or energy densities. We can resolve this contradiction by improving the hydrophilicity of the electrode surface to apply a higher concentration of vanadium. In contrast to **Figure 1A**, the variation in the trend in the surface tension was very slight when changing the H_2SO_4 concentration (**Figure 1B**). Such a different phenomenon might be attributed to the stronger hydration force of the V(III) compared with that of H_2SO_4. Therefore, the surface tension of the V(III) acidic electrolyte was mainly affected by the concentration of V(III).

The influence of the concentration of V(III) and H_2SO_4 on the viscosity and conductivity of the electrolyte was also investigated. As shown in **Figure 2**, there was a fourfold increase in the viscosity as the concentration of V(III) changed from 0.1 to 1.3 mol·L^{-1}. However, the viscosity of the electrolytes changed very little with different concentrations of H_2SO_4, which was similar to the changing features of the surface tension described above. This could be ascribed to the more complex structure of V(III). It can be concluded that the concentration of V(III) was the main factor in determining the viscosity of the V(III) acid electrolytes, and a suitable concentration of V(III) had a positive effect on its mass transfer performance.

Figure 3 shows the variations in the conductivity of the electrolytes with different concentrations of V(III) (a) and H_2SO_4 (b). When the concentration of V(III) increased from 0.1 to 1.3 mol·L^{-1}, the conductivity decreased by ~43.3% (from 480 to 272 mS·cm^{-1}), while there was an obvious increase in conductivity (about 6-fold) with increasing H_2SO_4 concentration. The significant difference should also be ascribed to the more complex form of V(III), which would result in a larger hydrated ionic radius and poorer mobility (Sepehr and Paddison, 2016). Therefore, it is necessary to investigate the optimum concentration of V(III) and H_2SO_4 to obtain better electrochemical performance.

Electrochemical Characteristics of the V(III) Acidic Electrolyte at Different Concentrations

The CV test was a useful tool to investigate the electrochemical performance of the battery materials. For a CV curve, the value of the peak currents of the oxidation and reduction reactions (i_{pa}, i_{pc}, respectively) and their ratio ($-i_{pa}/i_{pc}$), as well as the peak potential separation (ΔE_p), could be used to estimate the electrochemical activity. Generally, the lower the value of ΔE_p or the more similar the i_{pa} and $-i_{pc}$ values usually implied better electrochemical reversibility, and a higher peak current often suggested higher reactivity (Bard and Faulkner, 2001; Ding et al., 2013). However, the peak current (i_{pc}) is closely related to the electrochemical surface area of the electrode, which is difficult to read directly from the CV curve, so ΔE_p and $-i_{pa}/i_{pc}$ were more suitable for estimating the electrochemical properties.

Specifically, $-i_{pa}/i_{pc}$ can be calculated from the CV curves by the following equation (Bard and Faulkner, 2001):

$$\frac{i_{pc}}{i_{pa}} = \frac{(i_{pc})_0}{i_{pa}} + \frac{0.485(i_{sp})_0}{i_{pa}} + 0.086 \tag{1}$$

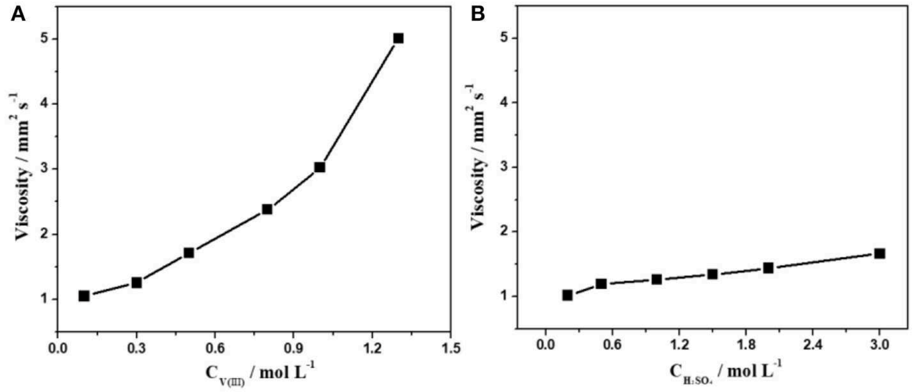

FIGURE 2 | Changes in the viscosity with different concentrations of V(III) **(A)** and H_2SO_4 **(B)**.

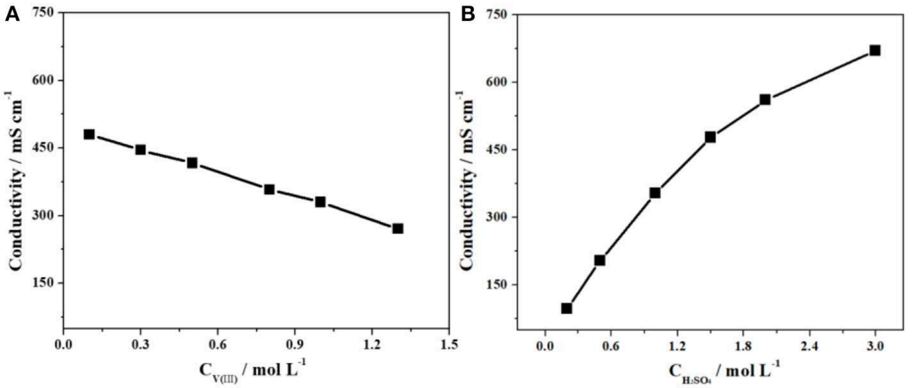

FIGURE 3 | Changes in conductivity with different concentrations of V(III) **(A)** and H_2SO_4 **(B)**.

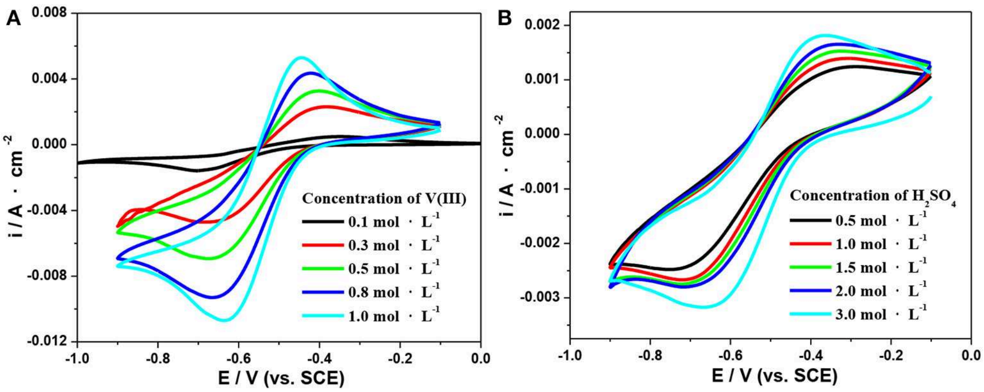

FIGURE 4 | CV curves on an SPGR in 2.0 mol·L^{-1} H_2SO_4 with different concentrations of V(III) **(A)** and 0.1 mol·L^{-1} V(III) with different concentrations of H_2SO_4 **(B)**. Scan rate, 10 mV·s^{-1}.

where $(i_{pc})_0$ is the uncorrected cathodic peak current density with respect to the zero current baseline and $(i_{sp})_0$ is the current density at the switching potential.

Herein, CV tests on the SPGR in 2.0 mol·L^{-1} H_2SO_4 with different concentrations of V(III) electrolytes (from 0.1 to 1.0 mol·L^{-1}) were first carried out at a scan rate of 10 mV·s^{-1} (**Figure 4A**). The detailed electrochemical parameters are listed in **Table 1**. As expected, the value of $-i_{pa}/i_{pc}$ gradually increased to 0.97 with increasing concentration of V(III), indicating a favorable electrochemical reversibility of V(III)/V(II) with a 1.0 mol·L^{-1} V(III) acidic electrolyte. In addition, ΔE_p gradually decreased with increasing concentration of V(III), also indicating increasing electrochemical activity of the electrolyte with higher concentrations of V(III). It can be concluded that a higher concentration of V(III) would facilitate the V(III)/V(II) electrochemical redox reaction.

Next, CV tests on the SPGR in 0.1 mol·L^{-1} V(III) with different concentrations of H_2SO_4 electrolytes (from 0.5 to 3.0 mol·L^{-1}) were carried out at a scan rate of 10 mV·s^{-1}. The corresponding CV curves are shown in **Figure 4B**; the detailed electrochemical parameters recorded from the CV curves in **Figure 4B** are also listed in **Table 1**. Compared with the CV curves in **Figure 4A**, the CV curves in the electrolytes at different H_2SO_4 concentrations showed a smaller difference. Even so, the value of ΔE_p obviously decreased with increasing concentration of H_2SO_4, which should be ascribed to the rapid transfer rate of H^+, resulting in favorable conductivity of the electrolytes with higher concentrations of H_2SO_4. In addition, the value of $-i_{pa}/i_{pc}$ increased first and then decreased, and the maximum value was obtained with 2.0 mol·L^{-1} H_2SO_4 electrolyte, which might be attributed to the coupling effect of both the increased conductivity and viscosity as well as the gradually increasing influence of the hydrogen evolution reaction with increasing H_2SO_4 concentration. However, the $-i_{pa}/i_{pc}$ values changed little with H_2SO_4 concentration, indicating that the H_2SO_4 concentration had a smaller effect on the electron transfer process.

Electrochemical impedance spectroscopy (EIS) is a powerful non-destructive technique for studying the electrochemical processes at the electrode/electrolyte interface. Electrochemical parameters such as the solution resistance (R_s), constant resistance (R_c), and electron transfer resistance (R_{ct}) can be obtained simultaneously through the appropriate equivalent circuit (Cao and Zhang, 2002).

Figure 5 shows the Nyquist plots of an SPGR recorded in different electrolytes at a polarization potential of −0.6 V, with an excitation signal of 5 mV and frequency ranging from 0.1 mHz to 10 mHz. As shown in **Figure 5**, the Nyquist plots for all samples consisted of a semicircle at high frequency and a linear part at low frequency, suggesting that the electrode reaction was dual controlled by the electrochemical reaction and diffusion

TABLE 1 | Electrochemical parameters recorded from the CV curves in **Figure 4**.

$C_{V(III)}$ (mol·L^{-1})	$-i_{pa}/i_{pc}$	ΔE_p/V	CH_2SO_4 (mol·L^{-1})	$-i_{pa}/i_{pc}$	ΔE_p/V
0.1	0.914	0.354	0.5	0.905	0.464
0.3	0.929	0.307	1.0	0.911	0.414
0.5	0.940	0.274	1.5	0.916	0.397
0.8	0.959	0.243	2.0	0.919	0.391
1.0	0.970	0.189	3.0	0.912	0.304

TABLE 2 | EIS parameters obtained by fitting the impedance plots with the equivalent electric circuits in **Figure 5**.

$C_{V(III)}$ (mol·L^{-1})	R_s (Ω)	R_{ct} (Ω)	CH_2SO_4 (mol·L^{-1})	R_s (Ω)	R_{ct} (Ω)
0.1	1.891	24.11	0.5	4.594	18.23
0.3	1.988	18.58	1.0	3.34	21.75
0.5	2.283	8.899	1.5	2.51	20.39
1.0	2.389	8.28	2.0	2.072	19.47
–	–	–	3.0	1.053	19.5

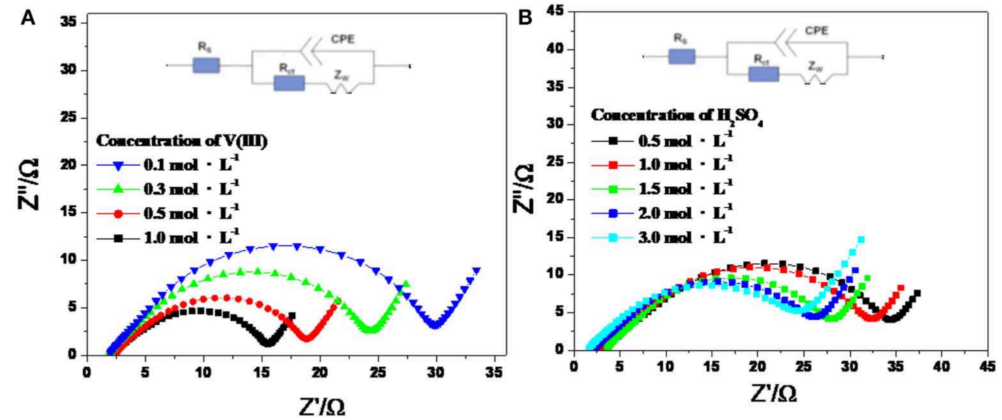

FIGURE 5 | Nyquist plots and the equivalent electric circuit of V(III)/V(II) redox couples with 2.0 mol·L^{-1} H_2SO_4 electrolyte with different concentrations of V(III) **(A)** and 0.1 mol·L^{-1} V(III) electrolyte with different concentrations of H_2SO_4 **(B)** at a polarization potential of −0.6 V.

processes (Wei et al., 2014). Thus, the Nyquist plots in **Figure 5** also show the equivalent circuits, where R_s is the bulk solution resistance; CPE is the constant phase element, which accounts for the double-layer capacitance; R_{ct} signifies the faradaic interfacial charge-transfer resistance; and Z_w is the diffusion capacitance attributed to the diffusion process of vanadium ions (Wang and Wang, 2007; Wei et al., 2014).

According to the fitting results in **Table 2**, R_s increased gradually with increasing V(III) concentration, which was caused by the decreased conductivity of the electrolytes. R_{ct} decreased dramatically with increasing concentration of V(III), indicating the better electrochemical reactivity of a higher concentration of V(III), which was consistent with the CV results. Comparing the increased R_s with the decreased R_{ct}, the latter was much more remarkable, thus the electrochemical polarization was more prominent than the ohmic polarization on the SPGR in the V(III) acid electrolytes. For the electrolytes with different H_2SO_4 concentrations, R_s rapidly decreased with increasing H_2SO_4

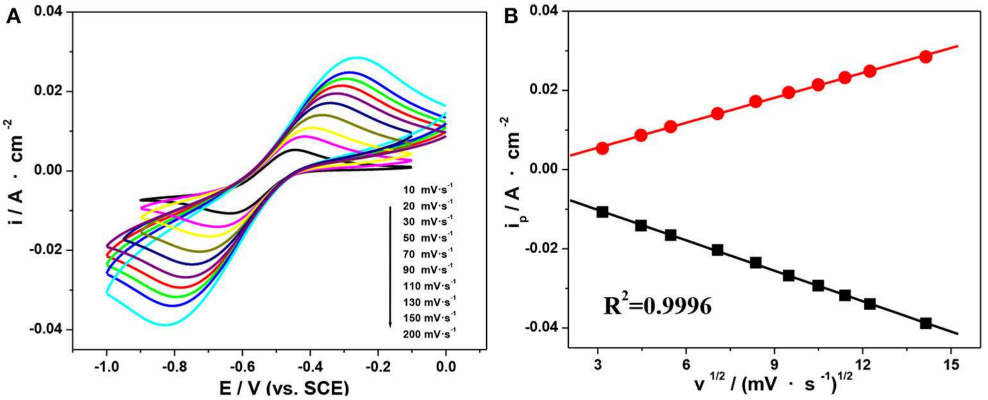

FIGURE 6 | CV curves on an SPGR recorded at different scan rates in 1.0 mol·L^{-1} V(III) with 2.0 mol·L^{-1} H_2SO_4 **(A)**. Peak current density as a function of the square root of the scan rate **(B)**.

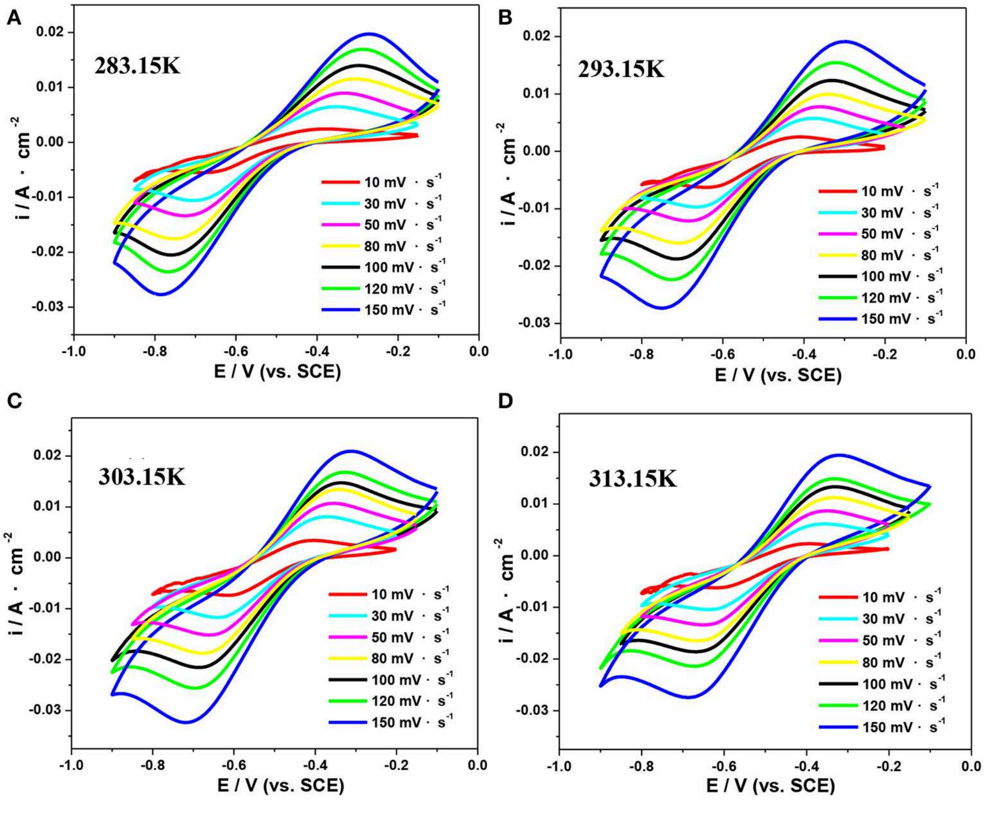

FIGURE 7 | CV curves of an SPGR in 0.5 mol·L^{-1} V(III) with 2.0 mol·L^{-1} H_2SO_4 electrolyte at 283.15 K **(A)**, 293.15 K **(B)**, 303.15 K **(C)**, and 313.15 K **(D)**.

concentration, owing to the greater conductivity of the electrolyte with a higher concentration of H^+. However, R_{ct} was almost unchanged with increasing H_2SO_4 concentration, suggesting that the electron transfer process of the V(III)/V(II) redox reaction had little relationship with H^+. In short, the concentration of H_2SO_4 mainly affected the ohmic resistance of the electrolyte, while the V(III) concentration mostly influenced its electron transfer resistance, which was consistent with the CV results.

Based on the above, the electrolyte containing 1.0 $mol \cdot L^{-1}$ V(III) and 2.0 $mol \cdot L^{-1}$ H_2SO_4 exhibited favorable electrochemical properties, so CV behaviors at different scan rates in that electrolyte were further investigated. As shown in **Figure 6A**, the oxidation and reduction peaks showed comparative symmetry at all scan rates, indicating a favorable electrochemical reversibility. In addition, the peak current proved to be proportional to the square root of the scan rate (**Figure 6B**), which suggested that the oxidation and reduction reaction of the V(III)/V(II) redox couples on an SPGR were controlled by the diffusion process (Wei et al., 2014).

Diffusion Kinetics Study of the V(III) Acid Electrolytes

CV is one of the most commonly used electrochemical techniques to study the electrode reaction kinetics. For an irreversible electrode process, the peak current density is given by Bard and Faulkner (2001):

$$i_p = 4.958 \times 10^{-4} nFC_b D^{1/2} V^{1/2} (-\alpha n_\alpha F/RT\ )^{1/2} \qquad (2)$$

where V is the potential sweep rate ($V \cdot s^{-1}$) and D is the diffusion coefficient of the active reactant ($cm^2 \cdot s^{-1}$). Based on Equation (2), we can obtain the value of $D_{V(III)}$ at different temperatures from the slope of the plot of i_p vs. $V^{1/2}$.

Moreover, the values of the reaction rate constant k_s can be calculated by Equation (3) (Bard and Faulkner, 2001):

$$i_p = 2.27 \times 10^{-4} nFC_b k_s \exp\left[-\alpha n_\alpha F\left(E_P - E^{O'}\right)/RT\right] \qquad (3)$$

where i_p is the peak current density ($A \cdot cm^{-2}$); E_p is the peak potential (V); C_b is the bulk concentration of the electroactive species ($mol \cdot L^{-1}$); k_s is the standard heterogeneous rate constant ($cm \cdot s^{-1}$); α is the charge transfer coefficient; $E^{O'}$ is the formal potential of the electrode; n is the number of electrons involved in the rate-limiting step; and other symbols such as F, R, and T have their usual meanings.

The formal potential $E^{O'}$ at different temperatures can be calculated by Equation (4) (Bard and Faulkner, 2001):

$$E^{\circ\prime} = \frac{\sum_{i=1}^{j}\left(E_{pa_j} + E_{pcj}\right)/2}{j} \qquad (4)$$

where j is the total number of potential scans applied in the CV tests; E_{pa} is the anodic peak potential; and E_{pc} is the cathodic peak potential.

TABLE 3 | The mean values of $-i_{pc}/i_{pa}$ and the formal potential ($E^{O'}$) calculated from the CV curves in **Figure 7**.

T (K)	**$-i_{pc}/i_{pa}$**	**$E^{O'}$ (V)**
283.15	1.48	−0.529
293.15	1.53	−0.524
303.15	1.49	−0.511
313.15	1.41	−0.509

TABLE 4 | Rate constant of the reduction reaction (k_s) and the diffusion coefficient ($D_{V(III)}$) of V(III) at different temperatures.

T (K)	**$D_{V(III)}$ (10^{-7} $cm^2 \cdot s^{-1}$)**	**k_s (10^{-5} $cm \cdot s^{-1}$)**	**η ($mm^2 \cdot s^{-1}$)**
283.15	5.03	6.84	2.22
293.15	5.53	14.2	1.71
303.15	8.27	16.6	1.37
313.15	11.9	26.6	1.13

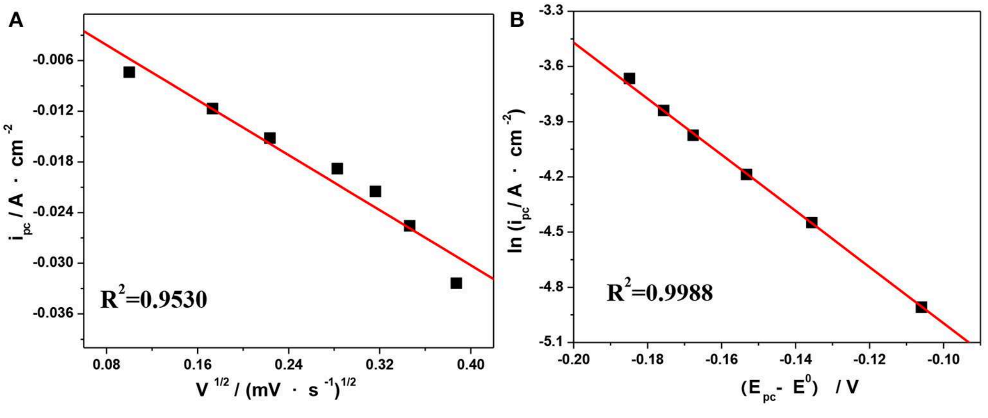

FIGURE 8 | Plots of i_{pc} vs. $V^{1/2}$ **(A)** and ln i_{pa} vs. (E_{pc}–$E^{O'}$) **(B)** at 303.15 K from the CV curves in **Figure 7C**.

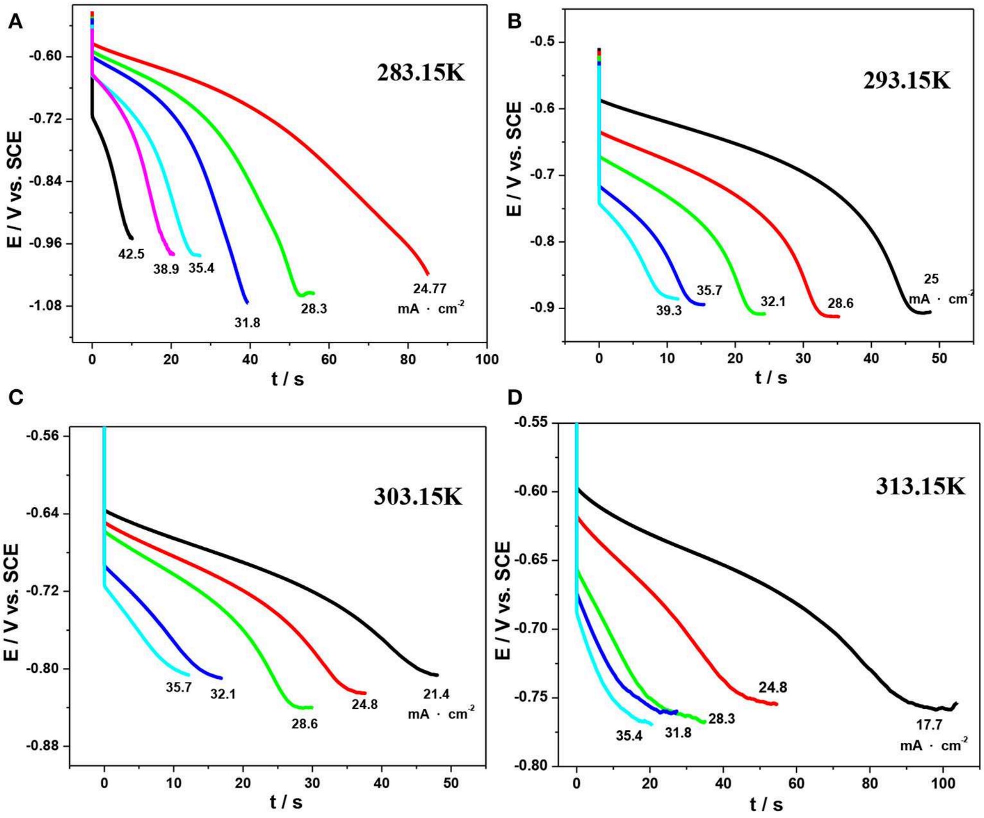

FIGURE 9 | Chronopotentiograms for the reduction reaction of V(III) on an SPGR in 1.0 mol·L^{-1} V(III) with 2.0 mol·L^{-1} H_2SO_4 at various temperatures: 283.15 K **(A)**, 293.15 K **(B)**, 303.15 K **(C)**, and 313.15 K **(D)**.

Herein, CV tests in an electrolyte consisting of 0.5 mol·L^{-1} V(III) with 2.0 mol·L^{-1} H_2SO_4 at different temperatures were conducted to study their electrode reaction kinetics. **Figure 7** shows the typical CV curves at scan rates ranging from 10 to 200 mV·s^{-1} at 283.15, 293.15, 303.15, and 313.15 K, respectively. As shown in **Figure 7**, ΔE_p was significantly >60 mV, indicating the electrochemical irreversibility of the V(III)/V(II) redox reaction (Kazacos et al., 1990; Aaron et al., 2013).

The mean values of $-i_{pc}/i_{pa}$ and the formal potential $E^{O'}$ at different scan rates obtained from the CV curves in **Figure 7** are listed in **Table 3**. The values of $-i_{pc}/i_{pa}$ changed slightly with the temperature, suggesting an insignificant effect of temperature on the reversibility of the V(III)/V(II) redox reaction.

The values of the anodic charge transfer coeffcient (α) and electron transfer number (n) have been estimated to be 0.56 and 1, respectively, according to our earlier work (Jing, 2017). Based on Equation (2–3) in Jing (2017), we can deduce a linear relationship between i_{pc} vs. $V^{1/2}$ and ln i_{pc} vs. (E_p- $E^{O'}$). The corresponding results measured at 303.15 K are shown in **Figures 8A,B**. Next, the values of $D_{\mathrm{V(III)}}$ and k_s at different temperatures can be calculated according to the slope of the linear curves in **Figures 8A,B**, respectively. For comparison, the viscosities (η) measured by Ubbelohde viscometry under different temperatures are listed in **Table 4**.

The results in **Table 4** show that the values of the reaction rate constants (k_s) were of the order of 10^{-5} cm·s^{-1} and became larger with increasing temperature, which suggested that a higher temperature might facilitate the V(III)/V(II) redox reaction. Furthermore, $D_{\mathrm{V(III)}}$ increased from 5.034×10^{-7} cm^2·s^{-1} at 283.15 K to 11.9×10^{-7} cm^2·s^{-1} at 313.15 K, suggesting that an increased temperature was beneficial to the mass transfer of V(III), which was also reflected in the change of viscosity. Indeed, the diffusion coefficient of the active ion has an important effect on the battery performance. The larger coefficient suggests a faster ion migration rate, which is conducive to the mass transfer kinetics of the electrode reaction reducing the concentration polarization of the battery under a higher current density and leading to a better rate capability and electrolyte utilization rate.

However, as mentioned above, CV is not an ideal quantitative method to determine the kinetic parameters of the peak current. Herein, chronopotentiometry was carried out as it is a promising approach to obtain the diffusion coefficient by Sand's equation (Kazacos et al., 1990; Sepehr and Paddison, 2016). The corresponding potential–time curves under various temperatures are shown in **Figure 9**.

For an irreversible or reversible reaction, Sand's equation is given by Kazacos et al. (1990):

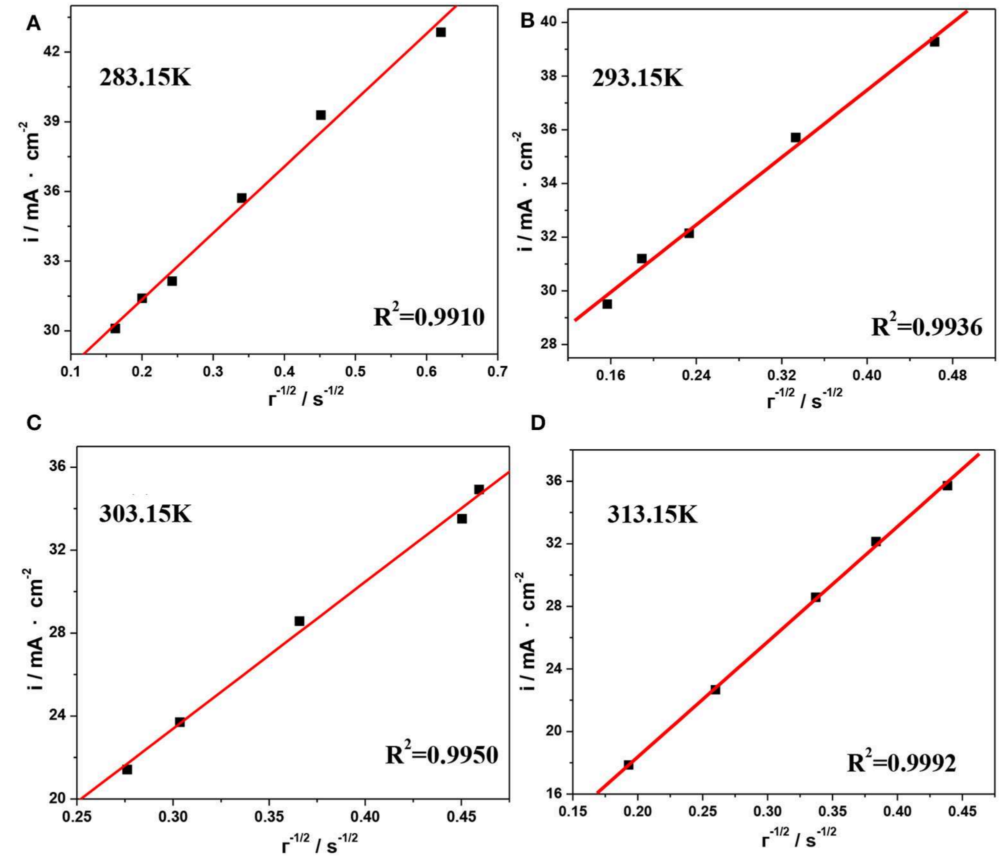

FIGURE 10 | Current density as a function of the reciprocal of the square root of the transition time for the reduction reaction of V(III) at different temperatures, **(A)** 283.15 K, **(B)** 293.15 K, **(C)** 303.15 K, and **(D)** 313.15 K.

TABLE 5 | Diffusion coefficients of V(III) ions calculated from **Figure 10** at different temperatures.

***T* (K)**	**$D_{V(III)}$ (10^{-7} $cm^2 \cdot s^{-1}$)**
283.15	1.09
293.15	1.30
303.15	1.60
313.15	1.95

$$\tau = \frac{n^2 F^2 \pi D C_b^2}{4i^2} \tag{5}$$

where τ is the total time taken to achieve an abrupt change in the potential of the electrode and i is the current density. The values of τ are determined as the transition time when the absolute values of the slope of the plots increase abruptly.

The plots of i vs. $\tau^{1/2}$ obtained from **Figure 9** are shown in **Figure 10**, and the values of $D_{V(III)}$ calculated from the slopes of these plots are listed in **Table 5**. By comparing the $D_{V(III)}$ values in **Tables 4**, **5**, it can be seen that the values of $D_{V(III)}$ obtained from CV and chronopotentiometry were of the same order (10^{-7} $cm^2 \cdot s^{-1}$), but there was a smaller variability when changing the temperature, which might result in a smaller deviation of the calculated $D_{V(III)}$ values.

Based on the chronopotentiometry results, the diffusion activation energy, E_D, can be obtained from the slope of the plot of ln $D(T)$ vs. $1/T$ by the Arrhenius equation (Zha, 2002):

$$D(T) = D_0 \exp(-E_D/RT) \tag{6}$$

where D_0 is a temperature-independent factor ($cm^2 \cdot s^{-1}$) and E_D is the diffusion activation energy.

The shift of ln $D(T)$ with $1/T$ is shown in **Figure 11**, from where the values of E_D and D_0 can be estimated as 13.7 kJ·mol^{-1} and 1.3×10^{-4} $cm^2 \cdot s^{-1}$, respectively. As a result, the diffusion coefficient of V(III) can be expressed as follows:

$$D_{V(III)} = 1.3 \times 10^{-4} \exp 13700/RT \tag{7}$$

which could be used to estimate the diffusion behavior of V(III). In summary, an increase in temperature could facilitate the V(III)/V(II) redox reaction and improve the mobility of V(III) ions in the negative electrolyte, which would result in improved electrochemcial performance. However, the more intense hydrogen evolution at higher temperatures should also be considered.

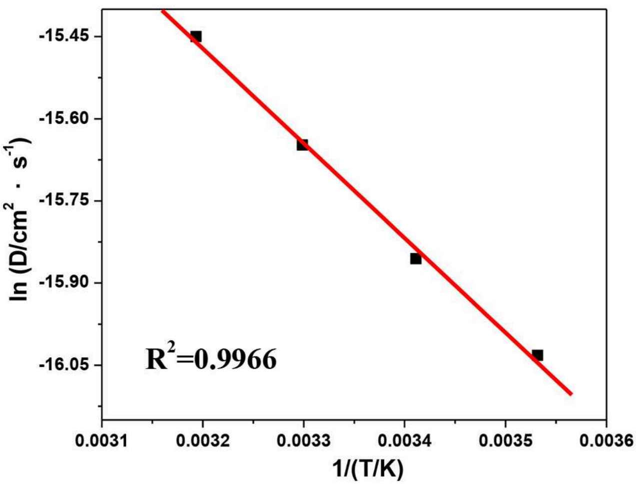

FIGURE 11 | Plot of ln *D(T)* vs. *1/T*.

CONCLUSION

In this work, the physical and electrochemical characteristics of the V(III) acidic electrolytes at different concentrations and with different diffusion kinetics have been systemically investigated. The results show that the surface tension and viscosity of the V(III) acidic electrolyte were mainly affected by the V(III) concentration and that they were in direct proportion to each other, which suggested the negative effects of a high concentration of V(III) on the mass transfer kinetics. As the supporting electrolyte, the H_2SO_4 concentration had a significant effect on the conductivity of the electrolyte; however, the higher H_2SO_4 concentration might result in significant hydrogen evolution and increased mass transfer resistance. The electrochemical measurements showed that a higher V(III) concentration would facilitate the redox reactions of V(III)/V(II), while the increase in H_2SO_4 concentration could improve the ion transmission and had little effect on the electron transfer process. In addition, the diffusion kinetics of V(III) were further studied by CV and the chronopotentiometry method. The results demonstrated that an elevated temperature would facilitate the V(III)/V(II) redox reaction, and so the reaction rate constant (k_s) and diffusion coefficient [$D_{\text{V(III)}}$] were obtained at different temperatures. On this basis, the diffusion activation energy (13.7 kJ·mol^{-1}) and the diffusion equation for V(III) are provided to integrate kinetic theory in the redox reaction of V(III)/V(II).

DATA AVAILABILITY STATEMENT

The raw data supporting the conclusions of this article will be made available by the authors, without undue reservation.

AUTHOR CONTRIBUTIONS

MJ, ZX, and XA carried out the experiment. MJ and CL wrote the manuscript with support from JL and CY. XF conceived the original idea and supervised the project. All authors contributed to the article and approved the submitted version.

FUNDING

This work was funded by the Natural Science Foundation of China (21703263), Open Project of the State Key Laboratory of Heavy Oil Processing in China University of Petroleum (Y7F1911191), Science and Technology Seedling Project of Education Department of Liaoning Province (LQN201911), and Youth Research Funding of Liaoning University (LDQN2019019).

REFERENCES

Aaron, D., Sun, C., Bright, M., Papandrew, A., Mench, M., and Zawodzinski, T. (2013). In situ kinetics studies in all-vanadium redox flow batteries. *ECS Electrochem. Lett.* 2, A29–A31. doi: 10.1149/2.001303eel

Agar, E., Dennison, C., Knehr, K., and Kumbur, E. (2013). Identification of performance limiting electrode using asymmetric cell configuration in vanadium redox flow batteries. *J. Power Sources* 225, 89–94. doi: 10.1016/j.jpowsour.2012.10.016

Bard, A., and Faulkner, L. (2001). *Electrochemical Methods-Fundamentals and Applications*, 2nd Edn. New York, NY: Wiley-Interscience.

Cao, C., and Zhang, J. (2002). *An Introduction to Electrochemical Impedance Spectroscopy*. Beijing: Science Press.

Chakrabarti, M., Brandon, N., Hajimolana, S., Tariq, F., Yufit, V., Hashim, M., et al. (2014). Application of carbon materials in redox flow batteries. *J. Power Sources* 253, 150–166. doi: 10.1016/j.jpowsour.2013.12.038

Ding, C., Zhang, H., Li, X., Liu, T., and Xing, F. (2013). Vanadium flow battery for energy storage: prospects and challenges. *J. Phys. Chem. Lett.* 4, 1281–1294. doi: 10.1021/jz4001032

Iwasa, S., Wei, Y., Fang, B., Arai, T., and Kumagai, M. (2003). Electrochemical behavior of the V(IV)/V(V) couple in sulfuric acid medium. *Bat. Bimonthly* 33, 339–341. Available online at: http://en.cnki.com.cn/Article_en/CJFDTotal-DACI200306022.htm

Jing, M. (2017). *Kinetics of the Negative Electrode Processes of the Vanadium Redox Flow Battery and Preparation of Highly Effective Electrode Materials*. University of Chinese Academy of Sciences.

Jing, M., Wei, Z., Su, W., He, H., Fan, X., Qin, Y., et al. (2016). Improved electrochemical performance for vanadium flow battery by optimizing the concentration of the electrolyte. *J. Power Sources* 324, 215–223. doi: 10.1016/j.jpowsour.2016.05.099

Joerissen, L., Garche, J., Fabjan, C., and Tomazic, G. (2004). Possible use of vanadium redox-flow batteries for energy storage in small grids and stand-alone photovoltaic system. *J. Power Sources* 127, 98–104. doi: 10.1016/j.jpowsour.2003.09.066

Kazacos, M., Cheng, M., and Skyllas-Kazacos, M. (1990). Vanadium redox cell electrolyte optimization studies. *J. Appl. Electrochem.* 20, 463–467.

Lee, J., Hong, J., and Kjeang, E. (2012). Electrochemical characteristics of vanadium redox reactions on porous carbon electrodes for microfluidic fuel cell applications. *Electrochim. Acta* 83, 430–438. doi: 10.1016/j.electacta.2012.07.104

Liu, H., Xu, Q., Yan, C., Cao, Y., and Qiao, Y. (2011). The effect of temperature on the electrochemical behavior of the V(IV)/V(V) couple on a graphite electrode. *Int. J. Electrochem. Sci.* 6, 3483–3496. Available online at: http://electrochemsci.org/papers/vol6/6083483.pdf

Lou, X., Yuan, D., Yu, Y., Lei, Y., Ding, M., Sun, Q., et al. (2020). A cost-effective nafion composite membrane as an effective vanadium-ion barrier for vanadium redox flow batteries. *Chem. Asian J.* 15, 1–8. doi: 10.1002/asia.202000140

Oriji, G., Katayama, Y., and Miura, T. (2005). Investigations on V(IV)/V(V) and V(II)/V(III) redox reactions by various electrochemical methods. *J. Power Sources* 139, 321–324. doi: 10.1016/j.jpowsour.2004.03.008

Rahman, F., and Skyllas-Kazacos, M. (2009). Vanadium redox battery: positive half-cell electrolyte studies. *J. Power Sources* 189, 1212–1219. doi: 10.1016/j.jpowsour.2008.12.113

Rychcik, M., and Skyllas-Kazacos, M. (1988). Characteristics of a new all-vanadium redox flow battery. *J. Power Sources* 22, 59–67. doi: 10.1016/0378-7753(88)80005-3

Sepehr, F., and Paddison, S. (2016). Effect of sulfuric and triflic acids on the hydration of vanadium cations: an *ab initio* study. *J. Phys. Chem. A* 119, 5749–5761. doi: 10.1021/acs.jpca.5b01794

Sukkar, T., and Skyllas-Kazacos, M. (2004). Membrane stability studies for vanadium redox cell applications. *J. Appl. Electrochem.* 34, 137–145. doi: 10.1023/B:JACH.0000009931.83368.dc

Sum, E., Rychcik, M., and Skyllas-Kazacos, M. (1985). Investigation of the V(V)/V(IV) system for use in the positive half-cell of a redox battery. *J. Power Sources* 16, 85–95. doi: 10.1016/0378-7753(85)80082-3

Sum, E., and Skyllas-Kazacos, M. (1982). A study of the V(II)/V(III) redox couple for redox flow cell applications. *J. Power Sources* 15, 179–190. doi: 10.1016/0378-7753(85)80071-9

Sun, B., and Skyllas-Kazacos, M. (1992). Modification of graphite electrode materials for vanadium redox flow battery application-I thermal treatment. *Electrochim. Acta* 37, 1253–1260. doi: 10.1016/0013-4686(92)85064-R

Sun, C., Delnick, F., Aaron, D., Papandrew, A., Mench, M., and Zawodzinski, T. (2016). Probing electrode losses in all-vanadium redox flow batteries with impedance spectroscopy. *ECS Electrochem. Lett.* 2, A43–A45. doi: 10.1149/2.001305eel

Wang, W., Fan, X., Liu, J., Yan, C., and Zeng, C. (2014). Temperature-related reaction kinetics of the vanadium (IV)/(V) redox couple in acidic solutions. *RSC Adv.* 4, 32405–32411. doi: 10.1039/C4RA04278F

Wang, W., and Wang, X. (2007). Investigation of Ir-modified carbon felt as the positive electrode of an all-vanadium redox flow battery. *Electrochim. Acta* 52, 6755–6762. doi: 10.1016/j.electacta.2007.04.121

Wei, G., Fan, X., Liu, J., and Yan, C. (2014). Investigation of the electrospun carbon web as the catalyst layer for vanadium redox flow battery. *J. Power Sources* 270, 634–645. doi: 10.1016/j.jpowsour.2014.07.161

Xia, L., Zhang, Q., Wu, C., Liu, Y., Ding, M., Ye, J., et al. (2019). Graphene coated carbon felt as a high-performance electrode for all vanadium redox flow batteries. *Surf. Coat. Tech.* 358, 153–158. doi: 10.1016/j.surfcoat.2018.11.024

Xiao, S., Yu, L., Wu, L., Liu, L., Qiu, X., and Xi, J. (2016). Broad temperature adaptability of vanadium redox flow battery—Part 1: electrolyte research. *Electrochim. Acta* 187, 525–534. doi: 10.1016/j.electacta.2015.11.062

Yamamura, T., Watanabe, N., Yano, T., and Shiokawa, Y. (2005). Electron-transfer kinetics of Np^{3+}/Np^{4+}, NpO_2^+ / NpO_2^{2+}, V^{2+}/V^{3+}, and VO^{2+}/VO_2^+ at carbon electrodes. *J. Electrochem. Soc.* 152, A830–A836. doi: 10.1149/1.1870794

Ye, J., Cheng, Y., Sun, L., Ding, M., Wu, C., Jia, C., et al. (2019). A green SPEEK/lignin composite membrane with high ion selectivity for vanadium redox flow battery. *J. Membrane Sci.* 572, 110–118. doi: 10.1016/j.memsci.2018.11.009

Ye, J., Wu, C., Qin, W., Zhong, F., and Ding, M. (2020a). Advanced sulfonated poly (Ether Ketone)/graphene-oxide/titanium dioxide nanoparticle composited membrane with superior cyclability for vanadium redox flow battery. *J. Nanosci. Nanotechnol.* 20, 4714–4721. doi: 10.1166/jnn.2020.18503

Ye, J., Zhao, X., Ma, Y., Su, J., Xiang, C., Zhao, K., et al. (2020b). Hybrid membranes dispersed with superhydrophilic TiO_2 nanotubes toward ultra-stable and high-performance vanadium redox flow batteries. *Adv. Energy Mater.* 10:1904041. doi: 10.1002/aenm.201904041

Yi, Q., Liu, Y., Zhao, H., Zhou, X., Liu, X., and Song, H. (2003). Effects of acidity, temperature and surfactants on electrochemical behavior of V^{5+} ion in sulfuric acid solutions. *T. Nonferr. Metal. Soc.* 13, 1465–1471. Available online at: http://www.cqvip.com/qk/85276x/200306/8999397.html

Yu, L., Lin, F., Xiao, W., Xu, L., and Xi, J. (2019). Achieving efficient and inexpensive vanadium flow battery by combining $Ce_xZr_{1-x}O_2$ electrocatalyst and hydrocarbon membrane. *Chem. Eng. J.* 356, 622–631. doi: 10.1016/j.cej.2018.09.069

Zha, Q. (2002). *Introduction to the Kinetics of Electrode Process*, 3rd Edn. Beijing: Science and Technology Education Press.

Zhang, H. (2014). *Flow Battery Technology*. Beijing: Chemical Industry Press.

Zhao, P., Zhang, H., Zhou, H., Chen, J., Gao, S., and Yi, B. (2006). *In situ* surface enhanced Raman spectroscopic studies of solid electrolyte interphase formation in lithium ion battery electrodes. *J. Power Sources* 162, 1416–1420. doi: 10.1016/j.jpowsour.2006.08.016

Zheng, Q., Li, X., Cheng, Y., Ning, G., Xing, F., and Zhang, H. (2016). Development and perspective in vanadium flow battery modeling. *Appl. Energy* 132, 254–266. doi: 10.1016/j.apenergy.2014.06.077

Zhong, S., and Skyllas-Kazacos, M. (1992). Electrochemical behaviour of vanadium(V)/vanadium(IV) redox couple at graphite electrodes. *J. Power Sources* 39, 1–9. doi: 10.1016/0378-7753(92)85001-Q

Conflict of Interest: The authors declare that the research was conducted in the absence of any commercial or financial relationships that could be construed as a potential conflict of interest.

frontiers
in Chemistry

MINI REVIEW
published: 24 July 2020
doi: 10.3389/fchem.2020.00557

Inhibition of Zinc Dendrites in Zinc-Based Flow Batteries

Leibin Guo[1], Hui Guo[1], Haili Huang[1]*, Shuo Tao[2] and Yuanhui Cheng[1]*

[1] College of Chemical Engineering, Beijing University of Chemical Technology, Beijing, China, [2] School of Chemistry and Chemical Engineering, Shandong Provincial Key Laboratory of Chemical Energy Storage and Novel Cell Technology, Liaocheng University, Liaocheng, China

Zinc-based flow batteries have gained widespread attention and are considered to be one of the most promising large-scale energy storage devices for increasing the utilization of intermittently sustainable energy. However, the formation of zinc dendrites at anodes has seriously depressed their cycling life, security, coulombic efficiency, and charging capacity. Inhibition of zinc dendrites is thus the bottleneck to further improving the performance of zinc-based flow batteries, but it remains a major challenge. Considering recent developments, this mini review analyzes the formation mechanism and growth process of zinc dendrites and presents and summarizes the strategies for preventing zinc dendrites by regulating the interfaces between anodes and electrolytes. Four typical strategies, namely electrolyte modification, anode engineering, electric field regulation, and ion transfer control, are comprehensively highlighted. Finally, remaining challenges and promising directions are outlined and anticipated for zinc dendrites in zinc-based flow batteries.

Keywords: flow battery, zinc deposition, zinc dendrites, interfaces engineering, energy storage and conversion, rechargeable battery

Edited by:
Chuankun Jia,
Changsha University of Science and Technology, China

Reviewed by:
Ao Tang,
Institute of Metals Research (CAS), China
Hui Chen,
Yancheng Institute of Technology, China

****Correspondence:***
Haili Huang
hlhuang@mail.buct.edu.cn
Yuanhui Cheng
chengyh@mail.buct.edu.cn

Specialty section:
This article was submitted to Electrochemistry,
a section of the journal Frontiers in Chemistry

Received: *30 April 2020*
Accepted: *02 June 2020*
Published: *24 July 2020*

Citation:
Guo L, Guo H, Huang H, Tao S and Cheng Y (2020) Inhibition of Zinc Dendrites in Zinc-Based Flow Batteries. Front. Chem. 8:557.
doi: 10.3389/fchem.2020.00557

INTRODUCTION

Energy and environment are the foundation of human survival and development (Zhang et al., 2019a). To meet increasing requirements, people are exploring sustainable and clean energy (Turner, 1999). However, sustainable and clean energy, represented by wind, solar, and tidal, are affected by climate and cannot directly generate continuous and stable electrical power (Yang et al., 2011; Lou et al., 2020). Large-scale energy storage devices seem to be the best choice for collecting the fluctuating energy and outputting high-quality power (Dunn et al., 2011; Leadbetter and Swan, 2012).

Flow batteries have received widespread attention due to their high safety and low cost (Liu et al., 2019a; Zhang et al., 2019a; Ye et al., 2020a,b). Their power and capacity can be designed independently. The power is determined by the number and size of the stacks, while the capacity is limited by the volume and concentration of the electrolyte outside stacks. Their capacity can be easily be increased by increasing the number of redox couples in the electrolyte without adding other equipment. Therefore, flow batteries are very suitable for large-scale energy storage.

Zinc-based flow batteries (ZFBs) have the advantages of low cost, high safety, flexible structure, and high energy efficiency and have been extensively studied (Arenas et al., 2018). Various ZFBs have been proposed, such as the zinc-bromine flow battery (Jeon et al., 2014; Suresh et al., 2014), zinc-iodine flow battery (Xie et al., 2019), zinc-nickel flow battery (Cheng et al., 2014b, 2019c; Huang et al., 2018), zinc-air flow battery (Cheng et al., 2018, 2019b), zinc-iron flow battery (Yuan et al., 2018a; Chang et al., 2019), and zinc-manganese flow battery (Liu et al., 2020). Some of these flow batteries, like the zinc-bromine flow battery, zinc-nickel flow battery, zinc-air flow battery, and zinc-iron battery, are already in the demonstration stage and are close to commercial application (Arenas et al., 2018).

The structure and mechanism of ZFBs are shown in **Figure 1A**. The electrochemical reaction at the anode side is zinc deposition and stripping. This is a little different in aqueous acid/neutral and alkaline solutions (Khor et al., 2018).

(1) Acid or neutral solution
$Zn^{2+} + 2e^- \leftrightarrow Zn \qquad E^o = -0.763\ V\ \ vs.\ SHE$
(2) Alkaline solution
$Zn(OH)_4^{2-} + 2e^- \leftrightarrow Zn + 4OH^- \qquad E^0 = -1.216 \quad V\ vs.\ SHE$

However, zinc dendrites are formed during the charging process and eventually pierce the separator, resulting in short circuit and battery failure (**Figure 1B**). Moreover, zinc dendrites can easily fall from anodes, resulting in a decrease in efficiency and capacity (Cheng et al., 2014a). Therefore, inhibiting zinc dendrite formation is very important for the further development of ZFBs. Recently, researchers have done a lot of work to solve zinc dendrite formation through modifications to the electrolyte, anodes, electric field, and zinc ion transfer. In this review, we will introduce the formation and growth mechanism of zinc dendrites, summarize typical methods for solving zinc dendrite formation, and outline promising future directions.

FORMATION MECHANISM OF ZINC DENDRITES

Zinc deposition begins with nucleation and continues with growth (Yufit et al., 2019; Zheng et al., 2019). The energy barrier for zinc nucleation is much higher than for zinc growth on the nucleus, as shown in **Figure 1C** (Zeng et al., 2019; Zhang et al., 2020). As a result, the overpotential of zinc nucleation is also larger than that of zinc growth on the nucleus (**Figure 1D**; Zhang et al., 2019b, 2020). This indicates that once a zinc nucleus forms, zinc ions prefer to deposit on the nucleus rather than to produce a new nucleus. Moreover, small nuclei have high surface energy and thermodynamically tend to aggregate into larger particles (Pei et al., 2017; Cheng et al., 2019a). Therefore, it is very difficult to obtain uniform zinc nuclei on the anode.

During the growth process, zinc ions migrate to a nucleus under the driving forces of electric fields and concentration gradients (Wang et al., 2015; Lacitignola et al., 2017). The distributions of the electric field and zinc ions at the interface between anodes and electrolytes play an important role in zinc deposition (Cheng et al., 2013b, 2014a). A uniform electric field is favorable for both the nucleation and growth of zinc deposits. Unfortunately, the electric field is much stronger in the areas adjacent to current collectors than at edges and corners far away from current collectors (Cheng et al., 2013b). After zinc ions at the interface are consumed, zinc ions that exist in the electrolyte far from the interface cannot migrate to the interface in time, resulting in severe concentration polarization (Wang et al., 2015). Simultaneously, zinc ions preferentially migrate to the protruding tips of anodes and subsequently grow on previously deposited zinc seeds, which accelerates the formation of zinc dendrites (Lu et al., 2018). Additionally, hydrogen evolution at an anode also makes mass transfer more difficult (Ito et al., 2011a; Dundalek et al., 2017). This phenomenon is more serious in the case of the rapid deposition of zinc ions at large anodes (Cheng et al., 2015, 2019c).

STRATEGIES TO PREVENT ZINC DENDRITE FORMATION

Recently, various methods have been proposed to inhibit zinc dendrite formation, including electrolyte modification (Wen et al., 2012; Banik and Akolkar, 2013; Kim et al., 2019), anode engineering (Lin, 2018; Suresh et al., 2019; Yin et al., 2020), electric field regulation (Cheng et al., 2014a; Nikiforidis et al., 2014; Yuan et al., 2018b), and ion transfer control (Ito et al., 2011b; Song et al., 2014; Wang et al., 2014). In this section, we will introduce the typical solutions for preventing zinc dendrite formation in ZFBs from the above four aspects, as shown in **Figure 2**.

Electrolyte Modification

Organic molecules, polymers, and metal ions are common additives for inhibiting zinc dendrites. Organic molecules and polymers can selectively adsorb onto the protruding parts of anodes and act as a barrier to the access of zinc ions (Mitha et al., 2018; Chladil et al., 2019). Therefore, they prevent zinc deposition on protruding parts and accelerate zinc nucleation and growth on dents by steric effects and/or electrostatic shielding. Compared with polymers, organic molecules have shorter chain lengths, and smaller end steric hindrances. Organic molecules are more likely to cover protruding parts and delay the deposition of zinc ions. Generally, the higher the polarity of the organic additives, the stronger the adsorption on anodes. However, excessively strong adsorption will result in severe electrochemical polarization for zinc deposition. Metal ions can affect the nucleation of zinc and thereby influence the growing process, and so, a uniform and compact zinc deposits layer can be obtained.

Organic molecules include non-ionic dimethyl sulfoxide (Hosseini et al., 2019), thiourea (Goh et al., 2014; Sun et al., 2017), diethyl ether (Xu et al., 2019), polyacrylic acid (Shimizu et al., 2019); cationic quaternary ammonium (Rossi et al., 2020), benzyl trimethyl ammonium hydroxide (Liu et al., 2019b), trimethyl octadecyl ammonium chloride (Shimizu et al., 2019), hexadecyl trimethyl ammonium bromide (Chladil et al., 2019), anionic sodium dodecyl sulfate (Miyazaki et al., 2016; Hosseini et al., 2018; Shimizu et al., 2019), and EMI-PF6 and EMI-TFSA (Song et al., 2016). Polymers include polyethyleneimine (Banik and Akolkar, 2015; Hashemi et al., 2017), Triton X-100 (Kan et al., 1998), polyvinyl alcohol (Ortiz-Aparicio et al., 2013), polyethylene glycol (Lee et al., 2006a; Ballesteros et al., 2007; Banik and Akolkar, 2013), polyacrylamide (Zhang et al., 2019b), Tween 20 (Chladil et al., 2019), and Pluronic F-127 (Hosseini et al., 2018). Metal ions comprise Pb^{2+} (Justinijanović et al., 1973;

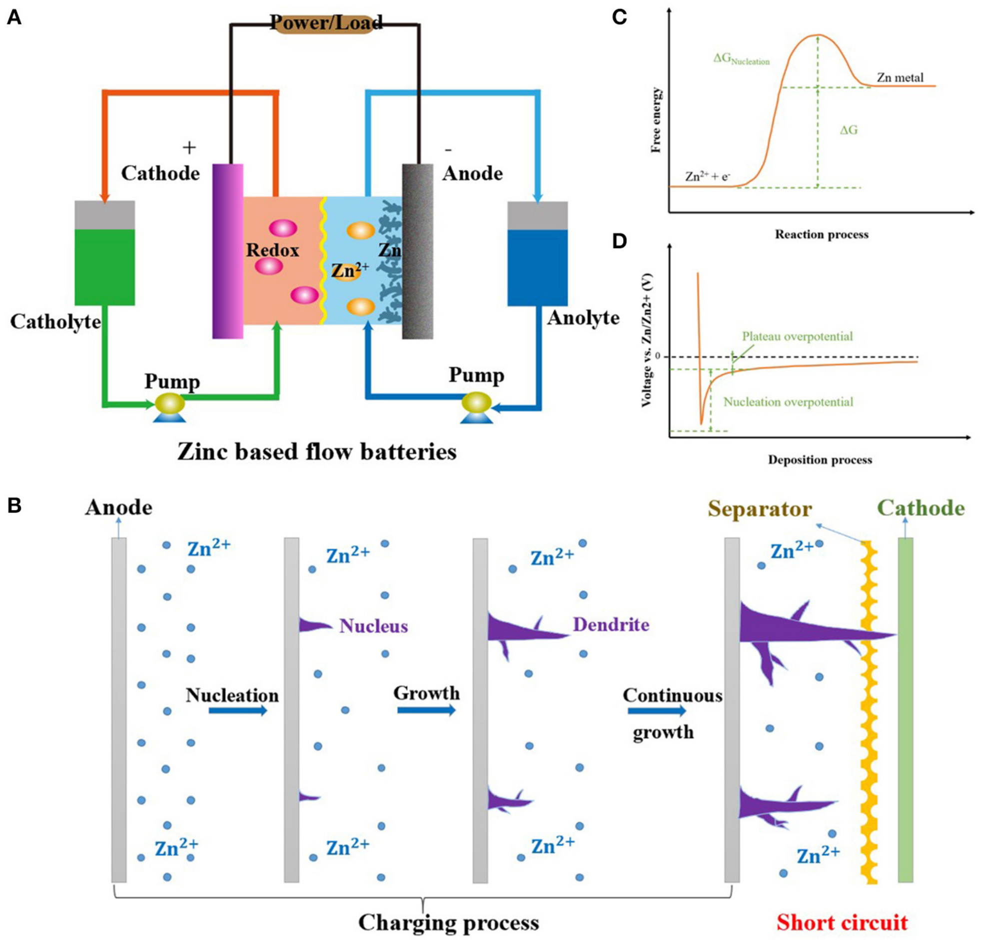

FIGURE 1 | (A) Principle and structure of typical ZFBs. **(B)** Schematic of the nucleation and growth processes of zinc dendrites. **(C)** The energy barrier for the zinc nucleation and growth processes. **(D)** Overpotential of zinc nucleation and growth processes. Reproduced from Pei et al. (2017) with permission. Copyright 2017 American Chemical Society.

Wen et al., 2012), Sn^{2+} (Yuan et al., 2007; Kim and Shin, 2015; Yao et al., 2019), Bi^{3+} (Wang et al., 2001), In^{3+} (Leung et al., 2011), and La^{3+} (Yang et al., 2004).

For example, cationic 1-Ethyl-1-methyl-pyrrolidinium bromide was employed as an additive in electrolytes of zinc-bromine flow batteries to prevent zinc-dendrite development through forming an electrostatic shield in and around the zinc dendrite during the charging process (**Figures 2a–c**; Kim et al., 2019). The zinc deposits were uniform and compact, but the charging overpotential increased by 47 mV, and discharging overpotential increased by 98 mV. The cycling life of zinc-bromine flow batteries was improved by sacrificing voltage efficiency.

Tin ions promote the formation of crystal seeds and substantially improve the charge retention of the zinc-nickel flow battery. Interestingly, only a slightly negative shift in the initial potential of zinc nucleation was observed, and the rate performance and polarization properties of zinc anodes were no significantly reduced (Yao et al., 2019).

The synergy between various additives should also be noted. The synergistic effect of lead ions and TBAB can inhibit the growth of zinc dendrites, thereby obtaining smooth and dense zinc deposits in alkaline zincate electrolytes. This is beneficial for improving the cycling life of zinc-nickel flow batteries (Wen et al., 2012).

Anode Engineering

The physicochemical properties and structure of anodes have an important effect on zinc deposition (Wei et al., 2016; Parker et al., 2017; Jiang et al., 2018). As zinc randomly deposits onto and strips from the anode, cracks are inevitable after repeated charge-discharge cycles when using pure zinc foils/sheets as anodes (Cheng et al., 2019b). To avoid rapid failure, conductive materials are usually used as a host for zinc deposition/dissolution, such as carbon (Jiang et al., 2018; Lin, 2018; Shen et al., 2018; Suresh et al., 2019; Zeng et al., 2019; Zhang et al., 2019b), nickel (Cheng et al., 2013a), copper (Zhang et al., 2019b), lead (Zhang et al., 2008), tin (Yin et al., 2020), chromium (Zhang et al., 2008), indium (Lee

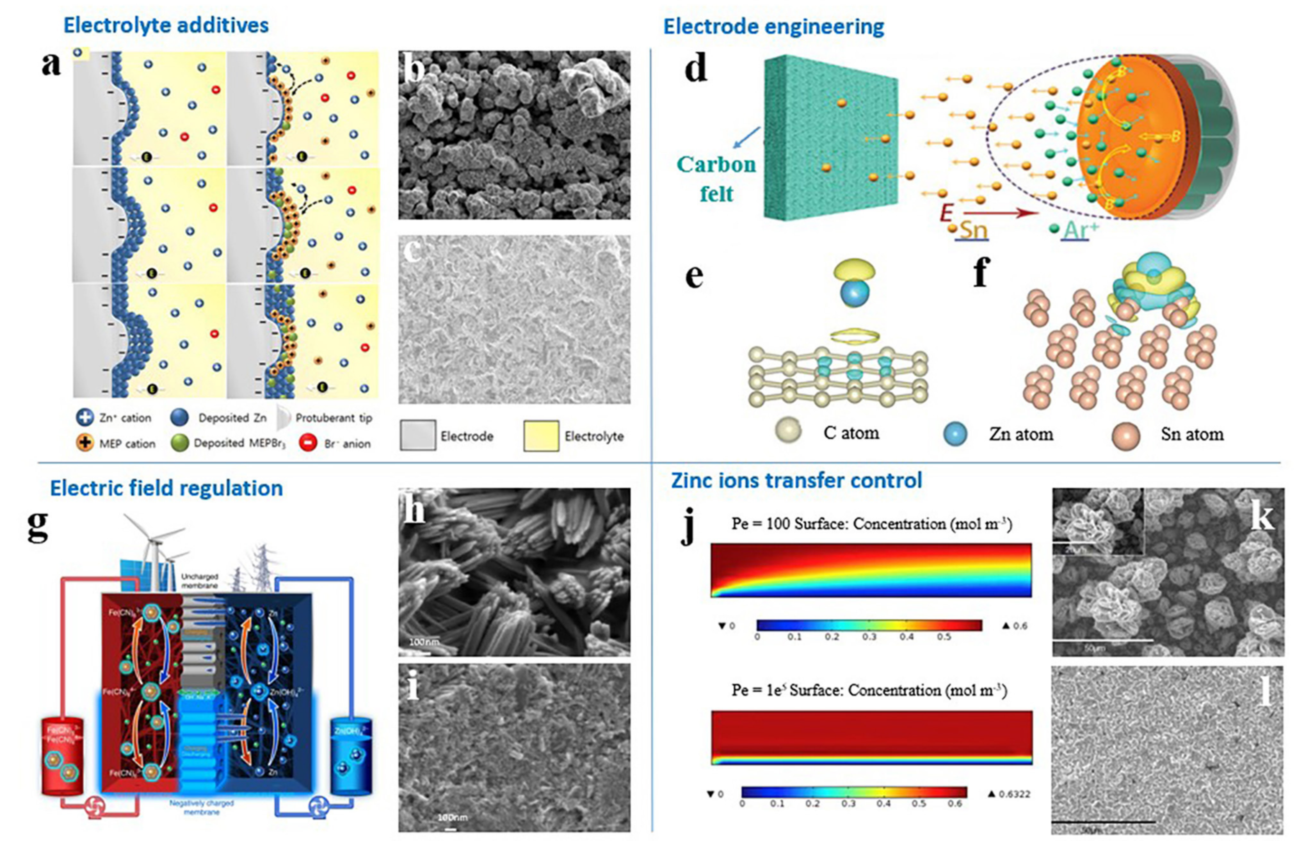

FIGURE 2 | (a) Illustration of the prevention of zinc dendrite formation by cationic 1-Ethyl-1-methyl-pyrrolidinium bromide (MEP·Br) through an electrostatic shielding effect. **(b)** Without and **(c)** with 1.2 M MEP·Br in 2.0 M zinc-bromide electrolyte solution. X100 magnification of deposited zinc. **(a–c)** Reproduced from Kim et al. (2019) with permission. Copyright 2019 Elsevier. **(d)** Schematic illustration for the fabrication process of Sn-coated carbon felt. Interfacial charge-density of **(e)** carbon and **(f)** Sn based on DFT calculation. **(d–f)** Reproduced from Yin et al. (2020) with permission. Copyright 2020 Wiley-VCH. **(g–i)** Schematic of zinc deposition when employing an uncharged (top) and a negatively charged (bottom) membrane in a zinc–iron flow battery, and corresponding zinc morphologies at the end of charging. Reproduced from Yuan et al. (2018b) with permission. Copyright 2018 Nature Publishing Group. **(j)** Electrolyte concentration distribution at Pe = 100 and Pe = $1e^5$. Morphologies of deposited zinc in **(k)** quiescent alkaline electrolyte and **(l)** flowing alkaline electrolyte at a current density of 100 mA cm^{-2}. **(j–l)** Reproduced from Wang et al. (2014) with permission. Copyright 2014 Elsevier.

et al., 2006b; Nikiforidis and Daoud, 2015), and their compounds (Kang et al., 2018). Additionally, a traditional flat electrode has a low specific surface area and limits the charging current and capacity (Cheng et al., 2013b). Further design or modifications of anodes is essential to obtain uniform and compact zinc deposits and improve the performance of ZFBs (Chamoun et al., 2015; Li et al., 2015; Yan et al., 2015).

Nickel and carbon materials are widely used as anodes due to their good corrosion resistance and high electric conductivity (Li et al., 2015, 2018; Wang et al., 2016, 2017b; Xia et al., 2019). Under a large charging current, a rapid zinc deposition process occurs, which leads to severe zinc dendrite development on flat anodes because of their lower specific surface area (Xie et al., 2019). Cheng et al. for the first time, introduced three-dimensional porous nickel foam into zinc-nickel flow batteries (Cheng et al., 2013b). Its high specific surface area reduces the actual current density. Its three-dimensional porous structure greatly reduces the internal resistance of the interface between electrodes and electrolytes. Thus, zinc dendrite was prevented, and improved power density, energy efficiency, and cycling life were reported. This indicates that three-dimensional porous electrodes are more suitable for zinc deposition and dissolution under a high charging current.

Recently, Yin et al. chose the low-cost metal Sn as the morphology-inducing material for zinc deposition (Yin et al., 2020). Magnetron sputtering technology was used to enable Sn to be firmly deposited on carbon felt without binders (**Figures 2d–f**). Sn possesses stronger adsorption ability to zinc atoms than does carbon, which effectively strengthened the affiliation between the Sn nanoparticles and zinc deposits. Sn-modified carbon felt thus affords more robust zinc nucleation sites and induces compact and uniform zinc deposition. The Cycling life and coulombic efficiency of zinc-bromine flow batteries were significantly improved.

Electric Field Regulation

The electric field drives zinc nucleation on anodes and the transfer of zinc ions to the interface between anodes and electrolytes. The electric field can be controlled by the charging current (Cheng et al., 2014a; Desai et al., 2014; Nikiforidis et al., 2014; Song et al., 2014), a charged separator (Yuan et al., 2018b), and a pulsed charging model (Wang et al., 2015, 2017a; Zelger et al., 2016; Garcia et al., 2017; Pichler et al., 2017; Yang et al., 2019).

A charged separator provides an effective way to solve zinc dendrite development in ZFBs. As shown in **Figures 2g–i**, Yuan et al. designed a porous membrane with negative charges on the pore wall and surface (Yuan et al., 2018b). The negatively charged zincate ions and the negatively charged porous membrane repel each other. Therefore, zinc ions can be deposited easily along the direction of the separator to the 3D carbon felt frame. A ZFB using a negatively charged membrane has no short circuit in about 240 cycles at current densities of 80 to 160 mA/cm^2 and exhibits stable performance.

Ito et al. studied the effect of charging currents on zinc morphology in flowing alkaline electrolytes (Ito et al., 2012). The ratio of the effective current density to the limiting current density (current density ratio) is directly related to the zincate concentration on the interface and determines the morphology of zinc deposits. When the current density ratio is <0.4, the zinc morphology is mossy and porous. When the current density ratio is between 0.4 and 0.9, it has a mixture of a mossy and crystal structure. Only when the current density ratio is higher than 0.9 will the zinc deposits become crystalline and dense.

The charging module can be designed and operated to inhibit zinc dendrite (Wang et al., 2015; Pichler et al., 2017, 2018; Yang et al., 2019). The Taguchi method was utilized to optimize the values of current density, duty cycle, and pulse frequency. As the nucleation is mainly determined by overpotentials and zinc ion distribution on anodes, large overpotentials can produce more zinc seeds. Interestingly, pulsed current or voltage provides more time for zinc transfer to reactive interfaces. This will be prone to form compact and uniform zinc deposits and prevent zinc dendrite development in zinc-air flow batteries (Yang et al., 2019).

Zinc Ion Transfer Control

Zinc ion transfer plays an important role in the growth of zinc on the nucleus. A uniform distribution of zinc ions will result in the same rate of zinc growth on anodes (Nikiforidis et al., 2014; Song et al., 2014). However, the concentration gradient of zinc ions may be different along the interfaces due to non-uniform zinc seeding. Accurate regulation of zinc ion transfer is needed. Currently, controlling the flow rate of electrolyte and adding extra magnetic field are two typical methods for achieving this (Shi et al., 2013; Wang et al., 2017a, 2018a,b).

Flowing electrolyte can change the mass transfer of zinc ions from diffusion control in static electrolytes to convection control (Wang et al., 2014). As shown in **Figures 2j–l**, the larger the flow velocity is, the greater the zinc concentration gradient is in the interfaces. The concentration gradient is the main driving force for zinc ion transfer. A large concentration gradient can ensure the timely delivery of reactants for the nucleation and growth process of zinc deposition. Therefore, zinc dendrites appear under quiescent electrolyte, while uniform and compact zinc deposits are obtained in flowing electrolyte (Wang et al., 2014).

Ito et al. also found that when the flow rate of the electrolyte is higher than 15 cm/s, the growth of zinc dendrites is deformed in the direction of the electrolyte flow, thereby avoiding short circuit of the battery. A zinc-nickel system with a 100 Wh battery was scaled up to evaluate the influence of zinc ion transfer on zinc morphology and battery performance. This system had a long cycling life of more than 200 cycles (Ito et al., 2011b).

A magnetic field can affect the movement of zinc ions (Wang et al., 2018a). The magnet is placed on the anode side to design an additional driving force for zinc ion transfer. The magnetic field accelerates zinc ion transfer and suppresses the dendritic growth of zinc deposits. As a result, the cycling life of batteries is improved.

SUMMARY AND OUTLOOK

Zinc anodes are usually used in aqueous electrolytes, enabling zinc-based batteries with high safety and low cost. Flowing electrolyte can enhance mass transfer and reduce concentration polarization. ZFBs have therefore been investigated widely and show prospects for practical application. The issue of zinc dendrite formation has been extensively studied since its emergence. Some effective strategies for inhibiting zinc dendrite development in ZFBs have been proposed, including electrolyte modification, anode engineering, electric field regulation, and ion transfer control. Although great progress has been made in the field of zinc dendrites, many methods are used in isolation, with strict working conditions, and costly implementation. Here, remaining challenges and promising directions for the inhibition of zinc dendrite formation in ZFBs are outlined and anticipated.

i) The forms of zinc ions existing in aqueous solution are very complex. Zinc ions can combine with different amounts of water and other anions, which has a significant impact on the nucleation and growth processes of zinc deposition.

ii) Zinc morphology depends strongly on specific operating conditions, such as the charging model, current density, flow rate, zinc ion concentration, and temperature. Most current studies only investigate one or two variables, idly fixing other parameters. It is necessary to systematically investigate the relationship between zinc morphologies and operating conditions. The theoretical basis of our understanding of zinc deposition needs to be enriched.

iii) The capacity and thickness of zinc deposits in ZFBs is much larger than that of lithium deposits in lithium batteries. The zinc deposits in ZFBs are expected to have a specific capacity of more than 100 mAh/cm^{-2} and to be thicker than 170 μm. The thicker the zinc deposit is, the more difficult it is to control its morphology. Therefore, great efforts are required to concentrate on the inhibition of zinc dendrites under large capacity or thick deposits.

iv) In static zinc batteries, brighteners, pretreatment of zinc anodes, and new electrolytes have made significant progress toward achieving a uniform zinc electroplating/electrostripping process, which may enable flow battery researchers to look into more possibilities in further work.

In short, we look forward to a better solution to the zinc dendrite problem with a view to achieving a long cycling life and high safety and eventually improving the competitiveness of ZFBs.

AUTHOR CONTRIBUTIONS

All authors listed have made a substantial, direct and intellectual contribution to the work, and approved it for publication.

FUNDING

This work was supported by the National Key Research and Development Program of China (2019YFA0210300), Distinguished Scientist Program at BUCT; Fundamental Research Funds for the Central Universities (buctrc201524), and BUCT Fund for Disciplines Construction and Development (XK1502).

REFERENCES

Arenas, L. F., Loh, A., Trudgeon, D. P., Li, X., Ponce de León, C., and Walsh, F. C. (2018). The characteristics and performance of hybrid redox flow batteries with zinc negative electrodes for energy storage. *Renew. Sust. Energ. Rev.* 90, 992–1016. doi: 10.1016/j.rser.2018.03.016

Ballesteros, J. C., Díaz-Arista, P., Meas, Y., Ortega, R., and Trejo, G. (2007). Zinc electrodeposition in the presence of polyethylene glycol 20000. *Electrochim. Acta* 52, 3686–3696. doi: 10.1016/j.electacta.2006.10.042

Banik, S. J., and Akolkar, R. (2013). Suppressing dendrite growth during zinc electrodeposition by PEG-200 additive. *J. Electrochem. Soc.* 160, D519–D523. doi: 10.1149/2.040311jes

Banik, S. J., and Akolkar, R. (2015). Suppressing dendritic growth during alkaline zinc electrodeposition using polyethylenimine additive. *Electrochim. Acta* 179, 475–481. doi: 10.1016/j.electacta.2014.12.100

Chamoun, M., Hertzberg, B. J., Gupta, T., Davies, D., Bhadra, S., Van Tassell, B., et al. (2015). Hyper-dendritic nanoporous zinc foam anodes. *NPG Asia Mater.* 7:8. doi: 10.1038/am.2015.32

Chang, S., Ye, J., Zhou, W., Wu, C., Ding, M., Long, Y., et al. (2019). A low-cost SPEEK-K type membrane for neutral aqueous zinc-iron redox flow battery. *Surf. Coat. Technol.* 358, 190–194. doi: 10.1016/j.surfcoat.2018.11.028

Cheng, Y., Ke, X., Chen, Y., Huang, X., Shi, Z., and Guo, Z. (2019a). Lithiophobic-lithiophilic composite architecture through co-deposition technology toward high-performance lithium metal batteries. *Nano Energy* 63:103854. doi: 10.1016/j.nanoen.2019.103854

Cheng, Y., Lai, Q., Li, X., Xi, X., Zheng, Q., Ding, C., et al. (2014a). Zinc-nickel single flow batteries with improved cycling stability by eliminating zinc accumulation on the negative electrode. *Electrochim. Acta* 145, 109–115. doi: 10.1016/j.electacta.2014.08.090

Cheng, Y., Li, D., Shi, L., and Xiang, Z. (2018). Efficient unitary oxygen electrode for air-based flow batteries. *Nano Energy* 47, 361–367. doi: 10.1016/j.nanoen.2018.03.013

Cheng, Y., Wang, Y., Wang, Q., Liao, Z., Zhang, N., Guo, Y., et al. (2019b). Hierarchically porous metal-free carbon with record high mass activity for oxygen reduction and Zn-air batteries. *J. Mater. Chem. A* 7, 9831–9836. doi: 10.1039/C9TA02220A

Cheng, Y., Xi, X., Li, D., Li, X., Lai, Q., and Zhang, H. (2015). Performance and potential problems of high power density zinc-nickel single flow batteries. *RSC Adv.* 5, 1772–1776. doi: 10.1039/C4RA12812E

Cheng, Y., Zhang, H., Lai, Q., Li, X., and Shi, D. (2013a). Performance gains in single flow zinc-nickel batteries through novel cell configuration. *Electrochim. Acta* 105, 618–621. doi: 10.1016/j.electacta.2013.05.024

Cheng, Y., Zhang, H., Lai, Q., Li, X., Shi, D., and Zhang, L. (2013b). A high power density single flow zinc–nickel battery with three-dimensional porous negative electrode. *J. Power Sources* 241, 196–202. doi: 10.1016/j.jpowsour.2013.04.121

Cheng, Y., Zhang, H., Lai, Q., Li, X., Zheng, Q., Xi, X., et al. (2014b). Effect of temperature on the performances and *in situ* polarization analysis of zinc-nickel single flow batteries. *J. Power Sources* 249, 435–439. doi: 10.1016/j.jpowsour.2013.10.115

Cheng, Y., Zhang, N., Wang, Q., Guo, Y., Tao, S., Liao, Z., et al. (2019c). A long-life hybrid zinc flow battery achieved by dual redox couples at cathode. *Nano Energy* 63:103822. doi: 10.1016/j.nanoen.2019.06.018

Chladil, L., Cech, O., Smejkal, J., and Vanýsek, P. (2019). Study of zinc deposited in the presence of organic additives for zinc-based secondary batteries. *J Energy Storage* 21, 295–300. doi: 10.1016/j.est.2018.12.001

Desai, D., Wei, X., Steingart, D. A., and Banerjee, S. (2014). Electrodeposition of preferentially oriented zinc for flow-assisted alkaline batteries. *J. Power Sources* 256, 145–152. doi: 10.1016/j.jpowsour.2014.01.026

Dundalek, J., Snajdr, I., Libansky, O., Vrana, J., Pocedic, J., Mazur, P., et al. (2017). Zinc electrodeposition from flowing alkaline zincate solutions: role of hydrogen evolution reaction. *J. Power Sources* 372, 221–226. doi: 10.1016/j.jpowsour.2017.10.077

Dunn, B., Kamath, H., and Tarascon, J.-M. (2011). Electrical energy storage for the grid: a battery of choices. *Science* 334, 928–935. doi: 10.1126/science.1212741

Garcia, G., Ventosa, E., and Schuhmann, W. (2017). Complete prevention of dendrite formation in Zn metal anodes by means of pulsed charging protocols. *ACS Appl. Mater. Interfaces* 9, 18691–18698. doi: 10.1021/acsami.7b01705

Goh, F. W. T., Liu, Z. L., Hor, T. S. A., Zhang, J., Ge, X. M., Zong, Y., et al. (2014). A near-neutral chloride electrolyte for electrically rechargeable zinc-air batteries. *J. Electrochem. Soc.* 161, A2080–A2086. doi: 10.1149/2.0311414jes

Hashemi, A. B., Kasiri, G., and La Mantia, F. (2017). The effect of polyethyleneimine as an electrolyte additive on zinc electrodeposition mechanism in aqueous zinc-ion batteries. *Electrochim. Acta* 258, 703–708. doi: 10.1016/j.electacta.2017.11.116

Hosseini, S., Abbasi, A., Uginet, L.-O., Haustraete, N., Praserthdam, S., Yonezawa, T., et al. (2019). The influence of dimethyl sulfoxide as electrolyte additive on anodic dissolution of alkaline zinc-air flow battery. *Sci. Rep.* 9:14958. doi: 10.1038/s41598-019-51412-5

Hosseini, S., Lao-Atiman, W., Han, S. J., Arpornwichanop, A., Yonezawa, T., and Kheawhom, S. (2018). Discharge performance of zinc-air flow batteries under the effects of sodium dodecyl sulfate and pluronic F-127. *Sci. Rep.* 8:13. doi: 10.1038/s41598-018-32806-3

Huang, H., Guo, Y., and Cheng, Y. (2018). Ultrastable alpha phase nickel hydroxide as energy storage materials for alkaline secondary batteries. *Appl. Surf. Sci.* 435, 635–640. doi: 10.1016/j.apsusc.2017.11.156

Ito, Y., Nyce, M., Plivelich, R., Klein, M., and Banerjee, S. (2011a). Gas evolution in a flow-assisted zinc–nickel oxide battery. *J. Power Sources* 196, 6583–6587. doi: 10.1016/j.jpowsour.2011.03.025

Ito, Y., Nyce, M., Plivelich, R., Klein, M., Steingart, D., and Banerjee, S. (2011b). Zinc morphology in zinc–nickel flow assisted batteries and impact on performance. *J. Power Sources* 196, 2340–2345. doi: 10.1016/j.jpowsour.2010.09.065

Ito, Y., Wei, X., Desai, D., Steingart, D., and Banerjee, S. (2012). An indicator of zinc morphology transition in flowing alkaline electrolyte. *J. Power Sources* 211, 119–128. doi: 10.1016/j.jpowsour.2012.03.056

Jeon, J.-D., Yang, H. S., Shim, J., Kim, H. S., and Yang, J. H. (2014). Dual function of quaternary ammonium in Zn/Br redox flow battery: capturing the bromine and lowering the charge transfer resistance. *Electrochim. Acta* 127, 397–402. doi: 10.1016/j.electacta.2014.02.073

Jiang, H. R., Wu, M. C., Ren, Y. X., Shyy, W., and Zhao, T. S. (2018). Towards a uniform distribution of zinc in the negative electrode for zinc bromine flow batteries. *Appl. Energy* 213, 366–374. doi: 10.1016/j.apenergy.2018.01.061

Justinijanović, I. N., Jovićević, J. N., and Despić, A. R. (1973). The effect of foreign atoms on the properties of electrolytic zinc powders. *J. Appl. Electrochem.* 3, 193–200. doi: 10.1007/BF00619161

Kan, J., Xue, H., and Mu, S. (1998). Effect of inhibitors on Zn-dendrite formation for zinc-polyaniline secondary battery. *J. Power Sources* 74, 113–116. doi: 10.1016/S0378-7753(98)00040-8

Kang, L. T., Cui, M. W., Jiang, F. Y., Gao, Y. F., Luo, H. J., Liu, J. J., et al. (2018). Nanoporous CaCO3 coatings enabled uniform Zn stripping/plating for long-life zinc rechargeable aqueous batteries. *Adv. Energy Mater.* 8:8. doi: 10.1002/aenm.201801090

Khor, A., Leung, P., Mohamed, M. R., Flox, C., Xu, Q., An, L., et al. (2018). Review of zinc-based hybrid flow batteries: from fundamentals to applications. *Mater. Today Energy* 8, 80–108. doi: 10.1016/j.mtener.2017.12.012

Kim, H.-I., and Shin, H.-C. (2015). SnO additive for dendritic growth suppression of electrolytic zinc. *J. Alloys Compd.* 645, 7–10. doi: 10.1016/j.jallcom.2015.04.208

Kim, M., Yun, D., and Jeon, J. (2019). Effect of a bromine complex agent on electrochemical performances of zinc electrodeposition and electrodissolution in Zinc–Bromide flow battery. *J. Power Sources* 438:227020. doi: 10.1016/j.jpowsour.2019.227020

Lacitignola, D., Bozzini, B., Frittelli, M., and Sgura, I. (2017). Turing pattern formation on the sphere for a morphochemical reaction-diffusion model for electrodeposition. *Commun. Nonlinear Sci. Numer. Simul.* 48, 484–508. doi: 10.1016/j.cnsns.2017.01.008

Leadbetter, J., and Swan, L. G. (2012). Selection of battery technology to support grid-integrated renewable electricity. *J. Power Sources* 216, 376–386. doi: 10.1016/j.jpowsour.2012.05.081

Lee, C. W., Sathiyanarayanan, K., Eom, S. W., Kim, H. S., and Yun, M. S. (2006a). Novel electrochemical behavior of zinc anodes in zinc/air batteries in the presence of additives. *J. Power Sources* 159, 1474–1477. doi: 10.1016/j.jpowsour.2005.11.074

Lee, C. W., Sathiyanarayanan, K., Eom, S. W., and Yun, M. S. (2006b). Novel alloys to improve the electrochemical behavior of zinc anodes for zinc/air battery. *J. Power Sources* 160, 1436–1441. doi: 10.1016/j.jpowsour.2006.02.019

Leung, P. K., Ponce-de-Leon, C., Low, C. T. J., and Walsh, F. C. (2011). Zinc deposition and dissolution in methanesulfonic acid onto a carbon composite electrode as the negative electrode reactions in a hybrid redox flow battery. *Electrochim. Acta* 56, 6536–6546. doi: 10.1016/j.electacta.2011.04.111

Li, H. F., Xu, C. J., Han, C. P., Chen, Y. Y., Wei, C. G., Li, B. H., et al. (2015). Enhancement on cycle performance of Zn anodes by activated carbon modification for neutral rechargeable zinc ion batteries. *J. Electrochem. Soc.* 162, A1439–A1444. doi: 10.1149/2.0141508jes

Li, M., Meng, J. S., Li, Q., Huang, M., Liu, X., Owusu, K. A., et al. (2018). Finely crafted 3D electrodes for dendrite-free and high-performance flexible fiber-shaped Zn-Co batteries. *Adv. Funct. Mater.* 28:10. doi: 10.1002/adfm.201802016

Lin, H. (2018). Pyrolytic carbon felt electrode inhibits formation of zinc dendrites in zinc bromine flow batteries. *Int. J. Electrochem. Sci.* 13, 12049–12061. doi: 10.20964/2018.12.18

Liu, N. N., Mohanapriya, K., Pan, J., Hu, Y., Sun, Y. Z., and Liu, X. G. (2020). A facile preparation of lambda-MnO2 as cathode material for high-performance zinc-manganese redox flow battery. *J. Electrochem. Soc.* 167:8. doi: 10.1149/1945-7111/ab75c2

Liu, W., Lu, W., Zhang, H., and Li, X. (2019a). Aqueous flow batteries: research and development. *Chem. Eur. J.* 25, 1649–1664. doi: 10.1002/chem.2018 02798

Liu, X. Y., Bolton, O., and Akolkar, R. (2019b). Experimental and modeling studies of the hysteresis behavior and dendrite suppression efficacy of an electrolyte additive in zinc electrodeposition. *J. Electrochem. Soc.* 166, D583–D588. doi: 10.1149/2.0411913jes

Lou, X., Yuan, D., Yu, Y., Lei, Y., Ding, M., Sun, Q., et al. (2020). A cost-effective nafion composite membrane as an effective vanadium-ion barrier for vanadium redox flow batteries. *Chem. Asi. J.* 607:118177. doi: 10.1002/asia.202000140

Lu, W., Xie, C., Zhang, H., and Li, X. (2018). Inhibition of zinc dendrite growth in zinc-based batteries. *ChemSusChem* 11, 3996–4006. doi: 10.1002/cssc.201801657

Mitha, A., Yazdi, A. Z., Ahmed, M., and Chen, P. (2018). Surface adsorption of polyethylene glycol to suppress dendrite formation on zinc anodes in rechargeable aqueous batteries. *ChemElectroChem* 5, 2409–2418. doi: 10.1002/celc.201800572

Miyazaki, K., Nakata, A., Lee, Y. S., Fukutsuka, T., and Abe, T. (2016). Influence of surfactants as additives to electrolyte solutions on zinc electrodeposition and potential oscillation behavior. *J. Appl. Electrochem.* 46, 1067–1073. doi: 10.1007/s10800-016-0987-4

Nikiforidis, G., Cartwright, R., Hodgson, D., Hall, D., and Berlouis, L. (2014). Factors affecting the performance of the Zn-Ce redox flow battery. *Electrochim. Acta* 140, 139–144. doi: 10.1016/j.electacta.2014.04.150

Nikiforidis, G., and Daoud, W. A. (2015). Indium modified graphite electrodes on highly zinc containing methanesulfonate electrolyte for zinc-cerium redox flow battery. *Electrochim. Acta* 168, 394–402. doi: 10.1016/j.electacta.2015.03.118

Ortiz-Aparicio, J. L., Meas, Y., Trejo, G., Ortega, R., Chapman, T. W., and Chainet, E. (2013). Effects of organic additives on zinc electrodeposition from alkaline electrolytes. *J. Appl. Electrochem.* 43, 289–300. doi: 10.1007/s10800-012-0518-x

Parker, J. F., Chervin, C. N., Pala, I. R., Machler, M., Burz, M. F., Long, J. W., et al. (2017). Rechargeable nickel-3D zinc batteries: an energy-dense, safer alternative to lithium-ion. *Science* 356, 414–417. doi: 10.1126/science.aak9991

Pei, A., Zheng, G., Shi, F., Li, Y., and Cui, Y. (2017). Nanoscale Nucleation and Growth of Electrodeposited Lithium Metal. *Nano Lett* 17, 1132–1139. doi: 10.1021/acs.nanolett.6b04755

Pichler, B., Berner, B. S., Rauch, N., Zelger, C., Pauling, H.-J., Gollas, B., et al. (2018). The impact of operating conditions on component and electrode development for zinc-air flow batteries. *J. Appl. Electrochem.* 48, 1043–1056. doi: 10.1007/s10800-018-1233-z

Pichler, B., Weinberger, S., Rescec, L., Grimmer, I., Gebetsroither, F., Bitschnau, B., et al. (2017). Bifunctional electrode performance for zinc-air flow cells with pulse charging. *Electrochim. Acta* 251, 488–497. doi: 10.1016/j.electacta.2017.08.128

Rossi, F., Mele, C., Boniardi, M., and Bozzini, B. (2020). Electrodeposition of zinc from alkaline electrolytes containing quaternary ammonium salts and ionomers: impact of cathodic-anodic cycling conditions. *Chemelectrochem* 7, 1752–1764. doi: 10.1002/celc.202000165

Shen, C., Li, X., Li, N., Xie, K. Y., Wang, J. G., Liu, X. R., et al. (2018). Graphene-boosted, high-performance aqueous Zn-Ion battery. *ACS Appl. Mater. Interfaces* 10, 25446–25453. doi: 10.1021/acsami.8b07781

Shi, J., Xu, H., Lu, L., and Sun, X. (2013). Study of magnetic field to promote oxygen transfer and its application in zinc–air fuel cells. *Electrochim. Acta* 90, 44–52. doi: 10.1016/j.electacta.2012.11.088

Shimizu, M., Hirahara, K., and Arai, S. (2019). Morphology control of zinc electrodeposition by surfactant addition for alkaline-based rechargeable batteries. *PCCP* 21, 7045–7052. doi: 10.1039/C9CP00223E

Song, S., Pan, J., Wen, Y., Cheng, J., Pan, J., and Cao, G. (2014). Effects of electrolyte flow speed on the performance of Zn-Ni single flow batteries. *Chem. J. Chin. Univ.-Chin.* 35, 134–139. doi: 10.7503/cjcu20130340

Song, Y. X., Hu, J. H., Tang, J., Gu, W. M., He, L. L., and Ji, X. B. (2016). Real-time X-ray imaging reveals interfacial growth, suppression, and dissolution of zinc dendrites dependent on anions of ionic liquid additives for rechargeable battery applications. *ACS Appl. Mater. Interfaces* 8, 32031–32040. doi: 10.1021/acsami.6b11098

Sun, K. E. K., Hoang, T. K. A., Doan, T. N. L., Zhu, Y. Y. X., Tian, Y., and Chen, P. (2017). Suppression of dendrite formation and corrosion on zinc anode of secondary aqueous batteries. *ACS Appl. Mater. Interfaces* 9, 9681–9687. doi: 10.1021/acsami.6b16560

Suresh, S., Kesavan, T., Munaiah, Y., Arulraj, I., Dheenadayalan, S., and Ragupathy, P. (2014). Zinc-bromine hybrid flow battery: effect of zinc utilization and performance characteristics. *RSC Adv.* 4, 37947–37953. doi: 10.1039/C4RA05946H

Suresh, S., Ulaganathan, M., and Pitchai, R. (2019). Realizing highly efficient energy retention of Zn–Br2 redox flow battery using rGO supported 3D carbon network as a superior electrode. *J. Power Sources* 438:226998. doi: 10.1016/j.jpowsour.2019.226998

Turner, J. A. (1999). A realizable renewable energy future. *Science* 285, 687–689. doi: 10.1126/science.285.5428.687

Wang, J. M., Zhang, L., Zhang, C., and Zhang, J. Q. (2001). Effects of bismuth ion and tetrabutylammonium bromide on the dendritic growth of zinc in alkaline zincate solutions. *J. Power Sources* 102, 139–143. doi: 10.1016/S0378-7753(01)00789-3

Wang, K., Liu, X., Pei, P., Xiao, Y., and Wang, Y. (2018a). Guiding bubble motion of rechargeable zinc-air battery with electromagnetic force. *Chem. Eng. J.* 352, 182–187. doi: 10.1016/j.cej.2018.07.020

Wang, K., Pei, P., Ma, Z., Chen, H., Xu, H., Chen, D., et al. (2015). Dendrite growth in the recharging process of zinc-air batteries. *J. Mater. Chem. A* 3, 22648–22655. doi: 10.1039/C5TA06366C

Wang, K., Pei, P., Ma, Z., Xu, H., Li, P., and Wang, X. (2014). Morphology control of zinc regeneration for zinc-air fuel cell and battery. *J. Power Sources* 271, 65–75. doi: 10.1016/j.jpowsour.2014.07.182

Wang, K., Pei, P., and Wang, Y. (2017a). Magnetic field improving interfacial behavior of the two-electrode system. *J. Electrochem. Soc.* 164, A3440–A3444. doi: 10.1149/2.0031714jes

Wang, K., Pei, P., Wang, Y., Liao, C., WAng, W., and Huang, S. (2018b). Advanced rechargeable zinc-air battery with parameter optimization. *Appl. Energy* 225, 848–856. doi: 10.1016/j.apenergy.2018.05.071

Wang, L. P., Li, N. W., Wang, T. S., Yin, Y. X., Guo, Y. G., and Wang, C. R. (2017b). Conductive graphite fiber as a stable host for zinc metal anodes. *Electrochim. Acta* 244, 172–177. doi: 10.1016/j.electacta.2017.05.072

Wang, X. W., Wang, F. X., Wang, L. Y., Li, M. X., Wang, Y. F., Chen, B. W., et al. (2016). An aqueous rechargeable Zn//Co3O4 battery with high energy density and good cycling behavior. *Adv. Mater.* 28, 4904–4911. doi: 10.1002/adma.201505370

Wei, X., Desai, D., Yadav, G. G., Turney, D. E., Couzis, A., and Banerjee, S. (2016). Impact of anode substrates on electrodeposited zinc over cycling in zinc-anode rechargeable alkaline batteries. *Electrochim. Acta* 212, 603–613. doi: 10.1016/j.electacta.2016.07.041

Wen, Y., Wang, T., Cheng, J., Pan, J., Cao, G., and Yang, Y. (2012). Lead ion and tetrabutylammonium bromide as inhibitors of the growth of spongy zinc in single flow zinc/nickel batteries. *Electrochim. Acta* 59, 64–68. doi: 10.1016/j.electacta.2011.10.042

Xia, L., Zhang, Q., Wu, C., Liu, Y., Ding, M., Ye, J., et al. (2019). Graphene coated carbon felt as a high-performance electrode for all vanadium redox flow batteries. *Surf. Coat. Technol.* 358, 153–158. doi: 10.1016/j.surfcoat.2018.11.024

Xie, C., Liu, Y., Lu, W., Zhang, H., and Li, X. (2019). Highly stable zinc–iodine single flow batteries with super high energy density for stationary energy storage. *Energy Environ. Sci.* 12, 1834–1839. doi: 10.1039/C8EE02825G

Xu, W. N., Zhao, K. N., Huo, W. C., Wang, Y. Z., Yao, G., Gu, X., et al. (2019). Diethyl ether as self-healing electrolyte additive enabled long-life rechargeable aqueous zinc ion batteries. *Nano Energy* 62, 275–281. doi: 10.1016/j.nanoen.2019.05.042

Yan, Z., Wang, E. D., Jiang, L. H., and Sun, G. Q. (2015). Superior cycling stability and high rate capability of three-dimensional Zn/Cu foam electrodes for zinc-based alkaline batteries. *RSC Adv.* 5, 83781–83787. doi: 10.1039/C5RA16264E

Yang, H. B., Meng, X. L., Yang, E. D., Wang, X. D., and Zhou, Z. X. (2004). Effect of La addition on the electrochemical properties of secondary zinc electrodes. *J. Electrochem. Soc.* 151, A389–A393. doi: 10.1149/1.1646407

Yang, T.-F., Lu, J.-H., Yan, W.-M., and Ghalambaz, M. (2019). Optimization of pulse current on energy storage of zinc-air flow batteries. *J. Power Sources* 442:227253. doi: 10.1016/j.jpowsour.2019.227253

Yang, Z., Zhang, J., Kintner-Meyer, M. C. W., Lu, X., Choi, D., Lemmon, J. P., et al. (2011). Electrochemical energy storage for green grid. *Chem. Rev.* 111, 3577–3613. doi: 10.1021/cr100290v

Yao, S., Chen, Y., Cheng, J., Shen, Y., and Ding, D. (2019). Effect of stannum ion on the enhancement of the charge retention of single-flow zinc–nickel battery. *J. Electrochem. Soc.* 166, A1813–A1818. doi: 10.1149/2.0311910jes

Ye, J., Wu, C., Qin, W., Zhong, F., and Ding, M. (2020a). Advanced sulfonated poly(Ether Ether Ketone)/Graphene-Oxide/Titanium dioxide nanoparticle composited membrane with superior cyclability for vanadium redox flow battery. *J. Nanosci. Nanotechnol.* 20, 4714–4721. doi: 10.1166/jnn.2020.18503

Ye, J., Zhao, X., Ma, Y., Su, J., Xiang, C., Zhao, K., et al. (2020b). Hybrid membranes dispersed with superhydrophilic TiO2 nanotubes toward ultra-stable and high-performance vanadium redox flow batteries. *Adv. Energy Mater.* 10:1904041. doi: 10.1002/aenm.201904041

Yin, Y., Wang, S., Zhang, Q., Song, Y., Chang, N., Pan, Y., et al. (2020). Dendrite-free zinc deposition induced by tin-modified multifunctional 3D host for stable zinc-based flow battery. *Adv Mater* 32:e1906803. doi: 10.1002/adma.201906803

Yuan, Y. F., Tu, J. P., Wu, H. M., Wang, S. F., Zhang, W. K., and Huang, H. (2007). Effects of stannous ions on the electrochemical performance of the alkaline zinc electrode. *J. Appl. Electrochem.* 37, 249–253. doi: 10.1007/s10800-006-9249-1

Yuan, Z., Duan, Y., Liu, T., Zhang, H., and Li, X. (2018a). Toward a low-cost alkaline zinc-iron flow battery with a polybenzimidazole custom membrane for stationary energy storage. *Science* 3, 40–49. doi: 10.1016/j.isci.2018.04.006

Yuan, Z., Liu, X., Xu, W., Duan, Y., Zhang, H., and Li, X. (2018b). Negatively charged nanoporous membrane for a dendrite-free alkaline zinc-based flow battery with long cycle life. *Nat Commun* 9:3731. doi: 10.1038/s41467-018-06209-x

Yufit, V., Tariq, F., Eastwood, D. S., Biton, M., Wu, B., Lee, P. D., et al. (2019). Operando visualization and multi-scale tomography studies of dendrite formation and dissolution in zinc batteries. *Joule* 3, 485–502. doi: 10.1016/j.joule.2018.11.002

Zelger, C., Laumen, J., Laskos, A., and Gollas, B. (2016). Rota-hull cell study on pulse current zinc electrodeposition from alkaline electrolytes. *Electrochim. Acta* 213, 208–216. doi: 10.1016/j.electacta.2016.07.108

Zeng, Y., Zhang, X., Qin, R., Liu, X., Fang, P., Zheng, D., et al. (2019). Dendrite-free zinc deposition induced by multifunctional CNT frameworks for stable flexible Zn-Ion batteries. *Adv. Mater.* 31:1903675. doi: 10.1002/adma.201903675

Zhang, H., Lu, W., and Li, X. (2019a). Progress and perspectives of flow battery technologies. *Electrochem. Energy Rev.* 2, 492–506. doi: 10.1007/s41918-019-00047-1

Zhang, L., Cheng, J., Yang, Y. S., Wen, Y. H., Wang, X. D., and Cao, G. P. (2008). Study of zinc electrodes for single flow zinc/nickel battery application. *J. Power Sources* 179, 381–387. doi: 10.1016/j.jpowsour.2007.12.088

Zhang, Q., Luan, J., Fu, L., Wu, S., Tang, Y., Ji, X., et al. (2019b). The Three-Dimensional Dendrite-Free Zinc Anode On A Copper Mesh With A Zinc-Oriented Polyacrylamide Electrolyte Additive. *Angew. Chem. Int. Ed.* 58, 15841–15847. doi: 10.1002/anie.201907830

Zhang, Q., Luan, J., Tang, Y., Ji, X., and Wang, H. Y. (2020). Interfacial design of dendrite-free zinc anodes for aqueous zinc-ion batteries. *Angew. Chem. Int. Ed. Engl.* 59, 2–14. doi: 10.1002/anie.202000162

Zheng, J., Zhao, Q., Tang, T., Yin, J., Quilty, C. D., Renderos, G. D., et al. (2019). Reversible epitaxial electrodeposition of metals in battery anodes. *Science* 366, 645–648. doi: 10.1126/science.aax6873

Conflict of Interest: The authors declare that the research was conducted in the absence of any commercial or financial relationships that could be construed as a potential conflict of interest.

frontiers in Chemistry

MINI REVIEW
published: 11 August 2020
doi: 10.3389/fchem.2020.00640

Polyethylene Oxide-Based Composites as Solid-State Polymer Electrolytes for Lithium Metal Batteries: A Mini Review

Shuangshuang Zhao[1], **Qinxia Wu**[1], **Wenqing Ma**[2] **and Lishan Yang**[1]*

[1] *Key Laboratory of Chemical Biology & Traditional Chinese Medicine Research (Ministry of Education of China), National and Local Joint Engineering Laboratory for New Petrochemical Materials and Fine Utilization of Resources, Key Laboratory of the Assembly and Application of Organic Functional Molecules of Hunan Province, Hunan Normal University, Changsha, China,*
[2] *School of Materials Science and Engineering, Qilu University of Technology (Shandong Academy of Sciences), Jinan, China*

Solid-state polymer electrolytes (SPEs) have great processing flexibility and electrode–electrolyte contact and have been employed as the promising electrolytes for lithium metal batteries. Among them, poly(ethylene oxide) (PEO)-based SPEs have attracted widespread attention because of easy synthesis, low mass density, good mechanical stability, low binding energy with lithium salts, and excellent mobility of charge carriers. In order to overcome the low room-temperature ionic conductivity and the poor thermodynamic stability in high-voltage devices (>4.2 V) of the PEO materials, composition modulations by incorporating PEO with inorganic and/or organic components have been designed, which could effectively enable the applications of PEO-based SPEs with widened electro-stable voltage ranges. In this mini review, we describe recent progresses of several kinds of PEO composite structures for SPEs, and we compare the synthesis strategies and properties of these SPEs in lithium batteries. Further developments and improvements of the PEO-based materials for building better rechargeable batteries are also discussed.

Keywords: solid-state polymer electrolytes, polyethylene oxide, lithium metal batteries, ionic conductivity, electrochemical stability

Edited by:
Du Yuan,
Nanyang Technological University, Singapore

Reviewed by:
Liqiang Xu,
Shandong University, China
Xifei Li,
Xi'an University of Technology, China
Zhicheng Ju,
China University of Mining and Technology, China

Correspondence:
Lishan Yang
lsyang.chemistry@gmail.com

Specialty section:
This article was submitted to Electrochemistry,
a section of the journal Frontiers in Chemistry

Received: *02 May 2020*
Accepted: *22 June 2020*
Published: *11 August 2020*

Citation:
Zhao S, Wu Q, Ma W and Yang L (2020) Polyethylene Oxide-Based Composites as Solid-State Polymer Electrolytes for Lithium Metal Batteries: A Mini Review. Front. Chem. 8:640. doi: 10.3389/fchem.2020.00640

INTRODUCTION

Lithium ion batteries (LIBs) are critical for large-scale applications, including power sources for 3C electronics, portable devices, and electric vehicle (Liu et al., 2019b). The innovation of advanced batteries with higher energy/power densities, longer cycling life, and, especially, guaranteed levels of safety at a satisfactory cost is crucially needed (Manthiram et al., 2017; Liu et al., 2018). As the most potential anode material, Li-metal possesses advantages such as high theoretical capacity (3,860 mA h g^{-1}), negative potential [−3.04 V vs. standard hydrogen electrode (SHE)], and low density (~0.59 g cm^{-3}) (He et al., 2018; Zhao C. Z. et al., 2019). However, Li-metal batteries (LMBs) with liquid electrolytes cannot coordinate a high energy density with excellent electro-stability for real applications (Choudhury et al., 2019b). The robustness and integrity of the electrode–electrolyte interface through cycling ensure the efficacy of the whole cell (Maleki Kheimeh Sari and Li, 2019). To address these issues, solid-state polymer electrolytes (SPEs) in the replacement electrolytes have already demonstrated feasibility and superiority in lithium secondary batteries (e.g., solid-state LMBs, lithium-sulfur batteries, and lithium-gas batteries) (Xiao et al., 2019; Zhou et al., 2019; Zhao et al., 2020).

SPEs are generally composed of polymeric solid host and lithium salt without the use of liquid solvents. The construct of SPEs was derived from the discovery by Fenton et al. (1973) that alkali metal salts dissolved in polyethylene oxide (PEO) could form conductive complexes (Fenton et al., 1973). In general, various lithium-ion conductive polymer materials, such as PEO (Zhao Q. et al., 2019), poly(acrylonitrile) (PAN) (Wang et al., 1996), poly(methyl methacrylate) (PMMA) (Appetecchi et al., 1995), and poly(vinylidene fluoride) (PVDF) (Choe et al., 1995), have been employed as SPEs for the development of solid-state LMB batteries. Generally, a preferred SPE, used to replace the electrolyte in lithium batteries, should contain a high dielectric host polymer and a lithium salt with a low lattice energy. In this regard, the polymers with polar functional groups are required for consideration from the dissociation and transportation of the lithium ions (Liang et al., 2019). Among all polymers, PEO is widely studied because of its excellent salt-solvating ability and electrode interfacial compatibility. From the above considerations, we selected and reviewed PEO-based SPEs (Xu et al., 2019; Nie et al., 2020; Qiu et al., 2020).

However, the room-temperature (RT) ionic conductivity of PEO-based SPEs is lower than that of the liquid-based counterpart. Moreover, the batteries constructed with PEO-based SPEs usually suffer from Li dendrite because of the poor mechanical strength of the polymer matrix. Therefore, future studies of PEO-based SPEs should focus on the improvement of the mechanical properties for preventing Li dendrite formation and increasing electrochemical stability of PEO-based SPEs. By compositing with inorganic solid oxides/organic molecules, as-obtained composite PEO-based polymer electrolytes show a high ionic conductivity and are stable under relative high voltage (Liang et al., 2019). For inorganic-PEO SPEs, the hybrid electrolyte consists of a soft polymer PEO electrolyte and a rigid inorganic solid-state electrolyte (SSE), which has a relatively high ionic conductivity at RT (Choudhury et al., 2019a; Qiu et al., 2020). As for organic material-modified PEO SPEs, chemical strategies (copolymerization and crosslinking) frustrate crystallization to enable acceptable ionic conductivities at temperatures near ambient or within the thermal window of applications, including in transport applications (Liu et al., 2019a; Zhao et al., 2020). Moreover, complex synergistic optimization is the primary efficient method of improving the antioxidant stability of systems with PEO-based electrolytes because of its high mechanical strength and high ionic conductivity (Feng et al., 2018; Zhang et al., 2019).

The amorphous PEO domain benefits Li^+ diffusion and is preferred as compared with the crystalline one. With the addition of filler particles, the PEO SPEs show increased mechanical strength and thermal stability and can thus suppress crystallization and facilitate the dissociation of the salt with an improved ionic conductivity (Zhao et al., 2020). With PEO-based electrolyte, the all-solid-state $Li|LiFePO_4$ (LFP) cell, $Li|LiCoO_2$ cell, and $Li|LiNi_{1-x-y}Mn_xCo_yO_2$ (NMC) cell all show excellent cycling stability and rate capability. The PEO-based SPEs are of great significance to improve the practical application of hot ternary cathode materials (Wang C. et al., 2019; Wang X. et al., 2019; Xu et al., 2019).

In this work, we review the recent progress in the synthesis strategies and polymer engineering of PEO-based electrolytes. We specifically compare the ion conductivity and electro-stability of different compound electrolytes and thus provide a certain reference for structural optimization of the PEO-based SPEs.

PEO POLYMER SOLID ELECTROLYTES BASED ON DIFFERENT COMPOSITIONS

PEO-based composite SPEs show a high probability in all-solid-state lithium batteries, including inorganic-PEO composite, organic-PEO composite, and other complex composite electrolytes. The relevant synthesis/modification avenues and their performance/characteristics are summarized in the following sections.

Inorganic-PEO Composite SPEs

In initial studies, PEO electrolyte is employed in solid-state LMBs but shows a low conductivity and inferior thermal stability. It is found that the increment of lithium salts within the polymeric matrix can lead to an improved ionic conductivity, accompanied by a degradation of mechanical strength and electro-stability of the PEO-based SPEs (Lopez et al., 2019). Integration of nanostructured inorganic fillers (including metal oxide, neotype lithium salts, and some oxide solid-solutions) into polymeric solid host, named as "inorganic-PEO composite," has emerged as an effective approach to design SPEs with the most needed improvements.

Basically, composite casting strategies can be divided into two-step solution casting and *in situ* casting combined with fillers. To date, the *in situ* approach, which possesses good distribution of nanofillers and is scalable for practical application, is commonly used for the syntheses of composite SPEs (Yap et al., 2013; Xu et al., 2020). Two-step reactions usually include the formation of the fillers (step I) and the incorporation operation (step II). For example, in a two-step synthesis process, self-synthesized $MgAl_2O_4$ nanoparticles were incorporated into PEO polymers through a rapid hot press procedure (Angulakshmi et al., 2013). For example, Al_2O_3-PEO SPEs synthesized via the *in situ* method could get a conductivity of 2.970×10^{-5} S cm^{-1} with microsized Al_2O_3 fillers at RT; however, composite SPEs with Al_2O_3 (<50 nm) displayed rougher surface structures and a reduced conductivity of 4.843×10^{-6} S cm^{-1} (Yap et al., 2013). Generally, the conductivity of the Al_2O_3-PEO SPEs can be improved with a small Al_2O_3 filler particle, which can probably have a more powerful impact on the immobilization of the long polymer chains. However, the fine (nanosized) filler grains would be too close to each other, inducing the blocking effect of the filler grains with enhanced immobilization and leading to the decrease in the ionic conductivity. Recently, through a rigid–flexible coupling technology, nano-SiO_2 particles were incorporated into 3D PEO networks to *in situ* construct SiO_2-PEO SPEs (shown in **Figures 1A–C**). SiO_2-PEO SPEs show an outstanding RT ionic conductivity ($\sigma \approx 1.1 \times 10^{-4}$ S cm^{-1}) along with dramatically improved solid–solid interface stabilization and excellent high-temperature capability (~90 mA h g^{-1} after 100 cycles under 2 C at 90°C) (Xu et al., 2020).

In recent years, neotype lithium salts (inorganic ion conductors) are regarded as the most promising filler materials for inorganic-PEO SPEs, which can effectively enhance the battery properties in the electrochemical aspect. Phosphate ion conductor nanomaterials such as $Li_{1.5}Al_{0.5}Ge_{1.5}(PO_4)_3$ (LAGP) (Wang X. et al., 2019) and $Li_{1+x}Al_xTi_{2-x}(PO_4)_3$ (LATP) (Zhai et al., 2017) are reported to present optimal ionic conductivities and superior flexibilities than do the SPEs before compounding. The inorganic particles were first dispersed into water and cast onto a substrate. Thereafter, the bottom of the dispersion is slowly cooled down and forms a vertical temperature gradient with ice nucleated from the bottom of the suspension, during which the ceramic particles are compelled to form vertically aligned structures. After ice sublimation, inorganic particles are sintered together to form vertically aligned walls (Wang X. et al., 2019). For example, PEO polymer combined with vertically aligned inorganic walls (shown in **Figure 1D**) shows an RT ionic conductivity level of 10^{-4} S cm^{-1}, which is three to six times higher than that of the PEO electrolyte with ceramic nanoparticles randomly dispersed inside. For the LLTO-PEO SPEs, the prepercolating structure in $Li_{0.35}La_{0.55}TiO_3$ (LLTO) could accelerate Li-ion conduction ($\sigma = 0.88 \times 10^{-4}$ S cm^{-1}) via its successive ion pathways, which could also further avoid agglomeration of particles (Bae et al., 2018). As a Li-ion fast ionic conductor, LLZO also owns remarkable electrochemical stability (even under 6.0 V). Thus, the Li symmetric cells using LLZO-PEO SPEs can stably cycle for 1,000 h without short-circuiting even at 60°C, which is due to the highly packed LLZO nanowires inside the SPEs and the uniform deposition of lithium metal (Wan et al., 2019). Furthermore, other lithium salts, such as sulfide (Li_3PS_4) and borate [lithium bis(modified imidazole)borate] (LiBMB), have been successfully used to ameliorate flexible PEO-based SPEs. Li_3PS_4 particles exhibit uniformly nanosized morphologies, and the particle diameter of the Li_3PS_4 is about 400–700 nm. *In situ* synthesis of Li_3PS_4 nanoparticles within the PEO matrix possesses good distribution of nanofillers. β-Li_3PS_4 glass-ceramic is a Li superionic conductor whose conductivity is higher than 10^{-4} S cm^{-1} at RT with a relatively stable electrochemical property (Chen et al., 2018). LiBMB-PEO SPEs display a highly ordered ionic pathways [the quasi-period value (T_p) is lower than 100 ns] associated with a high electro-stable potential of up to 7.2 V at 60°C (Yuan et al., 2019). The $LiFePO_4$|LiBMB-PEO SPEs|Li cell delivers an initial discharge capacity of 145.5 mA h g^{-1} at 0.1 C and ultra-high capacity retention (98.5% after 60 cycles), revealing good reliability of the produced cells.

Besides the aforementioned lithium salt, several metal oxide solid solutions such as $MgAl_2O_4$ have been supplied in the PEO-based composite SPEs (Angulakshmi et al., 2013). In this two-step synthesis case, the self-synthesized $MgAl_2O_4$ nanoparticles were incorporated with PEO polymer through a rapid hot press procedure. The assembled all-solid-state cells deliver a discharge capacity approaching 110 mA h g^{-1} after prolonged cycling (up to 100 cycles, 70°C), which renders them to be qualified for practical battery applications.

In short, inorganic-PEO SPEs show considerable superiority with an improved ionic conductivity, enhanced mechanical strength, and obvious accessibility for enlarging the preparation. Along with the introduction of inorganic fillers, the possible conductive mechanisms in the composite SPEs, especially with neotype lithium salts as the fillers, need more comprehensive and in-depth research. Also, improving the RT ionic conductivities of the current inorganic-PEO SPEs to the liquid-electrolyte level (10^{-3}-10^{-2} S cm^{-1}) becomes the most urgent work.

Organic-PEO Composite SPEs

Compared with inorganic-PEO composite SPEs, organic-PEO composite SPEs have been widely studied in previous works (Lopez et al., 2019). Related organic fillers can be briefly classified as metal-organic frameworks (MOFs), simple organisms, and molecular polymers.

MOF materials have been investigated for extensive application in the fields of electrochemical catalysis, electrodes, and electrolyte because of their high specific surface area and ordered microporous structure. For example, Zn_4O(1,4-benzenedicarboxylate)$_3$ (MOF-5) nanoparticles with a size of 20–30 nm were first synthesized and then incorporated into the polymer metric to form the MOF-PEO SPEs (Yuan et al., 2013). MOF-5 fillers show a strong absorbing ability for the solvent impurities and help SPEs to prevent those impurities from accumulating at the Li/SPEs interface. The reversible capacities of cells increase after filling MOF-5 particles as a result of reduced cell polarization of the electrode/SPE interface at both 60 and 80°C.

Also, simple organic fillers such as silicane (Mehdi et al., 2017; Mohanta et al., 2017) and carbonate (He et al., 2017) have been successfully introduced into the PEO-based SPEs, improving the ion conductivity and ameliorating the polymer crystallinity. For example, the monosilylated PEO precursor with the loose networks supplies higher segmental motion and amorphous networks, which are beneficial for a significantly enhanced capacity and faster Li-ion transmission (Mohanta et al., 2017). By a facile transesterification reaction, the carbonate-linked PEO SPEs could achieve a high yield with intrinsic amorphous nature and low glass transition temperature, which would be beneficial for getting a high ionic conductivity. Cycling performance of the cell with carbonate-linked PEO SPEs displays extremely stable capacity as well as coulombic efficiencies close to 100% up to 100 cycles at both 25 and 55°C.

Moreover, the ionic conductivity of a polymer electrolyte depends on the chain mobility. Various kinds of polymer fillers, such as polystyrene (PSt) (Niitani et al., 2005), PVDF (Deng et al., 2015), polyvinyl alcohol (PVA) (Jinisha et al., 2018), thermoplastic polyurethane (TPU) (Tao et al., 2017), and polystyrene (PS) (Chen et al., 2019), are discussed in the following portion. Copolymer PSt-PEO with microphase separation structure displays high tensile strengths (>3 MPa), which is high enough utilization in battery applications. PSt-PEO SPEs exhibit exceptionally

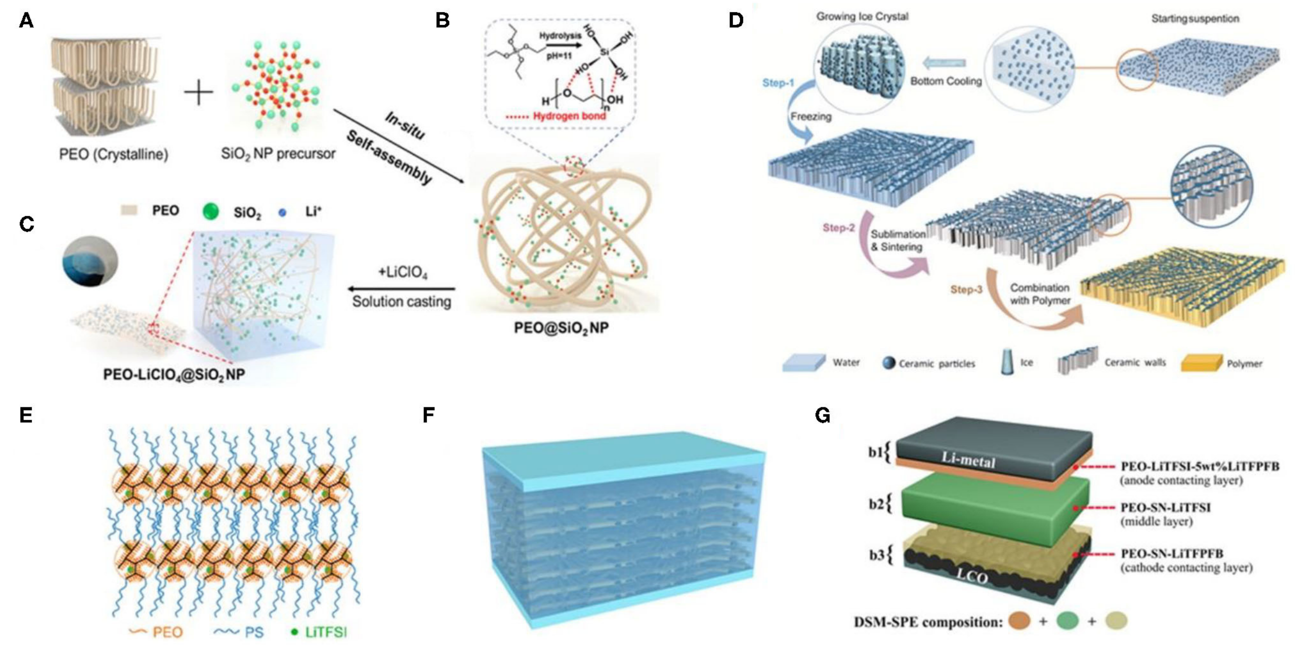

FIGURE 1 | (A–C) Synthetic routes of the SiO_2-PEO–$LiClO_4$ solid-state polymer electrolytes (SPEs). **(D)** The schematic preparation process of the ice-templated $Li_{1.5}Al_{0.5}Ge_{1.5}(PO_4)_3$ (LAGP)-PEO SPEs. Reproduced with permission from Wang X. et al. (2019) and Xu et al. (2020). **(E)** Schematic structure of the lamellar PS–PEO–LiTFSI SPEs. Reproduced with permission from Chen et al. (2019). **(F)** Schematic of the PEO|PEO–perovskite|PEO composite solid electrolyte. **(G)** Schematic of the multilayered solid polymer electrolyte (DSM-SPE). The bilateral layers are *in situ* formed on the surfaces of electrodes. Reproduced with permission from Wang C. et al. (2019) and Liu K. et al. (2019).

high Li^+ conductivity (3.03×10^{-3} S cm^{-1} at RT) and remarkable electrochemical stability (stable above 5.0 V vs. Li/Li^+). A similar RT ionic conductivity has been reported in the study of PVA-PEO composite SPEs. The superhigh conductivity value is evaluated in the PSt-PEO and PVA-PEO SPEs, which is quite close to that of the liquid electrolytes.

Thermogravimetric analysis is constantly used to directly investigate the thermal stability of the polymer electrolytes. In the case of TPU-PEO SPEs (Tao et al., 2017), copolymer electrolyte shows a high conductivity (5.3×10^{-4} S cm^{-1} at 60°C) and notably enhanced thermostability even under 200°C. A similar conductivity and electrochemical improvements could be observed for PS-PEO SPEs (Chen et al., 2019). PS-PEO SPEs have a high storage modulus of 1.4 MPa at 60°C. The Li|PS-PEO SPE|Li cell can be cycled for 400 h at 0.1 mA cm^{-2} without any Li dendrite failure. The charge passed is 144 C cm^{-2} with an average voltage increase of 0.6 mV C^{-1} cm^2. These results indicate that the Li/SPE interface is stable and that the mechanical strength of the SPEs is capable of suppressing Li dendrite growth. As illustrated in **Figure 1E**, PS arms would rearrange and entangle after phase separation, and then the lamellar structure would be reformed by alternating self-assembled PS and PEO layers. So far, several types of organic fillers of the PEO-based SPEs have been discussed in this portion, and more organic fillers will be explored and applied for high-performance flexibility SPEs.

Other Complex Composite SPEs

Except for simplex compound fillers in PEO-based composite SPEs, multiphase composites, such as PEO-inorganic-organic, PEO-organic-organic, and other complicated ones, have also been widely explored to satisfy the need of practical application. These multiblock copolymers with various fillers show improved properties in different aspects.

PEO-inorganic-organic SPEs composite possess the combined advantages of PEO, inorganic and organic components. For instance, the PEO–Al_2O_3-Pr_4NI (tetrapropylammonium iodide) composite SPEs show a high conductivity of 4.2×10^{-4} S cm^{-1} and an admirable PEO spherulitic crystallinity at 24°C with 5% Al_2O_3 filler (Bandara et al., 2017). The ceramic material $Li_{6.4}La_3Zr_{1.4}Ta_{0.6}O_{12}$ (LLZT) was introduced to the PEO–succinonitrile (SN) system (Zha et al., 2018). The one containing 60 wt% of LLZT and 10 wt% of SN shows a high ion conductivity of 1.22×10^{-4} S cm^{-1} at 30°C and a wide electrochemical window of 5.5 V vs. Li/Li^+. The SPEs composed of aluminate complexes (LiAl)–polyethylene glycol (PEG) and PEO could also be prepared via the common solution casting method (Feng et al., 2018). With PEO additive, the segmental mobility of the ether-chain bonded with Al atoms would be improved, providing PEO–LiAl–PEG hybrid SPEs with extra ionic pathways and high ionic conductivity. The new hopping transport mechanism was verified for the single Li-ion conductor system at the nanoscale.

PEO-organic-organic multiblock copolymer SPEs have recently garnered increasing attention because of their hard-separated segments and improved mechanical properties with their multiple microphase separated domains. A multiblock copolymer electrolyte composed of poly(butylene terephthalate) (PBT) and PEO alternating multiblock copolymers (mBCPs) (PBT-*b*-PEO-*b*-PBT)$_n$, is synthesized by the cascade polycondensation-coupling ring-opening polymerization (PROP) method (Huang et al., 2017). The mBCP electrolyte shows a high ionic conductivity of 8.2×10^{-4} S cm^{-1} at 90°C and considerable mechanical properties. A gel polymer electrolyte composed of PEO, PMMA, and P(VDF-HFP) (PEMVH) is synthesized by adding some inorganic oxide fillers (Shi et al., 2018). The PEMVH-oxide filler electrolyte possesses porous and amorphous structures, in which the oxide fillers can promote the formation of the pores of the polymer matrix and the segmental motion of the polymer chain. This unique structure of the polymer membranes contributes to the high ionic conductivity and interfacial stability of hybrid SPEs.

In addition, multilayered composite PEO-based SPEs are also developed to give excellent mechanical stability, ionic conductivity, and interfacial compatibility for the all-solid-state lithium batteries. The flexible composite SPEs composed of PEO layers on both sides of the PEO–perovskite composite are actually an integrated sandwich structure, which is denoted as PEO|PEO-perovskite|PEO (shown in **Figure 1F**). The synthesis routes PEO and LiTFSI were dissolved into acetonitrile. The solution was then dropped onto the surface of the $Li_{0.33}La_{0.557}TiO_3$ (LLTO) nanofiber mat. The wetted LLTO mat was predried in air for 6 h before drying in vacuum for 24 h at 65°C. Then, the membrane was turned to the other side, followed by repeating the wetting and drying processes to obtain the PEO–perovskite SPEs with an integrated sandwich structure. The 3D perovskite nanofiber network can enhance the ionic conductivity by offering Li-ion with abundant channels and improve the mechanical strength of the membrane (Liu K. et al., 2019). Besides, multilayered SPEs with a differentiated salt-based multilayered solid polymer electrolyte were synthesized via a facile slurry casting-drying method, which helped the Li symmetric battery to achieve a high capacity retention of 79.0% (after 300 cycles at 60 and 2°C) (Wang C. et al., 2019). The schematic of multilayered SPEs are displayed in **Figure 1G**. Every layer is purposefully designed to make full use of their respective advantages (i.e., the middle layer can provide a good ionic conductivity for the electrolyte), while the outer layers can enhance the interfacial contact and promote the formation of steady solid electrolyte interface (SEI) and cathode electrolyte interface (CEI) films. As compared with conventional PEO-based SPEs, the multilayer strategy is powerful to achieve high performance and solve electrolyte/electrode interfacial problems of the solid-state batteries.

A summary of the electrochemical window and the ionic conductivity of PEO-based SPEs is presented in **Figure 2** and **Table S1**. Most of them exhibit high electrochemical stable voltages (≥4.5 V) and ionic conductivity ($\geq 1 \times 10^{-4}$ S cm^{-1}). Generally, PEO-organic and multiple complex SPEs show superior high-temperature conductivity and mechanical

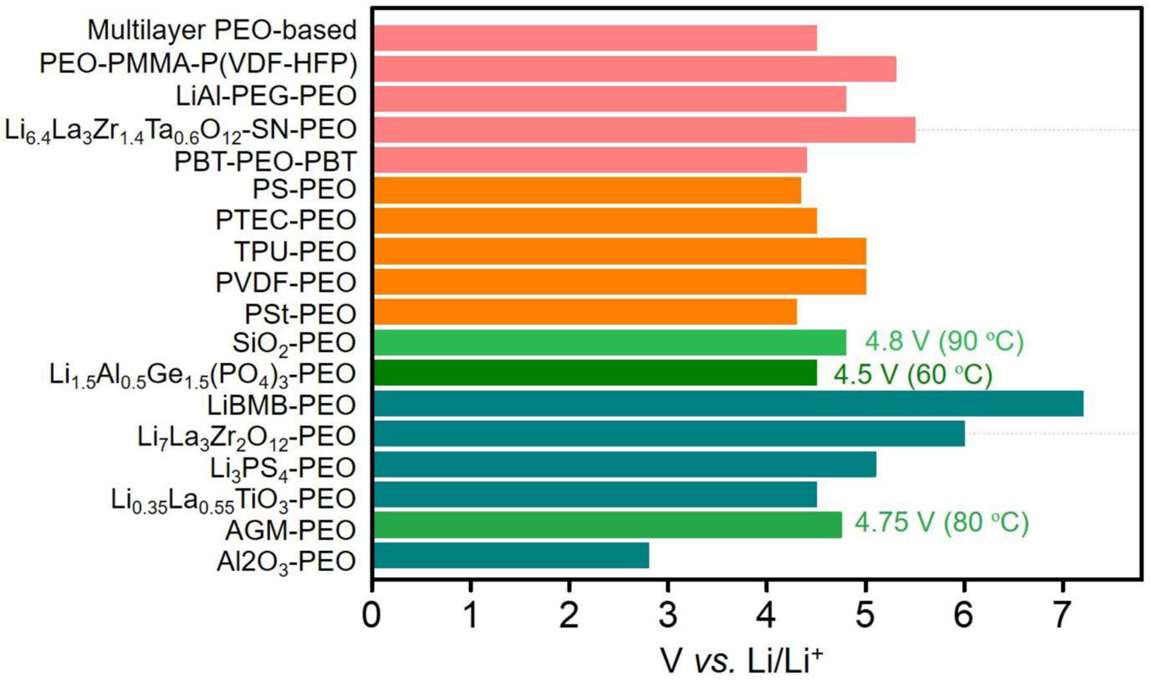

FIGURE 2 | Calculated electrochemical stability windows for the polyethylene oxide (PEO)-based solid-state polymer electrolyte (SPE) candidates in a lithium metal battery. The inorganic-PEO hybrid SPEs are marked by green and dark cyan bars; the organic-PEO hybrid SPEs are marked with an orange bar; and the complex PEO-based hybrid SPEs are marked with a rose bar.

property. In general, the multiple complex electrolyte with high ionic transport and electrode–electrolyte interfacial stability is expected for future commercial application of solid-state LMBs.

CONCLUSIONS

PEO-based SPEs have gained wide attention as promising electrolytes for lithium metal batteries (LMBs) because of their superior processing flexibility and electrode–electrolyte contact. Considerable research efforts have been devoted to improving the SPEs' limited room-temperature ionic conductivity and electrochemical stability of PEO. Inorganic and organic components have been introduced to the PEO-based SPEs to widen its electrochemical window of PEO. The inorganic fillers possess the advantages of low cost and high safety, while the organic ones can improve the SPEs' flexibility and change the polymer crystallinity with a crosslink or copolymerization approach. Moreover, by using multiple complex PEO-based SPEs, the LMBs can achieve much enhanced mechanical strength and electrode-electrolyte interfacial stability. At present, developing suitable PEO-based composite SPEs remains a challenge for the practical applications of high-performance LMBs with high safety and electro-stability.

AUTHOR CONTRIBUTIONS

LY supervised the implementation of the project. LY and SZ conceived the idea. SZ, QW, WM, and LY analyzed the data and wrote the manuscript. All authors contributed to the article and approved the submitted version.

FUNDING

This research was supported by the National Natural Science Foundation of China (21805083), Natural Science Foundation of Hunan Province (2018JJ3331), Science and Technology Planning Project of Hunan Province (2018TP1017), and Scientific Research Fund of Hunan Provincial Education Department (19K058).

SUPPLEMENTARY MATERIAL

The Supplementary Material for this article can be found online at: https://www.frontiersin.org/articles/10.3389/fchem.2020.00640/full#supplementary-material

REFERENCES

Angulakshmi, N., Nahm, K. S., Nair, J. R., Gerbaldi, C., Bongiovanni, R., Penazzi, N., et al. (2013). Cycling profile of $MgAl_2O_4$-incorporated composite electrolytes composed of PEO and $LiPF_6$ for lithium polymer batteries. *Electrochim. Acta* 90, 179–185. doi: 10.1016/j.electacta.2012.12.003

Appetecchi, G. B., Croce, F., and Scrosati, B. (1995). Kinetics and stability of the lithium electrode in poly(methylmethacrylate)-based gel electrolytes. *Electrochim. Acta* 40, 991–997. doi: 10.1016/0013-4686(94)00345-2

Bae, J., Li, Y., Zhang, J., Zhou, X., Zhao, F., Shi, Y., et al. (2018). A 3D nanostructured hydrogel-framework-derived high-performance composite polymer lithium-ion electrolyte. *Angew. Chem. Int. Ed. Engl.* 57, 2096–2100. doi: 10.1002/anie.201710841

Bandara, T. M. W. J., Karunathilaka, D. G. N., Ratnasekera, J. L., Ajith De Silva, L., Herath, A. C., and Mellander, B. E. (2017). Electrical and complex dielectric behaviour of composite polymer electrolyte based on PEO, alumina and tetrapropylammonium iodide. *Ionics* 23, 1711–1719. doi: 10.1007/s11581-017-2016-y

Chen, S., Wang, J., Zhang, Z., Wu, L., Yao, L., Wei, Z., et al. (2018). *In-situ* preparation of poly(ethylene oxide)/Li_3PS_4 hybrid polymer electrolyte with good nanofiller distribution for rechargeable solid-state lithium batteries. *J. Power Sources* 387, 72–80. doi: 10.1016/j.jpowsour.2018.03.016

Chen, Y., Shi, Y., Liang, Y., Dong, H., Hao, F., Wang, A., et al. (2019). Hyperbranched PEO-based hyperstar solid polymer electrolytes with simultaneous improvement of ion transport and mechanical strength. *ACS Appl. Energy Mater.* 2, 1608–1615. doi: 10.1021/acsaem.8b02188

Choe, H. S., Giaccai, J., Alamgir, M., and Abraham, K. M. (1995). Preparation and characterization of poly(vinyl sulfone)- and poly(vinylidene fluoride)-based electrolytes. *Electrochim. Acta* 40, 2289–2293. doi: 10.1016/0013-4686(95)00180-M

Choudhury, S., Stalin, S., Vu, D., Warren, A., Deng, Y., Biswal, P., et al. (2019a). Solid-state polymer electrolytes for high-performance lithium metal batteries. *Nat. Commun.* 10, :4398. doi: 10.1038/s41467-019-12423-y

Choudhury, S., Tu, Z., Nijamudheen, A., Zachman, M. J., Stalin, S., Deng, Y., et al. (2019b). Stabilizing polymer electrolytes in high-voltage lithium batteries. *Nat. Commun.* 10, :3091. doi: 10.1038/s41467-019-11015-0

Deng, F., Wang, X., He, D., Hu, J., Gong, C., Ye, Y. S., et al. (2015). Microporous polymer electrolyte based on PVDF/PEO star polymer blends for lithium ion batteries. *J. Membrane Sci.* 491, 82–89. doi: 10.1016/j.memsci.2015.05.021

Feng, Y., Tan, R., Zhao, Y., Gao, R., Yang, L., Yang, J., et al. (2018). Insight into fast ion migration kinetics of a new hybrid single Li-ion conductor based on aluminate complexes for solid-state Li-ion batteries. *Nanoscale* 10, 5975–5984. doi: 10.1039/C8NR00573G

Fenton, D. E., Parker, J. M., and Wright, P. V. P. (1973). Complexes of alkali metal ions with poly(ethylene oxide). *Polymer* 14, :589. doi: 10.1016/0032-3861(73)90146-8

He, W., Cui, Z., Liu, X., Cui, Y., Chai, J., Zhou, X., et al. (2017). Carbonate-linked poly(ethylene oxide) polymer electrolytes towards high performance solid state lithium batteries. *Electrochim. Acta* 225, 151–159. doi: 10.1016/j.electacta.2016.12.113

He, Y., Zhang, Y., Li, X., Lv, Z., Wang, X., Liu, Z., et al. (2018). A novel ZnO-based inorganic/organic bilayer with low resistance for Li metal protection. *Energy Storage Mater.* 14, 392–401. doi: 10.1016/j.ensm.2018.06.017

Huang, W., Pan, Q., Qi, H., Li, X., Tu, Y., and Li, C. Y. (2017). Poly(butylene terephthalate)-b-poly(ethylene oxide) alternating multiblock copolymers: synthesis and application in solid polymer electrolytes. *Polymer* 128, 188–199. doi: 10.1016/j.polymer.2017.09.027

Jinisha, B., Femy, A. F., Ashima, M. S., and Jayalekshmi, S. (2018). Polyethylene oxide (PEO) / polyvinyl alcohol (PVA) complexed with lithium perchlorate ($LiClO_4$) as a prospective material for making solid polymer electrolyte films. *Materials Mater. Today: Proceedings Proc.* 5, 21189–21194. doi: 10.1016/j.matpr.2018.06.518

Liang, J., Luo, J., Sun, Q., Yang, X., Li, R., and Sun, X. (2019). Recent progress on solid-state hybrid electrolytes for solid-state lithium batteries. *Energy Storage Mater.* 21, 308–334. doi: 10.1016/j.ensm.2019.06.021

Liu, K., Zhang, R., Sun, J., Wu, M., and Zhao, T. (2019). Polyoxyethylene (PEO)|PEO-Perovskite|PEO composite electrolyte for all-solid-state lithium metal batteries. *ACS Appl. Mater. Interfaces* 11, 46930–46937. doi: 10.1021/acsami.9b16936

Liu, W., Li, X., Xiong, D., Hao, Y., Li, J., Kou, H., et al. (2018). Significantly improving cycling performance of cathodes in lithium ion batteries: the effect of Al_2O_3 and $LiAlO_2$ coatings on $LiNi_{0.6}Co_{0.2}Mn_{0.2}O_2$. *Nano Energy* 44, 111–120. doi: 10.1016/j.nanoen.2017.11.010

Liu, Y., Xu, B., Zhang, W., Li, L., Lin, Y., and Nan, C. (2019a). Composition modulation and structure design of inorganic-in-polymer composite solid electrolytes for advanced lithium batteries. *Small* 16, :1902813. doi: 10.1002/smll.201902813

Liu, Y., Zhu, Y., and Cui, Y. (2019b). Challenges and opportunities towards fast-charging battery materials. *Nat. Energy* 4, 540–550. doi: 10.1038/s41560-019-0405-3

Lopez, J., Mackanic, D. G., Cui, Y., and Bao, Z. (2019). Designing polymers for advanced battery chemistries. *Nat. Rev. Mater.* 4, 312–330. doi: 10.1038/s41578-019-0103-6

Maleki Kheimeh Sari, H., and Li, X. (2019). Controllable cathode–electrolyte interface of $Li[Ni_{0.8}Co_{0.1}Mn_{0.1}]O_2$ for Lithium ion batteries: a review. *Adv. Energy Mater.* 9, :1901597. doi: 10.1002/aenm.201901597

Manthiram, A., Yu, X., and Wang, S. (2017). Lithium battery chemistries enabled by solid-state electrolytes. *Nat. Rev. Mater.* 2, :16103. doi: 10.1038/natrevmats.2016.103

Mehdi, A., Cerclier, C. V., Le Bideau, J., Guyomard, D., Dalmas, F., Chenal, J.-M., et al. (2017). PEO-silsesquioxane flexible membranes: organic-inorganic solid electrolytes with controlled homogeneity and nanostructure. *ChemistrySelect* 2, 2088–2093. doi: 10.1002/slct.201601798

Mohanta, J., Panda, S. K., Singh, U. P., and Si, S. (2017). Nanostructure PEO-Silica hybrids: a new class of additive material for composite polymer electrolytes. *ChemistrySelect* 2, 12019–12027. doi: 10.1002/slct.201702787

Nie, K., Wang, X., Qiu, J., Wang, Y., Yang, Q., Xu, J., et al. (2020). Pushing PEO stability up to 4.5 V by surface coating of cathode. *ACS Energy Lett*. 5, 826–832. doi: 10.1021/acsenergylett.9b02739

Niitani, T., Shimada, M., Kawamura, K., Dokko, K., Rho, Y.-H., and Kanamura, K. (2005). Synthesis of Li^+ Ion conductive PEO-PSt block copolymer electrolyte with microphase separation structure. *Electrochem. Solid ST* 8, A385–A388. doi: 10.1149/1.1940491

Qiu, J., Yang, L., Sun, G., Yu, X., Li, H., and Chen, L. (2020). A stabilized PEO-based solid electrolyte via a facile interfacial engineering method for a high voltage solid-state lithium metal battery. *Chem. Commun.* 56, 5633–5636. doi: 10.1039/D0CC01829E

Shi, J., Xiong, H., Yang, Y., and Shao, H. (2018). Nano-sized oxide filled composite PEO/PMMA/P(VDF-HFP) gel polymer electrolyte for rechargeable lithium and sodium batteries. *Solid State Ionics* 326, 136–144. doi: 10.1016/j.ssi.2018.09.019

Tao, C., Gao, M.-H., Yin, B.-H., Li, B., Huang, Y.-P., Xu, G., et al. (2017). A promising TPU/PEO blend polymer electrolyte for all-solid-state lithium ion batteries. *Electrochim. Acta* 257, 31–39. doi: 10.1016/j.electacta.2017.10.037

Wan, Z., Lei, D., Yang, W., Liu, C., Shi, K., Hao, X., et al. (2019). Low resistance-integrated all-solid-state battery achieved by $Li_7La_3Zr_2O_{12}$ nanowire upgrading polyethylene oxide (PEO) composite electrolyte and PEO cathode binder. *Adv. Functional Mat.* 29:1805301. doi: 10.1002/adfm.201805301

Wang, C., Wang, T., Wang, L., Hu, Z., Cui, Z., Li, J., et al. (2019). Differentiated lithium salt design for multilayered PEO electrolyte enables a high-voltage solid-state lithium metal battery. *Adv. Sci.* (Weinh*)* 6, :1901036. doi: 10.1002/advs.201901036

Wang, X., Zhai, H., Qie, B., Cheng, Q., Li, A., Borovilas, J., et al. (2019). Rechargeable solid-state lithium metal batteries with vertically aligned ceramic nanoparticle/polymer composite electrolyte. *Nano Energy* 60, 205–212. doi: 10.1016/j.nanoen.2019.03.051

Wang, Z., Huang, B., Huang, H., Chen, L., Xue, R., and Wang, F. (1996). Investigation of the position of Li^+ ions in a polyacrylonitrile-based electrolyte by Raman and infrared spectroscopy. *Electrochim. Acta* 41, 1443–1446. doi: 10.1016/0013-4686(95)00392-4

Xiao, W., Wang, J., Fan, L., Zhang, J., and Li, X. (2019). Recent advances in $Li_{1+x}Al_xTi_{2-x}(PO_4)_3$ solid-state electrolyte for safe lithium batteries. *Energy Storage Mater.* 19, 379–400. doi: 10.1016/j.ensm.2018.10.012

Xu, H., Chien, P. H., Shi, J., Li, Y., Wu, N., Liu, Y., et al. (2019). High-performance all-solid-state batteries enabled by salt bonding to perovskite in poly(ethylene oxide). *Proc. Natl. Acad. Sci. U.S.A.* 116, 18815–18821. doi: 10.1073/pnas.1907507116

Xu, Z., Yang, T., Chu, X., Su, H., Wang, Z., Chen, N., et al. (2020). Strong Lewis acid-base and weak hydrogen bond synergistically enhancing ionic conductivity of poly(ethylene oxide)@SiO_2 electrolytes for a high rate capability Li-metal battery. *ACS Appl. Mater. Interfaces* 12, 10341–10349. doi: 10.1021/acsami.9b20128

Yap, Y. L., You, A. H., Teo, L. L., and Hanapei, H. (2013). Inorganic filler sizes effect on ionic conductivity in polyethylene oxide (PEO) composite polymer electrolyte. *Int. J. Electrochem. Sci.* 8, 2154–2163.

Yuan, C., Li, J., Han, P., Lai, Y., Zhang, Z., and Liu, J. (2013). Enhanced electrochemical performance of poly(ethylene oxide) based composite polymer electrolyte by incorporation of nano-sized metal-organic framework. *J. Power Sources* 240, 653–658. doi: 10.1016/j.jpowsour.2013.05.030

Yuan, F., Yang, L., Zou, X., Dong, S., Chi, S., Xie, J., et al. (2019). Flexible all-solid-state electrolytes with ordered fast Li-ion-conductive nano-pathways for rechargeable lithium batteries. *J. Power Sources* 444:227305. doi: 10.1016/j.jpowsour.2019.227305

Zha, W., Chen, F., Yang, D., Shen, Q., and Zhang, L. (2018). High-performance $Li_{6.4}La_3Zr_{1.4}Ta_{0.6}O_{12}$/poly(ethylene oxide)/succinonitrile composite electrolyte for solid-state lithium batteries. *J. Power Sources* 397, 87–94. doi: 10.1016/j.jpowsour.2018.07.005

Zhai, H., Xu, P., Ning, M., Cheng, Q., Mandal, J., and Yang, Y. (2017). A flexible solid composite electrolyte with vertically aligned and connected ion-conducting nanoparticles for lithium batteries. *Nano Lett.* 17, 3182–3187. doi: 10.1021/acs.nanolett.7b00715

Zhang, H., Armand, M., and Rojo, T. (2019). Innovative polymeric materials for better rechargeable batteries: strategies from CIC energigune. *J. Electrochem. Soc.* 166, A679–A686. doi: 10.1149/2.0811904jes

Zhao, C. Z., Duan, H., Huang, J. Q., Zhang, J., Zhang, Q., Guo, Y. G., et al. (2019). Designing solid-state interfaces on lithium-metal anodes: a review. *Sci. China Chem.* 62, , 1286–1299. doi: 10.1007/s11426-019-9519-9

Zhao, Q., Liu, X., Stalin, S., Khan, K., and Archer, L. A. (2019). Solid-state polymer electrolytes with in-built fast interfacial transport for secondary lithium batteries. *Nat. Energy* 4, 365–373. doi: 10.1038/s41560-019-0349-7

Zhao, Q., Stalin, S., Zhao, C.-Z., and Archer, L. A. (2020). Designing solid-state electrolytes for safe, energy-dense batteries. *Nat. Rev. Mater.* 5, 229–252. doi: 10.1038/s41578-019-0165-5

Zhou, D., Shanmukaraj, D., Tkacheva, A., Armand, M., and Wang, G. (2019). Polymer electrolytes for lithium-based batteries: advances and prospects. *Chem.* 5, 2326–2352. doi: 10.1016/j.chempr.2019.05.009

Conflict of Interest: The authors declare that the research was conducted in the absence of any commercial or financial relationships that could be construed as a potential conflict of interest.

ORIGINAL RESEARCH
published: 23 October 2020
doi: 10.3389/fchem.2020.00827

Investigation on the Effect of Different Mild Acidic Electrolyte on ZIBs Electrode/Electrolyte Interface and the Performance Improvements With the Optimized Cathode

Yang Gui*, Yang Lei and Bao An Fan

Key Laboratory of Hubei Province for Coal Conversion and New Carbon Materials, School of Chemistry and Chemical Engineering, Wuhan University of Science and Technology, Wuhan, China

Zinc ion batteries (ZIBs), as promising alternatives of lithium ion batteries (LIBs), have aroused revived interest in the energy storage field recently. To obtain good performance, the choice of electrolyte plays a vital role. Therefore, in this work, three kinds of aqueous electrolyte have been assessed for interfacial effect and ZIB performance. Through the comparison, $ZnSO_4$ electrolyte showed advantages on ionic conductivity over both $Zn(NO_3)_2$ and $Zn(CH_3COO)_2$ solution, $Zn(CH_3COO)_2$ exhibited considerable Zn stripping/plating kinetics with $ZnSO_4$, and there was no characteristic peak pair of Zn dissolution/deposition found in $Zn(NO_3)_2$. Additionally, a lower charge transfer resistance was proved when the cell with 1 M $ZnSO_4$ solution. Besides, to further study on cathodic graphite paper, activation and optimization has been conducted, and cells with optimized graphite paper showed an outstanding enhancement.

Keywords: aqueous electrolye, interfacial effect, ZIB performance, electrochemical assessment, Zn stripping/plating kinetics

Edited by:
Du Yuan,
Nanyang Technological University, Singapore

Reviewed by:
Jin Zhao,
Nanjing University of Posts and Telecommunications, China
Xiaolei Huang,
Northwestern Polytechnical University, China

****Correspondence:***
Yang Gui
guiyang@wust.edu.cn

Specialty section:
This article was submitted to Electrochemistry, a section of the journal Frontiers in Chemistry

Received: *02 July 2020*
Accepted: *05 August 2020*
Published: *23 October 2020*

Citation:
Gui Y, Lei Y and Fan BA (2020) Investigation on the Effect of Different Mild Acidic Electrolyte on ZIBs Electrode/Electrolyte Interface and the Performance Improvements With the Optimized Cathode. Front. Chem. 8:827. doi: 10.3389/fchem.2020.00827

INTRODUCTION

Nowadays, different types of rechargeable batteries, as lithium-ion battery (LIB) alternatives, have attracted attention of researchers due to that (1) limited sources of lithium; (2) higher flammable risk of organic electrolyte in LIBs; (3) high chemical activity of lithium leading to a harsh requirement on its preparation process (Whittingham, 2004; Armand and Tarascon, 2008). Therefore, it is significant to search for new ion battery resources with considerable or even higher capacity but much safer and convenient fabrication methods. Systems built up on elements with electropositive characters such as Na, Mg, Al, Ca, and Zn have attracted extensive interest because of promising theoretical capacity, abundant material and effective cost (Li et al., 2014; Muldoon et al., 2014; Yabuuchi et al., 2014; Lin et al., 2015; Choi and Aurbach, 2016; Ponrouch et al., 2016; Zhang et al., 2016). Meanwhile, replacing the organic electrolyte with an aqueous one offers advantages including more convenient manufacturing conditions as well as advantageous cost, greener, safer, and better ionic conductivity (Lu et al., 2011; Kim et al., 2014). Regarding these superior features, aqueous Zn-ion battery (ZIB)/capacitor (ZIC) technology plays a particular role as a promising alternative based on its property of good water compatibility, low flammability and, especially when compared with LIBs, Zn exhibits higher charge density (Lee et al., 2015; Pan et al., 2016).

Following the development history of ZIBs, the first ZIB prototype was made in 1999 by using zinc metal as electrode and alkaline as electrolyte which presented excellent characters of low redox potential [−0.76 V vs. standard hydrogen electrode (SHE)]. Since then, Zinc metal has been applied widely in different batteries like Ni-Zn battery, MnO_2-Zn battery, Zinc ion battery, and Zinc air battery (Yang and Lin, 2002; Cheng et al., 2005). However, the sever zinc dendrite formation in alkaline solution extremely shortened its cycling life and limited the corresponding discharge capacity. To deal with this problem, the displacement of alkaline electrolyte with mild solution of zinc sulfate was firstly investigated by Yamamoto and Shoji (1986). According to the observation, due to mild acidic condition, the appearance of ZnO, $Zn(OH)_2$, etc. by-products on zinc anode has been effectively inhibited (Yamamoto and Shoji, 1986). Hence, the choice of electrolyte plays a vital role for the overall performance of ZIBs. Firstly, the function of the electrolyte does not only provide pathways for ion migration but also determines the reversibility of Zn plating/stripping process and SEI formation (Wang F. et al., 2018; Wang Z. et al., 2018; Qiu et al., 2019; Yuan et al., 2019; Zhao et al., 2019). Secondly, the accurate choice of electrolyte, including its concentration, pH value, coordination number and so on, could maximize the energy storage capacity of the whole system to achieve its optimized performance (Li et al., 2016; Wang F. et al., 2018; Wang Z. et al., 2018; Zhao et al., 2018). Up to now, the exploration on electrolytes for ZIBs is still in its infancy, and more details on the understanding of the effect of electrolytes on the electrochemical performance is required. In this paper, to reveal the relationship between electrolyte and zinc storage performance, we investigated three kinds of electrolyte by using zinc and graphite paper as counter and working electrode, respectively, from the perspectives of stripping/plating kinetics, interfacial kinetics, and its behavior on zinc storage performance. Furthermore, cathode optimization has been designed as well and harvested outstanding enhancement on ZIB performance.

EXPERIMENTS

Chemicals and Materials

Zinc acetate dihydrate (ALADDIN); Zinc nitrate hexahydrate (ALADDIN); Zinc sulfate monohydrate (ALADDIN); Ethanol (ALADDIN); concentrated sulfuric acid (ALADDIN); Acetone (ALADDIN). Zn plate (34 × 150 × 0.2 mm); Graphite paper (125 × 200 × 0.1 mm).

Material Pretreatment

Zn plate was cut into a dimension of 34 × 25 × 0.2 mm, then placed into a mixture solution of ethanol and acetone with a volume ratio of 1:1, followed by exposure to an ultrasound bath for 15 min, after that the sample was taken out and readied for later use. The graphite paper wascut into a dimension of 30 × 20 × 0.1 mm and cleaned with acetone.

The activation of graphite paper was realized by exposing one clean piece of graphite paper in a three-electrode system at a constant potential for a certain period. The potential sweep rate was set at $0.01\,V\ s^{-1}$. The system was constructed by a piece of graphite paper, platinum foil, and saturated calomel (SCE) as working, counter, and reference electrode, respectively. The electrolyte was composed by 2 M H_2SO_4. Five samples were prepared and named as S1, S2, S3, S4, and S5, respectively. S1 was treated by exposing one piece of graphite paper in 2 M H_2SO_4 under 4 V for 60 s. When the treatment was finished, S1 was taken out and flushed by DI water until pH of the solution close to ∼6.7 (pH value of the DI water), then placed in an oven at 60° overnight. The treatment condition for S2 was the same as S1 except the final potential at 6 V for a period of 300 s. S3 and S4 was treated at 6 V as well but within a period of 450 and 600 s independently. S5 was activated at 8 V for 450 s.

Electrochemical Tests

Three Electrode System Measurement

The testing system was constructed by a piece of graphite paper with a dimension of $2 \times 3\ cm^2$ as the working electrode, a piece of Zn plate ($2.5 \times 3.5\ cm^2$) as the counter electrode and another piece of Zn plate ($2.5 \times 3.5\ cm^2$) as the reference electrode. The series of cyclic voltammograms (CVs) in different electrolytes were recorded at a potential sweep rate of $1\,mV\ s^{-1}$ within a proper electrochemical window. Electrochemical impedance spectroscopy (EIS) measurement was conducted through a CHI600E electrochemical workstate with an AC voltage of 5 mV amplitude in the frequency ranging from 100 kHz to 100 mHz. This measurement was used to differentiate the effect on different electrolyte on electrode interfaces when considering a ZIB performance.

Two Electrode System Measurement

The two-electrode system consisted of using a CR2032 coin-type. CR2032 coin cell was assembled by the pristine or activated graphite paper as a working electrode, Zn foil as a counter electrode, filter paper as a membrane and 1 M $ZnSO_4$ as an electrolyte. The galvanostatic charge/discharge performance of the cell has been conducted by a LAND-CT2001A battery-testing instrument.

Morphology Characterization

Scanning electron microscopy (SEM) was taken by Nova NanoSEM400 microscopes equipped with energy dispersive spectroscopy (EDS) for elemental analysis.

RESULTS AND DISCUSSION

A three-electrode system consisting of Zn/Zn/graphite paper as counter/reference/working electrode wasbuilt up. Three kinds of electrolytes havebeen selected. As shown in **Figure 1**, the cyclic voltammetry in $Zn(CH_3COO)_2$ and $ZnSO_4$ electrolyte reveals an obvious reversible electrochemical stripping/plating process of Zn (Xu et al., 2012; Li et al., 2016). However, no characteristic peak pair corresponding to Zn dissolution/deposition has been found in 1 M $Zn(NO_3)_2$ due to the instability of NO_3^- (Zhang et al., 2016). Notably, the onset potential for deposition/dissolution of Zn plating/stripping is −0.13/−0.034 V and −0.11/−0.055 corresponding to $Zn(CH_3COO)_2$ and $ZnSO_4$ separately (Liu et al., 2016, 2017). Compared with $ZnSO_4$, a smaller potential separation was observed in $Zn(CH_3COO)_2$ which reflects better reversibility. Furthermore, a lower oxidation peak at around 0.48 V is suspected due to the oxidation of CH_3COO^-. However, the higher current density exhibited in $ZnSO_4$ solution assists a faster kinetics. Therefore, from the cyclic voltammetry analysis on these three electrolytes, it is concluded that (1) there is no obvious Zn stripping/plating process captured in 1 M $Zn(NO_3)_2$ electrolyte at the corresponding electrochemical reactive potential range; (2) relative to 1 M $Zn(CH_3COO)_2$ solution, the system in 1 M $ZnSO_4$ behaves faster kinetics of Zn dissolution/deposition.

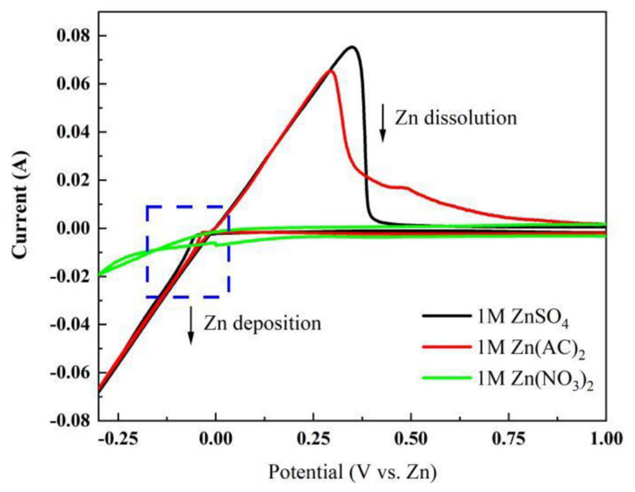

FIGURE 1 | Cyclic voltammetry characterization in a three-electrode system at a scan rate of 1 mV s^{-1} in different electrolytes.

To further investigate the interface effects between the electrolyte and electrode surface, an electrochemical impedance spectrum (EIS) was designed. The measurement was set at open circuit potential with respect to the chosen three electrolytes as shown in **Figure 2**. In their Nyquist plots in **Figure 2A**, through the inset image, a depressed semicircle in the high-frequency region can be seen in all these three electrolytes. In further detail, the cross section at the X-axis tells resistance difference due to the different ionic conductivity of respective electrolyte (Hwang, 2018). Hence, the result may indicate an ionic conductive sequence of 1 M $ZnSO_4$, 1 M $Zn(CH_3COO)_2$ and 1 M $Zn(NO_3)_2$ from high to low. In addition, the highest imaginary point of the enlarged semicircle in the high-frequency region corresponds to the phase transition in their Bode plots in **Figure 2B** (Wang et al., 2001), which represents a charge transfer process involving stripping/plating of Zn/Zn^{2+}. Based on their characteristic frequencies, the lowest one corresponds

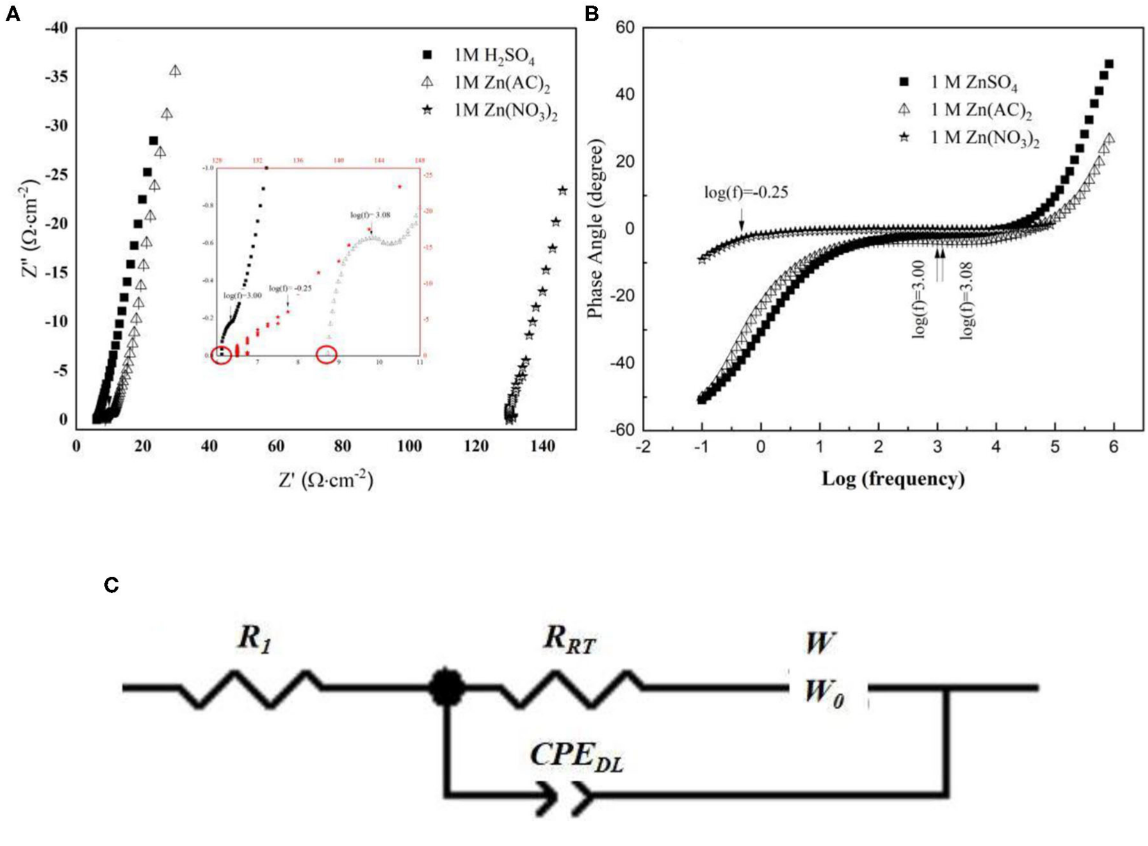

FIGURE 2 | (A) EIS Nyquist plots and Bode plots **(B)** collected from a three-electrode system with different electrolyte; **(C)** Equivalent Circuit for data fitting.

to 1 M $Zn(NO_3)_2$ and indicates a slower kinetics while the other two show higher kinetics, which is in agreement with their cyclic voltammetry observation. Furthermore, the platform extended farthest to 60° describes a diffusion process, which is characterized by the size of warburg. The size of warburg time constant is inversely proportional to the square-root of Zn^{2+} diffusivity (Gui and Blackwood, 2015). The fitting results based on the equivalent circuit displayed in **Figure 2C** were listed in **Table 1**, where R_s represents the series resistance originated from electrode, electrolyte, and the contact; CPE_{DL} denotes a constant phase element designating the double layer capacitance arising from the charges accumulated on the surface of electrode; R_{CT} is the resistance produced by the charge transfer process from the electrolyte to Zn surface, which also associates with this process kinetics; and *Wo* is symbolized as an open circuit Warburg impedance reflecting ion diffusion from electrolyte to the electrode/electrolyte interface. From **Table 1**, the series resistance in 1 M $ZnSO_4$ is the lowest and the highest one is assigned to 1 M $Zn(NO_3)_2$, which is suspected to be caused by the different solvation condition in different electrolytes and further the various ionic conductivity. From this aspect, it means that $ZnSO_4$ solution should be the most preferred electrolyte with favorable ionic conductivity, hence benefit for ions diffusion. Simultaneously, the value of R_{CT} also keeps the same sequence with *Rs*. The smaller charge transfer resistance in $ZnSO_4$ demonstrates a faster kinetics which is consistent with the anodic current density recorded in **Figure 1**. Additionally, a highest value of CPE_{DL} in 1 M $ZnSO_4$ electrolyte was captured as well which could be due to the faster charge transfer kinetics making a rougher surface of the Zn electrode. However, the system with 1 M $ZnSO_4$ exhibits the longest time period for ions diffusion onto electrode surface that may indicate a longer path length the ions in 1 M $ZnSO_4$ will travel. This elongation may be due to the formation of $Zn(OH)_x(SO_4)_y{\cdot}zH_2O$ on the electrode surface which takes up the near surface for ions to reach and a further study on SEI on Zn has to be designed to clear the observation (Lee et al., 2016; Pan et al., 2016; Parker et al., 2017).

To explore the impact of different electrolytes on ZIB performance, CVs of the coin cell with different electrolytes has been performed. The coin cell was constructed by Zn foil and non-activated graphite paper as a counter and working electrode separately. From **Figure 3A**, shapes of CVs for both 1 M $Zn(CH_3COO)_2$ and 1 M $Zn(NO_3)_2$ are almost the same as in a three-electrode system, but a sharp decrease on the deposition/dissolution peak pair was observed for a coin cell with 1 M $ZnSO_4$ electrolyte, which could be due to formation of a surface layer (Konarov et al., 2018). Additionally, the cyclic shapes enclosed from 0.8 to 2.0 V for the three electrolytes are all close to rectangular, which can be contributed to by the capacitive property of the graphite paper. Furthermore, the ratio of anodic area over its correlated cathodic one is closer to 1 in 1 M $ZnSO_4$. This good symmetric behavior implies a better reversibility. In order to reveal the impact of these chosen electrolytes on ZIBs performance, the respective charge/discharge polarization curves at a current density of 0.02 A g^{-1} has been collected and shown in **Figure 3B**. The overall specific capacities of the ZIBs are low due to the low surface area of the working electrodes, i.e., the graphite papers. Even though, under the same condition, the different behaviors due to various electrolytes are still distinguishable. **Figure 3B** points out that the ZIB with 1 M $ZnSO_4$ performs the highest potential on the electrochemical energy storage capacity. Besides, the good symmetry of its charge/discharge polarization curve reflects the high coulomb efficiency, which is consistent with its symmetric cyclic voltammetry curve. However, coulomb efficiencies of the ZIBs with 1 M $Zn(NO_3)_2$ and $Zn(CH_3COO)_2$ are only 47.4 and 64.8% individually.

Based on **Figure 3B**, realizing the poor performance by the non-activated surface of the graphite paper, electro-activation method has been adopted to activate the graphite paper surface. The respective treatment condition for samples of S1, S2, S3, S4, and S5 was stated in the experiment section. To visualize the effect of the activation result, SEM images have been collected and displayed in **Figure 4**. Through the comparison, from S1 to S5, there are more and more folds on the graphite paper surface as compared with pristine graphite paper in **Figure 4A**. The larger rugae area reflects an increased surface area. Hence, it is supposed to harvest enhanced ion storage capability when assembled in an ZIB cell. Meanwhile, we found that the treatment was sensitive to potential rather than the exposure time. As can be seen that the surface of S1 in **Figure 4B** is much smoother than S3 in **Figure 4D**. Even though, unlike S4 and S5, the surface of S3 still keeps as a whole with shallow wrinkles rather than fractures in **Figures 4E,F**. Accordingly, all samples show a certain degree of surface oxidization and sulfidation based on their EDS analysis. The overall content of oxygen is higher than sulfur (at. 12 vs. at. 2% on average) which was donated by SO_4^{2-}.

To discuss the effects of activated graphite papers (AGP) on ZIB performance, CVs of the coin cell with non-activated (pristine GP) and different activated graphite paper (AGP) as cathode has been measured and compared. **Figure 5A** displays the CV curves of coin cells at 1 mV s^{-1}. As compared to the CV of

TABLE 1 | Fitting results list based on the equivalent circuit in **Figure 2C**.

System with different electrolyte	R_s (Ω cm^{-2})	R_{CT} (Ω cm^{-2})	*W*		CPE_{DL} (F cm^{-2})	
			W-P	*W-T*	*CPE-T*	*CPE-P*
1 M $ZnSO_4$	6.15	0.55	0.61	17.61	0.0023	0.75
1 M $Zn(CH_3COO)_2$	8.82	0.82	0.35	0.12	9.90×10^{-6}	1.00
1 M $Zn(NO_3)_2$	126.44	3.03	0.61	11.72	$3.15 \times 1\ 0^{-6}$	0.65

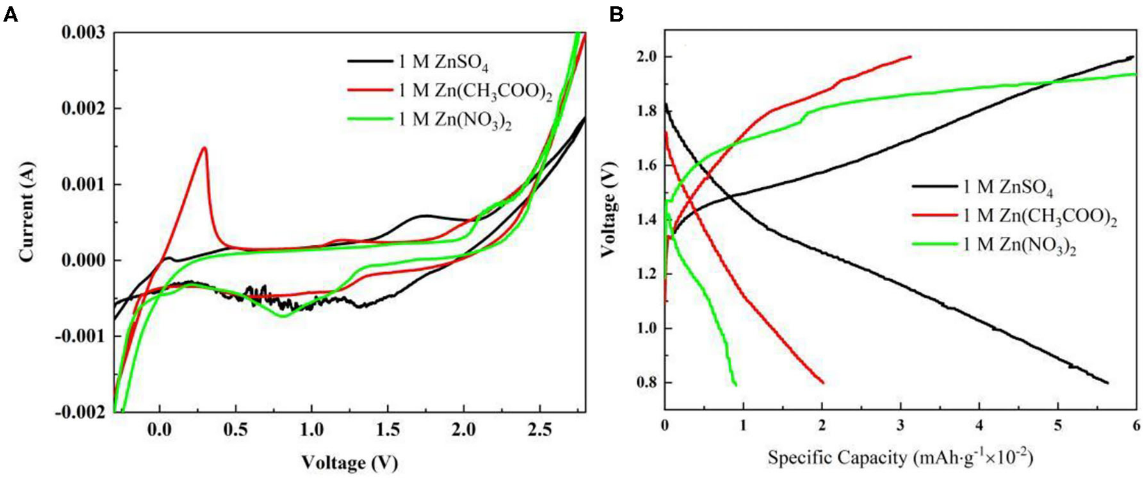

FIGURE 3 | (A) Electrode Electrochemical performance characterization in different electrolyte using coin cell construction: **(A)** Cyclic voltammetry (CV) of coin cells at a scan rate of 1 mV s^{-1}; **(B)** Galvanostatic charge/discharge curves of coin cells at a current density of 0.02 A g^{-1}.

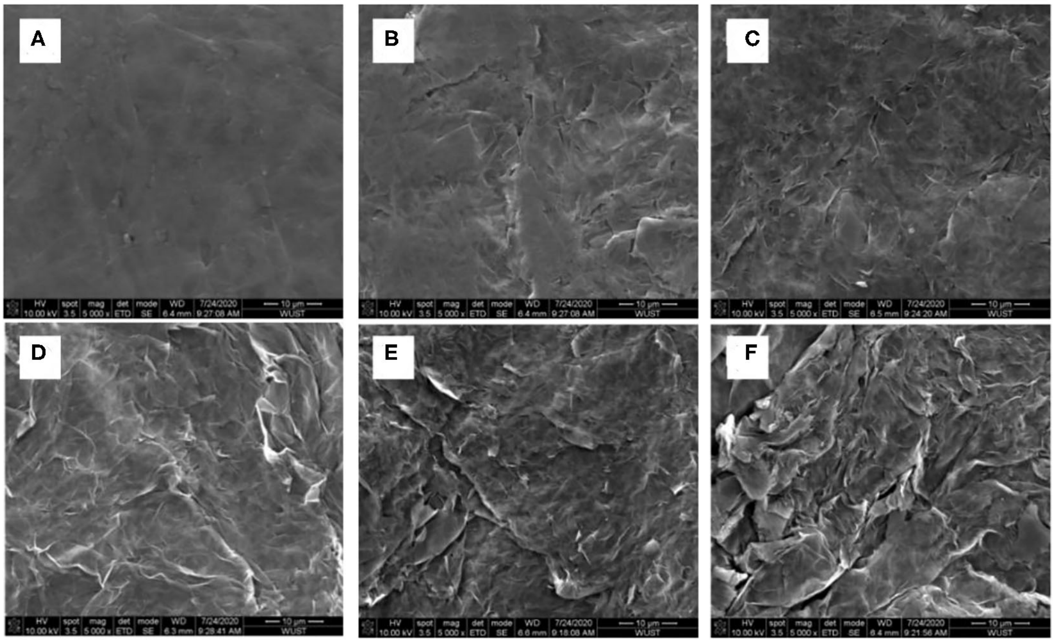

FIGURE 4 | SEM images of **(A)** pristine graphite paper, **(B)** S1, **(C)** S2, **(D)** S3, **(E)** S4, and **(F)** S5.

the cell with non-activated graphite paper (NAGP), the observed anodic peak in all cells with AGP migrates more negatively, which could be related to the electrode activation effects, similar to the observation of the initial profile changes in MnO_2-based cathodes in ZIBs (Zhang et al., 2016). Further comparison finds that during the anodic sweeping, peaks centered at 1.55 and 1.50 V for S1 and S2, respectively, become sharp at 1.62, 1.67, and 1.7 V in CV of S3, S4, and S5 separately. The change is suspected to be induced by anions (SO_4^{2-}) intercalation into graphite interlayers as discussed in zinc graphite battery (Fan et al., 2019). Moreover, through comparing the half peak width and anodic current density, the anodic peak located at 1.62 V shows the narrowest and highest, which implies a faster kinetic process on S3 interface than on the others'. In cathodic scan, a large cathodic peak centered at 1.29 and 1.34 V for S1 and S2, respectively, is converted into two distinctive peaks as captured in CV of S3, S4, and S5. Enlightened by the phenomenon observed in $LiMn_2O_4$, that two distinct cathodic peaks correspond to a two-step insertion of Li^+ into a Li-rich and Li-depleted state (Lu et al., 2014; Suo et al., 2015), these two distinct cathodic peaks

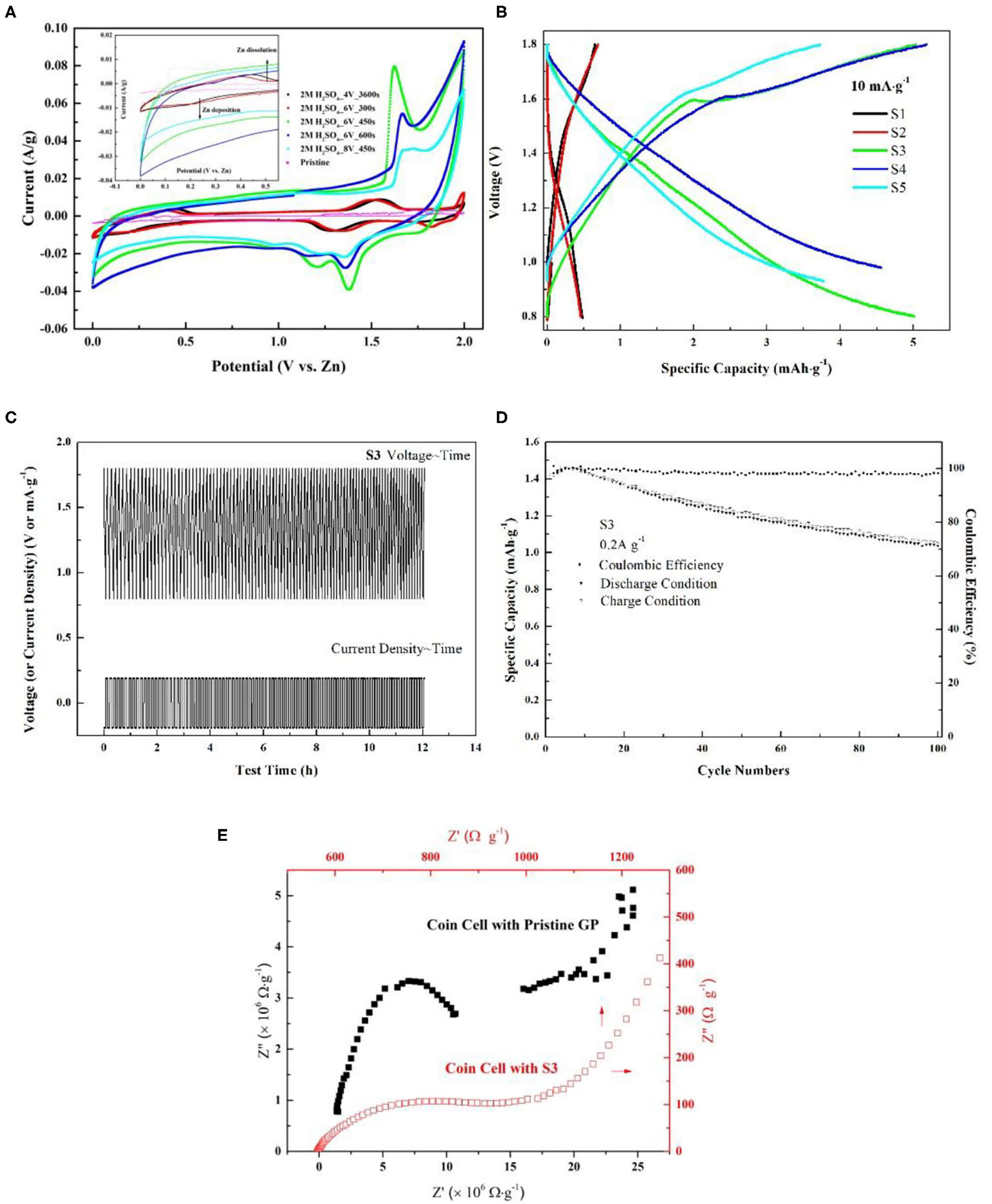

FIGURE 5 | **(A)** Cyclic voltammetry comparison among pristine GP, S1, S2, S3, S4, and S5. The measurement was conducted by using CR2032 coin-type cell with Zn foil as counter electrode and 1 M $ZnSO_4$ as electrolyte. The scan rate was 1 mV s^{-1}; **(B)** Galvanostatic charge/discharge curves of AGP/Zn between 0.8 and 1.9 V at 10 mA g^{-1}; **(C)** Gavanostatic cycling of S3 at 0.2 A g^{-1} for 100 cycles; **(D)** Cycling performance of the cell with S3 as cathode at 0.2 A g^{-1}; **(E)** EIS Nyquist plots comparison between coin cell with pristine GP and S3. The data was captured under their respective open circuit potential.

could be attributed to gradual insertion of Zn^{2+} into the near-surface and deep interlayer of AGP. Because that the specific area of all these three samples show great enhancement as compared with the other two and pristine one in **Figure 4**. Furthermore, as can be seen in the enlarged curves (**Figure 5A**, inset), the redox couple for deposition/dissolution of Zn^{2+}/Zn is less significant due to the improved capacitive behavior after the activation. This benefit is given by the increased specific surface area as shown in **Figure 4**.

In order to assess ZIB performance with AGPs, galvanostatic charge/discharge curves of AGP/Zn between 0.8 and 1.9 V at 10 mA g^{-1} have been detected. From the comparison shown in **Figure 5B**, it points out that AGP of S3 shows the highest specific capacity of 5.0 mAh g^{-1} which is two orders of magnitude higher than the pristine one and one orders than S1 and S2. After the assessment, S3 is proved to be the optimized cathode in this study. Therefore, gavanostatic cycling of S3 at 0.2 A g^{-1} was conducted to evaluate its stability. As elaborated in **Figure 5C**, from the start to the end of 100 cycles, there is no changes on its voltage∼ time profile which supports its good reversibility and high stability. Based on **Figure 5C**, coulombic efficiency of the cell with S3 has been calculated and was placed in **Figure 5D**. After 100 cycles of charge/discharge circulation, its coulombic efficiency can still attain at 96%. Hence, concluded from above discussion, GP activated under S3 condition gives good ZIB performance. To elucidate the extraordinary improvement of ZIB performance by using S3, EIS comparison in **Figure 5E** between coin cell with NAGP and S3 has been discussed. From the interfacial standpoint, it can be seen that the electrode resistance of coin cell with NAGP is four orders of magnitude higher than the one with S3. The high contact resistance should be due to the hydrophobic nature of graphite without the treatment. In addition, the large semi-circle diameter of coin cell with NAGP also presents a high charge transfer resistance. This observation is actually in agreement with the CV conclusion, the large half peak width and low current density of which tells the sluggish kinetic process in coin cell with NAGP. Due to this high charge transfer resistance, the coin cell with NAGP also shows low specific capacity as compared with that of S3. To conclude, from an interfacial perspective, the improvements of using S3 should be contributed to by the increased hydrophilic property of GP after the treatment, hence decreasing the contact resistance and corresponding charge transfer resistance. Finally, the coin cell with S3 exhibits an advantageous ZIB performance in this study.

To reveal the interfacial behavior of S3 in ZIB, the electrochemical impedance spectra of the coin cell under different voltage have been investigated and exhibited in **Figure 6**. The choice of voltage is based on the electrochemical process corresponding to CV of S3 in **Figure 5A**. The Nyquist plots in **Figure 6A** displays one depressed semi-circle which concatenates one semi-circle in mid frequency region, followed by a large semi-circle in low frequency at all voltages. The semi-circle in low frequency is related to peaks in the corresponding frequency region in **Figure 6B**. To quantitatively analyze the electrochemical interfacial process during ZIB operation via S3, Zn foil, and 1 M $ZnSO_4$, the equivalent circuit in **Figure 2C** compatible with below impedance spectra is adopted and the corresponding fitting parameters are listed in **Table 2**. In the table, parameter of *Rs* represents the series resistance from electrode, solution, and contact; charge transfer resistance (R_{CT}) with a parallel constant phase element (*CPE*) which relates to Zn^{2+}/Zn reaction at the surface of the Zn foil along with extraction/insertion of Zn^{2+} from/into S3; the serial open circuit Warburg impedance (*Wo*) in the circuit reflects ion diffusion kinetics from electrolyte to the electrode/electrolyte interface. As shown, comparing parameters obtained at 1.25, 1.38, and 1.63 V, R_S, $R_{CT,}$ and Warburg impedance W_o-*R* shows the lowest value at 1.63 V. This decrease corresponds to the sharp peak in CV of S3 (**Figure 5A**), revealing the fast extraction of Zn^{2+} from S3 which possibly promotes the charge transfer rate for Zn^{2+} diffusion and Zn deposit. However, all these three values are high at 0.8 V. Combining with **Figure 5A**, a typical capacitive behavior is shown as the nature of carbon-based material. Therefore, the high resistance should originate from the double layer on the

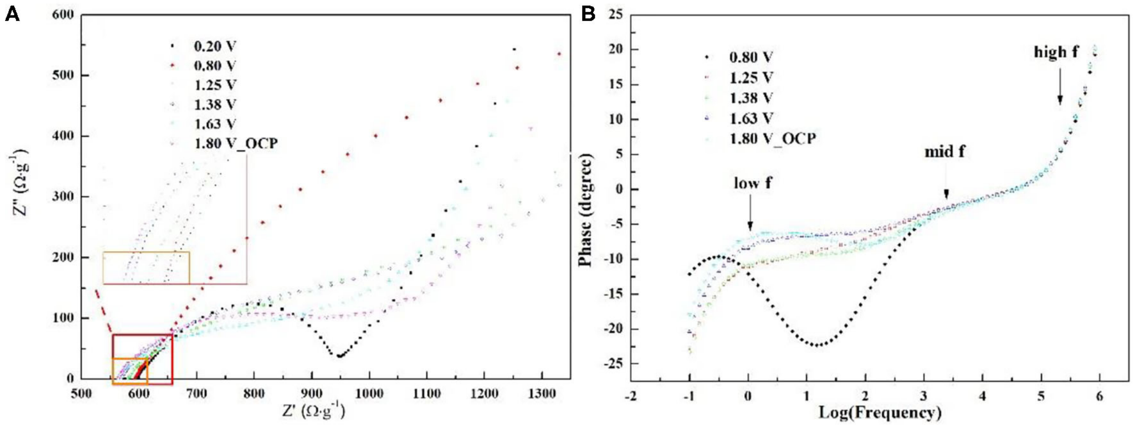

FIGURE 6 | Nyquist plots **(A)** and Bode plots **(B)** of the ZIB with S3, Zn foil, and 1 M $ZnSO_4$ in a CR2032 coin under different voltage (the chosen voltage was based on the platform and peak location in CV of S3).

TABLE 2 | List of EIS fitting parameters.

Voltage V	*Rs* $\Omega\cdot g^{-1}$	R_{CT} $\Omega\cdot g^{-1}$	*CPE-T* $F \times g^{-1}$	*CPE-P*	W_O-*R* $\Omega\cdot g^{-1}$	W_O-*P* s	W_O-*T*
0.8	592.6	2128.7	0.053	0.64	8.48	0.001	0.30
1.25	567.6	249.4	0.287	0.53	1377.78	4.917	0.34
1.38	556.5	305.4	0.160	0.56	1359.57	4.413	0.36
1.63	553.7	221.7	0.185	0.54	834.57	3.762	0.35

electrode surface. Consistently, a minimum *CPE-P* is obtained at 0.8 V due to the limited contribution from the double layer on near-surface. To conclude, during the operation window, the cell goes through a conversion from capacitive predominance to a fast charge transfer process involving extraction/insertion of Zn^{2+}.

CONCLUSION

The interfacial effect of three kinds of inorganic mild electrolyte on ZIBs performance have been investigated by electrochemical techniques. The construction of ZIBs includes Zn foil, graphite paper, and the chosen electrolyte. Through the comparison, it reveals that $ZnSO_4$ is the most preferred electrolyte among the chosen three. It provides faster Zn stripping/plating kinetics. And the electrolyte of $Zn(CH_3COO)_2$ exhibited the most promising alternative in the ZIB system. However, ZIB with $Zn(NO_3)_2$ as electrolyte exhibits poor performance. Even though the overall ZIB performance based on pristine graphite paper presents limited specific capacity. Therefore, an electro-activation method has been adopted for the activation of graphite paper. After the optimization, through the comparison, it was found that sample S3, activated at 6 V for 450 s in 2 M H_2SO_4, displays outstanding improvements. After the activation, firstly, the surface of S3 becomes rougher than the pristine one but intact as a whole rather than exhibiting the breaks seen in other samples; secondly, the coherency of its surface ensures a fast charge transfer kinetics reflected by CV with high current density and narrow half peak width; thirdly, the specific capacity based on CR2032 coin with S3 exhibits two orders of magnitude higher than the one with pristine graphite paper. Moreover, coin cell CR2032 with S3 also shows the highest specific capacity in this study.

DATA AVAILABILITY STATEMENT

All datasets generated for this study are included in the article/supplementary material.

AUTHOR CONTRIBUTIONS

YG designed experiments, carried out experiments, analyzed experimental results, and wrote the manuscript. BF supported required experimental instruments and helped revising the manuscript. YL supported required experimental instruments, publish payment, and helped revising the final manuscript. All authors contributed to the article and approved the submitted version.

FUNDING

This work was supported by Key Laboratory of Hubei Province for Coal Conversion and New Carbon Materials, School of Chemistry and Chemical Engineering, Wuhan University of Science and Technology, P. R. China (Project no. 1050010) and the National Nature Science Foundation of China (Project no. 21706198).

REFERENCES

Armand, M., and Tarascon, J. M. (2008). Building better batteries. *Nature* 451, 652–657. doi: 10.1038/451652a

Cheng, F., Chen, J., Gou, X., and Shen, P. (2005). High-power alkaline Zn-MnO_2 batteries using γ-MnO_2 nanowires/nanotubes and electrolytic zinc powder. *Adv. Mater.* 17, 2753–2756. doi: 10.1002/adma.200500663

Choi, J. W., and Aurbach, D. (2016). Promise and reality of post-lithium-ion batteries with high energy densities. *Nat. Rev. Mater.* 1:16013. doi: 10.1038/natrevmats.2016.13

Fan, J. X., Xiao, Q. Q., Fang, Y. B., Li, L., and Yuan, W. H. (2019) A rechargeable zn/graphite dual-ion battery with an ionic liquid-based electrolyte. *Ionics* 25, 1303–1313. doi: 10.1007/s11581-018-2644-x

Gui, Y., and Blackwood, D. J. (2015). Honey-comb structured WO_3/TiO_2 thin films with improved. *J. Electrochem. Soc.* 162, E205–E212. doi: 10.1149/2.0031510jes

Hwang, J. (2018). Symmetric cell electrochemical impedance spectroscopy of $Na_2FeP_2O_7$ positive electrode material in ionic liquid electrolytes. *J. Phys. Chem. C* 122, 26857–26864. doi: 10.1021/acs.jpcc.8b09233

Kim, H., Hong, J., Park, K. Y., Kim, H., Kim, S. W., and Kang, K. (2014). Aqueous rechargeable li and na ion batteries. *Chem. Rev.* 114, 11788–11827. doi: 10.1021/cr500232y

Konarov, A. K. A., Voronina, N., Jo, J. H., Bakenov, Z., Sun, Y. K., and Myung, S. T. (2018). Present and future perspective on electrode materials for rechargeable zinc-ion batteries, *ACS Energy Lett.* 3, 2620–2640. doi: 10.1021/acsenergylett.8b01552

Lee, B., Lee, H. R., Kim, H., Chung, K. Y., Cho, B. W., and Oh, S. H. (2015). Elucidating the intercalation mechanism of zinc Ions into α-MnO_2 for rechargeable zinc batteries. *Chem. Commun.* 51, 9265–9268. doi: 10.1039/C5CC02585K

Lee, B., Seo, H. R., Lee, H. R., Yoon, C. S., Kim, J. H., Chung, K. Y., et al. (2016). Critical role of ph evolution of electrolyte in the reaction mechanism for rechargeable zinc batteries. *Chem. Sus. Chem.* 9, 2948–2956. doi: 10.1002/cssc.201600702

Li, G., Yang, Z., Jiang, Y., Jin, C., Huang, W., Ding, X., et al. (2016). Towards polyvalent ion batteries: a zinc-ion battery based on NASICON structured $Na_3V_2(PO_4)_3$. *Nano Energy* 25, 211–217. doi: 10.1016/j.nanoen.2016.04.051

Li, S., Dong, Y., Xu, L., Xu, X., He, L., and Mai, L. (2014). Effect of carbon matrix dimensions on the electrochemical properties of $Na_3V_2(PO_4)_3$ nanograins for high-performance symmetric sodium-ion batteries. *Adv. Mater.* 26, 3545–3553. doi: 10.1002/adma.201305522

Lin, M. C., Gong, M., Lu, B., Wu, Y., Wang, D. Y., Guan, M., et al. (2015). An ultrafast rechargeable aluminium-ion battery. *Nature* 520, 324–328. doi: 10.1038/nature14340

Liu, Z., Bertram, P., and Endres, F. (2017). Bio-degradable zinc-ion battery based on a prussian blue analogue cathode and a bio-ionic liquid-based electrolyte. *J. Solid State Electrochem.* 21, 2021–2027. doi: 10.1007/s10008-017-3589-0

Liu, Z., Pulletikurthi, G., and Endres, F. (2016). A prussian blue/zinc secondary battery with a bio-ionic liquid-water mixture as electrolyte. *ACS Appl. Mater. Interfaces* 8, 12158–12164. doi: 10.1021/acsami.6b01592

Lu, J., Zhan, C., Wu, T., Wen, J., Lei, Y., Kropf, A. J., et al. (2014). Effectively suppressing dissolution of manganese from spinel lithium manganate via a nanoscale surface-doping approach. *Nat. Commun.* 5:5693. doi: 10.1038/ncomms6693

Lu, Y., Goodenough, J. B., and Kim, Y. (2011). Aqueous cathode for next-generation alkali-ion batteries. *J. Am. Chem. Soc.* 133, 5756–5769. doi: 10.1021/ja201118f

Muldoon, J., Bucur, C., and Gregory, T. (2014). Quest for nonaqueous multivalent secondary batteries: magnesium and beyond. *Chem. Rev.* 114, 11683–11720. doi: 10.1021/cr500049y

Pan, H., Shao, Y., Yan, P., Cheng, Y., Han, K. S., Nie, Z., et al. (2016). Reversible aqueous zinc/manganese oxide energy storage from conversion reactions. *Nat. Energy* 1:16039. doi: 10.1038/nenergy.2016.39

Parker, J. F., Chervin, C. N., Pala, I. R., Machler, M., Burz, M. F., Long, J. W., et al. (2017). Rechargeable nickel-3D zinc batteries: an energy-dense, safer alternative to lithium-ion *Science* 356, 415–418. doi: 10.1126/science.aak9991

Ponrouch, A., Frontera, C., Barde, F., and Palacin, M. R. (2016). Towards a calcium-based rechargeable battery. *Nat. Mater.* 15, 169–172. doi: 10.1038/nmat4462

Qiu, H. Y., Du, X. F., Zhao, J. W., Wang, Y. T., Ju, J. W., Chen, Z., et al. (2019). Zinc anode-compatible in-situ solid electrolyte interphase via cation solvation modulation. *Nat. Comm.* 10:5374. doi: 10.1038/s41467-019-13436-3

Suo, L., Borodin, O., Gao, T., Olguin, M., Ho, J., Fan, X., et al. (2015). "Water-in-Salt" electrolyte enables high-voltage aqueous lithium-ion chemistries. *Science* 350, 938–943. doi: 10.1126/science.aab1595

Wang, C., Appleby, A. J., and Little, F. E. (2001). Electrochemical study on nano-Sn, $Li_{4.4}$ Sn and $AlSi_{0.1}$ powders used as secondary lithium battery anodes. *J. Power Sources* 93, 174–185. doi: 10.1016/S0378-7753(00)00576-0

Wang, F., Borodin, O., Gao, T., Fan, X. L., Sun, W., Han, F. D., et al. (2018). Highly reversible zinc metal anode for aqueous batteries. *Nat. Mat.* 17, 543–549. doi: 10.1038/s41563-018-0063-z

Wang, Z., Li, H., Tang, Z., Liu, Z., Ruan, Z., Ma, L., et al. (2018). Hydrogel electrolytes for flexible aqueous energy storage devices. *Adv. Funct. Mater.* 28:1804560. doi: 10.1002/adfm.201804560

Whittingham, M. S. (2004). Lithium batteries and cathode materials. *Chem. Rev.* 104, 4271–4302. doi: 10.1021/cr020731c

Xu, C., Li, B., Du, H., and Kang, F. Y. (2012). Energetic zinc ion chemistry: the rechargeable zinc ion battery. *Angew. Chem. Int. Ed. Engl.* 51, 933–935. doi: 10.1002/anie.201106307

Yabuuchi, N., Kubota, K., Dahbi, M., and Komaba, S. (2014). Research development on sodium-ion battery. *Chem. Rev.* 114, 11636–11682. doi: 10.1021/cr500192f

Yamamoto, T., and Shoji, T. (1986). Rechargeable $Zn|ZnSO_4|MnO_2$-type cells. *Inorg. Chim. Acta* 117, L27–L28. doi: 10.1016/S0020-1693(00)82175-1

Yang, C., and Lin, S. (2002). Improvement of high-rate capability of alkaline Zn-MnO_2 battery. *J. Power Sources* 112, 174–183. doi: 10.1016/S0378-7753(02)00354-3

Yuan, D., Manalastas, W. Jr,, Zhang, L. P., Chan, J. J., Meng, S. Z., Chen, Y. Q., et al. (2019). Lignin@ nafion membranes forming zn solid-electrolyte interfaces enhance the cycle life for rechargeable zinc-ion batteries. *ChemSusChem* 12, 4889–4900. doi: 10.1002/cssc.201901409

Zhang, N., Cheng, F. Y., Liu, Y. C., Zhao, Q., Lei, K. X., Chen, C. C., et al. (2016). Cation-deficient spinel $ZnMn_2O_4$ cathode in $Zn(CF_3SO_3)_2$ electrolyte for rechargeable aqueous zn-ion battery. *J. Am. Chem. Soc.* 138, 12894–12901. doi: 10.1021/jacs.6b05958

Zhao, H., Xu, J., Yin, D., and Du, Y. (2018). Electrolytes for batteries with earth-abundant metal anodes. *Chem. Eur. J.* 24, 18220–18234. doi: 10.1002/chem.201802438

Zhao, J., Ren, H., Liang, Q. H., Yang, D., Xi, S. B., Wu, C., et al. (2019). High-performance flexible quasi-solid-state zinc-ion batteries with layer-expanded vanadium oxide cathode and zinc/stainless steel mesh composite anode. *Nano Energy* 62, 94–102. doi: 10.1016/j.nanoen.2019.05.010

Conflict of Interest: The authors declare that the research was conducted in the absence of any commercial or financial relationships that could be construed as a potential conflict of interest.

Advantages of publishing in Frontiers

OPEN ACCESS
Articles are free to read
for greatest visibility
and readership

FAST PUBLICATION
Around 90 days
from submission
to decision

HIGH QUALITY PEER-REVIEW
Rigorous, collaborative,
and constructive
peer-review

TRANSPARENT PEER-REVIEW
Editors and reviewers
acknowledged by name
on published articles

Frontiers
Avenue du Tribunal-Fédéral 34
1005 Lausanne | Switzerland

Visit us: www.frontiersin.org
Contact us: info@frontiersin.org | +41 21 510 17 00

REPRODUCIBILITY OF RESEARCH
Support open data
and methods to enhance
research reproducibility

DIGITAL PUBLISHING
Articles designed
for optimal readership
across devices

FOLLOW US
@frontiersin

IMPACT METRICS
Advanced article metrics
track visibility across
digital media

EXTENSIVE PROMOTION
Marketing
and promotion
of impactful research

LOOP RESEARCH NETWORK
Our network
increases your
article's readership